Aberrant Epigenetic Patterning Defines an Aggressive Molecular Subtype of Adrenocortical Carcinoma and Exposes a Tissue-Specific Therapeutic Vulnerability

by

Dipika R. Mohan

A dissertation submitted in partial fulfillment
of the requirements for the degree of
Doctor of Philosophy
(Cancer Biology)
in the University of Michigan
2021

Doctoral Committee:

Professor Gary D. Hammer, Chair
Associate Professor Sundeep Kalantry
Associate Professor Andrew G. Muntean
Associate Professor Sriram Venneti
Professor Thomas E. Wilson

Dipika R. Mohan

drmohan@umich.edu

ORCID iD: 0000-0002-6334-9416

DEDICATION

To Drew, and all the patients and their families,

who have selflessly given all they can to help us find a cure.

To my future patients, who motivate me always. This work is for you.

To my parents, who have given me everything.

To my sister, who grows with me every day.

To my partner, who inspires me through every moment.

ACKNOWLEDGEMENTS

This work would not be possible without the contributions of many people who have enabled our research and my personal development.

First, I would like to thank all the patients and their families who have not only donated samples for our studies, but contributed their time and efforts toward advocacy to advance research and care to fight adrenal cancer. You are the reason for this work, and kept me going through every moment of my PhD. I would especially like to thank Sean, Lisa, and Patrick O'Donoghue, and the board members of the Drew O'Donoghue Fund, for supporting me and supporting our team. You made it all possible!

I would like to express my sincere appreciation and gratitude to my research advisor and Doctoral Committee Chair, Gary D. Hammer, MD, PhD, for his ideas, enthusiasm, lessons in leadership, and always encouraging my independence. Gary, your work to create an Adrenal Cancer program and lead large international efforts like The Cancer Genome Atlas on ACC is truly inspirational. I am so grateful that you have given me the freedom to follow the science, countless opportunities to excel beyond what is typically required of a graduate student, and the mechanism to start translating our scientific discoveries to clinic. Your confidence in my abilities and scientific aptitude has helped me in so many ways, especially during those moments of uncertainty that seem

to last forever in a PhD. I would also like to thank the other members of my Doctoral Committee – Sundeep Kalantry, PhD; Andrew G. Muntean, PhD; Sriram Venneti, MD, PhD; Thomas E. Wilson, MD, PhD. Thank you so much for your time, your expertise in genetics and epigenetics, your focused guidance through the years, your collaboration, and for always challenging me to get better! I have grown enormously as a scientist with your support, and I absolutely could not have dreamed up a better committee. I am honored to have your names on the cover page of my thesis.

I would like to express my deepest gratitude to Antonio Marcondes Lerario, MD, PhD, Assistant Research Scientist in the Hammer lab, whom I have been immensely fortunate to work with throughout my PhD. Antonio, I am so grateful for your endless support, guidance, mentorship and friendship through the years. I truly believe my training is as important to you as it is to me. I hope that one day I become a physician scientist even infinitesimally as brilliant, curious, thoughtful, and compassionate as you. Thank you for being there for every moment – the Eureka!'s, rejections, thought experiments, awards, failures, and the in between – and for always making sure I had the opportunity to experience the joy of discovery and witness the beauty of science and medicine. OVOL1 p.U4L!

I would also like to thank current and former members of the Hammer lab for supporting me and my quirks, always being willing to sit through my (data dump) presentations, and resetting my perspective especially during the many times I tried to abandon my hypotheses. I would especially like to thank Isabella Finco, PhD, a former Research Investigator in our group, for her kindness, insights, patience, and willingness

to teach me anything and everything. Isabella, you are such a wonderful teacher and I have learned so much from you! Your insights and inspiring work developing an ACTH-dependent adrenal regeneration model have irreplaceably advanced our ability to explore the physiological roles of these epigenetic programs and place our findings in context. You helped me every step of the way – from performing our PLA rituals when the moon was in the fifth house of Capricorn to even reading through and giving me feedback on my thesis. *Vade retro beta catenina!* I would also like to thank Christopher R. LaPensee, PhD, Assistant Research Scientist in the Hammer lab (and lab manager), for his support and dedication to keeping the wheels turning. Chris, thank you for taking the time to elevate our work by leading the ATAC-seq efforts, your continued willingness to help me advance the project in any way you can, and your magic with finessing all my last-minute orders. I would also like to thank Donald W. Little, III, soon to be PhD in the Hammer lab, for his support, encouragement, and willingness to help always. Donald, I am so glad I had the opportunity to train alongside you! Thank you for being the best kind of team mate – willing to go on coffee breaks, commiserate, give gentle advice on presentations, and tag-team mouse experiments with me during COVID. I hope I can audit one of your courses one day.

Our work would be impossible without our local and international network of collaborators (many of whom I have already thanked). I would especially like to thank a few of our collaborators at Faculdade de Medicina da Universidade de Sao Paulo. Suely K. N. Marie, MD, PhD – Professora, thank you so much for your unconditional support, generous collaboration, and for opening up your lab and resources to Antonio and me so

that we could begin investigating the molecular roles of these epigenetic modifiers in ACC and develop our biomarker assay together. Your confidence, insights, encouragement, and warmth has helped me and our project in so many ways, and I am so honored and appreciative to work in your team! Berenice B. Mendonca, MD, PhD – Professora, thank you for your willingness to share the truly precious resources of LIM42 with Antonio and me, and for having the confidence that our work would translate to meaningful outcomes for patients with adrenal disease. Maria Candida B. V. Fragoso, MD, PhD – Professora, thank your encouragement, kindness, support, and confidence in our work. I am so grateful that I had the opportunity to develop a translational research project throughout my PhD, and that is in large part thanks to your collaboration and enthusiasm!

I would also like to thank the Michigan Adrenal Research Group, especially Thomas J. Giordano, MD, PhD; William E. Rainey, MD, PhD; and Tobias Else, MD. Thank you so much for your support, connecting me to researchers in your team, coming to my research in progress seminars, sharing samples, and always giving me constructive feedback and great advice. I would also like to especially thank Juilee Rege, PhD, for her insights, support, and always being willing to spend time to share her expertise!

I would like to additionally acknowledge several investigators and research teams we have had the opportunity to work with. Thank you all for your collaboration that has been absolutely essential to our work!:

University of Michigan, Ann Arbor, MI, USA: Bhramar Mukherjee, PhD; Michelle Vinco, MS; April Solon, Ryoma Ohi, PhD; April Apfelbaum, Elizabeth R. Lawlor, MD, PhD (now at Seattle Children's, Seattle, WA, USA)

Faculdade de Medicina da Universidade de Sao Paulo, Sao Paulo, BR: Sueli Oba-Shinjo, PhD, Stella Goncalves, Isabele F. Moretti; Beatriz M. P. Mariani; Madson Q. Almeida, MD, PhD; Maria Claudia N. Zerbini, MD, PhD, Alda Wakamatsu, MS; Ana Claudia Latronico, MD, PhD; Claudimara Lotfi, PhD

Harvard Medical School, Boston, MA, USA: Kleiton S. Borges, PhD; David T. Breault, MD, PhD

I am fortunate to be part of an incredible graduate program and dual degree MD/PhD program. I would like to thank the Doctoral Program in Cancer Biology for the Program's tremendous support through the years, especially Director David B. Lombard, MD, PhD, and the amazing Dawn Storball, MSW.

I would also like to thank the Medical Scientist Training Program (MSTP). I would especially like to thank our former Director, Ronald J. Koenig, MD, PhD – Ron, you are a true inspiration and I am so honored to have been part of the program under your direction! Thank you so much for your thoughtful advice and perennial support. I would also like to thank everyone in the MSTP office, but especially Justine Hein. Justine, thank you for always looking out for me and keeping our Program running smoothly!

I have been very fortunate to have amazing mentors at every step of my research journey, and would not be at this stage without them. I would especially like to thank Timothy A. Graubert, MD, for his incredible mentorship and unconditional support during my undergraduate and beyond. Dr. Graubert, you helped me to realize how much I loved asking questions and solving biological puzzles (even when they are not solvable), and inspired me to start the journey of becoming a physician scientist. I am so grateful for your

time, thoughtfulness, encouragement, and honest, always perfect advice. I am delighted that I had the chance to share a little piece of Ann Arbor with you! I would also like to thank Theresa Okeyo-Owuor, PhD, who not only taught me how to think about biology while she was a graduate student in the Graubert lab, but also taught me almost every molecular biology skill I needed to know. Treeza, thank you for always encouraging me to be classy and sassy, your mentorship and friendship, and for converting me from a pre-med student to a scientist. And to both of you – for training me to do so many Western blots using Santa Cruz antibodies, milk, homemade gels, and film, that I became a Western pro (see **Chapters 3, 5, 6**)! I would also like to thank Jonathan Wren, PhD, for his guidance and support during such a formative time in my career. Dr. Wren, thank you for giving me the chance to pick up a pipet for the first time when I was just out of high school, and for helping me to see the beauty and power in thinking logically and philosophically about science.

Last but in no way least, I would like to thank my family and friends, especially my parents, sister, and partner. Mama, Daddy (the original Dr. Mohan), Preeti (soon to be second Dr. Mohan), and Trey, words cannot express how deeply grateful I am for your boundless love, support, encouragement, and willingness to be my *ad hoc* thesis advisors, so I am not going to try. Thank you for always believing in me and helping me find my way.

Financial Support: University of Michigan Medical Scientist Training Program (fellowship support from T32 GM7863 to DRM), the Doctoral Program in Cancer Biology (scholarship

to DRM), the Drew O'Donoghue Fund (funding to GDH/our adrenal cancer research program and scholarship to DRM), Rogel Cancer Center (grant to GDH and scholarship to DRM), Rackham Graduate School (award and grant to DRM), and United States Department of Defense (CA180750, CA180751 to GDH).

TABLE OF CONTENTS

LIST OF TABLES

LIST OF FIGURES

LIST OF APPENDICES

LIST OF ABBREVIATIONS, ACRONYMS, AND ALIASES

ACA: adrenocortical adenoma(s)

ACC: adrenocortical carcinoma(s); adrenal cancer(s)

ACC-TCGA: The Cancer Genome Atlas study on ACC

ACT: adrenocortical tumor(s)

ACTH: adrenocorticotropic hormone

AngII: angiotensin II

ATAC-seq: assay for transposase-accessible chromatin sequencing

ATC7L: murine ACC cell line derived from mouse expressing adrenocortical SV40 Tag

AR: autosomal recessive

AD: autosomal dominant

β-catenin: canonical transcriptional co-activator of the Wnt pathway, encoded by *CTNNB1*

bp: base pair

cAMP: cyclic AMP

CBP: CREB-binding protein, encoded by *CREBBP*

CBPi: CBP inhibition/inhibitor, e.g. PRI-724

cDNA: complementary DNA

ChIP-seq: chromatin immunoprecipitation sequencing

CIMP-low/-int/-high: CpG island methylator phenotype low/intermediate/high

co-IP: complex immunoprecipitation

CpGi: CpG island

CRE: *Cis*-regulatory element

C_t: copy threshold

DFS: disease-free survival

DMR: differentially methylated region

DMSO: dimethyl sulfoxide; alias for DMS

DNMT: DNA methyltransferase, e.g. DNMT1, encoded by *DNMT1*

EED: embryonic ectoderm development, encoded by *EED*

EZH2: enhancer of zeste 2 polycomb repressive complex 2 subunit, encoded by *EZH2*

EZH2i: EZH2 inhibition/inhibitor, e.g. GSK126, EED226, EPZ-6438

FFPE: formalin-fixed, paraffin-embedded

FPKM: fragments per kilobase of transcript per million mapped reads

FSK: Forskolin

gDNA: genomic DNA

GOF: gain of function

GPCR: G protein-coupled receptor

G0S2: G0/G1 switch 2, encoded by *G0S2*

H3K27ac: histone H3 lysine 27 acetylation

H3K27me/me2/me3: histone H3 lysine 27 mono-/di-/tri-methylation

H3K27MT: H3K27 methyltransferase, e.g. EZH2

ICR: imprinting control region

IP-MS: complex immunoprecipitation mass spectrometry

kb: kilobase

LiCl: lithium chloride

log_2FC (A/B) or log_2FC (A v. B): logarithm base 2 of the ratio (fold change) of A over B

LOF: loss of function

MC2R: G_s-coupled GPCR for ACTH, encoded by *MC2R*

Neo: neomorph function

NCI-H295R: human ACC cell line

NGS: next generation sequencing

NR5A1: nuclear receptor subfamily 5 group A member 1; alias for SF1, AD4BP

OS: overall survival

PKA: protein kinase A

PLA: proximity ligation assay

PRC2: Polycomb repressive complex 2

PCL: Polycomb like PRC2 accessory protein

qPCR: quantitative polymerase chain reaction

RNA-seq: RNA sequencing

RPKM: reads per kilobase of transcript per million mapped reads

SE: super-enhancer

SF1: steroidogenic factor 1, encoded by *NR5A1*; alias for NR5A1, AD4BP

siRNA: small interfering RNA

SpC: spectral counts

SUZ12: SUZ12 polycomb repressive complex 2 subunit, encoded by *SUZ12*

SV40 Tag: simian virus 40 large T antigen

SWI/SNF: ATP-dependent chromatin remodeling complex

SW13: undifferentiated SWI/SNF-deficient cancer cell line, derived from cancer presenting in adrenal cortex

TAD: topology associated domain

TCF/LEF: transcriptional effectors of the canonical Wnt pathway, drive transcription through complexing with β-catenin; relevant LEF family member encoded by *LEF1*

TF: transcription factor

TSS: transcription start site

Wnt: paracrine signal that stimulates β-catenin/TCF/LEF-dependent transcription to effect stem/progenitor maintenance in many tissues including the adrenal cortex

XLR: X-linked recessive

XLD: X-linked dominant

Y1: murine ACC cell line

zF: adrenocortical zona fasciculata

zG: adrenocortical zona glomerulosa

zR: adrenocortical zona reticularis

5mC: 5-methylcytosine

450k array: Illumina Infinium HumanMethylation450 BeadChip

850k array: Illumina Infinium MethylationEPIC Array

ABSTRACT

The adrenal glands are endocrine organs that produce steroid hormones and catecholamines critical for life. Adrenocortical carcinoma (ACC) is a rare cancer of these glands. Up to 75% of patients with ACC develop metastases, for which therapies are limited and ineffective. Standard of care for metastatic disease comprises administration of the adrenolytic agent mitotane +/- cytotoxic chemotherapy, sometimes paired with palliative local therapies, but <10% of patients survive beyond five years. These statistics highlight an urgent need for novel medical therapies for ACC, contingent on a deeper understanding of targetable molecular circuits driving this disease.

Advances in high-throughput profiling of genetic, epigenetic, and transcriptional programs have revolutionized our understanding of molecular predictors of disease states. Through such studies, we identified that tumors of patients with uniformly rapidly recurrent, routinely fatal ACC (comprising ~40% of all ACC) are characterized by an epigenetic signature of DNA hypermethylation directed to CpG islands, “CIMP-high.” We show these genomic regions are protected from methylation in physiological tissues including the adrenal gland, suggesting cancer-specific mechanisms drive aberrant epigenetic patterning. The focus of this dissertation is to characterize CIMP-high ACC as a molecular subtype from a pan-genomic perspective, to develop a strategy enabling

prospective biomarker-based identification of CIMP-high ACC, and to investigate the biological consequences of CpG island hypermethylation.

Here, we re-analyze publicly available datasets including The Cancer Genome Atlas study on ACC (ACC-TCGA) to demonstrate CIMP-high ACC is a homogeneous molecular subtype characterized by hyperactivation of three programs: steroidogenic differentiation, coordinated by master adrenal transcription factor SF1; stemness, through somatic alterations driving constitutive activation of Wnt/β-catenin; and proliferation, through somatic alterations in cell cycle regulators. To enable prospective identification of CIMP-high ACC, we leverage ACC-TCGA to identify a locus that is hypermethylated and silenced exclusively in CIMP-high ACC (*G0S2*) and develop and validate an overnight biomarker assay in an independent cohort of >100 adrenocortical tumors.

In most human cancers, rapid proliferation and CpG island hypermethylation is associated with increased stemness at the expense of differentiation; the convergence of these programs in CIMP-high ACC is paradoxical. We identify that DNA hypermethylation is directed to embryonic targets of a complex known to suppress differentiation, the Polycomb repressive complex 2 (PRC2). PRC2 represses gene expression through EZH2-mediated histone H3 lysine 27 trimethylation (H3K27me3), and DNA methylation at these sites may hamper PRC2 activity. We show CIMP-high ACC exhibit high expression of EZH2/H3K27me3 despite DNA methylation and use high-throughput approaches to demonstrate: the most widely used *in vitro* model of ACC is CIMP-high, EZH2 assembles in a DNA methylation-sensitive PRC2 complex, EZH2 is globally excluded from hypermethylated regions, and EZH2 catalytic activity does not coordinate

DNA methylation. We then show EZH2 catalytic activity is required for sustained proliferation *in vitro* and identify two novel complexes coordinating transcriptional programming in ACC, SF1/β-catenin and EZH2/β-catenin, that are conserved in mouse models of adrenal carcinogenesis. Finally, we show SF1/β-catenin globally coordinates a cancer-specific and physiological steroidogenic differentiation program that is stabilized in CIMP-high ACC and erased by EZH2 inhibition.

Taken together, our studies illustrate how CpG island hypermethylation defines an ACC molecular class and exposes a tissue-specific therapeutic vulnerability centered on the pharmacologically targetable enzyme EZH2. Ultimately, we hope this work enables prospective molecular subtyping of ACC and illuminates novel strategies for tissue-specific disruption of the aberrant epigenetic wiring supporting this devastating disease.

CHAPTER 1. Epigenetics, Tissue Specificity, and Cancer

1.1. Disclosure of relevant publications

Portions of this work are being prepared for publication:

> **Mohan DR**, Borges KS, Finco I, LaPensee CR, Solon A, Rege J, Little III DW, Else T, Almeida MQ, Apfelbaum A, Vinco M, Wakamatsu A, Mariani BMP, Latronico AC, Mendonca BB, Zerbini MCN, Fragoso MCBV, Lawlor ER, Ohi R, Rainey WE, Venneti S, Marie SKN, Giordano TJ, Breault DT, Lerario AM*, Hammer GD*. A differentiation program coordinated by SF1/β-catenin is a targetable epigenetic vulnerability in aggressive adrenocortical carcinoma. In preparation. *co-senior author

1.2. Introduction

DNA is the genetic material of every organism, instructing development, forming the basis for inheritance, and templating evolution. Each eukaryotic cell packages meters of DNA into a micron-scale nucleus, and this physical compartmentalization is achieved through several levels of organization. At a rudimentary level, DNA is spun around an octamer of closely related proteins, histones, forming chromatin. The association between DNA and histones, and accessibility of encoded information therein, is proximally influenced by covalent chemical modifications on DNA and histone tails. Through short- and long-range contacts, chromatin is further compacted into gene regulatory domains (topology associated domains, (Dixon et al., 2012)), and these domains are assembled into larger active and inactive compartments (Lieberman-Aiden et al., 2009). These

organizing principles enable context-specific gene expression and underlie the diversity of transcriptional programs deployed in different cell types, tissues, and disease states. Our work seeks to understand how cancer-specific changes in chromatin enable context-dependent sustained proliferation and expose therapeutic vulnerabilities, using a rare cancer of the adrenal gland (adrenocortical carcinoma, ACC) as a model. Here, I will briefly overview core principles of epigenetics and cancer to place the scope of this thesis in context.

1.3. Epigenetics overview

Epigenetics refers to heritable alterations to the genome that modify how genetic programs are expressed without changes to the underlying DNA sequence. Principles of chromatin organization provide a molecular platform for epigenetics and allow a multiplicity of cell types to arise from the same genome in multicellular organisms. Covalent chemical modifications on histone tails and DNA demarcate *cis*-regulatory elements in the genome (**Table 1.1**) for activation or repression, and may combine with other modifications to create a combinatorial gene regulatory code.

Table 1.1. *Cis*-regulatory elements and definitions.

Term	Definition
Cis-regulatory element (CRE)	Non-coding region of the genome bearing motifs or consensus sequences that enable binding of transcription factors (TF), transcriptional machinery, or other proteins/complexes required for activation or maintenance of gene expression. CREs can be proximal or distal to the target gene, and a single CREs may control one or many genes.
Promoter	CRE proximal to target gene transcription start site (TSS); definition of proximal varies, typically anywhere from +/- 2000 bp. Includes motifs or other consensus sequences that enable binding of proteins (e.g. transcription factors, basal transcriptional machinery) that activate gene expression in response to relevant cues.
Enhancer	CRE distal to the TSS of target gene and may be upstream or downstream of TSS; definition of distal varies, typically on the order of multiple kb. A single enhancer may control expression of multiple genes and contain consensus sequences or motifs that enable transcription factor control. Though enhancers are distal from target genes in terms of the linear DNA sequence, enhancer control of gene expression is often mediated topologically, through enhancer-promoter contacts (Jung et al., 2019; Sanyal et al., 2012).
Insulator	Long-range CRE that may contain motifs for DNA binding proteins such as CTCF. Insulators can restrict the range of enhancer action by enabling binding of proteins that instruct 3D chromatin structure (e.g. loops) that prevent formation of undesirable enhancer-promoter contacts and restrict enhancer actions to a given topology associated domain (TAD, (Dixon et al., 2012)). Insulators may also serve a barrier function by recruiting proteins that restrict the spread of repressive chromatin.

Active chromatin often coincides with genomic regions that are open and accessible for binding of tissue-specific and basal *trans* factors like transcription factors and machinery that initiate transcription. A special class of transcription factors, pioneer transcription factors, can open inaccessible regions of the genome directly or through recruitment of chromatin remodeling complexes, enabling tissue differentiation (Iwafuchi-Doi and Zaret, 2014). Repressive chromatin often coincides with regions of the genome that are inaccessible to most *trans* factors that activate or sustain transcription, excepting pioneers (Iwafuchi-Doi and Zaret, 2014). In each cell type this repressive state may be transient and/or poised/primed to respond to external cues (Bernstein et al., 2006), or permanent independent of the environment (Hawkins et al., 2010). Cellular and tissue specificity of transcriptional programs is conferred by varying patterns of active and repressive chromatin genome-wide (Hawkins et al., 2010), and variable expression of *trans* factors, a concept that has been reinforced by recent landmark studies performing molecular profiling of single cells (Cao et al., 2020; Domcke et al., 2020; Han et al., 2020). Deposition of epigenetic marks that define chromatin states is catalyzed by specialized enzymes and complexes (“writers”), interpreted by specific proteins (“readers”), and removed by an entirely different class of enzymes and complexes (“erasers”). Examples of relevant epigenetic marks and their regulation are detailed in **Table 1.2.**

Table 1.2. Overview of relevant epigenetic code.

Substrate	Epigenetic mark	Genomic location/CRE targeted	Gene expression impact	Writer	Reader	Eraser
Histone	H3K27ac	promoters, enhancers	activating	CBP, p300	BET	HDAC
Histone	H3K27me3	promoter CpGi, intergenic, enhancers	repressive	PRC2	PRC2, PRC1	KDM6A-C, KDM7A
Histone	H3K4me1	enhancers	activating, poising, priming	COMPASS (MLL)	mSWI/SNF	KDM1A/B
Histone	H3K4me3	promoters	activating, poising	COMPASS (MLL, SET1)	many proteins, often through PHD domain	KDM5A-D
Histone	H3K9me3	pericentromeric, coding, intergenic, repetitive elements	repressive	SUV39H, SETDB1, G9a/GLP, PRDM	HP1	KDM3,4,7
Histone	H3K36me3; H3K36me2	gene bodies, promoters; intergenic	activating, mixed; repressive	NSD, SETD2	PRC2 via PCL, DNMT3A, NSD2	KDM2A-B, KDM4A-D
Histone	H2AK119ub	promoter CpGi	repressive	PRC1	PRC2	PR-DUB
DNA	5mC	CpG motifs in promoters, repetitive elements; gene bodies; insulators	repressive; activating; mixed	DNMT	traditionally MBD, but DNA methylation may affect binding of other proteins	TET

NOTE. List of writers, readers, and erasers may not be complete for a given epigenetic mark. H3K27ac/me3 = histone H3 lysine 27 acetylation/trimethylation; H3K4me1/me3 = histone H3 lysine 4 monomethylation/trimethylation; H3K9me3 = histone H3 lysine 9 trimethylation; H3K36me3/me2 = histone H3 lysine 36 trimethylation/dimethylation H2AK119ub = histone H2A lysine 119 monoubiquitination; 5mC = 5-methylcytosine; CpGi = CpG island; PRC2/1 = Polycomb repressive complex 2/1; MLL = mixed lineage leukemia family of K4 methyltransferases; SET1 = SET1 family of H3K4 methyltransferases; NSD = NSD family of H3K36 methyltransferases; DNMT = DNA methyltransferase; BET = bromodomain and extraterminal motif protein family; mSWI/SNF = mammalian SWI/SNF ATP-dependent chromatin remodeling complex; HP1 = heterochromatin protein 1; PCL = Polycomb like PRC2 accessory protein; HDAC = histone deacetylase family; KDM = lysine demethylase family; PR-DUB = Polycomb repressive deubiquitinase complex; TET = ten-eleven translocation methylcytosine dioxygenase family.

Many epigenetic programs are highly conserved across eukaryotes (conservation of two key programs are depicted in **Figure 1.1**) and are critical for embryonic development and appropriate differentiation of tissues and organs. Indeed, germline alterations in epigenetic machinery are associated with numerous multi-organ clinical syndromes. The broad spectrum of phenotypes associated with these syndromes underscores the essential, diverse, and often tissue-specific roles epigenetic modifiers adopt in development and homeostasis, and illuminates promising molecular avenues for investigation that are only beginning to be explored (**Table 1.3**). I will now discuss two epigenetic modifications/programs that will be studied in detail in this thesis, 5-methylcytosine (5mC) DNA methylation mediated by DNA methyltransferases (DNMTs) and histone H3 lysine 27 trimethylation (H3K27me3) mediated by the Polycomb repressive complex 2 (PRC2).

						Metazoa				
Complex	**Membership**	**Protein**	**Plantae**	**Fungi**	**Choanoflagellata**	**Ctenophora**	**Porifera**	**Placozoa**	**Cnidaria**	**Bilateria**
PRC2	core	EZH1-2	■	■	■	■	■	■	■	■
PRC2	core	SUZ12	■	■	■	■	■	■	■	■
PRC2	core	EED	■	■	■	■	■	■	■	■
PRC2	accessory	PCL1-3				■	■	■	■	■
PRC2	accessory	JARID2				■	■	■	■	■
PRC2	accessory	AEBP2			■	■	■	■	■	■
PRC2	accessory	EPOP								■
PRC2	accessory	LCOR								■
DNMT	core	DNMT1	■	■		■	■		■	■
DNMT	core	DNMT3A/B	■				■		■	■

Figure 1.1. PRC2 and DNMT machinery are conserved across eukaryotes.
Adapted from (Schuettengruber et al., 2017). Presence of orthologs in at least one organism in indicated phyla denoted by shaded box. Conservation data for DNMTs obtained from (Dabe et al., 2015; Zemach and Zilberman, 2010). Note that some DNMTs are partially conserved down to prokaryotes (Bhattacharyya et al., 2020). Intriguingly, despite its strong conservation, DNA methylation is absent from the genomes of some frequently used model organisms, like *C. elegans* and *D. melanogaster* (Greenberg and Bourc'his, 2019).

Table 1.3. Examples of germline mutations in epigenetic modifiers that cause human disease.

Gene	Func.	Mut.	Inherit.	Phenotype	Molecular features	OMIM/Reference
DNMT1	5mC writer	LOF	AD	Hereditary sensory neuropathy type IE – adult-onset peripheral sensory loss, deafness, dementia; Adult-onset ataxia, deafness, narcolepsy, dementia	Global DNA hypometh. including at PRC2 targets	OMIM 614116; OMIM 604121; (Sun et al., 2014)
DNMT3A	5mC writer; H3K36me2/3 reader	Neo; LOF	AD	Microcephalic dwarfism; Tatton-Brown-Rahman syndrome – overgrowth/intellectual disability spectrum with increased susceptibility to AML	DNA methylation directed to PRC2 targets; intergenic DNA hypometh.	(Heyn et al., 2019; Weinberg et al., 2019); OMIM 615879
DNMT3B	5mC writer	partial LOF	AR	Immunodeficiency-centromeric instability-facial anomalies syndrome 1, includes developmental delay	Chromosomal rearrangements, pericentromeric hypomethylation	OMIM 242860
MECP2	DNA methylation reader	LOF	XLD; XLR	Rett syndrome – microcephaly, seizures, developmental arrest and regression at 6-18 months with intellectual disability, stereotyped hand movements and speech loss; other intellectual disability or encephalopathy	Altered chromosomal topology	OMIM 300005; OMIM 312750; (Xiang et al., 2020)
NSD1	H3K36me2 writer	LOF	AD	Sotos syndrome – overgrowth/ID spectrum with accelerated bone maturation, and characteristic craniofacial features (enlarged skull, pointed chin), brain anomalies, seizures	Intergenic DNA hypometh.	OMIM 117550
EZH2	PRC2 catalytic member; H3K27me3 writer	LOF	AD	Weaver syndrome – overgrowth/ID with macrocephaly, accelerated bone maturation, and characteristic craniofacial features (e.g. micrognathia, long philtrum, down-slanting palpebral fissures large bifrontal diameter), soft and doughy skin, low-pitched cry	PRC2 LOF DNA meth. signature	OMIM 277590; (Choufani et al., 2020)
EED	PRC2 member	LOF	AD	Cohen-Gibson syndrome, similar to Weaver syndrome and along overgrowth/ID spectrum	PRC2 LOF DNA meth.signature	OMIM 617561; (Choufani et al., 2020)
SUZ12	PRC2 member	LOF	AD	Imagawa-Matsumoto syndrome, similar to Weaver syndrome and along overgrowth/ID spectrum	PRC2 LOF DNA meth.signature	OMIM 618786; (Choufani et al., 2020)
CREBBP	H3K27ac writer	LOF	AD	Menke-Hennekam syndrome 1 – intellectual disability, short stature, microcephaly, autism, characteristic facial features; Rubinstein-Taybi syndrome 1 – characteristic facies (downslanted palpebral fissures, arched eyebrows, long eyelashes, abnormal smile, micrognathia), intellectual disability, growth deficiency, microcephaly	Disrupted histone acetyltransferase activity; genome-wide consequences not well understood	OMIM 618332; OMIM 180849

(Table continued on next page)

Gene	Func.	Mut.	Inherit.	Phenotype	Molecular features	OMIM/Reference
SMARCB1	mSWI/SNF member	LOF	AD	Coffin-Siris syndrome 3 – intellectual disability, developmental delay, hypoplastic fifth digits, seizures, microcephaly, feeding difficulties; susceptibility to rhabdoid tumors; susceptibility to schwannomatosis	Disruption in mSWI/SNF ATPase activity and/or genome-wide recruitment	OMIM 601607; (Valencia et al., 2019)

NOTE. Func. = physiological function; Mut. = mutation impact on protein function; Inherit. = inheritance; LOF = loss of function; Neo = neomorph function; AD = autosomal dominant; XLR/XLD = X-linked recessive/dominant; ID = intellectual disability; AML = acute myeloid leukemia; -meth/meth.= methylation. Note that many of these germline mutations present *de novo*.

1.4. DNA methylation – roles, regulation and conservation

DNA methylation is an ancient epigenetic modification (**Figure 1.1**, (Zemach et al., 2010)) and in eukaryotes is often deposited as 5mC on cytosines in CpG dinucleotide motifs (**Table 1.2**). The genomic distribution of 5mC is dynamically remodeled during fetal development, tissue differentiation, aging, and disease (**Table 1.3**, (Greenberg and Bourc'his, 2019; Horvath, 2013; Lister et al., 2009; Maegawa et al., 2010; Wang et al., 2014)). In humans, 5mC is written by three catalytically active DNMTs (DNMT1, DNMT3A, DNMT3B, conservation depicted in **Figure 1.1**), and germline mutations in these enzymes cause human disease (**Table 1.3**). DNMT1 is widely considered to have maintenance methyltransferase activity, bearing higher affinity for hemi-methylated DNA (Pradhan et al., 1999) and enabling faithful transmission of DNA methylation signatures through cell divisions and guarding against aneuploidy (Chen et al., 2007), though recent evidence suggests in some contexts it can write DNA methylation *de novo* (Li et al., 2018). DNMT3A and DNMT3B are considered *de novo* methyltransferase enzymes, capable of writing 5mC on unmethylated DNA and required for establishment of the methylation landscape in embryonic development (Okano et al., 1999). 5mC is erased through oxidation by TET enzymes (**Table 1.2**), a mechanism that is metabolically inhibited in some cancers (discussed in section **1.6**).

DNA methylation is classically involved in dosage compensation, e.g. X-chromosome inactivation to equalize male and female genomes in mammals (Mohandas et al., 1981). Like many epigenetic modifications, DNA methylation is also involved in

genomic imprinting at imprinting control regions (ICRs; these CREs are typically classified as insulators, **Table 1.1**) that instruct allele-specific gene expression and may interface with non-coding RNAs (Monnier et al., 2013). Appropriate global genomic imprinting is required for embryonic viability (McGrath and Solter, 1984; Surani et al., 1984), and locus-specific disorders in imprinting are the root cause of several fetal- and pediatric-onset clinical syndromes (**Table 1.4**).

Table 1.4. Examples of human disease caused by germline defects in imprinting.

Syndrome	Mutation	Molecular consequence	Phenotype	OMIM/Ref.
Beckwith-Wiedemann syndrome	Molecular aberrations at 11p15; hypermeth. of *H19/IGF2* ICR1, mutations in *CDKN1C*, hypometh. of *KCNQ1OT1* ICR; paternal uniparental disomy	Biallelic expression of *IGF2*	Pre- and postnatal overgrowth, visceromegaly (including fetal adrenocortical cytomegaly), macroglossia, neonatal hypoglycemia, ear abnormalities, abdominal wall defects; increased risk of neoplasms including ACC	OMIM 130650
Silver-Russel syndrome-1	Molecular aberrations at 11p15; hypometh. of *H19/IGF2* ICR1, maternal uniparental disomy	Biallelic expression of *H19* and downregulation of *IGF2*	Severe intrauterine growth restriction, body asymmetry, characteristic craniofacial features (e.g. triangular-shaped face, broad forehead), dwarfism	OMIM 180860
Angelman syndrome	Maternal microdeletion in ICR on 15q11-q13; paternal uniparental disomy; mutations in *UBE3A*; deletions in *SNRPN*	LOF of genes expressed exclusively from maternal chromosome	Severe intellectual disability, developmental delay, "happy disposition," macrostomia accompanied with frequent ear-to-ear smile, frequent episodic laughter, tongue thrusting, widely spaced teeth, prognathism, limited speech and language, poor balance and stereotyped movements (ataxic gait), epilepsy	OMIM 105830
Prader-Willi syndrome	Paternal microdeletion in ICR on 15q11-q13; maternal uniparental disomy; deletions in *SNRPN*, *NDN*	LOF of genes expressed exclusively from paternal chromosome	Feeding difficulties until 6 months of age which by 1-1.5 years reverts to uncontrollable hyperphagia for the rest of life; compulsive behaviors including excessive skin picking/scratching; small hands with characteristic facies (upslanted almond-shaped eyes, full cheeks, strabismus, muscle hypotonia); intellectual disability; hypopigmentation compared to family members	OMIM 176270
Pseudohypo-parathyroidism Ia (PHP1A)	LOF alterations in maternal *GNAS*	Haploinsufficiency due to uncompensated expression of *GNAS* exclusively from paternal allele (*GNAS* levels are 50% of normal in tissues that express both alleles)	End-organ resistance to PTH, may include resistance to other hormones (TSH, gonadotropins); Albright hereditary osteodystrophy – small stature, round facies, obesity, subcutaneous ossification, skeletal abnormalities (e.g. brachydactyly); intellectual disability	OMIM 103580
Pseudopseudo-hypoparathyroidism	LOF alterations in paternal *GNAS*	Haploinsufficiency due to uncompensated expression of *GNAS* exclusively from maternal allele (*GNAS* levels are 50% of normal in tissues that express both alleles)	Same as PHP1A without end-organ PTH resistance	OMIM 612463
Diabetes mellitus, transient neonatal type 1	Missense/nonsense mutations in *ZFP57*; 6q22-q23 duplication or paternal uniparental isodisomy	Maternal hypometh. at DMR on 6q24 (encompassing *PLAGL1*) and mosaic hypometh. at ICRs genome-wide	Transient neonatal diabetes, macroglossia, intrauterine growth restriction, low birth weight; diabetes may relapse after puberty	OMIM 601410

NOTE. ICR = imprinting control region; DMR = differentially methylated region; LOF = loss of function; -meth.= methylation.

Despite a plethora of studies investigating deposition of 5mC at ICRs and during development, the molecular mechanisms influencing global and tissue-specific patterns of DNA methylation are still poorly understood. In addition to regulation of ICRs, a major role of 5mC deposition is to silence repetitive regions (Miller et al., 1974) and protect against aberrant expression of integrated viral repetitive elements (reviewed in (Greenberg and Bourc'his, 2019)), a mechanism which is exploited to increase the efficacy of immunotherapies in cancer (Topper et al., 2020). The evolutionary history of regions of the genome that are protected from DNA methylation and how DNA methylation may interface with other histone modifications also tells a story.

There is reduced CpG content in genomes of organisms that have 5mC, occurring at 20-25% of the expected frequency in vertebrates and likely reflective of the mutagenic potential of 5mC over the course of evolution (Bird, 1980; Holliday and Grigg, 1993; Rošić et al., 2018). However, in vertebrate genomes, some CpG motifs are densely arranged in regions of 0.5-2 kb in length (CpG islands, CpGi) that are protected from DNA methylation (Cooper et al., 1983; Gardiner-Garden and Frommer, 1987). This contrasts strikingly with CpGs outside of CpG islands, which are frequently methylated and contribute to 5mC in 70-80% of all CpGs globally (Li and Zhang, 2014). CpG islands are found in most mammalian promoters (Larsen et al., 1992; Li and Zhang, 2014). Intriguingly, many CpG islands are hyperconserved (Tanay et al., 2007) and the DNA sequence alone may be sufficient to confer protection from DNA methylation (Long et al., 2016). These phenomena suggest that deposition of 5mC is influenced by other conserved factors, including epigenetic modifiers/modifications that target the same loci and exclude DNA

methylation. Indeed, such CpG islands are known binding sites for the highly conserved PRC2 (**Figure 1.1**, (Tanay et al., 2007)), suggesting that aberrant DNA methylation at these sites may disrupt PRC2 actions – a molecular interaction which is one of the core focuses of this thesis.

Numerous proteins that directly read DNA methylation (recognizing 5mC) or indirectly read DNA methylation (binding disrupted by 5mC) allow this modification to interface intricately with other epigenetic modifications as part of the epigenetic code (Bartke et al., 2010; Hawkins et al., 2010; Lister et al., 2009). DNA methylation at an ICR otherwise controlled by PRC2 disrupts PRC2-mediated repression during embryonic development and controls postnatal growth potential (Greenberg et al., 2017). DNA methylation also influences binding of the protein CTCF that delimits TAD boundaries, thereby coordinating 3D chromatin architecture and the establishment of gene regulatory domains (Dixon et al., 2012; Wang et al., 2012) that restrict the actions of enhancers marked by H3K27ac (**Table 1.2**). Indeed, even though DNA methylation and methyltransferases are conserved down to organisms that lack histones (Bhattacharyya et al., 2020), the ability of DNMTs to read histone marks like H3K9 methylation also exhibits profound evolutionary conservation, even in organisms that lost *de novo* DNMT activity millennia ago (Catania et al., 2020). Taken together, decades of research in this area demonstrate the critical role of DNA methylation in mammalian development and identify an evolutionarily conserved axis through which dysfunction may result in profound molecular and physiological consequences.

1.5. Polycomb repressive complex 2

Polycomb repressive complex 2 (PRC2) is a highly conserved multiprotein complex (**Figure 1.1**, (Laible et al., 1997)) that can write mono-, di- and trimethylation of H3K27 genome-wide. H3K27me3 is the final repressive epigenetic mark (**Table 1.2**) that is central to this thesis. PRC2 is comprised of four core members: an H3K27 methyltransferase EZH2 or EZH1, SUZ12, EED, and RBBP4 or RBBP7. PRC2 also binds accessory proteins that give rise to various context-specific PRC2 assemblies and direct PRC2 binding to hyperconserved CpG islands (Tanay et al., 2007) and potentially other sites on chromatin (**Table 1.5**, **Figure 1.2**).

Table 1.5. PRC2 core and accessory members and their roles.

Protein	Membership	Role
EZH2	Core PRC2	H3K27 methyltransferase, especially required for H3K27me3 deposition in the setting of rapid cell cycle activity (Wassef et al., 2019)
EZH1	Core PRC2	Weak H3K27 methyltransferase but strong transcriptional repressor, more abundant in non-cycling tissues (Margueron et al., 2008)
SUZ12	Core PRC2	Required for PRC2 catalytic activity on chromatin (Cao and Zhang, 2004; Pasini et al., 2004); can bind DNA (Højfeldt et al., 2018)
EED	Core PRC2	Required for PRC2 catalytic activity on chromatin and H3K27me3 reader (Margueron et al., 2009; Montgomery et al., 2005)
RBBP4	Core PRC2	Scaffolding/histone binding (Kuzmichev et al., 2002)
RBBP7	Core PRC2	Scaffolding/histone binding (Kuzmichev et al., 2002)
EZHIP	Accessory (both PRC2.1 and PRC2.2) in eutharians	Inhibits PRC2 catalytic activity in restricted cell types including germ cells (Ragazzini et al., 2019)
PHF1 (PCL1)	Accessory (PRC2.1)	PRC2 recruitment to CpG islands genome-wide, with preference for unmethylated CpG (Li et al., 2017); enhances EZH2-mediated H3K27me2 to H3K27me3 (Sarma et al., 2008) and increases PRC2 residence time (Choi et al., 2017)
MTF2 (PCL2)	Accessory (PRC2.1)	PRC2 recruitment to CpG islands genome-wide, with preference for unmethylated CpG (Li et al., 2017; Perino et al., 2018)
PHF19 (PCL3)	Accessory (PRC2.1)	PRC2 recruitment to CpG islands genome-wide, with preference for unmethylated CpG (Li et al., 2017); enhances PRC2 catalytic activity (Ballaré et al., 2012)
LCOR	Accessory (PRC2.1) in vertebrates	Stimulates PRC2 catalytic activity (Conway et al., 2018)
EPOP	Accessory (PRC2.1)	Associates with CpG islands genome-wide and attenuates PRC2 catalytic activity at PRC2/EPOP co-targets (Beringer et al., 2016; Liefke et al., 2016; Liefke and Shi, 2015)
JARID2	Accessory (PRC2.2)	PRC2 recruitment genome-wide, especially in embryonic and undifferentiated tissues; may attenuate or stimulate PRC2 catalytic activity (Li et al., 2010; Pasini et al., 2010; Peng et al., 2009; Shen et al., 2009)
AEBP2	Accessory (PRC2.2)	PRC2 recruitment genome-wide, in biochemical assays preferentially binds methylated CpG (Wang et al., 2017); stimulates PRC2 catalytic activity (Cao and Zhang, 2004; Lee et al., 2018)

NOTE. Though EZH1/2 are indeed the catalytically active members of PRC2, PRC2 recruitment even in the absence of EZH2 catalytic activity is sufficient to induce transcriptional repression (Hansen et al., 2008), suggesting PRC2 occupancy at high affinity targets is favored over spurious transcription (taking precedence over the repressive impact of the H3K27me3 mark) and may be sufficient to restrict transcriptional machinery.

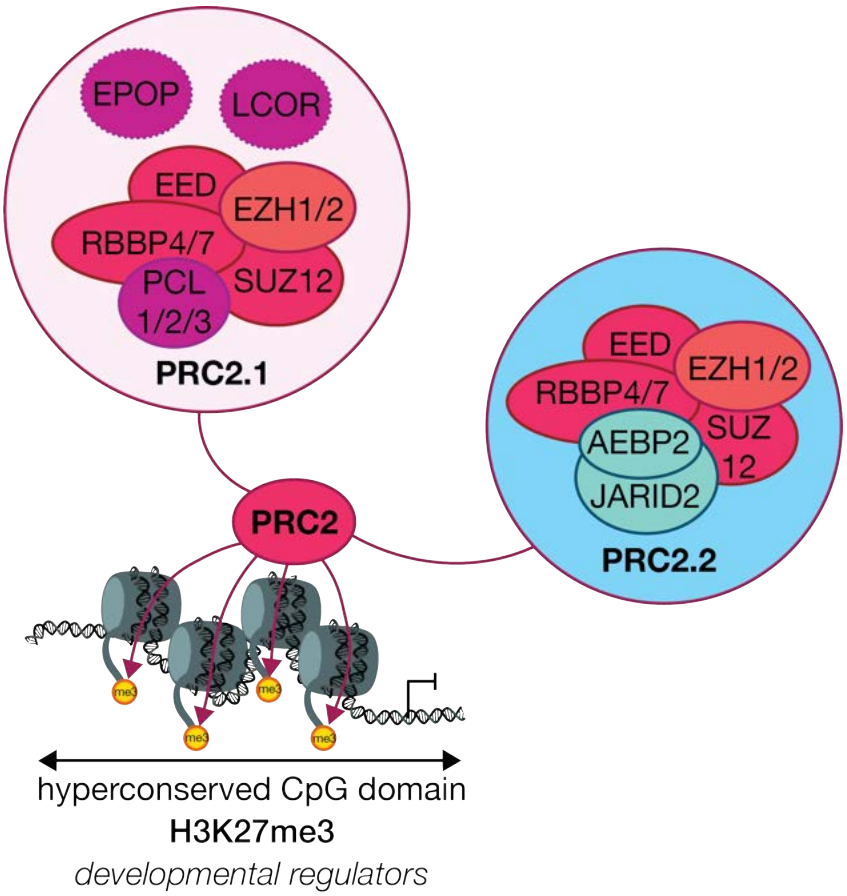

Figure 1.2. Schematic of mutually exclusive PRC2.1 and PRC2.2 assemblies.
PRC2.1 schematic based on (Chen et al., 2020), PRC2.2 schematic based on (Chen et al., 2018; Kasinath et al., 2018). Structural studies suggest that AEBP2/PCL3 and JARID2/EPOP respectively compete for the same interface on SUZ12 (Chen et al., 2018). EZHIP is not depicted, though it would be predicted to interact with either PRC2 assembly in restricted contexts in which *EZHIP* is expressed (Ragazzini et al., 2019). Graphic brushes to draw DNA were used with permission of the designer and downloaded from K8Baldwin.com.

PRC2 was first discovered as a critical *trans* regulator of segmental anterior-posterior patterning in *D. melanogaster* (Lewis, 1978; Struhl, 1981), suggesting that PRC2 activity is required for context-specific gene expression and therefore represented a mechanism of epigenetic control. This discovery laid the groundwork for studies in mammalian systems identifying PRC2 orthologs and characterizing similar and essential roles for this complex in development and differentiation (**Table 1.6**).

Table 1.6. Consequences of whole-body deletion of PRC2 components in murine development and mESCs.

Gene	Membership	Phenotype	Molecular consequences	Reference
Ezh2	Core PRC2	Embryonic lethal (E7.5-E8.5) with gastrulation defects	Complete H3K27me2/3 loss in parthenogenetic *Ezh2*-deficient embryos, global H3K27me2/3 reduction in mESCs	(Erhardt et al., 2003; O'Carroll et al., 2001)
Ezh1	Core PRC2	None – viable, healthy and fertile	No changes in H3K27me1/2/3 in mESCs; however, in combination with *Ezh2* deletion leads to complete loss of H3K27me1/2/3 in mESCs	(Ezhkova et al., 2011; Højfeldt et al., 2018; Lavarone et al., 2019; Shen et al., 2008)
Suz12	Core PRC2	Embryonic lethal (E7.5-E8.5) with gastrulation defects	H3K27me2/3 loss at E7.5-E8.5 in mouse model; complete H3K27me1/2/3 loss in mESCs	(Højfeldt et al., 2018; Pasini et al., 2004)
Eed	Core PRC2	Embryonic lethal (E7.5-E8.5) with gastrulation defects	Complete H3K27me1/2/3 loss in mESCs	(Faust et al., 1998; Faust et al., 1995; Højfeldt et al., 2018; Montgomery et al., 2005; Schoeftner et al., 2006; Shumacher et al., 1996)
Mtf2 (PCL2)	Accessory (PRC2.1)	Embryonic lethal (E15.5) with growth restriction and anemia	Global H3K27me3 reduction in mESCs	(Perino et al., 2018; Rothberg et al., 2018)
Pali1 (LCOR)	Accessory (PRC2.1)	Perinatal lethality	Global H3K27me2/3 reduction at E11.5 in mouse model; moderate global H3K27me3 reduction	(Conway et al., 2018)
Jarid2	Accessory (PRC2.2)	Embryonic lethal (E10-E18.5) with strain-dependent developmental abnormalities	No clear consensus; possible that consequences of *Jarid2* deficiency are dependent on the endogenous abundance of PRC2.1 complexes (Healy et al., 2019)	(Landeira and Fisher, 2011; Lee et al., 2000; Motoyama et al., 1997; Pasini et al., 2010; Takeuchi et al., 1999; Takeuchi et al., 1995)
Aebp2	Accessory (PRC2.2)	Perinatal lethality with anterior skeletal abnormalities	Increase in PRC2 target H3K27me3 (mESCs)	(Grijzenhout et al., 2016)

NOTE. Table adapted from (Deevy and Bracken, 2019). mESC = murine embryonic stem cells.

The context- and tissue-specific consequences of germline PRC2 deficiency (**Table 1.3**, **Table 1.6**) suggest that PRC2 and H3K27me3 are uniquely positioned to establish and interface with the tissue-specific chromatin environment. Indeed, while the roles of PRC2 in embryogenesis are well understood (**Table 1.6**), the actions of this complex and its requirements in somatic tissues are less clear. Catalytically active PRC2 can be purified from a broad spectrum of cell lines and differentiated tissues, and is required to maintain active gene repression even in the setting of cell cycle blockade (Gould et al., 1990), suggesting PRC2 may continue to have context-specific roles in somatic cells. Studies in plants (*A. thaliana*) identified that PRC2 is actively deployed to facilitate cell state transitions like induction of flowering after prolonged cold (Jiang and Berger, 2017; Yang et al., 2017), or to maintain terminal differentiation (Ikeuchi et al., 2015). In mammalian models, investigators have observed that PRC2 occupancy at embryonic targets diminishes with differentiation (Kloet et al., 2016) and that PRC2 occupancy is highly cell type specific (Squazzo et al., 2006). Indeed, most regions of the genome that are marked with H3K27me3 in embryonic stem cells also possess methylation of H3K4 and are thought to be “poised” to turn on in response to differentiation cues; with differentiation, these domains are no longer poised and revert to pure H3K27me3 or H3K4me in a cell type-specific manner (Bernstein et al., 2006). Taken together, these studies point to a model in which PRC2 has its broadest actions on the genome during embryonic pluripotency and more focal or restricted actions in differentiated and somatic cells.

Along these lines, several groups have explored the consequences of conditional PRC2 or EZH2 deficiency using tissue-specific Cre recombinase drivers. These studies have collectively demonstrated that PRC2/EZH2 are often required for stem and/or progenitor cell pluripotency, and that deficiency hampers differentiation (e.g. (Ezhkova et al., 2011; Mathieu et al., 2018; Su et al., 2003; Xie et al., 2014; Yin et al., 2015)). Of importance to this dissertation, a report published while this study was ongoing demonstrated that EZH2 is required to program cells of a specific zone of the adrenal cortex to respond to endocrine hormone signaling (Mathieu et al., 2018), highlighting that the paradigm of tissue-specific PRC2 actions is also true in the adrenal cortex. This mouse model will be discussed in more detail in **Chapter 2**.

Further supporting the existence of a tissue-specific role of PRC2, the transcriptional consequences of EZH2 inhibition (EZH2i) are cell type specific (**Chapter 6** and **Appendix C**). The tissue specificity of PRC2 actions is conferred not only by its genomic distribution but by tissue-specific subunit composition. For example, during erythropoiesis, differential stage-specific enhancer utilization results in an expression switch between *EZH2* and *EZH1*, culminating in an abundance of EZH1-containing PRC2 complexes in differentiated cells and a reduction in PRC2 target gene repression (Xu et al., 2015). PRC2 accessory components are also dynamically switched during differentiation (Kloet et al., 2016; Oliviero et al., 2016). Given the differential affinity of accessory proteins for methylated or unmethylated CpG islands (**Table 1.5**), it is likely that the PRC2 interactome plays a crucial role in targeting PRC2 on and off chromatin in physiology and cancer (**Chapters 5 – 6**).

1.6. Cancer – general principles and relevant epigenetic programs

Cancer is a disease caused by inherited or acquired genetic defects that arises from cell types with proliferative potential. Cells of origin for cancer include short- or long-term retained stem cell populations that undergo asymmetric division to replenish a tissue in response to injury (Barker et al., 2009; Gregorieff et al., 2015; Wong et al., 2015), or transit-amplifying cell populations that proliferate in coordinated bursts in response to homeostatic demands (Wang et al., 2009) (mechanisms reviewed in (Clarke and Fuller, 2006; Visvader, 2011)). During physiological tissue homeostasis, cell cycle entry of these populations is tightly controlled by signaling cues (Hsu et al., 2014); however, genome replication required for each successful cell cycle is an error-prone process, and represents an opportunity for the acquisition of mutations and other somatic alterations (Visvader, 2011). Stem and progenitor cells in a tissue are naturally subject to clonal selection as a physiological mechanism to optimize tissue function (Ellis et al., 2019). Occasionally, a dividing cell will acquire an activating somatic alteration in a gene/CRE that enables autonomous cell growth or proliferation, or an inactivating alteration in a gene/CRE that restricts cell growth. Consequently, this cell will cycle faster, acquire additional genetic alterations, and clonal selection will favor the accumulation of alterations that promote proliferation (hyperplasia), breach of tissue structure/organ boundaries (cancer), and dissemination to distal sites (metastasis) (Gerlinger et al., 2012; Walter et al., 2012).

Recurrent somatic alteration profiles for each cancer type are therefore uniquely shaped by the tissue of origin, and exploit tightly regulated and critical signaling,

transcriptional, and epigenetic programs that are context-specific drivers of carcinogenesis. In the case of ACC, these converge on paracrine and endocrine signaling pathways required for adrenal homeostasis, including Wnt/β-catenin and ACTH/PKA (**Chapter 2 – Chapter 3**; (Zheng et al., 2016)). Landmark studies performing high throughput and multiplatform molecular profiling of human cancers, such as The Cancer Genome Atlas (TCGA) (NCI, 2005-2018), have reinforced this concept and highlight how genetic alterations induce deeply hard-wired shifts in transcriptional and epigenetic landscapes. This can be direct, through mutations in transcription factors, coactivators, epigenetic machinery (e.g. (Kadoch et al., 2013)), and histones; or indirect, through mutations in regulators of essential pathways.

For example, sustained proliferation potential is a hallmark of cancer (Hanahan and Weinberg, 2000, 2011), often achieved through driver alterations in regulators of the G1/S checkpoint of the cell cycle. Cancer cells bearing such mutations bypass this checkpoint and exhibit constitutive activation of the classical E2F transcriptional program (Rhodes et al., 2005). Physiologically, this program is turned on during S phase, and E2F directs transcription of a variety of genes required for progression through the cell cycle, including those required for DNA/chromatin replication like epigenetic modifiers including *EZH2* (e.g. (Bracken et al., 2003)). Across human cancer, cell cycle activation is associated with substantial upregulation of a broad spectrum of epigenetic modifiers (**Figure 1.3**), and the presence of these enzymes and proteins at excess and perhaps non-stoichiometric levels raises the possibility that epigenetic equilibria are no longer maintained in cancer.

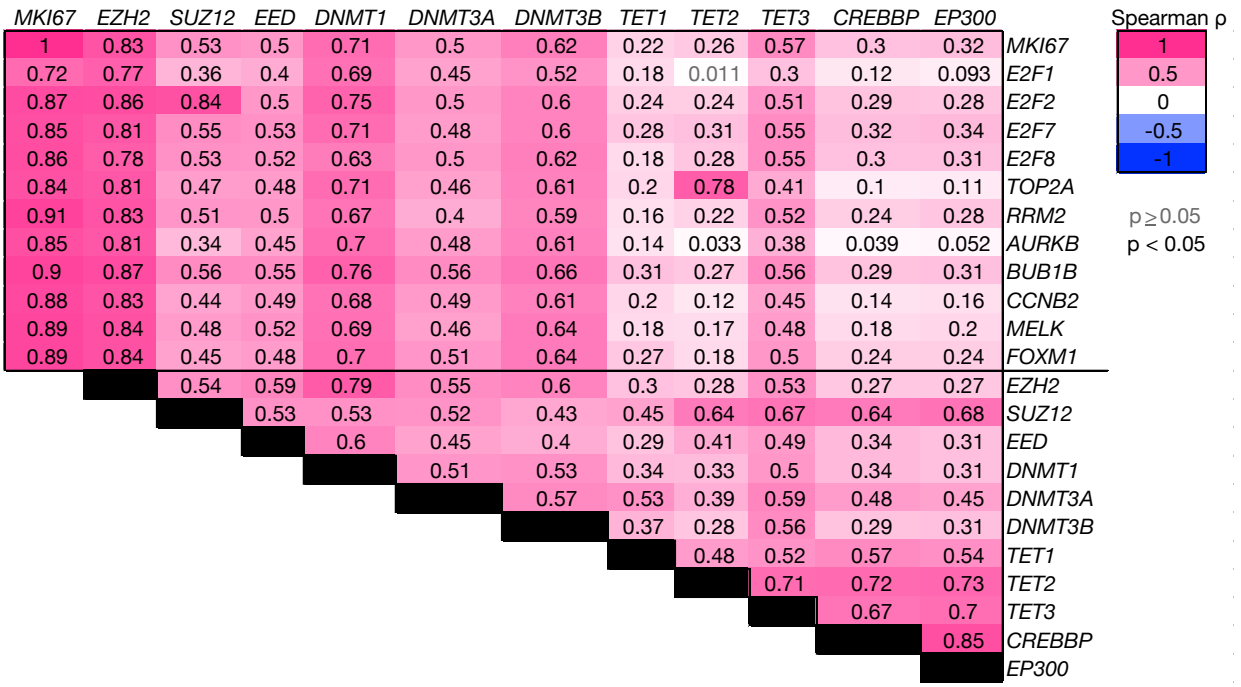

Figure 1.3. Epigenetic modifiers exhibit concordant and cell cycle-dependent transcriptional regulation.
GEPIA (Tang et al., 2017) was used to mine expression data from all cancer samples enrolled in The Cancer Genome Atlas series of studies for genes encoding cell cycle regulators expressed in a cell cycle-dependent manner (*MKI67, E2F1, E2F2, E2F7, E2F8, TOP2A, RRM2, AURKB, BUB1B, CCNB2, MELK, FOXM1*) and genes encoding epigenetic modifiers (*EZH2, SUZ12, EED, DNMT1, DNMT3A, DNMT3B, TET1, TET2, TET3, CREBBP, EP300*). Spearman ρ and p-value was calculated for each pair-wise comparison. Spearman ρ is denoted in each box comparison and shaded according to scale right. Comparisons where $p < 0.05$ is indicated by black text, while insignificant comparisons ($p \geq 0.05$) are indicated by grey text. The strong positive correlation between virtually all comparisons depicted in the correlation matrix suggests that epigenetic modifiers are transcriptionally co-regulated in a cell cycle-dependent manner in cancer, consistent with early studies identifying epigenetic modifiers like *EZH2* are targets of the E2F family of transcription factors (Bracken et al., 2003).

Epigenetic programs coordinating cell identity are recurrently disrupted through a variety of mechanisms, and may represent a route through which cancer cells immortalize pro-proliferation cell states. Somatic loss of imprinting characterizes a variety of cancers including ACC (Gicquel et al., 1997), and promotes malignant transformation (Holm et al., 2005). Strong driver mutations and/or non-coding alterations in CREs alter the epigenetic landscape by shaping enhancer utilization (Corces et al., 2018; Flavahan et al., 2019). Cancers also frequently exhibit profound abnormalities in PRC2 function, secondary to

cell cycle-dependent *EZH2* overexpression or recurrent somatic alterations (**Figure 1.3**, **Table 1.7**). Many cancers including ACC possess aberrant genome-wide DNA hypermethylation of CpG islands, secondary to dysfunction of TET DNA demethylases or other unknown mechanisms. Many of these CpG islands are direct targets of the PRC2, and this abnormal DNA methylation signature is likely reflective of or shapes cancer-specific PRC2 actions, as investigated in this thesis (**Table 1.7**; **Chapter 5**). Given that adequate silencing of PRC2 target gene expression helps to maintain stemness potential, it is possible that CpG island DNA hypermethylation is selected for in cancers because this signature induces a differentiation arrest that permits sustained proliferation (Lu et al., 2012) or because it stabilizes silencing of negative regulators of pathways known to drive carcinogenesis (Tao et al., 2019) (**Table 1.7**). In the context of ACC, the most differentiated tumor classes paradoxically possess CpG island hypermethylation (**Chapter 3**), suggesting that the mechanisms supporting clonal selection of this signature are highly specific to the tissue-of-origin context of malignant transformation ((Tao et al., 2019); **Chapter 6**).

Indeed, epigenetic abnormalities in cancer often have tissue-specific oncogenic roles, highlighted by the two faces of EZH2 as both a tumor suppressor and oncogene (**Table 1.7**). In germinal center-derived B cell lymphomas, recurrent mutations in the SET domain of *EZH2* lead to hyperactive PRC2 function genome-wide (Morin et al., 2010; Sneeringer et al., 2010), and is selected for because of the role of EZH2 in sustaining proliferation of pre-malignant lesions in the germinal center compartment (Béguelin et al., 2013; Béguelin et al., 2016; Béguelin et al., 2020). In malignant peripheral nerve sheath

tumors, recurrent genetic alterations lead to loss of function of PRC2, and restoration of PRC2 catalytic activity restricts cell proliferation (Lee et al., 2014). Overexpression of *EZH2* may also be associated with tissue-specific non-canonical roles. In prostate cancer, inhibiting androgen receptor signaling (medical castration), is therapeutic (Sharifi et al., 2005); in prostate cancer refractory to anti-androgen therapy, EZH2 induces therapeutic resistance by functioning as a transcriptional coactivator of the androgen receptor (Xu et al., 2012). EZH2 has non-nuclear roles in a subset of breast cancers with high levels of cytoplasmic EZH2 and low H3K27me3, and may regulate cytoskeletal proteins (Anwar et al., 2018). Understanding the context-specific roles of epigenetic modifiers is critical to defining novel single-drug and combination medical therapies for cancer subtypes; in the context of some cancer types with PRC2 gain of function (GOF), small molecule inhibitors of PRC2 catalytic activity have recently been FDA approved (**Table 1.7**), and several clinical trials are ongoing.

Table 1.7. Mechanisms of aberrant EZH2/PRC2 function in cancer.

Phenomenon	Cancers affected	Etiology	PRC2 molecular consequence	EZH2i susceptible?
Overexpression of *EZH2*	Virtually all human cancers including ACC	*EZH2* is a highly cell cycle dependent gene (target of the E2F program (Bracken et al., 2003); **Figure 1.3**), and aberrant cell cycle activation (exceeding the cycling rate of normal and benign tissue) is a hallmark cancer. Somatic amplifications of *EZH2* have also been reported (Consortium, 2017). *EZH2* may also be upregulated through other somatic alterations (Wilson et al., 2010)	Variable. Can be associated with enhanced canonical PRC2 catalytic activity (Wilson et al., 2010), may be required to maintain canonical PRC2 catalytic activity (e.g. to prevent replication dilution, (Jadhav et al., 2020)), and may be associated with novel PRC2-independent nuclear (Xu et al., 2012) and non-nuclear (Anwar et al., 2018) functions.	Context-dependent, unclear as a general mechanism
EZH2 SET domain mutations, especially Y641	Diffuse large B cell lymphoma (DLBCL), follicular lymphoma (Morin et al., 2010)	Somatic alteration, leads to enhanced B cell proliferation because of critical role of PRC2 in the germinal center B cell compartment (Béguelin et al., 2013; Béguelin et al., 2016; Béguelin et al., 2020)	PRC2 GOF, enhanced H3K27me2 to H3K27me3 conversion that requires wild type *EZH2* allele for full effect (Sneeringer et al., 2010)	Yes (McCabe et al., 2012), tazemetostat (EPZ-6438) FDA approved for follicular lymphoma
H3K27M	Diffuse intrinsic pontine glioma (DIPG)	Somatic alteration (Schwartzentruber et al., 2012; Wu et al., 2012)	Largely PRC2 LOF, but H3K27me3 is retained at some sites and PRC2 still required for DIPG proliferation (Mohammad et al., 2017; Piunti et al., 2017).	Yes (Mohammad et al., 2017), but other promising targets exist (Chung et al., 2020)
Aberrant *EZHIP* overexpression	H3K27 WT posterior fossa type A (PFA) ependymomas, endometrial stromal sarcoma (ESS)	Somatic *MBTD1-EZHIP* translocation in ESS; recurrent missense mutations and aberrant expression in PFA ependymomas (Pajtler et al., 2018)	PRC2 LOF (Jain et al., 2019; Piunti et al., 2019)	Unlikely, *EZHIP* abolishes PRC2 catalytic activity (Jain et al., 2019; Piunti et al., 2019)
PRC2 deficiency	Myelodysplastic syndromes, malignant peripheral nerve sheath tumors, acute myeloid leukemia (AML) relapse, T-cell acute lymphoblastic leukemia	Somatic alteration – inactivating mutations in PRC2 machinery or other alt. leading to PRC2 or H3K27me3 deficiency (Göllner et al., 2017; Lee et al., 2014; Ntziachristos et al., 2012)	PRC2 LOF (Göllner et al., 2017; Lee et al., 2014) likely via replication dilution of H3K27me3 in absence of PRC2 catalysis (Jadhav et al., 2020)	No (Göllner et al., 2017; Lee et al., 2014)
SWI/SNF deficiency	Many (SWI/SNF is mutated in ~20% of all human cancers (Kadoch et al., 2013)), e.g. malignant rhabdoid tumor, epithelioid sarcoma, ovarian clear cell carcinoma, colorectal carcinoma	LOF somatic alteration in SWI/SNF component e.g. *SMARCB1*, *SMARCA4*, *SMARCA2, ARID1A*	PRC2 GOF secondary to loss of SWI/SNF antagonism (Kadoch et al., 2017; Nakayama et al., 2017; Wilson et al., 2010)	Yes, tazemetostat (EPZ-6438) currently FDA approved for epithelioid sarcoma

(Table continued on next page)

Phenomenon	Cancers affected	Etiology	PRC2 molecular consequence	EZH2i susceptible?
SWI/SNF neomorph	Likely several cancers, best example is synovial sarcoma	Somatic SS18-SSX translocation	PRC2 LOF secondary to strong avidity of SS18-SSX for many novel genomic sites including repressive chromatin (Banito et al., 2018; Kadoch and Crabtree, 2013; McBride et al., 2020; McBride et al., 2018)	No, would not be predicted to be effective on a molecular basis and phase II trial failed to meet endpoint (Schoffski et al., 2017)
PR-DUB dysfunction	Several cancers; myeloid leukemias, melanoma, mesothelioma, renal cell carcinoma	Somatic alterations in *ASXL1*, *BAP1*	Variable. *BAP1* deficiency is associated with PRC2 GOF and increased H3K27me3; *ASXL1* deficiency is associated with PRC2 LOF and decreased H3K27me3 (LaFave et al., 2015)	Likely in the context of *BAP1* deficiency (LaFave et al., 2015)
MLL deficiency or neomorph	Likely several cancers, best example is mixed lineage leukemia	Somatic *MLL* rearrangement, typically abolishing SET domain (Milne et al., 2002), e.g. MLL-AF9	Expression of an ES-like transcriptional program, including potent repression of PRC2 targets (Kim et al., 2010)	Possible (Neff et al., 2012), but other promising targets exist (Krivtsov et al., 2019; Muntean et al., 2010)
CIMP-high; DNA hypermethylation of PRC2 targets	Many, e.g. ACC, colorectal carcinoma, AML, glioblastoma multiforme (GBM), PFA ependymomas	Somatic inactivating mutation in *IDH1/2*, leading to accumulation of 2-hydroxyglutarate (Ward et al., 2010) and TET/KDM inhibition (Figueroa et al., 2010; Lu et al., 2012; Turcan et al., 2012); *IDH1/2* wild type etiology still poorly understood – may be linked to similar but as yet uncharacterized metabolic abnormalities, may result from chronic DNA damage (Vaz et al., 2017), may represent selection of stochastic events that lead to potent silencing of tumor suppressors (Xie et al., 2018), or may represent a cellular proliferation/aging “clock” (Tao et al., 2019). Early models suggest PRC2 directs DNA methyltransferase machinery to PRC2 targets ((Viré et al., 2006); **Chapter 5**).	Unclear and complex, may be PRC2 LOF, PRC2 GOF or neomorph. Some studies suggest PRC2 directs DNA methylation (Viré et al., 2006), others suggest PRC2 is excluded from the sites of DNA hypermethylation coincident with an H3K27me3 to H3K9me3 epigenetic class switch (Ohm et al., 2007), and others suggest that CIMP is at the expense of H3K27me3 (Bayliss et al., 2016). DNA demethylation has also been reported to dilute PRC2 “out” in mESCs, suggesting that CIMP-high in cancer may concentrate PRC2 activity at regions of the genome without DNA methylation and mimic PRC2 GOF (Douillet et al., 2020). Consistent with this idea, CIMP induced by *IDH* mutations bears higher levels of H3K27me3 in addition to DNA methylation (Lu et al., 2012; Turcan et al., 2012).	Context-dependent, unclear as a general mechanism. Some studies suggest yes (Mack et al., 2014), but therapeutic response may not be directly attributable to CIMP status. EZH2i likely to be more relevant during transformation (Vaz et al., 2017) or if PRC2/EZH2 has taken on new/GOF roles in CIMP-high disease (**Chapter 6**).

NOTE. SET domain enables catalysis of lysine methylation and is required for methyltransferase activity of almost all histone methyltransferase enzymes. EZH2i = EZH2 inhibition. mESC = murine embryonic stem cell.

1.7. Endocrine tumorigenesis and cancer

Endocrine cancers and their tissues of origin represent a unique opportunity to study how tissue-specific programs interface with pharmacologically targetable epigenetic modifiers. Generally, the major function of the endocrine system is to coordinate the adaptive response of an organism to external and internal stimuli through centralized release of tropic hormones that stimulate target tissues. Tropic hormones induce tissue differentiation (hormone production) or proliferation in this context, and target tissue homeostasis is governed by a balance between these physiological cues and a paracrine signaling niche. Endocrine and endocrine-related cancers often hijack this crosstalk and acquire genetic events that enable simultaneous autonomous hormone production, sustained paracrine signaling, and tropic hormone-independent rapid proliferation (Russo et al., 1995; Visakorpi et al., 1995). By these means, endocrine cancer cells get “trapped” in a tissue-specific differentiation state that enables sustained proliferation and is likely stabilized through epigenetic programming.

Benign and malignant adrenocortical tumors frequently harbor somatic alterations that lead to sustained endocrine and paracrine signaling (**Chapter 2** – **Chapter 3**). In the case of ACC, this leads to a paradoxical activation of stemness, differentiation, and proliferation programs. Several recent landmark studies investigating the molecular basis of ACC, namely ACC-TCGA (Zheng et al., 2016), have identified that this cancer is comprised of discrete molecular subtypes and that the most aggressive subtype also features recurrent global abnormalities in the DNA methylation landscape including DNA

hypermethylation of PRC2 targets (**Chapter 5**). The consequences of this aberrant epigenetic patterning, its translational value, and how it intersects with recurrently activated transcriptional programs in ACC, are completely unknown. Our goals are therefore to design a strategy to enable translation of molecular subtyping to clinical diagnostics, and to resolve the contribution of aberrant epigenetic patterning to adrenocortical carcinogenesis.

1.8. Thesis summary

Epigenetic programs are critical for organism survival and tissue homeostasis and are frequently disrupted in cancers. Next, I will briefly describe the physiological programs supporting adrenocortical differentiation, and how these programs are disrupted in tumorigenesis (**Chapter 2**). I will then detail how ACC is comprised of discrete homogeneous molecular subtypes with uniform clinical outcomes, and will present data that places frequently used model systems in the context of these subtypes (**Chapter 3**). I will then describe an unambiguous biomarker-based strategy to enable prospective ACC molecular subtyping (**Chapter 4**). Finally, I will detail studies that investigate how aberrant CpG island hypermethylation in ACC disrupts PRC2 recruitment genome-wide (**Chapter 5**) and may create novel dependencies on PRC2 for coordinating lineage-defining differentiation programs that are required for sustained proliferation in ACC (**Chapter 6**), and molecular and therapeutic implications for targeting these programs (**Chapter 7**).

CHAPTER 2. Adrenocortical Differentiation and Tumorigenesis

2.1. Disclosure of relevant publications

Portions of this work have been published:

> **Mohan DR**, Lerario AM, Finco I, Hammer GD. New strategies for applying targeted therapies to adrenocortical carcinoma. *Current Opinion in Endocrine and Metabolic Research*. 2019 Oct 1. 8:66-71.
>
> Finco I, **Mohan DR**, Hammer GD, Lerario AM. Regulation of stem and progenitor cells in the adrenal cortex. *Current Opinion in Endocrine and Metabolic Research*. 2019 Oct 1. 8:72-79.

Portions of this work are being prepared for publication:

> Lerario AM, **Mohan DR**, Giordano TJ, Hammer GD. "10. Genetics of Adrenal Tumors," in New MI, Lekarev O, Parsa A, Yuen TT, O'Malley B, Hammer GD (Eds.) *Genetic Steroid Disorders*. 2nd ed. San Diego: Academic Press. Invited book chapter. Submitted and undergoing editorial review.
>
> **Mohan DR**, Borges KS, Finco I, LaPensee CR, Solon A, Rege J, Little III DW, Else T, Almeida MQ, Apfelbaum A, Vinco M, Wakamatsu A, Mariani BMP, Latronico AC, Mendonca BB, Zerbini MCN, Fragoso MCBV, Lawlor ER, Ohi R, Rainey WE, Venneti S, Marie SKN, Giordano TJ, Breault DT, Lerario AM*, Hammer GD*. A differentiation program coordinated by SF1/β-catenin is a targetable epigenetic vulnerability in aggressive adrenocortical carcinoma. In preparation. *co-senior author
>
> Lerario AM*, **Mohan DR***, Rege J, Rainey WE, Hammer GD. Meta-analysis of adrenocortical tumors identifies cell of origin programs derailed in tumorigenesis and malignancy. In preparation. *co-first author

2.2. Introduction

The adrenal glands are paired endocrine organs that reside above each kidney and produce a variety of hormones critical for life. Each gland is comprised of two embryonically distinct endocrine compartments, enveloped by a non-endocrine mesenchymal layer of cells, the capsule. Beneath the capsule, the adrenal is subdivided into an outer cortex and inner medulla, which produce steroid hormones and catecholamines, respectively. The inner medulla is considered a distinct tissue from the adrenal cortex and capsule, with minimal contribution to adrenocortical homeostasis. The tissue of origin of ACC is the adrenal cortex. The adrenal cortex consists of three concentric histologically and functionally distinct zones: the outer zona glomerulosa (zG), which produces mineralocorticoids; the inner zona fasciculata (zF), which produces glucocorticoids; and the innermost zona reticularis (zR), which produces androgens (**Figure 2.1**). Importantly, while many features of the adrenal cortex are conserved between mouse and human, adult mice (*M. musculus*) do not have a functional zR and do not express the machinery required to produce adrenal androgens (van Weerden et al., 1992).

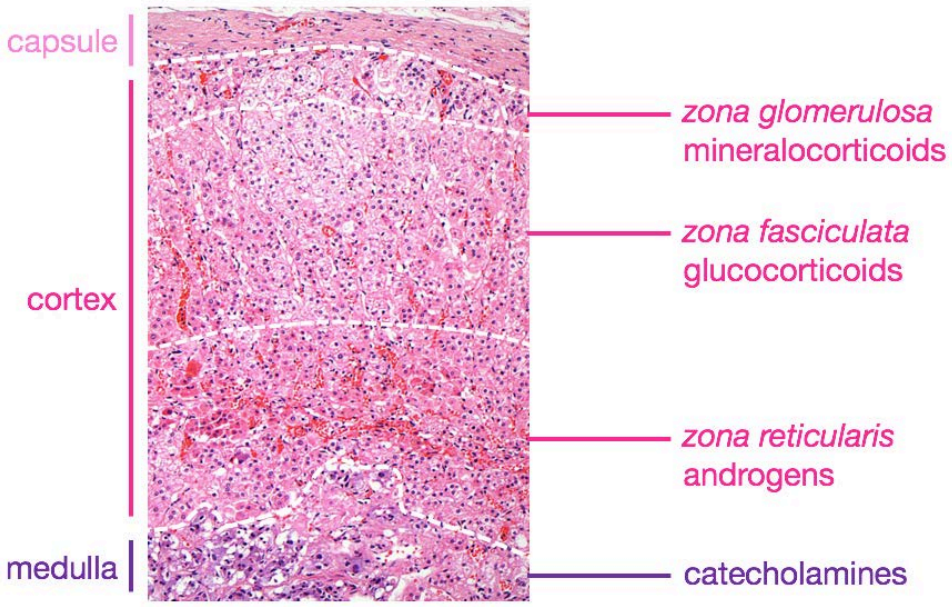

Figure 2.1. Histological structure of the human adult adrenal gland.
Human adult adrenal gland was stained with hematoxylin (purple, primarily stains nuclei) and eosin (pink, primarily stains cytoplasm), revealing three major compartments (capsule, cortex, medulla) and three major adrenocortical zones (zona glomerulosa, produces mineralocorticoids; zona fasciculata, produces glucocorticoids; zona reticularis, produces androgens). The murine adrenal gland is similar in structure, with the exception that mice do not possess a zona reticularis. Image adapted from (Lerario, 2014) with permission of the author.

2.3. Adrenal steroidogenesis, development, and SF1

Adrenocortical production of steroids (steroidogenesis) is a complex and tightly regulated process, reliant on the coordinated actions of several enzymes located in the mitochondria and endoplasmic reticulum that sequentially chemically modify cholesterol and are expressed in a zone-specific manner (**Figure 2.2**). Steroidogenesis is established by the master transcription factor of the adrenal cortex, steroidogenic factor 1 (SF1, encoded by *NR5A1* in humans and *Nr5a1* in mice), which coordinates the expression of the vast majority of adrenocortical steroidogenic enzymes via regulation of proximal and distal CREs (e.g. (Lala et al., 1992; Morohashi et al., 1992); **Table 2.1**).

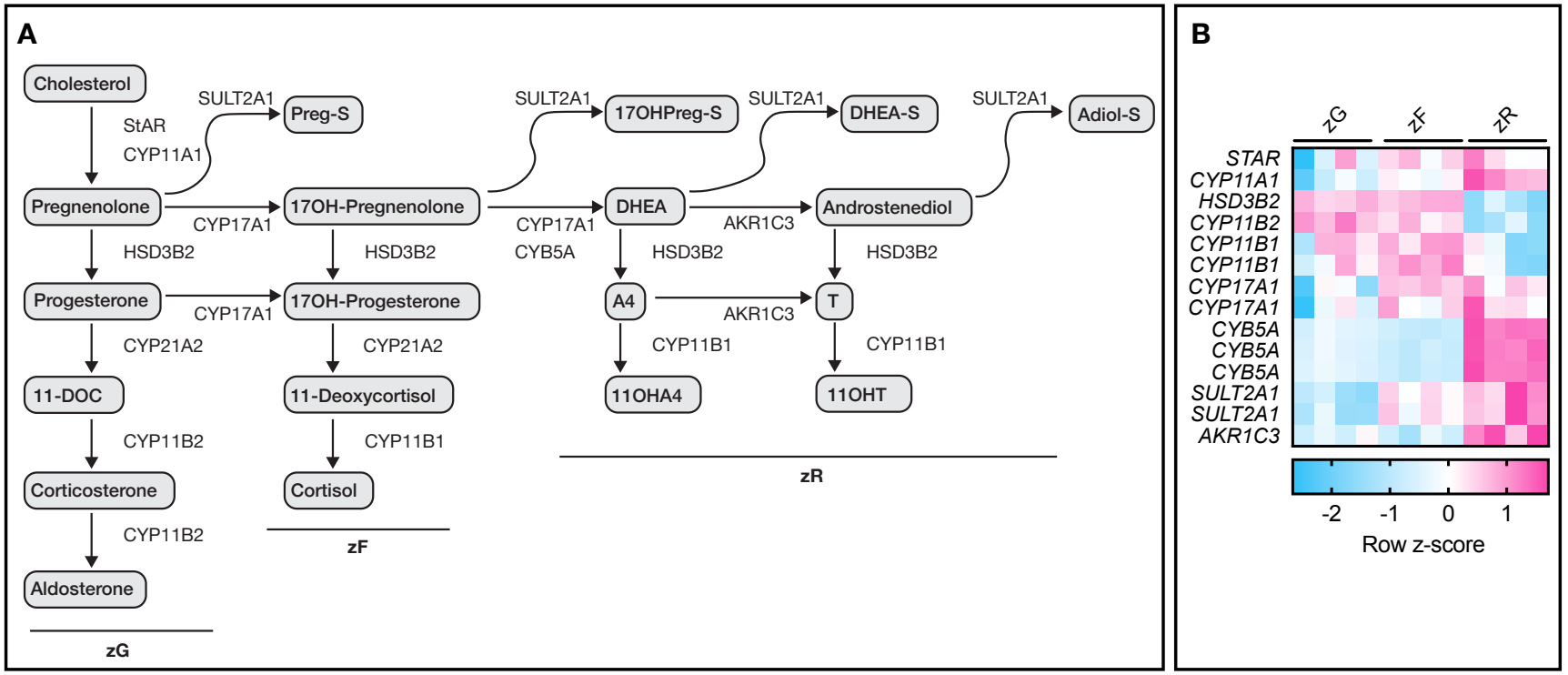

Figure 2.2. Zonation of adrenocortical steroidogenesis.
A. Steroidogenesis cascade in the adrenal cortex. Cholesterol, steroid precursors, and steroid end-products are labeled in grey boxes. Enzymes catalyzing each step in steroidogenesis are labeled beside the line. Mineralocorticoids (aldosterone) are produced from the adrenal zG, glucocorticoids (cortisol) are produced from the zF, and androgens (DHEA-S, 11OHT, etc.) are produced from the zR. Adapted from (Rege et al., 2019). B. Expression of steroidogenic enzymes in microdissected human adrenal cortex reveals zonal expression of steroidogenic enzymes; microarray data from (Nishimoto et al., 2015).

Table 2.1. SF1-dependent regulation of adrenal steroidogenic enzymes.

Steroidogenic enzyme	Zonal expression	FPKM	SF1 peak in promoter?	SF1 peak in putative active enhancer?
STAR	Expressed in all zones, highest in zF and zR	177.7995509	Yes	Yes
CYP11A1	Expressed in all zones, highest in zF and zR	92.17966058	Yes	Yes
HSD3B2	zG, zF	34.9175176	Yes, but more distal than standard promoters; most proximal peak to TSS is ~4 kb upstream	Yes
CYP21A2	zG, zF (Coulter and Jaffe, 1998)	110.7300255	Yes	No
CYP11B2	Likely exclusive to zG based on more recent single-cell RNA-seq data (Han et al., 2020)	0.492083793	Yes, but more distal than standard promoters; most proximal peak to TSS is ~3kb upstream	Region too repetitive for accurate mapping
CYP11B1	Expressed in all zones, highest in zF	0.104993238	Region too repetitive for accurate mapping	Region too repetitive for accurate mapping
CYP17A1	Expressed in all zones, highest in zR	18.98799553	Yes	Yes
CYB5A	zR	3.184535105	No	No
SULT2A1	Expressed in zF and zR, highest in zR	39.47136271	Yes	Yes
AKR1C3	zR	12.95087875	Yes	Yes

NOTE. Zonal expression determined based on **Figure 2.2** and the literature. FPKM = fragments per kilobase of transcript per million mapped reads (expression value) from RNA-seq performed on baseline *in vitro* model of ACC, NCI-H295R cell line (data introduced in **Chapter 3**). For reference, in this dataset median gene expression is an FPKM of ~3.8. SF1 peaks identified from SF1 ChIP-seq performed on baseline NCI-H295R cell line (data introduced in **Chapter 6**). Putative active enhancers of a given gene were identified by overlapping human adrenal promoter capture Hi-C contact tables (Jung et al., 2019) with H3K27ac peaks identified from H3K27ac ChIP-seq performed on baseline NCI-H295R (data introduced in **Chapter 5**). An active enhancer is defined as a distal CRE overlapping with an H3K27ac peak. Putative active enhancers were manually inspected for the presence of SF1 binding.

SF1 is also required for adrenal and gonadal organogenesis and development. During weeks 4-6 of gestation in humans and embryonic day 9.5 (E9.5) in mice, specialized mesoderm tissue give rise to the adrenogonadal primordium (AGP). The fetal adrenal cortex derives from the AGP coincident with the initiation of SF1 expression (Schimmer and White, 2010) via the fetal adrenal-specific enhancer (FAdE), active exclusively during late AGP development in mice (Zubair et al., 2008). The AGP then divides into adrenal and gonadal primordia (week 8 of gestation; E10.5), and by the ninth week of gestation (E12.5), cells of the neural crest infiltrate the adrenal primordium to form the central adrenal medulla. Mesenchymal cells coalesce around the adrenal primordium and form the adrenal capsule. Beneath the capsule, the definitive cortex (which will ultimately become the adult adrenal cortex) begins to nucleate as a discrete structure. In humans, the fetal adrenal cortex regresses during the weeks following birth and is eventually replaced by the definitive adult cortex (Mesiano and Jaffe, 1997). Though the mechanisms supporting the transition between the fetal and definitive adult adrenal cortex are still poorly understood, FAdE is repressed during the transition from fetal to definitive cortex (Zubair et al., 2008). Upon FAdE repression, steroidogenic cells from the fetal zone shut down SF1 expression and are incorporated into the capsule, which in turn will reactivate SF1 expression in a FAdE-independent manner, possibly involving a putative definitive adrenal-specific enhancer (DAdE), to give rise to the definitive cortex. The mechanisms by which SF1 expression is restored in the definitive cortex, and the DAdE controlling this program, have still not been identified though may be partially addressed through this work (**Chapter 6**).

As expected based on its role in adrenal development, mice deficient in SF1 possess no adrenals or gonads and die within a few days of birth due to glucocorticoid deficiency, remediable with exogenous glucocorticoids (Ingraham et al., 1994; Luo et al., 1994; Majdic et al., 2002). However, while SF1 is expressed in all steroidogenic adrenocortical cells, anatomic and functional zonation of the adrenal cortex suggests that additional factors, like post-translational modifications, context-specific binding partners, or epigenetic patterning, may influence SF1 actions in a zone- and tissue-specific manner (Hammer et al., 1999; Nachtigal et al., 1998). While SF1 is key for steroidogenesis, SF1 may also be a central nexus for a variety of programs including cellular proliferation (Doghman et al., 2007) and glycolytic metabolism (Baba et al., 2014). Supporting this concept, the requirement for SF1 in adrenal organogenesis likely extends far beyond its role in steroidogenesis as mice incapable of steroidogenesis still develop adrenals (Caron et al., 1997). SF1-dependent transcriptional programming is active in ACC through somatic alterations (Almeida et al., 2010) and additional, previously unknown mechanisms. In this thesis, we demonstrate that β-catenin is a critical binding partner of SF1 and modulator of its activity in physiology and cancer (**Chapter 6**). This observation is particularly interesting given that Wnt/β-catenin signaling is critical for definitive adrenocortical homeostasis (section **2.5**) and is recurrently targeted for somatic alteration in ACC (**Chapter 3**).

The current model of adrenocortical differentiation is that it is centripetal, that is, terminally differentiated cells of the zG, zF, and zR all arise from a progenitor cell pool that resides in the histological zG and the mesenchymal capsule. Adrenocortical

differentiation status is defined by both endocrine and paracrine signaling pathways, and the interface between these pathways and SF1-dependent transcriptional programming enables the unique hormonal profile of each zone. Genetic abnormalities uncoupling endocrine and paracrine signaling are hallmarks of adrenocortical tumors and cancer. I will now provide a brief overview of endocrine and paracrine determinants of adrenal differentiation, and within these sections will briefly discuss how these pathways are disrupted through somatic alterations in adrenocortical tumors.

2.4. Endocrine determinants of adrenal differentiation

Endocrine determinants of adrenal differentiation dictate the hormonal output of each adrenocortical zone. The zG produces mineralocorticoids (aldosterone is the predominant mineralocorticoid in humans) as part of the renin-angiotensin-aldosterone system (RAAS) to meet hemodynamic demands and maintain blood pressure through coupled sodium and water retention (**Figure 2.3A**). Aldosterone production in the zG is stimulated by Angiotensin II (AngII). AngII binds the angiotensin receptor (ATR) on the surface of zG cells, leading to membrane depolarization, activation of the calcium/calmodulin-dependent protein kinase (CAMK) signaling cascade, upregulation of aldosterone synthase (encoded by *CYP11B2*) and aldosterone production (**Figure 2.3B**).

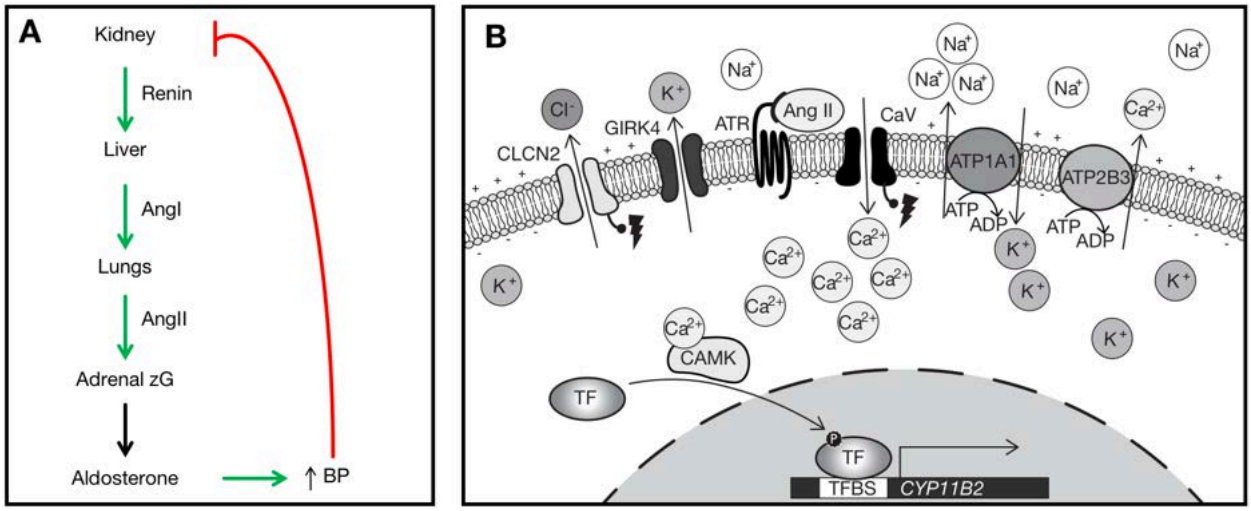

Figure 2.3. Endocrine control of zG aldosterone production.
A. In response to low perfusion pressure of the afferent arteriole (a proxy for low blood pressure), the kidney releases renin, which stimulates the liver to convert the prohormone Angiotensinogen to Angiotensin I (AngI). The liver releases AngI into circulation, and when AngI reaches the lungs, it is converted to Angiotensin II (AngII) by angiotensin-converting enzyme (ACE). Circulating AngII binds cells of the adrenocortical zG to stimulate aldosterone production. Aldosterone will stimulate sodium and water reabsorption in the kidney to raise blood pressure. High blood pressure will suppress renin release from the kidney and consequently aldosterone production by the adrenal zG. B. AngII binds to the angiotensin receptor (ATR) at the zG cell membrane, promoting inhibition of the ATP1A1 Na/K ATPase and decreased permeability of the GIRK4 potassium channel, leading to membrane depolarization. Decreased transmembrane potential leads to the opening of voltage-gated calcium channels (CaV), allowing calcium influx, accumulation in the cytoplasm, and subsequent activation of the calcium/calmodulin-dependent protein kinase (CAMK). CAMK activation promotes phosphorylation and/or upregulation and nuclear translocation of immediate early response transcription factors such as CREB, NURR1, NGFIB and ATF1, leading to transcription of *CYP11B2* (encoding aldosterone synthase). In the absence of Ang II, the activities of ATP1A1 and GIRK4 restore baseline membrane potential. In parallel, other ATPases, including ATP2B3, remove calcium from the cytoplasm, bringing the pathway activity to the resting state. "TFBS" = transcription factor binding site.

Aldosterone overproduction is rare in ACC (Zern et al., 2019); however, mutations in genes that encode ion channels or ATPases that regulate transmembrane potential or intracellular calcium homeostasis are recurrent in familial syndromes associated with aldosterone overproduction and benign sporadic adrenocortical tumors, specifically aldosterone-producing adrenocortical adenomas (**Table 2.2**). Aldosterone-producing adrenocortical adenomas may rarely possess activating somatic alterations in *CTNNB1*, encoding β-catenin, a classical paracrine determinant of zG differentiation (section **2.5**).

Table 2.2. Genetics of syndromic and sporadic benign adrenocortical aldosterone overproduction.

Syndrome	Inheritance	Gene(s)	Clinical features	Association with sporadic ACT
FH I	AD	*CYP11B1/ CYP11B2*	Early onset hyperaldosteronism with bilateral adrenal hyperplasia	None reported
FH II	AD	*CLCN2*	Early onset hyperaldosteronism with bilateral adrenal hyperplasia	Recurrent somatic alterations in *CLCN2* in sporadic aldosterone-producing ACA (Dutta et al., 2019)
FH III	AD	*KCNJ5* (encodes GIRK4)	Early onset hyperaldosteronism with bilateral adrenal hyperplasia	Recurrent somatic alterations in *KCNJ5* in sporadic aldosterone-producing ACA (Choi et al., 2011)
FH IV	AD	*CACNA1H*	Early onset hyperaldosteronism with bilateral adrenal hyperplasia	Recurrent somatic alterations in *CACNA1H* in sporadic aldosterone-producing ACA (Nanba et al., 2020)
PASNA	AD	*CACNA1D*	Early onset hyperaldosteronism with bilateral adrenal hyperplasia; cardiovascular and neurological abnormalities (seizures and developmental delay)	Recurrent somatic alterations in *CACNA1D* in sporadic aldosterone-producing ACA (Azizan et al., 2013; Scholl et al., 2013), APCC (Nishimoto et al., 2015)
N/A – associated with sporadic ACT only	N/A	*ATP1A1*, *ATP2B3*, rarely *CTNNB1*	N/A	Recurrent somatic alterations in ATPases and *CTNNB1* in sporadic aldosterone-producing ACA (Azizan et al., 2013; Beuschlein et al., 2013; Åkerström et al., 2016); recurrent somatic alterations in *CTNNB1* in ACC (Zheng et al., 2016)

NOTE. FH = Familial hyperaldosteronism; PASNA = Primary aldosteronism, seizures, and neurological abnormalities; AD = autosomal dominant; ACT = adrenocortical tumor(s); ACA = adrenocortical adenoma(s); APCC = aldosterone-producing cell cluster(s)

The zF of the adrenal cortex produces glucocorticoids (cortisol is the predominant glucocorticoid in humans) under control of pituitary adrenocorticotropic hormone (ACTH) in response to circadian shifts and/or physiological stress (**Figure 2.4A**). ACTH binds MC2R, a G_s-coupled G protein-coupled receptor (GPCR), on the surface of zF cells and

activates the cyclic AMP/protein kinase A (cAMP/PKA) signaling pathway, driving increased cellular proliferation and glucocorticoid production through upregulation of enzymes essential for cortisol production, e.g. *CYP11B1* (**Figure 2.4B**). The zR of the human adrenal cortex also produces androgens under control of ACTH.

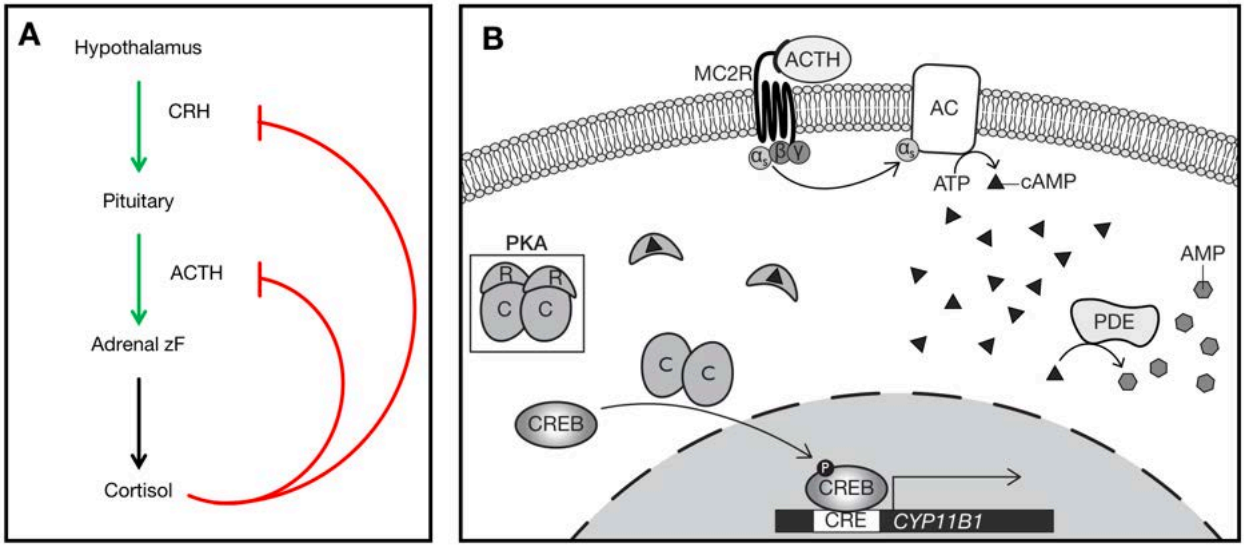

Figure 2.4. Endocrine control of zF cortisol production.
A. Corticotropin-releasing hormone (CRH) is released from the hypothalamus in a circadian manner (in humans, peak CRH release is in the morning; in nocturnal organisms like mice, peak CRH release is at night) or in response to stress. Hypothalamic CRH stimulates the anterior pituitary to produce ACTH, which acts on cells of the adrenocortical zF to stimulate glucocorticoid production. Serum levels of cortisol are regulated by negative feedback, where high serum cortisol suppresses ACTH production from the pituitary and CRH production from the hypothalamus. B. Physiologically, ACTH binds to MC2R on the surface of zF cells to activate the PKA pathway. Activation of MC2R promotes the dissociation of the α subunit of the heterotrimeric G_s protein from its other subunits. $G_{s,\alpha}$ binds to and activates adenylyl cyclase (AC), which converts ATP into cyclic AMP (cAMP), which acts as a second messenger to activate PKA. PKA is a tetramer comprised of two catalytic (C) and two regulatory (R) subunits. At baseline, PKA catalytic activity is inhibited by the regulatory subunits. Upon cAMP binding, the tetramer destabilizes and releases the catalytic units which subsequently catalyze phosphorylation of transcription factor CREB in the cytoplasm. Phosphorylated CREB is translocated to the nucleus where it interacts with CREB response elements (CRE) in the promoters of its target genes (e.g. *CYP11B1*) to drive transcription. Transcriptional transduction of PKA signaling may also be achieved by other immediate early response transcription factors, e.g. ATF/Jun/Fos. Phosphodiesterase (PDE) activity terminates PKA signaling by converting cAMP to its inactive form AMP, allowing the reassembly of the PKA tetramer.

Cortisol overproduction is frequent in ACC (Else et al., 2014a; Wajchenberg et al., 2000). Constitutive activation of the PKA pathway is observed in virtually all forms of

cortisol overproduction, including adrenocortical hyperplasia, benign adrenocortical adenomas and ACC, secondary to recurrent germline and somatic mutations targeting genes encoding several PKA components (**Table 2.3**). Intriguingly, cortisol-producing adenomas and ACC frequently possess activating somatic alterations in *CTNNB1*, suggesting that classical paracrine determinants of zG differentiation may alter zF endocrine identity (section **2.5**).

Table 2.3. Genetics of syndromic and sporadic benign adrenocortical cortisol overproduction.

Syndrome	Inheritance	Gene(s)	Clinical features	Association with sporadic ACT
McCune–Albright syndrome	Sporadic (post-zygotic somatic mosaicism)	*GNAS*	Cortisol-producing bilateral nodular hyperplasia; polyostotic bone dysplasia, gonadotropin-independent precocious puberty, café-au-lait spots, pituitary adenomas	Recurrent somatic alterations in *GNAS* in sporadic cortisol-producing ACA (Cao et al., 2014; Goh et al., 2014; Ronchi et al., 2016)
Carney's complex	AD	*PRKAR1A*	Micronodular pigmented adrenal hyperplasia; cutaneous lentigines, pituitary adenomas, cardiac myxomas, pancreatic, and cutaneous tumors	Recurrent somatic alterations in *PRKAR1A* in sporadic cortisol-producing ACA (Bertherat et al., 2003) and ACC (Zheng et al., 2016)
Primary Macronodular Adrenal Hyperplasia (PMAH)	AD	*ARMC5*	Bilateral nodular enlargement of adrenal glands associated with Cushing's syndrome; multiple meningiomas	None reported
N/A – associated with sporadic ACT only	N/A	*PRKACA, PRKACB, CTNNB1*	N/A	Recurrent somatic alterations in PKA catalytic subunit and *CTNNB1* in cortisol-producing ACA (Beuschlein et al., 2014; Cao et al., 2014; Espiard et al., 2018; Goh et al., 2014; Sato et al., 2014); recurrent somatic alterations in *CTNNB1* in ACC (Zheng et al., 2016)

NOTE. AD = autosomal dominant; ACT = adrenocortical tumor; ACA = adrenocortical adenoma(s). The molecular role of ARMC5 in PMAH and how it leads to constitutive PKA activation is still poorly understood.

2.5. Paracrine determinants of adrenal differentiation

Paracrine signaling in the adrenal cortex may reinforce or antagonize cellular differentiation states established by endocrine cues to enable cortical renewal. The homeostatic unit of the adrenal cortex is the corticocapsular unit, which includes the top layer of mesenchymal capsular cells and all layers of the adrenal cortex. Capsular, zG, and upper zF cells may be deployed to replenish other steroidogenic cells based on physiological and homeostatic demands, and differentiation is centripetal (**Figure 2.5**).

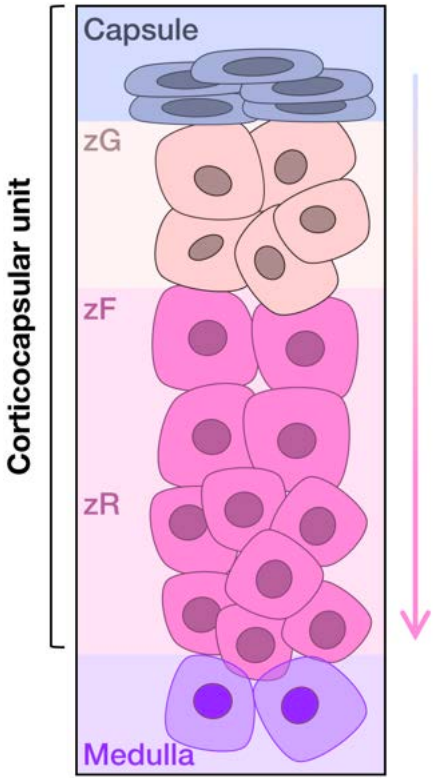

Figure 2.5. Schematized homeostatic corticocapsular unit of the adrenal cortex.
Capsular, subcapsular (histological zG) and upper zF cells may be deployed to renew the adrenal cortex in response to physiological homeostatic and endocrine demands. Differentiation is centripetal (indicated by the arrow right), and lower zR cells (humans) or lower zF cells (mice) are terminally differentiated and undergo apoptosis at the boundary between the cortex and the medulla (corticomedullary boundary).

The principal paracrine regulators in the adrenal cortex are Wnt ligands and Sonic hedgehog (Shh), expressed predominantly in the subcapsular region of the adrenal cortex (histological zG). Shh signaling enables crosstalk between the cortex and the capsule (the capsule expresses an Shh-responsive gene encoding the transcriptional effector of Shh-signaling, Gli1), is critical for adrenocortical homeostasis and ACTH-dependent renewal, and facilitates the differentiation of capsular cells into steroidogenic adrenocortical cells in the setting of high physiological demand (Finco et al., 2018). However, this pathway is virtually never disrupted in ACC, as ACC grow autonomously, independently from endocrine and capsular cues, and often breach capsular boundaries (Weiss et al., 1989). In contrast, members of the Wnt pathway (including canonical transcriptional co-activator β-catenin) are recurrently targeted for somatic alteration in ACC, and approximately 40% of ACC possess mutations leading to constitutive pathway activation ((Zheng et al., 2016), **Chapter 3**). Humans with germline defects in Wnt signaling components develop adrenocortical hyperplasia and cancer (Kartheuser et al., 1999; Marshall et al., 1967; Nishisho et al., 1991). The focus of this section is therefore on highlighting molecules that define the differentiation status of different layers of the corticocapsular unit and on how paracrine Wnt signaling interfaces with these and endocrine signaling programs (particularly ACTH/PKA) to coordinate adrenocortical differentiation.

The capsule is comprised of thin layers of mesenchymal cells, almost invariably expressing mesenchymal transcription factor *Nr2f2* (encoding COUP-TFII, (Pereira et al., 1995; Suzuki et al., 2000)). Several long-term retained populations of distinct

developmental origins have been characterized in the capsule. These include populations expressing genes that are not expressed in the adrenal cortex including *Wt1, Tcf21, Gli1,* and *Rspo3*. Several of these cell types are essential for maintenance of progenitor cells residing in the adrenal cortex, and can differentiate into steroidogenic cells in times of high physiological demand (Bandiera et al., 2013; Ching and Vilain, 2009; Finco et al., 2018; Huang et al., 2010; King et al., 2009; Mathieu et al., 2018; Val et al., 2007; Wilhelm and Englert, 2002; Wood et al., 2013). All capsular cells are SF1-negative and not steroidogenic. However, some capsular populations derive from cells expressing SF1 under control of FAdE during development (Bandiera et al., 2013; Wood et al., 2013), suggesting epigenetic memory of adrenocortical identity may underlie the capsular contribution to cortical renewal.

Recent studies have also implicated the subcapsular outer adrenal cortex (histological zG) as the location of adrenocortical progenitors recruited in response to endocrine and paracrine factors. Under physiologic conditions, these progenitors are likely the major contributors to cortical homeostasis. The current model suggests that descendants of these cells differentiate and migrate centripetally, undergoing apoptosis at the corticomedullary boundary, thus giving rise to steroidogenic cells of the zG and zF (Ching and Vilain, 2009; Finco et al., 2018; Freedman et al., 2013; Huang et al., 2010; King et al., 2009; Vinson, 2016). Of particular importance to adrenocortical homeostasis and cancer is the Wnt/β-catenin signaling pathway, a conserved paracrine signaling cascade broadly required for stem/progenitor cell maintenance in many tissues including the adrenal cortex (Nusse and Clevers, 2017). In the canonical Wnt signaling pathway,

Wnt ligands bind to cell surface receptors (Farin et al., 2016), leading to β-catenin stabilization and translocation into the nucleus, where it complexes with TCF/LEF transcription factors to initiate target gene transcription (Wiese et al., 2018). Canonical Wnt signaling is established after AGP formation (E9.5) and encapsulation (E12.5), defines the definitive adrenal cortex, and facilitates establishment of definitive adrenocortical steroidogenesis (Kim et al., 2008). The dosage of β-catenin is critical at this stage, as both β-catenin excess and deficiency are associated with adrenal aplasia and hypoplasia (Drelon et al., 2016b; Huang et al., 2012; Kim et al., 2008).

The definitive adrenal cortex is characterized by a gradient of Wnt ligands that propels from the zG toward the upper zF and activates canonical Wnt signaling in this region (Basham et al., 2019; Drelon et al., 2016b; Heikkila et al., 2002; Kim et al., 2008). The long-held model of Wnt signaling in the adrenal cortex is that Wnt ligands act as a paracrine determinant of zG differentiation that antagonizes ACTH/PKA signaling and zG to zF lineage conversion. This is supported by mouse models that possess defects in ACTH/PKA signaling and exhibit a reduction in cortical cells with Wnt/β-catenin signaling in the case of ACTH/PKA GOF (Drelon et al., 2016b), and an expansion in cortical cells with Wnt/β-catenin signaling in the case of ACTH/PKA LOF (Finco et al., 2018; Novoselova et al., 2018). This paradigm is also supported by mouse models bearing conditional LOF or GOF in adrenal Wnt/β-catenin signaling components and consequent mineralocorticoid deficiency or excess (Berthon et al., 2010; Drelon et al., 2016b; Heikkila et al., 2002; Pignatti et al., 2020).

More recently, genetic models disrupting novel regulators of the Wnt/β-catenin signaling pathway or disrupting this pathway in novel contexts have identified that Wnt/β-catenin also plays a critical role in zF homeostasis. Particularly relevant for this thesis, ACTH-dependent zF renewal is also reliant on intact canonical Wnt signaling (Finco et al., 2018), and a mouse model developed by our group wherein SF1+ and CYP11B2+ adrenocortical cells lose expression of a negative regulator of Wnt signaling, ZNRF3, exhibits zG/zF boundary hyperplasia and ACTH suppression suggestive of early stages of autonomous corticosterone production (Basham et al., 2019). Additionally, constitutive activation of Wnt/β-catenin signaling in combination with genetic alterations leading to genomic instability/constitutive cell cycle activation causes zG/zF hyperplasia, combined aldosterone and glucocorticoid overproduction, and fully penetrant metastatic adrenal cancer (Borges et al., 2020). Though not through direct targeting Wnt/β-catenin, constitutive cell cycle activation induced by adrenocortical expression of the SV40 large T-antigen (SV40 Tag) also leads to expansion of a zG/zF boundary population that retains high levels of nuclear β-catenin, secretes glucocorticoids autonomously, and evolves to malignancy (Batisse-Lignier et al., 2017).

These advances in mouse modeling of adrenocortical homeostasis (**Table 2.4**) suggest that there is a population of cells residing at the zG/zF boundary that exhibit partial zF differentiation (capable of glucocorticoid production), are responsive to Wnt ligands with proliferation/transit amplification, and are susceptible to malignant transformation. Though additional studies certainly need to be performed to definitively prove this, these cells may represent the cell of origin for Wnt-active, cortisol-producing

ACC (**Figure 2.6**). These studies also reconcile the observation that both benign and malignant adrenocortical tumors bearing somatic alterations leading to constitutive Wnt pathway activation frequently have cortisol overproduction or are hormonally silent, and only rarely have aldosterone overproduction (**Table 2.2 – Table 2.3**).

Table 2.4. Mouse models with genetic disruption of adrenal Wnt/β-catenin signaling.

Cre driver	Cells targeted	Genetic alteration	Molecular consequence	Adrenal phenotype	Reference
Gli1-CreERT2, cCAG-CreERT	Gli+ capsular cells, whole body upon tamoxifen administration	*Rspo3*$^{fl/fl}$	Wnt LOF via loss of positive regulator of ligand-dependent Wnt signaling	Loss of zG zonation, capsular adjacent zF, loss of *Cyp11b2* expression	(Vidal et al., 2016)
SF1-cre	Entire SF1+ cortex	*Ctnnb1*$^{fl(ex3)}$/+	Wnt GOF via constitutive stabilization of β-catenin	Unilateral adrenal aplasia and/or hypoplasia	(Drelon et al., 2016b; Huang et al., 2012)
AS-cre	CYP11B2+ cells (steroidogenic zG)	*Ctnnb1*$^{fl(ex3)}$/+	Wnt GOF via constitutive stabilization of β-catenin	zG hyperplasia with aldosterone excess	(Pignatti et al., 2020)
Akr1b7-cre	Stochastic targeting of steroidogenic cortex	*Ctnnb1*$^{fl(ex3)}$/+	Wnt GOF via constitutive stabilization of β-catenin	zG hyperplasia with aldosterone excess, and cortical proliferation is accelerated by *Prkaca* deficiency (reduction in ACTH/PKA signaling)	(Berthon et al., 2010; Drelon et al., 2016b)
SF1-cre (stochastic)	Stochastic targeting of SF1+ cortex	*Apc*$^{loxP/loxP}$	Wnt GOF via defective destruction of β-catenin	Late onset cortical hyperplasia, remediated with concomitant *Ctnnb1* deletion	(Heaton et al., 2012)
SF1-cre, AS-cre	Entire SF1+ cortex, CYP11B2+ cells	*Znrf3*$^{fl/fl}$	Wnt GOF via loss of negative regulator of ligand-dependent Wnt signaling	zG/zF boundary hyperplasia with corticosterone output compensated by ACTH suppression; SF1-cre model remediated with concomitant deletion of *Porcn* (required for Wnt ligand secretion) or *Ctnnb1*	(Basham et al., 2019)
SF1-cre, SF1-cre (stochastic)	Entire SF1+ cortex, stochastic targeting of SF1+ cortex	*Ctnnb1*^{tm2kem}	Wnt LOF via loss of β-catenin	Adrenal regression by E18.5, adrenal failure by 15 weeks	(Kim et al., 2008)
Axin2-creERT2	Axin2+ cells (adrenal zG and upper zF) upon tamoxifen administration	*Ctnnb1*^{tm2kem}	Wnt LOF via loss of β-catenin	Inadequate zF recovery during ACTH-dependent adrenocortical regeneration	(Finco et al., 2018)
None	Whole body	*Wnt4*$^{-/-}$	Wnt LOF via loss of Wnt ligand	Reduction in *Cyp11b2* expression; aldosterone deficiency with corticosterone excess	(Heikkila et al., 2002)
SF1-cre	Entire SF1+ cortex	*Wnt4*$^{fl/fl}$	Wnt LOF via loss of Wnt ligand	zG hypoplasia and zF hyperplasia	(Drelon et al., 2016b)

(Table continued on next page)

Cre driver	Cells targeted	Genetic alteration	Molecular consequence	Adrenal phenotype	Reference
Akr1b7 (transgene)	Stochastic targeting of steroidogenic cortex	SV40 Tag	Wnt GOF in the setting of cell cycle activation via simultaneous inhibition of p53 and pRb via unknown mechanisms. SV40 may immortalize adrenocortical cells capable of Wnt signaling	zG/zF boundary dysplasia to carcinoma with corticosterone excess and ACTH suppression	(Batisse-Lignier et al., 2017)
AS-Cre	CYP11B2+ cells (steroidogenic zG)	*Ctnnb1*$^{fl(ex3)}$/+, *Trp53*$^{fl/fl}$	Wnt GOF via constitutive stabilization of β-catenin, genomic instability and constitutive cell cycle activation via loss of p53	zG/zF boundary dysplasia to carcinoma with aldosterone and corticosterone excess and ACTH suppression	(Borges et al., 2020)

NOTE. Corticosterone, and not cortisol, is the predominant glucocorticoid produced by the mouse adrenal cortex.

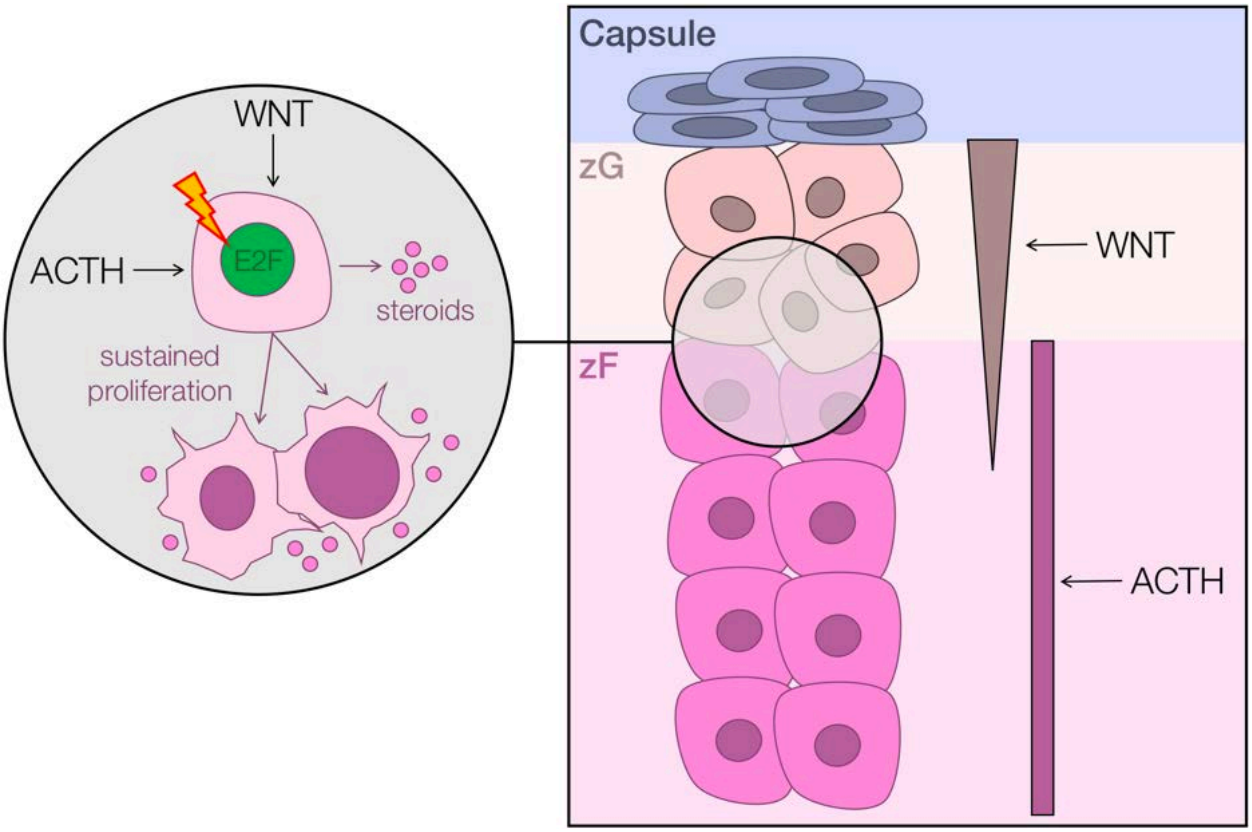

Figure 2.6. Murine models of Wnt/β-catenin adrenocortical homeostasis and cancer point to a putative cell of origin for Wnt-active ACC.
Schematized right is an abbreviated portion of the corticocapsular unit of the adrenal cortex. The upper layer of the adrenal cortex, the zG and upper zF, bears a gradient of active Wnt signaling and produces mineralocorticoids. The second layer of the adrenal cortex, the zF, proliferates and produces glucocorticoids in response to ACTH/PKA (Finco et al., 2018). Comprehensive molecular profiling studies identified recurrent mutations leading to constitutive activation of both ACTH/PKA and Wnt signaling in ACC (**Table 2.3**, **Chapter 3**) and demonstrated that Wnt/β-catenin pathway alterations are significantly associated with clinical cortisol production (**Table 2.3**, **Chapter 3**; (Zheng et al., 2016)). Recent mouse models of ACTH-driven zF regeneration (Finco et al., 2018), augmented Wnt/β-catenin signaling supported by ZNRF3 deficiency (Basham et al., 2019), sustained proliferation triggered by adrenocortical expression of the SV40 Tag (Batisse-Lignier et al., 2017), or combined simultaneous Wnt/β-catenin and cell cycle activation (Borges et al., 2020) also demonstrate a unique interplay between Wnt/β-catenin and ACTH/PKA signaling in enabling proliferation of cells residing in the zG/zF boundary. Taken together, these studies support the existence of a small population of zG/zF boundary cells that are capable of rapidly proliferating in response to sustained Wnt/β-catenin and/or ACTH signaling. Prolonged cell cycle activation (schematized here by E2F) may render these cells susceptible to malignant transformation and ligand-independent growth.

2.6. Epigenetic control of adrenocortical differentiation

Recurrent genetic alterations in benign and malignant adrenocortical tumors classically uncouple endocrine and paracrine regulation, and tumors may display a broad spectrum of quantitatively and qualitatively variable hormonal secretion patterns. The defects in zG to zF lineage conversion in mouse models of Wnt/β-catenin and ACTH/PKA dysfunction suggest that non-genetic factors like epigenetic programming fine tune subtle shifts in the chromatin environment to facilitate differentiation. Supporting this argument, both *in vivo* models of adrenocortical carcinogenesis exhibit cell cycle-dependent upregulation of *Ezh2* in dysplastic lesions and cancer (Batisse-Lignier et al., 2017; Borges et al., 2020). To add granularity to this hypothesis, we analyzed data from a recent study performing single-cell RNA-seq profiling of the adrenal gland as part of a human single-cell atlas (Han et al., 2020). This analysis revealed that continuous and often fine changes in gene expression facilitate differentiation and transit-amplification in the corticocapsular unit (**Figure 2.7**).

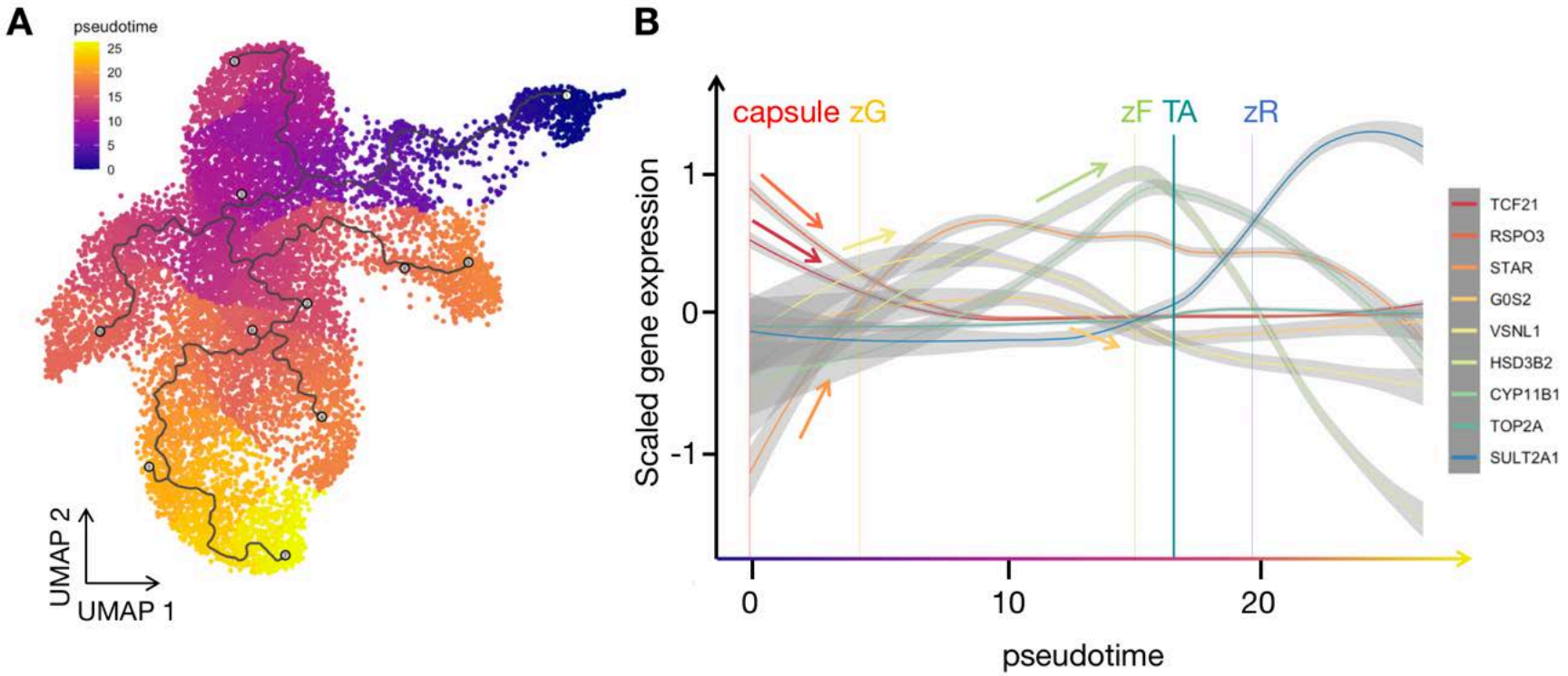

Figure 2.7. Continuous shifts in gene expression mediate differentiation in the adrenal corticocapsular unit and identify a transit-amplifying cell population with partial zF differentiation.
Gene expression matrices of human fetal, neonatal and adult adrenal single-cell RNA-seq data (Han et al., 2020) were filtered, normalized, batch-corrected, integrated, scaled, and UMAP clustered using Seurat with CCA integration algorithm (Stuart et al., 2019). Suspected doublet cells or low-quality cells (fewer than 500 unique transcripts) were excluded. Non-adrenocortical/capsular cells (e.g. immune cells, medulla cells) were excluded by serial rounds of UMAP clustering and cluster marker identification. Gene expression was scaled so that mean expression across all cells is 0 and variance across all cells is 1, and regressed against mitochondrial content and total number of transcripts/cell. Cluster marker identification also enabled assignment of single cell clusters to known adrenocortical/capsular cell populations. Adrenocortical/capsular cells were subject to pseudotime trajectory analysis using Monocle 3 (Cao et al., 2019; Qiu et al., 2017a; Qiu et al., 2017b; Trapnell et al., 2014), with UMAP embeddings from Seurat and origin (pseudotime = 0) set at the presumed adrenocortical capsule (A). This analysis revealed persistence of the centripetal corticocapsular differentiation trajectory, confirmed by analysis of marker gene expression across pseudotime in adult adrenocortical cells from this dataset (B). Importantly, this analysis supports the idea that transit-amplifying cells in the adrenal cortex (TA) exhibit partial zF differentiation, and highlights the dramatic step change in capsule to cortical and zF to zR identity. In contrast, many genes that are thought to be all or none zG/zF markers (Nishimoto et al., 2015) exhibit gradual shifts across the adrenocortical differentiation trajectory.

The concept that epigenetic patterning supports adrenocortical differentiation (particularly zG to zF differentiation) was demonstrated by a recent mouse model with SF1-cre driven *Ezh2* deletion (Mathieu et al., 2018). EZH2 expression in the adult cortex is highest in the proliferating cells residing in the zG/zF boundary, though EZH2 protein is actually broadly expressed throughout the murine adrenal cortex (data and communications, not shown). Mice with SF1-cre driven *Ezh2* deletion strikingly developed primary glucocorticoid insufficiency with severe zonation defects, notably zF hypoplasia concomitant with zG expansion and increased zG-specific gene expression (Mathieu et al., 2018). These investigators intriguingly did not observe changes in expression of Wnt/β-catenin target genes, and attributed the zF hypoplasia to a claim that adrenocortical EZH2 deposits H3K27me3 on the promoters of a few genes encoding negative regulators of PKA signaling (genes encoding PDEs, **Figure 2.4**). These findings suggest EZH2 may be crucial for priming cells of the zF to respond to ACTH with both proliferation and differentiation (Mathieu et al., 2018), though several modes of EZH2 action remain unexplored.

For example, the molecular mechanism for EZH2's function in cells transitioning from zG to zF identity and a rationale supporting why EZH2 would have additional roles in a more differentiated part of the cortex, unlike known models of PRC2 function (section **1.5**), remain unclear. Deletion of *Ezh2* also fails to dissect a catalytic (PRC2-dependent) or non-catalytic (PRC2-independent) requirement for EZH2 in the adrenal cortex, which is further complicated by the observation that EZH2-deficient cells could achieve zG differentiation. Finally, the onset of the SF1-cre is embryonic, occurring as early as the

AGP (E10.5) (Bingham et al., 2006), and several defects in this model may be attributed solely to defective AGP specification and/or adrenocortical development. We therefore turned to alternative models to evaluate the somatic requirement for PRC2/EZH2 in adrenocortical homeostasis.

Our group recently developed a mouse model of ACTH-dependent zF regeneration (Finco et al., 2018). In this model, mice are treated for two weeks with dexamethasone, a synthetic glucocorticoid that acts similarly to cortisol and also suppresses ACTH release from the pituitary (**Figure 2.4**). Two-week administration of dexamethasone leads to potent suppression of ACTH and complete loss of endogenous glucocorticoid production, *Cyp11b1* expression, and variable collapse of the zF with reduction in adrenal weight/body weight ratio. Dexamethasone is then withdrawn to enable mice to recover ACTH and endogenous glucocorticoid production. Adrenal regeneration occurs in several phases. By the last day of dexamethasone administration/first day of withdrawal (R0), mouse adrenals exhibit a higher proportion of cells bearing nuclear β-catenin, which diminishes during regeneration and likely reflects the loss of ACTH in stimulating zG to zF lineage conversion. By three days after dexamethasone withdrawal (R3), mouse adrenals exhibit a proliferative burst coincident with a rise in expression of cell cycle-dependent genes like *Ezh2.* By seven days after dexamethasone withdrawal (R7), mouse adrenals recover ACTH-dependent steroidogenesis. Finally, by 14 days after dexamethasone withdrawal, ACTH and adrenocortical function are completely restored (Finco et al., 2018).

Given the rise of *Ezh2* expression during zF regeneration (Finco et al., 2018), we took advantage of this model to evaluate if inhibition of EZH2's catalytic activity (EZH2i) during the regeneration phase hampers adrenal recovery. Though our analysis of this data is still preliminary, we observed that EZH2i delays recovery of adrenal weight (**Figure 2.8**) and is associated with persistence of an augmented Wnt/β-catenin signaling gradient (**Figure 2.9**). These data suggest that, in somatic adrenocortical cells, EZH2 catalytic activity is required to enable faithful ACTH-dependent zF differentiation. Taken together, our work and others' support an essential role for EZH2 in enabling cell cycle-avid/transit-amplifying zF cells to respond to ACTH during development and cortical renewal, illustrating highly tissue-specific actions for this epigenetic modifier, which will later be relevant in the context of ACC (**Chapter 6**).

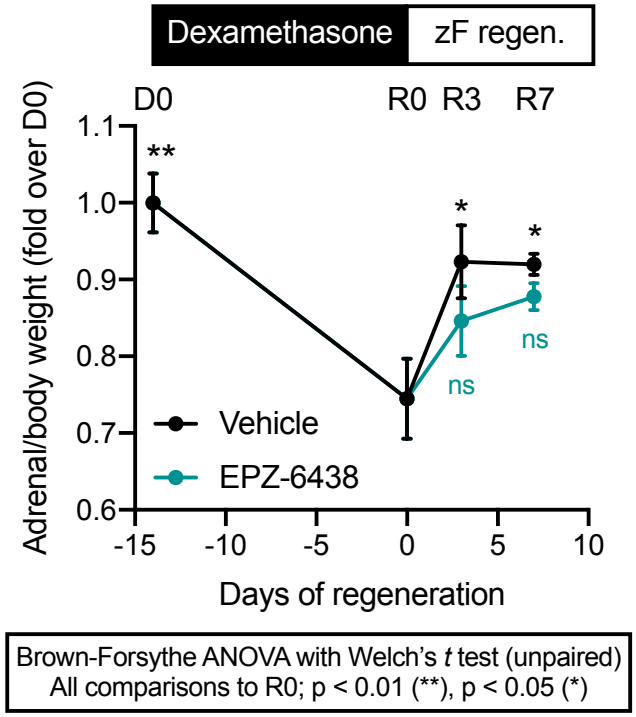

Figure 2.8. Inhibition of EZH2 catalytic activity hinders adrenocortical regeneration.
Mice (C57/BL6 male, 6-14 weeks of age) were treated with 2 weeks of dexamethasone water to suppress ACTH-dependent zF renewal, after which time dexamethasone water was withdrawn to enable ACTH-dependent zF regeneration as in (Finco et al., 2018). During regeneration, mice received daily or almost daily oral gavage with vehicle or 200 mg/kg EZH2 inhibitor (EZH2i) EPZ-6438. Mice were sacrificed immediately prior to dexamethasone administration (D0), after 14 days of dexamethasone administration immediately prior to dexamethasone withdrawal (R0), after 3 days of adrenal regeneration (R3) or after 7 days of adrenal regeneration (R7). Sacrifice was performed from 9-11 AM. Body weights were obtained in the afternoon on the day prior to sacrifice. Points indicate the mean adrenal/body weight (fold change compared to one mouse in D0 group) and whiskers reflect standard error of the mean. D0, 6 mice; R0, 5 mice; R3, 12 mice (Vehicle), 11 mice (EPZ-6438); R7, 3 mice (Vehicle), 4 mice (EPZ-6438).

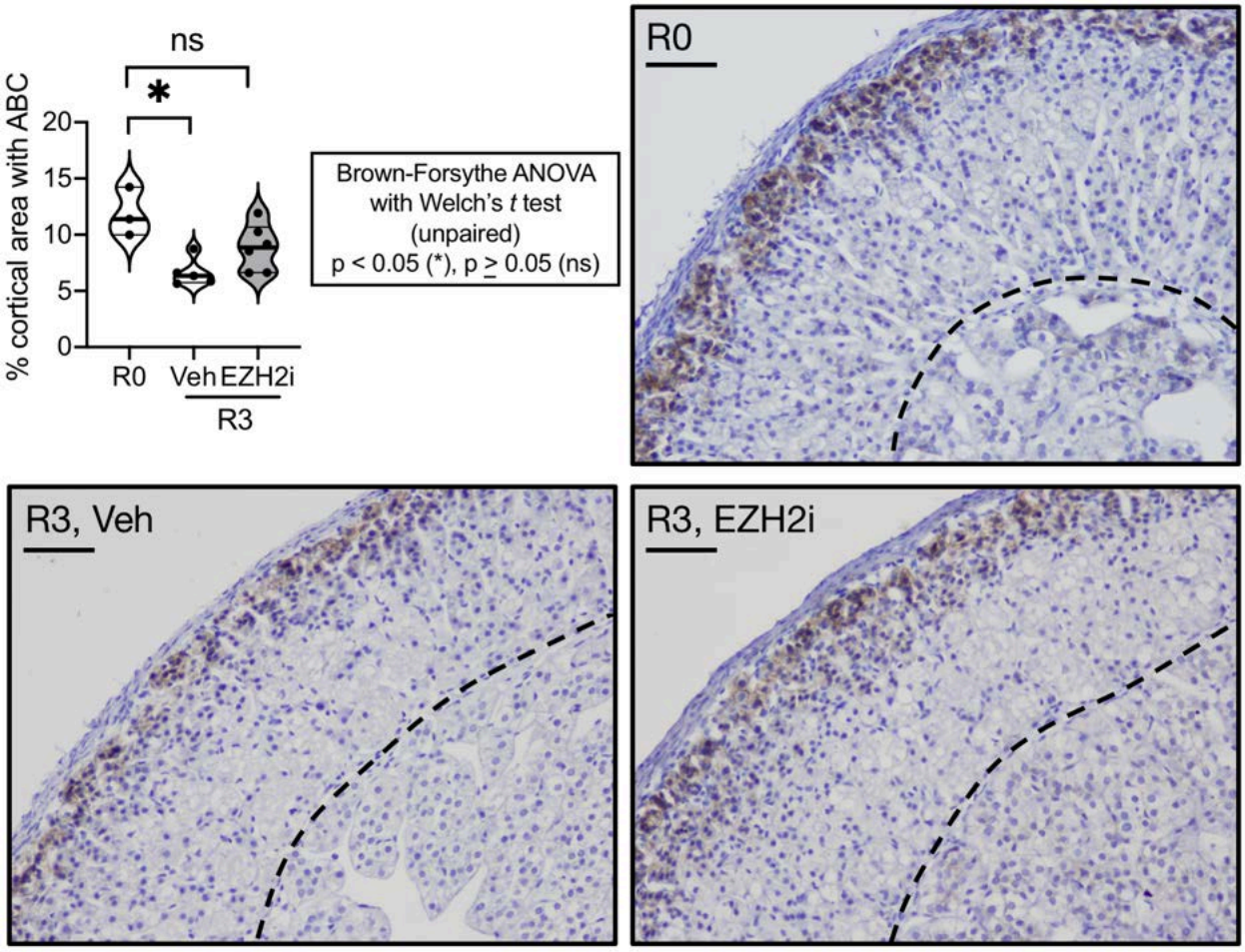

Figure 2.9. EZH2i during adrenocortical regeneration disrupts zG to zF lineage conversion.
Adrenals from mice enrolled in regeneration experiment in **Figure 2.8** were processed for immunohistochemical (IHC) evaluation of active β-catenin (signal is detected using DAB, brown; nuclei are counterstained with hematoxylin). β-catenin typically appears as a centripetal gradient in the adrenal cortex with highest nuclear/cytoplasmic staining in the zG, membranous/faint nuclear and cytoplasmic staining at the zG/zF boundary, and no staining in the lower zF. Following dexamethasone administration, the β-catenin-staining zone encompasses a larger portion of the adrenal cortex, likely because zG cells that cannot undergo ACTH-dependent zG/zF lineage conversion accumulate at the zG/zF boundary (Finco et al., 2018). As shown here, following 3 days of adrenal regeneration, vehicle-treated mice recover a reduction in the proportion of cortical β-catenin-staining cells compared to R0, while EZH2i-treated mice do not. Top left panel, cortical IHC DAB signal was quantified on two 20x images per mouse using a homemade macro in Fiji (Schindelin et al., 2012); each dot in the plot represents an individual mouse. R0, 3 mice; R3, 5 mice (Vehicle, "Veh"), 6 mice (EZH2i). Representative images are shown top right (R0), bottom left (R3, Veh) and bottom right (R3, EZH2i); bar = 100 μm. Dashed line drawn at corticomedullary boundary (cortex is to the left of the dashed line and medulla is to the right of the dashed line).

2.7. Adrenocortical differentiation and tumorigenesis

Mechanisms supporting adrenocortical differentiation are also relevant for tumorigenesis. ACC possesses a spectrum of zF differentiation, and almost never exhibit steroidogenic zG differentiation (e.g. autonomous aldosterone secretion) despite recurrent Wnt/β-catenin pathway alterations. The most aggressive ACC are CIMP-high and bear hyperactivation of the Wnt pathway, cell cycle, and zF programming (Zheng et al., 2016). These key features of aggressive ACC will be discussed in more detail and investigated in **Chapters 3 – Chapter 6**. Despite the apparent relative differentiation of aggressive ACC, ACC in general are less differentiated than the normal cortex and benign adrenocortical tumors (Giordano et al., 2009; Giordano et al., 2003). This observation suggests aggressive ACC may be trapped in a less differentiated upper zF or zG/zF boundary state which favors sustained proliferation and is maintained through epigenetic mechanisms. Inspection of our epigenome data from the ACC cell line NCI-H295R for a few loci known to be zonally expressed or restricted to the capsule supports this argument, and suggests ACC may be trapped in a transit-amplifying state (**Table 2.5**). Genes that are expressed exclusively in the capsule are silenced in NCI-H295R and retain PRC2 control and promoter H3K27me3/EZH2. zG/zF boundary and cell cycle genes are highly expressed, retain H3K27ac, and are coordinated by SF1 at proximal and distal elements. *G0S2* is silenced in this cell line indicating that it is a model of CIMP-high ACC (**Chapter 3 – 4**). Intriguingly, *SULT2A1*, a zR gene, is highly expressed and possesses H3K27ac and SF1 at relevant CREs. This may reflect the penetrance of the SF1-dependent transcriptional program in ACC and highlights the potential for cell identity

plasticity in this cell line, suggesting that alternative differentiation states (if favorable for sustained proliferation) may be achievable. This theme will begin to be explored in **Chapter 3** and will be particularly relevant for **Chapters 5** and **6**.

Table 2.5. Zonal genes and their epigenetic regulation in NCI-H295R.

Gene	Adrenal expression pattern	FPKM	Promoter H3K27me3?	Promoter EZH2?	Promoter H3K27ac?	Promoter SF1?	Putative active enhancer SF1?
WT1	Capsule	Undetectable	Yes	Yes	No	No	No
TCF21	Capsule	Undetectable	Yes	Yes	No	No	No
RSPO3	Capsule	Undetectable	Yes	Yes	No	No	No
STAR	All zones, highest in zF and zR	177.7995509	No	No	Yes	Yes	Yes
VSNL1	zG	11.0478147	No	No	Yes	Yes (more distal from annotated TSS than traditional promoter, inside transcript and ~5kb upstream from first exon)	Yes
HSD3B2	zG, zF; will classify as a zF gene for simplicity	34.9175176	No	No	Yes	Yes but more distal than standard promoters; most proximal peak to TSS is ~4 kb upstream	Yes
G0S2	zG (Han et al., 2020)/zF (Nishimoto et al., 2015); will classify as a zF gene for simplicity. Silenced by methylation in CIMP-high ACC and NCI-H295R (**Chapters 3 – 4**)	Undetectable	No	No	No	No	No
CYP11B1	Expressed in all zones, highest in zF	0.104993238	Region too repetitive for accurate mapping	Region too repetitive for accurate mapping	Region too repetitive for accurate mapping	Region too repetitive for accurate mapping	Region too repetitive for accurate mapping
TOP2A	zF transit-amplifying	89.3720762	No	No	Yes	No	Yes
SULT2A1	zR	39.47136271	No	No	Yes	Yes	Yes

NOTE. Zonal expression determined based on **Table 2.1**, **Figure 2.2**, **Figure 2.7** and the literature. FPKM from RNA-seq performed on baseline *in vitro* model of ACC, NCI-H295R cell line (data introduced in **Chapter 3**). For reference, in this dataset median gene expression is an FPKM of ~3.8. H3K27me3, EZH2, H3K27ac, SF1 peaks identified from ChIP-seq performed on baseline NCI-H295R cell line (data introduced in **Chapter 6**). Putative active enhancers of a given gene were identified by overlapping human adrenal promoter capture Hi-C contact tables (Jung et al., 2019) with H3K27ac peaks identified from H3K27ac ChIP-seq performed on baseline NCI-H295R (data introduced in **Chapter 5**). An active enhancer is defined as a distal CRE overlapping with an H3K27ac peak. Putative active enhancers were manually inspected for the presence of SF1 binding.

2.7. Materials and methods

Analysis of microarray data from microdissected adrenals. Raw microarray data was downloaded from GEO (GSE68889) and analyzed as in (Finco et al., 2018). RMA normalization was used to obtain expression values (Irizarry et al., 2003).

Analysis of adrenal promoter-centered Hi-C. Promoter-other contact tables were downloaded from GEO (GSE86189) and overlapped with NCI-H295R ChIP-seq data as described in the notes for **Tables 2.1** and **2.5** to link active enhancers to genes. Overlaps between regions were computed using *bedtools* (Quinlan and Hall, 2010).

NCI-H295R RNA-seq and ChIP-seq. This data and relevant analysis will be introduced in **Chapters 3, 5,** and **6.**

Analysis of single-cell RNA-seq data. DGE matrices from human adrenal single-cell RNA-seq were downloaded from GEO (GSE134355), and analyzed using Seurat (Stuart et al., 2019) and Monocle 3 (Cao et al., 2019; Qiu et al., 2017a; Qiu et al., 2017b; Trapnell et al., 2014) as detailed in the legend for **Figure 2.7**.

Adrenal regeneration experiments. Adrenal regeneration experiments, acquisition of adrenal tissue, and tissue processing were performed as described in (Finco and Hammer, 2018; Finco et al., 2018) and **Figures 2.8 – 2.9**.

IHC. IHC was performed using the VECTASTAIN Elite ABC-HRP Kit, Peroxidase (Rabbit IgG) (Vector Labs, Cat. No. PK-6101) according to manufacturer's instructions with the following modifications: all kit reagents were prepared using PBS as the buffer, and washes were performed with PBS + 0.1% Tween-20. Antigen retrieval was performed with boiling 10 mM sodium citrate pH 6.0, 20 minutes, followed by benchtop cooling for 20 minutes. Endogenous peroxidase was quenched with 3% H_2O_2 in MilliQ water at room temperature for 20 minutes. Blocking was performed in a humidified chamber at room temperature for 2 hours. Primary antibody incubation (1:500 Active β-catenin, Cell Signaling Technology, Cat. No. 8814) was performed in a humidified chamber at 4°C overnight, and secondary antibody incubation was performed in a humidified chamber at room temperature for 30 minutes. SIGMAFAST™ 3,3′-Diaminobenzidine (DAB) tablets (Sigma-Aldrich, Cat. No. D4168-50SET) served as the peroxidase substrate and were used according to manufacturer's instructions with same development time for all samples. Slides were equilibrated with tap water and counterstained with Gills #1 Hematoxylin for 30 seconds prior to dehydration. Slides were mounted with Vectamount Permanent Mounting Medium (Vector Labs, Cat. No. H-5000).

IHC quantification. Quantification of IHC signal was performed using Fiji (Schindelin et al., 2012). Briefly, IHC slides were imaged at 20x brightfield using a Nikon Optiphot 2 with capsule aligned at the top of the field. A polygon was then drawn to encompass the entire cortical area (excluding capsule and medulla). Image was deconvoluted using H DAB vectors, and the DAB channel was then automatically thresholded. Thresholded DAB

signal was measured as a proportion of the cortical area demarcated by the polygon. Two representative images (covering different areas of the adrenal) per mouse were used for quantification with average value per mouse plotted in **Figure 2.9**.

CHAPTER 3. ACC Molecular Subtypes and Model Systems

3.1. Disclosure of relevant publications

Portions of this work have been published:

> **Mohan DR**, Lerario AM, Finco I, Hammer GD. New strategies for applying targeted therapies to adrenocortical carcinoma. *Current Opinion in Endocrine and Metabolic Research*. 2019 Oct 1. 8:66-71.
>
> **Mohan DR**, Lerario AM, Hammer GD. Therapeutic Targets for Adrenocortical Carcinoma in the Genomics Era. *Journal of the Endocrine Society.* 2018 Sep 26;2(11):1259-1274

Portions of this work are being prepared for publication:

> **Mohan DR**, Borges KS, Finco I, LaPensee CR, Solon A, Rege J, Little III DW, Else T, Almeida MQ, Apfelbaum A, Vinco M, Wakamatsu A, Mariani BMP, Latronico AC, Mendonca BB, Zerbini MCN, Fragoso MCBV, Lawlor ER, Ohi R, Rainey WE, Venneti S, Marie SKN, Giordano TJ, Breault DT, Lerario AM*, Hammer GD*. A differentiation program coordinated by SF1/β-catenin is a targetable epigenetic vulnerability in aggressive adrenocortical carcinoma. In preparation. *co-senior author
>
> Lerario AM*, **Mohan DR***, Rege J, Rainey WE, Hammer GD. Meta-analysis of adrenocortical tumors identifies cell of origin programs derailed in tumorigenesis and malignancy. In preparation. *co-first author

3.2. Introduction

ACC is a rare cancer of the adrenal cortex with a global annual incidence of 0.5 to 2 individuals per million (Kerkhofs et al., 2013; Wajchenberg et al., 2000). Despite its rarity, outcomes for patients diagnosed with ACC remain dismal, with 5-year overall

survival of ~35% (Else et al., 2014a). Furthermore, while 50% of patients are diagnosed with surgically resectable locoregional disease, ~75% of all patients will ultimately develop metastases (Glenn et al., 2019). Treatment options for patients with metastatic disease are limited and often ineffective: patients receive the DDT-derived adrenolytic agent mitotane +/- cytotoxic chemotherapy, sometimes paired with palliative surgery for resectable lesions, but <10% of patients with metastatic disease survive 5 years on these agents (Fassnacht et al., 2013; Lerario et al., 2019). Taken together, these statistics highlight a critical need for novel therapeutic strategies to fight ACC, contingent on a deeper understanding of the molecular basis of this disease.

Recent advances in comprehensive molecular profiling, biomarker identification (**Chapter 4**) and *in vivo* (**Chapter 2**) and *in vitro* modeling have now illuminated a spectrum of pharmacologically targetable molecular programs essential for adrenocortical development and homeostasis and uniquely derailed in cancer. In this chapter, I will summarize these developments, detail our efforts to characterize *in vitro* ACC models that will be utilized in this dissertation, and describe their implications for the next generation of targeted therapies for ACC.

3.3. Multiplatform genomics reveal ACC is comprised of 3 distinct subtypes and provide pan-cancer contextualization

Our current understanding of the molecular basis of ACC is informed by two landmark studies utilizing multiplatform omics approaches to profile primary tumors – Assie, Letouze *et al.* (Assie et al., 2014) and ACC-TCGA (Zheng et al., 2016). These

studies confirmed that 90% of ACC exhibit loss of heterozygosity of the *IGF2* locus leading to upregulation of IGF2/IGF1R signaling (Assie et al., 2014; Zheng et al., 2016). ACC also bear recurrent somatic alterations facilitating rapid cell cycling (*TP53, CDKN2A, RB1, CDK4, CCNE1*), telomere maintenance (*TERT, TERF2*), constitutive Wnt/β-catenin signaling (*ZNRF3*, *CTNNB1*), and constitutive PKA signaling (*PRKAR1A*); and involved in chromatin remodeling (*MEN1*, *DAXX*), transcription (*MED12*), and translation (*RPL22*) (Assie et al., 2014; Zheng et al., 2016). While Assie, Letouze *et al.* observed ACC exhibit frequent copy number changes (Assie et al., 2014), ACC-TCGA identified three recurrent somatic copy number alteration (SCNA) signatures: "quiet" (rare; tumors possess a diploid genome), "chromosomal" (~2/3 of tumors possess loss of heterozygosity of entire chromosomes +/- hypodiploidy or whole genome doubling), and "noisy" (~1/3 of tumors possess frequent arm-level gains and losses throughout the genome +/- whole genome doubling) (Zheng et al., 2016).

ACC-TCGA provided a novel molecular classification of ACC, identifying three comparably frequent and distinct molecular subtypes via a cluster of cluster (COC) analysis – COC1, COC2, and COC3 (**Figure 3.1**) (Zheng et al., 2016). Good prognosis COC1 ACC have fewer somatic alterations, a quiet or chromosomal SCNA profile, a transcriptional signature characterized by immune infiltration and low expression of steroidogenic machinery (termed "Steroid-low," overlapping with a signature identified by Assie, Letouze *et al.* as "C1B") (Zheng et al., 2016). Intermediate prognosis COC2 and dismal prognosis COC3 ACC bear frequent Wnt/β-catenin pathway alterations (Zheng et al., 2016). COC2 ACC bear a quiet or chromosomal SCNA profile and high expression of

zF differentiation genes/steroidogenic machinery (termed “Steroid-high,” overlapping with Assie, Letouze *et al.* C1A). COC3 ACC bear frequent cell cycle alterations, a noisy SCNA profile, and high expression of zF differentiation genes/steroidogenic and proliferative machinery (termed “Steroid-high+prolif,” also overlapping with C1A) (Zheng et al., 2016). Finally, on an epigenetic level, COC1 tumors bear low levels of genome-wide CpG island methylation (CIMP-low), COC2 bear intermediate levels (CIMP-intermediate), and COC3 bear high levels (CIMP-high) (Zheng et al., 2016). The convergence of Wnt/β-catenin activation (stemness), cell cycle activation (proliferation), CIMP-high status (may be maintaining stemness, e.g. **Table 1.7**), and steroidogenesis (differentiation) in COC3/CIMP-high ACC is paradoxical, and unraveling this convergence will be the focus of **Chapters 5 – 6**. As will also be iterated in **Chapter 4**, COC3, CIMP-high status, noisy SCNA, and high expression of steroidogenic and proliferative machinery are virtually synonymous in ACC-TCGA ($p < 0.0001$, Chi-square = 48.32, df = 4, Chi-square test for COC status vs. SCNA profile; $p < 0.0001$, Chi-square = 59.34, df = 4, Chi-square test for COC status vs. CIMP status; $p < 0.0001$, Chi-square = 72.97, df = 6 for COC status vs. mRNA class) and may be used interchangeably (particularly COC3/CIMP-high) throughout this thesis.

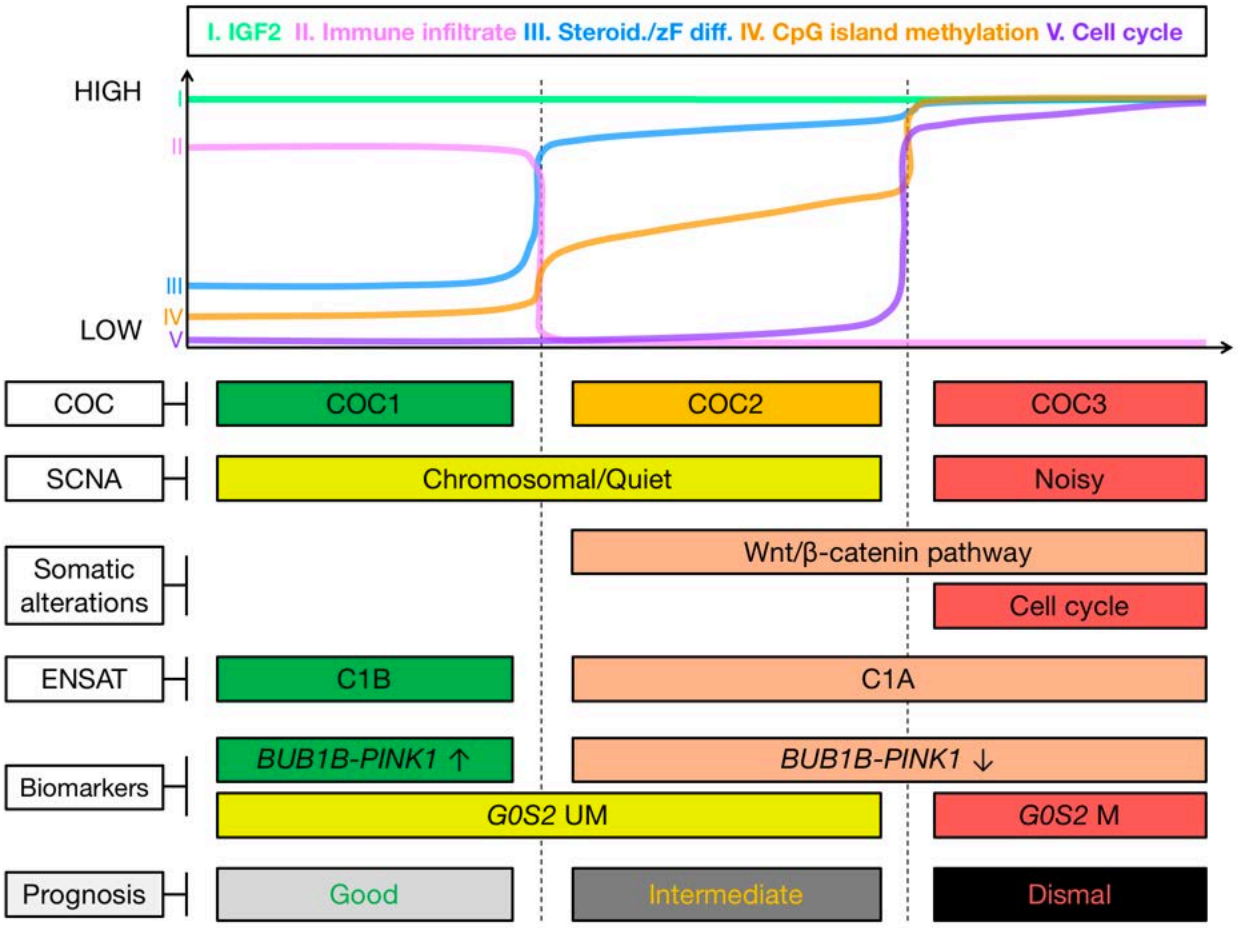

Figure 3.1. ACC is comprised of three distinct molecular subtypes amenable to targeted assessment.
As described in this chapter, ACC-TCGA (Zheng et al., 2016) identified that ACC is comprised of three distinct molecular subtypes, COC1, COC2 and COC3. COC1 tumors have the best prognosis (longest progression-free survival), while COC2 tumors have intermediate prognosis and COC3 tumors have dismal prognosis. All subtypes have high expression of *IGF2* (I). COC1 tumors bear the highest degree of immune infiltration (II), while COC2-3 tumors bear higher expression of steroidogenic machinery/zF differentiation genes (III). COC3 tumors bear CpG island hypermethylation (IV) and high expression of cell cycling machinery (V). ($p < 0.0001$, Chi-square = 59.34, df = 4, Chi-square test for COC status vs. CIMP status; $p < 0.0001$, Chi-square = 72.97, df = 6 for COC status vs. mRNA class). COC1-COC2 tumors bear a somatic copy number alteration (SCNA) profile termed chromosomal or quiet, while COC3 tumors bear an SCNA profile termed noisy ($p < 0.0001$, Chi-square = 48.32, df = 4, Chi-square test for COC status vs. SCNA profile). COC2-3 tumors bear a higher burden of somatic alterations leading to constitutive activation of the Wnt pathway, while COC3 tumors bear a higher burden of somatic alterations leading to constitutive cell cycling. ACC-TCGA also showed that COC1 tumors possess a transcriptional program identified by de Reynies, Assie and colleagues as C1B (de Reynies et al., 2009), while COC2-COC3 tumors possess a transcriptional program akin to C1A (de Reynies et al., 2009). Notably, these molecular subtypes can be captured using biomarkers, namely *BUB1B-PINK1* score (de Reynies et al., 2009) and *G0S2* methylation (**Chapter 4**).

The completion of ACC-TCGA enabled the incorporation of ACC into pan-cancer analyses. These studies reveal that ACC has the lowest degree of immune infiltration of nearly all TCGA cancers ((Hoadley et al., 2018; Thorsson et al., 2018), **Appendix B**) and a subset of ACC also exhibit a genomic signature suggestive of homologous recombination deficiency (Knijnenburg et al., 2018). While primary ACC are notable for bearing a lower mutational burden than most TCGA cancers (Hoadley et al., 2018), metastatic ACC bear a mutational burden nearly 3-fold higher than that of primary tumors (Gara et al., 2018). A recent landmark study using ATAC-seq on TCGA samples revealed that the chromatin accessibility landscape of ACC is largely driven by critical transcription factor for adrenal organogenesis and steroidogenesis, SF1 (encoded by *NR5A1*), consistent with the hallmark steroidogenic transcriptional program active in most ACC (Corces et al., 2018).

3.4. Novel biomarkers stratify ACC into homogeneous classes

Currently, proliferation-based grade measured by Ki67 or mitotic counts on histologic sections of primary tumor samples is used to prognosticate ACC (Beuschlein et al., 2015; Giordano, 2011; Weiss et al., 1989). However, the availability of high-throughput and multiplatform genomics data profiling ACC has enabled the discovery of several novel biomarkers that stratify ACC into molecular subtypes; such stratification is essential for the application of targeted therapies to specific subgroups of patients. The first of these molecular markers was developed by de Reynies, Assie, and colleagues, who demonstrated that cell cycle avid C1A and adenoma-like C1B tumors can be

distinguished using a score derived from the mRNA expression of genes *BUB1B* and *PINK1* (*BUB1B-PINK1* score) (de Reynies et al., 2009). More recently, in line with ACC-TCGA, investigators have also shown that high mRNA expression of E2F target genes like *EZH2* (Drelon et al., 2016a) or novel SF1 transcriptional targets like *VAV2* are also associated with worse clinical outcomes (Ruggiero et al., 2017; Sbiera et al., 2017).

Recent biomarkers take advantage of orthogonal approaches to capture the DNA hypermethylation signature characteristic of aggressive ACC (Jouinot et al., 2017). Our group recently demonstrated that uniform hypermethylation and silencing of the gene *G0S2* accurately captures a subgroup of patients with homogeneously dismal disease course akin to patients with COC3/CIMP-high tumors in ACC-TCGA (this is the focus of **Chapter 4**). Indeed, this signature can be combined with *BUB1B-PINK1* to approximate the three molecular subtypes described by ACC-TCGA (**Chapter 4**; **Figure 3.1**).

While promising, most molecular biomarker studies use frozen primary tumor tissues, which are not available at all clinical centers. In an integrated study performing targeted assessment of somatic alterations, gene expression, and methylation in formalin-fixed paraffin-embedded (FFPE) tissues, Lippert *et al.* demonstrated that it is possible to molecularly prognosticate ACC using routinely available clinical samples (Lippert et al., 2018). A strategy to enable molecular subtyping from FFPE tissues is also described in **Chapter 4**. Other investigators have assessed less invasive approaches, demonstrating that benign and malignant lesions of the cortex can be distinguished by circulating steroids (Schweitzer et al., 2019) or circulating microRNAs (Decmann et al., 2019), and that it is possible to measure circulating tumor DNA from patients with ACC

(Garinet et al., 2018; McCabe et al., 2019); such approaches may ultimately enable molecular subtype-directed neoadjuvant therapy and radiation-free tracking of ACC burden.

3.5. Clinical trials expose weaknesses of single pathway, "one size fits all" therapy

Molecular biomarkers are not currently used to direct therapies in ACC; patients with advanced and/or high-risk disease are uniformly directed to cytotoxic chemotherapy with or without mitotane (Fassnacht et al., 2018; Fassnacht et al., 2012; Lerario et al., 2019). However, ongoing trials are evaluating the efficacy of prognostic grade in predicting therapeutic response to adjuvant mitotane alone or with combination cytotoxic chemotherapy (ADIUVO – NCT00777244, ADIUVO-2 – NCT03583710). While grade is certainly effective in pinpointing patients who are less likely to respond to standard of care, such an approach still falls short of rationally directing patients to therapy based on oncogenic pathways driving their specific type of ACC. Moreover, the therapeutic potential of mitotane is poorly understood in the context of ACC subtypes as recent studies suggest this drug may drive cytotoxic ER stress in responsive cells through SOAT-1 (Ruggiero et al., 2018; Sbiera et al., 2015), the target of the investigational adrenolytic agent nevanimibe (ATR-101) (Langlois et al., 2018; LaPensee et al., 2016). The molecular biomarker-directed application of novel or existing targeted agents to specific subtypes will be essential for advances in the care of this disease. However, previous evaluation of targeted therapies for ACC weaves a cautionary tale.

Overexpression of *IGF2* in 90% of ACC (confirmed in (Assie et al., 2014; Zheng et al., 2016)) and early observations that inhibition of IGF2/IGF1R signaling was efficacious in subcutaneous xenograft models (Barlaskar et al., 2009) fueled phase I-III clinical trials evaluating IGF2/IGF1R inhibition by figitumumab, cixutumumab, or linsitinib in patients with advanced ACC (Fassnacht et al., 2015; Haluska et al., 2010; Lerario et al., 2014). Shockingly, these studies revealed that only 3-5% of patients with refractory metastatic ACC responded to IGF2/IGF1R inhibition with long-term regression (Fassnacht et al., 2015), suggesting downstream genetic events may confer resistance to IGF2/IGF1R monotherapy (this is investigated in **Appendix A**). ACC-TCGA suggests that patients with COC2-3 tumors will likely require additional therapies targeting the Wnt pathway and cell cycle ((Zheng et al., 2016); **Figure 3.1**). More recently, the US Food and Drug Administration's accelerated approval of PD-1/PD-L1 checkpoint therapy for patients with mismatch repair-deficient solid tumors has fueled studies demonstrating such therapies may be effective for some patients with ACC (Le Tourneau et al., 2018; Mota et al., 2018; Raj et al., 2020). However, the immunosuppressive effects of glucocorticoids (Fiorentini et al., 2019) and the anti-correlation between steroidogenesis and immune infiltration in ACC-TCGA (Zheng et al., 2016) suggests combination inhibition of steroidogenesis may be additionally required in mismatch repair-deficient, functional COC2-3 ACC (additional preliminary studies supporting this concept are detailed in **Appendix B**). Taken together, these studies suggest that the application of targeted therapies to ACC likely requires multiple agents and a deeper understanding of the collaborative oncogenic pathways turned on in each tumor subtype.

3.6. Revisiting ACC at the bench

Advances in *in vivo* modeling of adrenocortical homeostasis and cancer have refined the understanding of oncogenic pathways derailed in ACC. Among the earliest of such studies was by Heaton *et al.*, who demonstrated that *IGF2* overexpression likely requires collaboration with additional pathways (e.g. Wnt/β-catenin signaling) to promote adrenocortical tumorigenesis (Heaton et al., 2012). More recent *in vivo* models point to one putative cell of origin of a subset of ACC, perhaps lying in the boundary between the mineralocorticoid-producing zona glomerulosa (zG) and glucocorticoid-producing zona fasciculata (zF) (these models are discussed in **Chapter 2**, **Table 2.4**, and **Figure 2.6**).

Xenograft and *in vitro* modeling of ACC also hold promise for enabling a deeper understanding of ACC biology. The steroidogenic NCI-H295R cell line has long been the classical, most established model of ACC (Wang and Rainey, 2012), possessing high expression of SF1, constitutively active β-catenin (Tissier et al., 2005), and inactivation of pRb (Hadjadj et al., 2017; Ragazzon et al., 2014) and p53 (Cerquetti et al., 2008), and is the principal model used in this thesis. There are two additional long-standing *in vitro* models of murine ACC, the Y1 cell line (Yasumura et al., 1966) and SV40-Tag-derived ATC7L cell line (Ragazzon et al., 2006). There are similarities between murine and human mechanisms of adrenocortical carcinogenesis (Batisse-Lignier et al., 2017; Borges et al., 2020), though it is not necessarily clear that the ACC molecular subtypes in human ACC (Zheng et al., 2016) will also exist in mice. However, given the presence of cell cycle alterations (**Table 3.1**) in both cell lines, we believe that the transcriptional programs active in these two cell lines best mimic COC3/CIMP-high ACC. An important

caveat here that underscores differences in murine and human carcinogenesis is that both cell lines express *G0s2* and are therefore unlikely to exhibit *G0s2* CpG island hypermethylation, a hallmark of CIMP-high ACC, **Chapter 4**.

Table 3.1. ACC cell lines utilized in this thesis resemble COC3/CIMP-high ACC.

Pathway	Gene (HGNC)	CIMP-high	NCI-H295R	ATC7L	Y1
Cell cycle	*TP53*	31.6%	LOF	SV40 Tag LOF	
Wnt/β-catenin	*ZNRF3*	21.0%			
Cell cycle	*CDKN2A*	21.0%			LOF - deletion
Wnt/β-catenin	*CTNNB1*	21.0%	p.S45P GOF		
Telomere maintenance	*TERT*	26.3%			
Mismatch repair	MMR	10.5%			
ACTH/PKA	*PRKAR1A*	10.5%			
Ribosome	*RPL22*	5.3%			
Ras/MAPK	*NF1*	10.5%			
Cell cycle	*CDK4*	31.6%			
Telomere maintenance	*TERF2*	5.3%			
Cell cycle	*RB1*	5.3%	LOF	SV40 Tag LOF	
Epigenetics	*MEN1*	5.3%			
Cell cycle	*CCNE1*	15.8%			
Epigenetics	*MLL4*	15.8%			

NOTE. Table includes list of recurrently altered genes identified in ACC-TCGA (Zheng et al., 2016). Third column describes the frequency of driver somatic alteration affecting that gene in CIMP-high ACC (Zheng et al., 2016). Genetic alterations for NCI-H295R and Y1 cell lines were identified and confirmed by inspecting BAM files from RNA-seq data generated by our group and others (Baba et al., 2014). Next-generation sequencing data is not available for ATC7L cell line and genetic alterations are therefore predicted based on known biological features of this line. Importantly, ATC7L is unlikely to harbor alterations leading to autonomous Wnt/β-catenin pathway activation since this line is very responsive to Wnt pathway stimulation (Walczak et al., 2014).

Recently, several new ACC cell lines and xenograft models have emerged. Pinto *et al.* characterized the first pediatric xenograft model of ACC, SJ-ACC3, enabling the preclinical identification of topotecan as an efficacious medical therapy for a child with recurrent ACC (Pinto et al., 2013). Hantel, Beuschlein and colleagues developed the adult ACC-derived, steroidogenic, and Wnt/β-catenin-active MUC-1 xenograft model and cell line which exhibited resistance to IGF-targeting therapy and recapitulated resistance to cytotoxic chemotherapy observed in the original patient (Beuschlein et al., 2016; Hantel

and Beuschlein, 2016; Hantel et al., 2016). Kiseljak-Vassiliades and colleagues also developed two new adult ACC-derived cell lines and xenograft models, CU-ACC1 and CU-ACC2; CU-ACC1 is a cortisol-producing cell line bearing constitutively active β-catenin, whereas CU-ACC2 is a mismatch repair-deficient cell line bearing a mutation in *TP53* (Kiseljak-Vassiliades et al., 2018a). Comprehensive molecular profiling of the NCI-H295R cell line as well as these novel models will be essential for preclinical evaluation of ACC subtype-specific therapeutic approaches. The *in vitro* work in this thesis is restricted to three long-standing models of ACC, NCI-H295R, Y1, and ATC7L; efforts to comprehensively profile and characterize *in vitro* models of ACC are detailed in the subsequent sections.

3.7. Human cell line NCI-H295R is a faithful *in vitro* model of CIMP-high ACC

We have performed several molecular profiling studies in the NCI-H295R cell line, which will also be detailed in **Chapters 5 – 6**. Two pivotal studies that enabled us to classify this cell line as CIMP-high are our profiling of the NCI-H295R transcriptome by RNA-seq and DNA methylome by Illumina 850k array. Transcriptome profiling of NCI-H295R identified GOF genetic alterations in *CTNNB1* and LOF alterations in *TP53* and *RB1*, consistent with the literature and pointed to classification of this cell line as COC3/CIMP-high (**Table 3.1**). We then evaluated NCI-H295R expression of key genes that are differentially expressed across CIMP-high vs. non-CIMP-high ACC (this list is identified in **Chapter 4**, Supplementary Table S1 published in (Mohan et al., 2019)), and

identified that their expression patterns (silenced in CIMP-high, or upregulated in CIMP-high) are completely preserved in NCI-H295R (**Figure 3.2**).

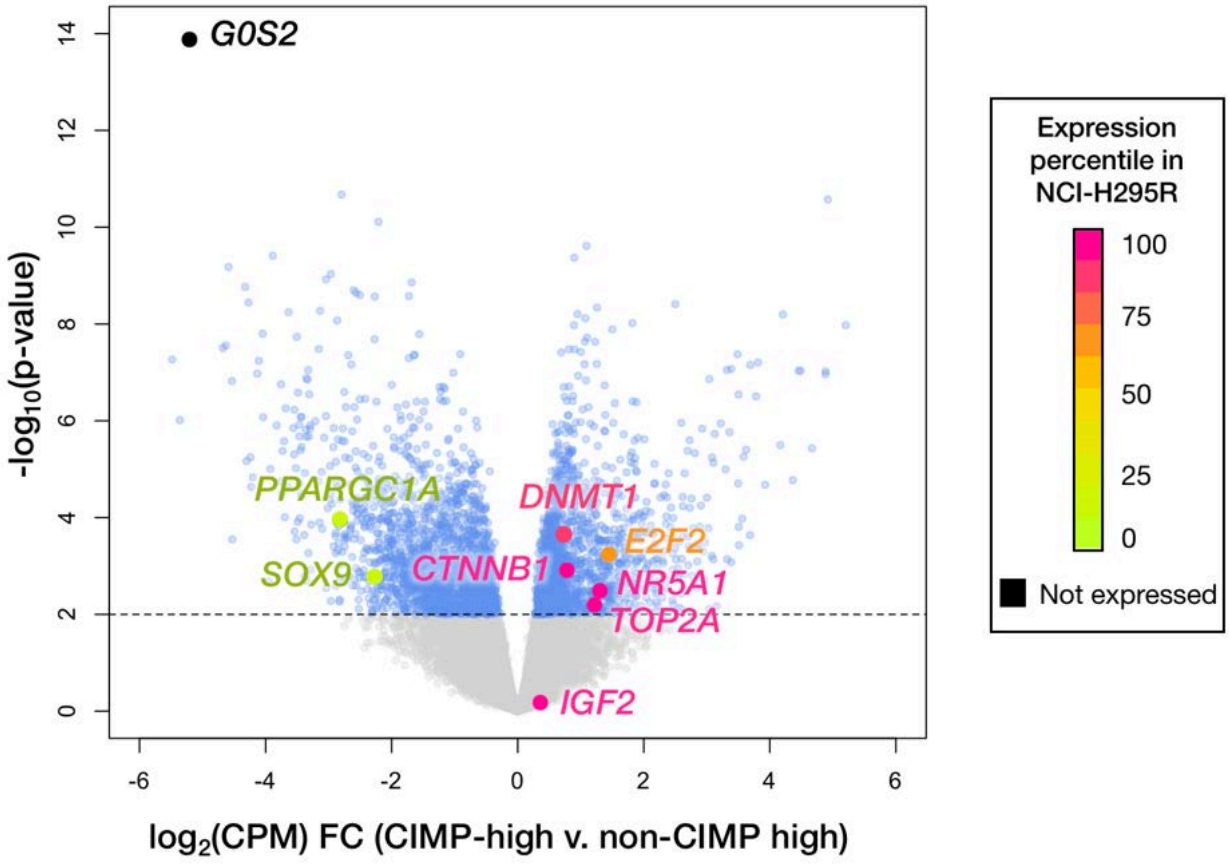

Figure 3.2. NCI-H295R transcriptome resembles CIMP-high ACC.
Volcano plot depicts -$\log_{10}$(p-value) for differential gene expression vs. $\log_2$(CPM) fold change in CIMP-high vs. non CIMP-high ACC (differential gene expression table introduced in **Chapter 4** and published as Supplementary Table S1 in (Mohan et al., 2019)). Dashed line indicates p-value threshold corresponding to Benjamini-Hochberg-corrected p-value of 0.05 (threshold for significance). Genes that are upregulated in CIMP-high ACC are on the right of the plot and genes that are downregulated in CIMP-high ACC are on the left side of the plot. Significantly differentially expressed genes are indicated in blue. We color-coded key genes on the plot by their expression profile in the NCI-H295R cell line at baseline. Genes like *G0S2* that are silenced in CIMP-high ACC (**Chapter 4**) have undetectable transcript expression in NCI-H295R, whereas cell cycle genes and *NR5A1* are in the top quartile of gene expression. As expected, given that 90% of ACC have loss of imprinting leading to *IGF2* overexpression, *IGF2* is not differentially expressed between CIMP-high and non-CIMP-high ACC, but is positioned in the top quartile (close to the 100th percentile) of NCI-H295R gene expression.

We then sought to evaluate the DNA methylome of this cell line. Using the set of probes that defines CIMP-status in ACC-TCGA, we identified that the NCI-H295R DNA methylation landscape is identical to CIMP-high tumors, including methylation of the CIMP-high hallmark gene *G0S2* (**Chapter 4**) and PRC2 targets (**Chapter 5**) (**Figure 3.3**).

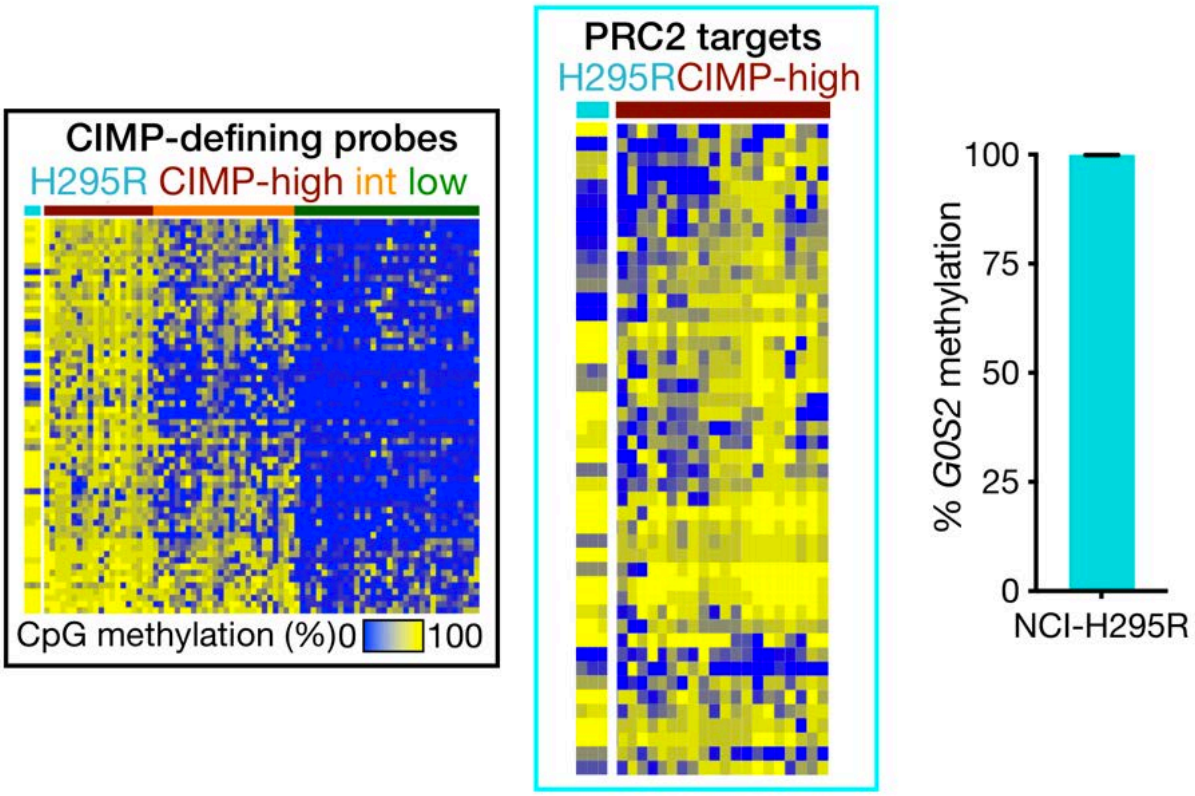

Figure 3.3. DNA methylome of NCI-H295R is identical to CIMP-high ACC.
Left, heatmap depicting Illumina 450k array probes that define CIMP groups from ACC-TCGA. Each column is a patient sample sorted into CIMP subgroup or the NCI-H295R cell line (n = 3). Qualitatively, NCI-H295R resembles CIMP-high tumors at these loci. Not shown, unsupervised hierarchical clustering of NCI-H295R (as if the cell line was a patient sample in ACC-TCGA) clusters NCI-H295R with CIMP-high tumors. Middle, NCI-H295R also possesses hypermethylation of PRC2 targets, like many CIMP-high tumors including CIMP-high ACC (**Chapter 1**, **Chapter 5**). Right, NCI-H295R possesses hypermethylation of the *G0S2* locus, measured by targeted assessment using EpiTect as in **Chapter 4**; n = 4 biological replicates, mean represented by the teal bar and standard error of the mean by the black error bars.

DNA methylation arrays measure both unmethylated and methylated CpG signal. The total signal at a given CpG therefore represents the total amount of DNA at that

position. We took advantage of this feature to characterize the copy number profile of NCI-H295R. We identified that this cell line possesses a noisy copy number alteration profile, characterized by frequent focal, arm-level gains and losses painting the picture of a “shattered” tumor genome (**Figure 3.4**).

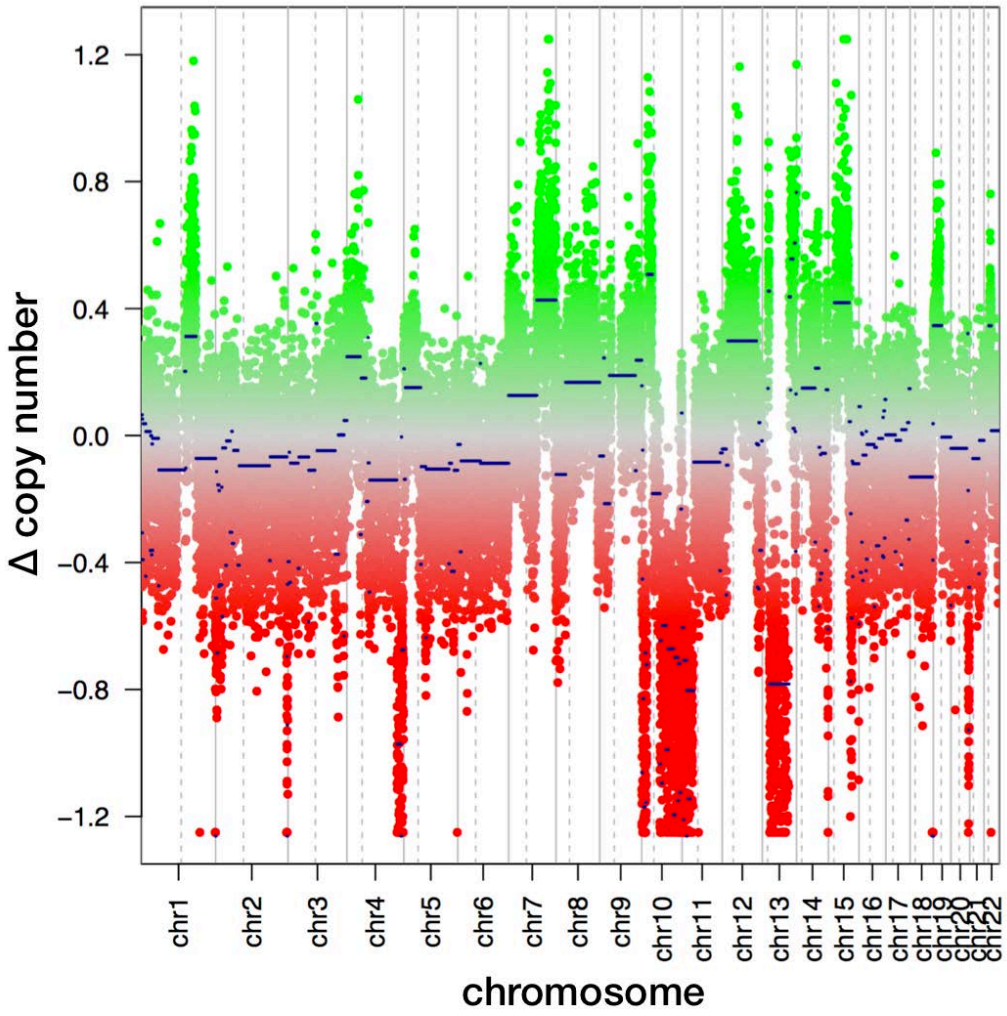

Figure 3.4. Summing signal obtained through DNA methylome profiling enables identification of a noisy copy number alteration profile in NCI-H295R.
Putative chromosomal segments are indicated by lines and terminate at predicted chromosomal breakpoints. Displacement from the 0.0 position on the y axis indicates a predicted gain or loss in copy number.

Taken together, these analyses establish the NCI-H295R cell line as a definitive *in vitro* model of human CIMP-high ACC, bearing all key features that define this multiplatform molecular subtype.

3.8. Murine ACC cell lines exhibit variable zF differentiation and response to differentiation cues

The NCI-H295R cell line will be our core *in vitro* model of CIMP-high ACC in this thesis, largely due to our extensive characterization (section **3.7**) and the history of this cell line in serving as the sole human *in vitro* ACC model (Wang and Rainey, 2012). Our group has also expended substantial effort in characterizing two murine ACC cell lines, ATC7L and Y1. Given the spectrum of adrenocortical differentiation across ACC (**Figure 3.1**) and the possibility that ACC resemble a partially differentiated adrenocortical cell state (**Chapter 2**), we sought to evaluate the extent of zF and zG differentiation in ATC7L and Y1. To do this, we measured expression of a select panel of genes orthologous to those that characterize zF or zG differentiation in the human adult adrenal cortex (**Figure 3.5**). For the purposes of the studies in this section, *G0s2* is used as a marker of zF differentiation (**Table 2.5, Figure 3.5**).

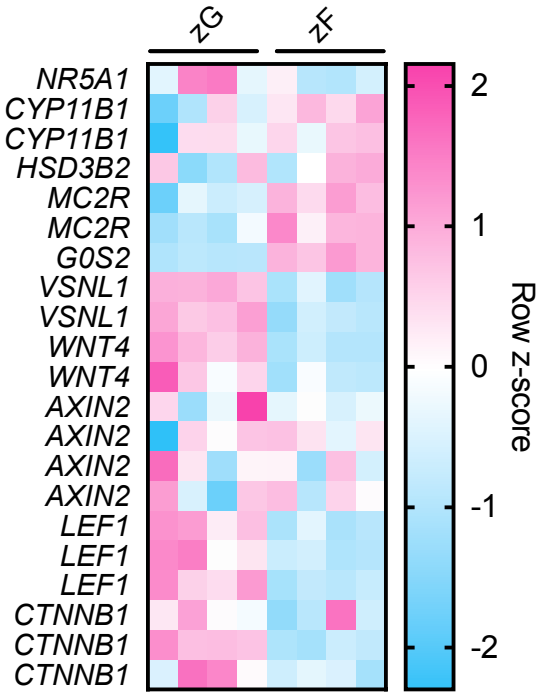

Figure 3.5. Expression of genes in microdissected human adrenal cortex enables identification of markers of zG or zF differentiation.
Microarray data from (Nishimoto et al., 2015), largely consistent with recent human adrenal single-cell RNA-seq ((Han et al., 2020), **Figure 2.7**). Genes were selected based on the literature and their involvement in pathways of interest. Genes encoding steroidogenic enzymes – *CYP11B1, HSD3B2*. Wnt/β-catenin pathway – *WNT4, AXIN2*, *LEF1*, *CTNNB1*. *G0S2* is targeted for methylation-dependent silencing in cancer, *NR5A1* encodes SF1, *MC2R* encodes the ACTH receptor, and *VSNL1* is highly zG-specific gene upregulated in aldosterone-producing adrenocortical adenomas (Trejter et al., 2015; Williams et al., 2012)

Through this study, we identified that ATC7L exhibit stronger zF differentiation than Y1, and despite the absence of Wnt pathway alterations in the Y1 cell line (**Table 3.1**), the Y1 cell line expresses high levels of zG-defining genes that are also canonical Wnt targets (*Axin2, Lef1*; **Figure 3.6**, **Table 3.2**). Cellular fractionation experiments revealed that both cell lines possess nuclear SF1 and PRC2 (as expected), but only Y1 cells express substantial nuclear β-catenin at baseline (**Figure 3.7**).

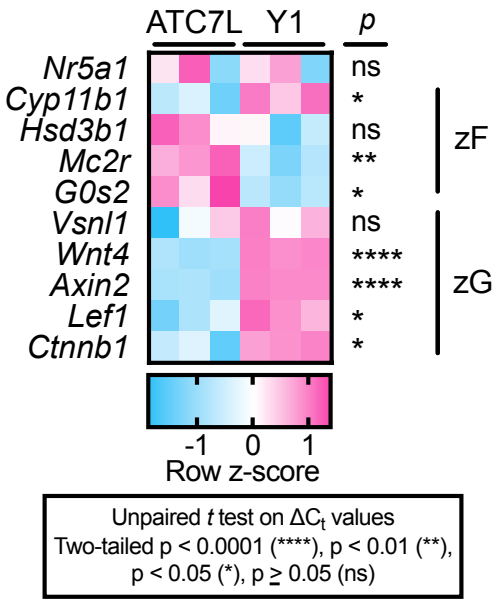

Figure 3.6. ATC7L bears stronger zF differentiation than Y1.
zF and zG gene classification was determined based on **Figures 2.7, 3.5** and the literature. Note that the genomic context of *Hsd3b1* (BLAST alignment with *HSD3B2* locus including upstream enhancer, data not shown) and its expression pattern render it the murine ortholog of *HSD3B2* (Simard et al., 2005).

Table 3.2. Average -ΔC_t values for gene expression z-score calculated in Figure 3.6.

Gene	ATC7L	Y1	Gene classification
Nr5a1	-6.139	-6.215	steroidogenic adrenal cortex
Cyp11b1	-8.534	-5.726	zF
Hsd3b1	-14.837	-18.144	zF
Mc2r	-6.409	-9.202	zF
G0s2	-4.552	-7.626	zF
Vsnl1	-15.986	-14.048	zG
Wnt4	-8.225	-2.818	zG
Axin2	-12.831	-6.212	zG
Lef1	-12.727	-10.460	zG
Ctnnb1	-9.377	-7.356	zG

NOTE. $-\Delta C_t$ is defined by $-[C_t(gene) - C_t(Actb)]$, and a higher, less negative value reflects a higher level of gene expression. Gene expression was measured by qPCR on reverse transcribed total mRNA from 3 independent biological replicates of ATC7L and Y1 cell lines grown in culture under standard conditions. Gene classification was determined based on **Figures 2.7**, **3.5** and the literature.

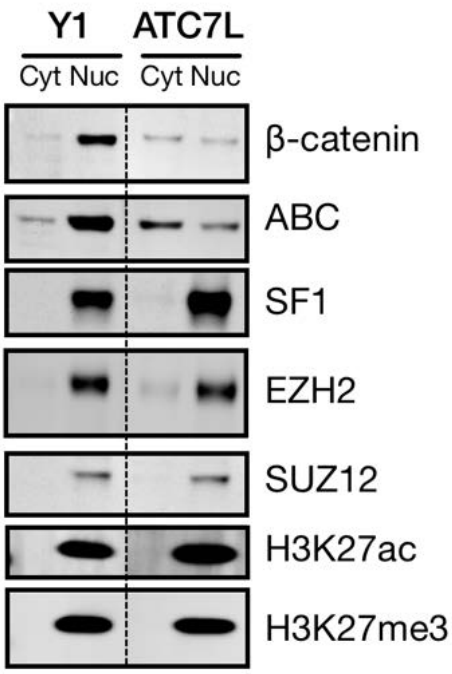

Figure 3.7. Sub-cellular localization of proteins of interest in Y1 and ATC7L.
Y1 and ATC7L cell lines were fractionated into cytoplasmic (Cyt) and nuclear (Nuc) compartments, and protein lysates prepared from each compartment were analyzed by western blot. A representative blot is shown here, 15 µg protein loaded per lane. For each epitope, Y1 and ATC7L lysates were run on the same gel/membrane. Irrelevant lanes between the two sets of samples are cropped at the dashed line. Y1 express high levels of nuclear β-catenin, measured by total β-catenin in the top row, and active β-catenin (ABC) in second row; ATC7L express substantially lower levels of nuclear β-catenin. SF1 and PRC2 are nuclear and relatively comparable across both cell lines. H3K27ac and H3K27me3 are also comparable across cell lines and are shown here to demonstrate purity of cytoplasmic fraction.

We then sought to evaluate the response of ATC7L and Y1 cell lines to paracrine zG and endocrine zF differentiation agents. To induce zG differentiation, we treated both cell lines with LiCl or Wnt3a conditioned medium to activate Wnt/β-catenin signaling (**Figure 3.8**). We observed that, as expected, the ATC7L cell line gained expression of zG genes and lost expression of some zF genes in a dose-dependent manner (**Figure 3.8A, Figure 3.8C**), consistent with prior work from our group (Walczak et al., 2014). Surprisingly, the Y1 cell line only minimally responded to Wnt/β-catenin stimulation with broad and inconsistent induction of zG and zF genes (**Figure 3.8B** – **Figure 3.8C**).

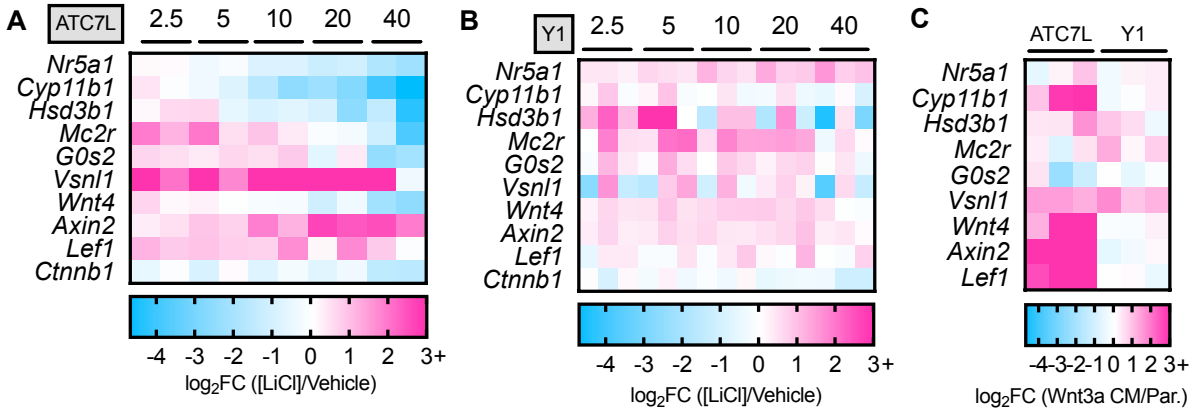

Figure 3.8. ATC7L (and not Y1) respond to Wnt pathway activation with partial zG differentiation at the expense of zF differentiation.
ATC7L (**A**) or Y1 (**B**) were stimulated overnight (18.5-19.5 hrs) with LiCl and harvested for total mRNA and evaluation of gene expression by qPCR with *Actb* as a housekeeping gene. LiCl is a potent and well characterized inhibitor of GSK3β, a core member of the destruction complex that targets β-catenin for degradation in the absence of Wnt ligands; LiCl administration mimics Wnt pathway activation (Stambolic et al., 1996). Concentration of LiCl in mM is indicated above each set of biological replicates (n=2 for ATC7L, **A**; n=3 for Y1, **B**), and heatmap is color coded by $\log_2$ of the fold change between the given concentration of LiCl over vehicle according to the legend below each plot. In **A**, ATC7L exhibits a dose dependent increase in expression of zG genes and canonical Wnt targets like *Axin2*, at the expense of zF genes. In contrast, Y1 changes in gene expression in response to LiCl are minimal and encompass a broad upregulation of both zG and zF genes. In **C**, ATC7L and Y1 were stimulated with 20% Wnt3a conditioned medium (Wnt3a CM) or negative control (parental medium without Wnt3a, Par.), derived from L cells as in (Shibamoto et al., 1998), for 24 hours and harvested for total mRNA and evaluation of gene expression by qPCR. n = 3 biological replicates for each cell line, and heatmap is color coded by $\log_2$ of the fold change between Wnt3a CM and Par. according to the legend below each plot. As in **A** and **B**, Wnt pathway activation could induce expression of zG genes in ATC7L only and had minimal effect on Y1 cells.

To induce zF differentiation, we treated both cell lines with forskolin to stimulate intracellular accumulation of cAMP and consequent PKA activation, mimicking the actions of ACTH (**Figure 2.4**). We observed that, as expected, the Y1 cell line exhibited a faithful induction of zF genes; in contrast, ATC7L exhibited mixed induction of both zG and zF genes (**Figure 3.9**).

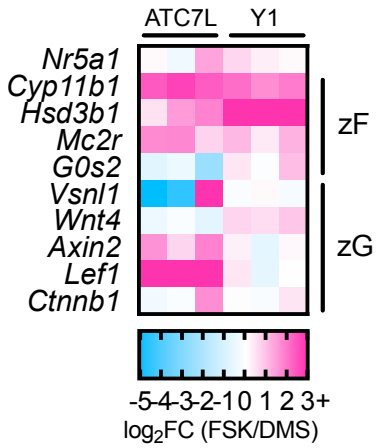

Figure 3.9. Y1 (and not ATC7L) exhibits exclusive induction of zF genes in response to PKA activation.
Y1 and ATC7L were stimulated for 24-26 hours with 10 μM forskolin (FSK) or equivalent volume of vehicle (DMS) and harvested for total mRNA and evaluation of gene expression by qPCR with *Actb* as a housekeeping gene. Forskolin is a well characterized stimulant of the PKA pathway, inducing intracellular accumulation of cAMP (Seamon et al., 1981). Heatmap is color coded by $\log_2$ of the fold change between FSK over DMS according to the legend below each plot, n = 3 for each cell line. Treatment of adrenocortical cell lines with forskolin imitates the actions of ACTH (Xing et al., 2011). Forskolin administration in Y1 cells exclusively induced expression of zF genes; in contrast, forskolin administration in ATC7L cells induced expression of zF and zG genes.

Taken together, these data suggest that the extent of zF differentiation delimits the boundaries of differentiation fidelity for ACC cell lines responding to zG/zF differentiation agents. In other words, zF-differentiated ATC7L can faithfully respond to traditional agents that stimulate paracrine zG identity with zG differentiation, but cannot get further zF differentiated with traditional agents that stimulate endocrine zF identity. In contrast, less zF-differentiated/more zG-differentiated Y1 can faithfully respond to traditional agents that stimulate endocrine zF identity with zF differentiation, but cannot get further zG differentiated with traditional agents that stimulate paracrine zG identity. The ability of these cell lines to respond to adrenocortical differentiation agents broadly is not particularly surprising, as both the NCI-H295R and Y1 cell lines have served as long-standing models of adrenocortical steroidogenesis (e.g. (Wilson et al., 1993)). However,

the distinct responses of the Y1 and ATC7L cell lines suggest that the spectrum of steroidogenic differentiation across ACC (**Figure 3.1**) may in fact reflect the existence of a multiplicity of attainable modes that favor context-specific sustained proliferation, pointing to differentiation plasticity as a key pharmacologically targetable axis (**Chapter 6**).

3.9. Implications for novel strategies to direct targeted therapies

The new molecular classification of ACC paired with biomarkers capturing molecular subtypes (**Figure 3.1**, **Chapter 4**) and recent clinical and translational studies have clarified our understanding of ACC's molecular basis and illuminated several novel therapeutic strategies. Notably, these studies have suggested that COC1, COC2, and COC3 ACC may be differentially responsive to therapies targeting the IGF2/IGF1R pathway, Wnt/β-catenin pathway, cell cycle, and immune system. The apparent reliance of most ACC on multiple oncogenic pathways may explain the observed broad resistance to IGF2/IGF1R monotherapy (Fassnacht et al., 2015), suggesting that biomarker-based strategies to improve patient selection and new strategies incorporating combination therapy are paramount. Indeed, recently developed biomarkers that approximate ACC-TCGA molecular subtypes hold promise for enabling both prospective classification of ACC (**Figure 3.1**) and application of efficacious adjuvant therapies to patients likely to recur on standard of care (**Chapter 4**). Advances in biomarker detection in archival material ((Lippert et al., 2018), **Chapter 4**) and blood (Decmann et al., 2019; Garinet et

al., 2018; McCabe et al., 2019; Schweitzer et al., 2019) will undoubtedly expand the patient population for which biomarker assessment is feasible.

The outlook for targeted therapies in ACC is promising. Currently, only a fraction of individuals with ACC respond to immunotherapy as a single agent (Mota et al., 2018; Raj et al., 2020); however, it is possible that combination therapy with inhibitors of steroidogenesis and/or cytotoxic agents (Paz-Ares et al., 2018) may enhance neoantigen presentation and immune clearance (**Appendix B**). The enrichment for Wnt/β-catenin pathway alterations in COC2-COC3 ACC suggests that individuals with these ACC types may be responsive to therapies targeting this pathway. Those tumors with ZNRF3 deficiency are likely reliant on Porcupine-dependent Wnt ligand secretion (Basham et al., 2019) and may be responsive to Porcupine inhibitors currently in phase I trials (e.g. NCT01351103). Tumors with mutations in *CTNNB1* leading to constitutive stabilization of β-catenin may instead be responsive to therapies targeting the oncogenic β-catenin/CBP transcriptional program, which have recently completed phase I trials for solid tumors (e.g. NCT01302405, NCT01764477). Patients with COC3 ACC likely require additional therapies targeting the cell cycle, perhaps in combination with DNA demethylating agents (Azad et al., 2013; Matei et al., 2012). Well characterized *in vitro* and *in vivo* models of ACC will undoubtedly facilitate preclinical assessment of these approaches (Beuschlein et al., 2016; Borges et al., 2020; Hantel and Beuschlein, 2016; Hantel et al., 2016; Kiseljak-Vassiliades et al., 2018a; Pinto et al., 2013; Wang and Rainey, 2012).

Finally, recent developments in murine modeling of adrenocortical homeostasis and cancer have implicated a role for collaboration between ACTH/PKA and Wnt/β-

catenin signaling in enabling cell cycle activation in a proliferating population of cells residing in the zG/zF boundary (**Figure 2.6**). While it is yet unknown how targeting these cells will influence established ACC, the susceptibility of this population to hyperplasia and malignant transformation (Basham et al., 2019; Batisse-Lignier et al., 2017; Borges et al., 2020) suggests that targeting interplay between paracrine and endocrine signaling may ultimately be required to extinguish at least one type of ACC cell of origin. As we will detail in **Chapters 5 – 6**, it is likely that targeting the epigenetic modifiers that enable differentiation plasticity will be crucial in this regard. Next, in **Chapter 4**, we will detail a strategy to enable prospective identification of CIMP-high ACC.

3.10. Materials and methods

Analysis of microarray data from microdissected adrenals. Performed as described in **Chapter 2**.

Cell culture. All cell lines were cultured under standard sterile conditions and maintained in a humidified tissue culture incubator with 5% CO2 at 37°C. NCI-H295R were obtained from ATCC and cultured in DMEM/F12 (Gibco, Cat. No. 11330-032) supplemented with 10% Nu serum (Corning, Cat. No. 35500), 1% ITS-X (Gibco, Cat. No. 51500-056), and 1% penicillin/streptomycin (Gibco, Cat. No. 15140-122). Y1 were obtained from ATCC and cultured in high glucose DMEM (Invitrogen, Cat. No. 11995-065), supplemented with 2.5% fetal bovine serum (Sigma-Aldrich, Cat. No. F2442-500ML), 7.5% horse serum (Invitrogen, Cat. No. 16050122), and 1% penicillin/streptomycin. ATC7L were a generous

gift to our laboratory from A. Lefrançois-Martinez and A. Martinez (GReD, CNRS, Inserm, Université Clermont-Auvergne, Clermont-Ferrand, France) and cultured as previously described (Walczak et al., 2014), in DMEM/F12 supplemented with 2.5% fetal bovine serum, 2.5% horse serum, 1% ITS-X, and 1% penicillin/streptomycin. All cell lines were routinely screened (at every 3-5 passages and/or each experimental plating) for microbial contamination by DAPI staining and/or e-Myco Mycoplasma PCR Detection Kit (Bulldog Bio, Cat. No. 2523348). Cell lines were discarded after 20-25 passages post-thaw, or when exponential growth was no longer evident (whichever came first).

Wnt or PKA pathway activation experiments. Y1 or ATC7L were plated at a density of 600,000 cells/well in 6 well plates. 18-24 hours after plating, media was changed to media containing 10 µM forskolin or equivalent volume of vehicle (DMSO), media containing 2.5 – 40 mM LiCl or equivalent volume of vehicle (water; % vehicle was kept constant for all doses), media containing 20% Wnt3a CM or 20% parental medium. Cells were harvested at the indicated timepoints. Gene expression from vehicle-treated cells in LiCl series were used for Y1/ATC7L comparison in **Figure 3.6**.

Nucleic acid extraction and quantification. Nucleic acid extraction was performed as described in **Chapter 4** with optional nuclease treatments or using the RNeasy Plus Mini Kit (Qiagen, Cat. No. 74134) according to manufacturer's instructions.

RNA-seq. RNA-seq was performed by the University of Michigan Advanced Genomics Core. Libraries were prepared from total mRNA extracted from baseline NCI-H295R according to standard Illumina protocols. 50 bp paired-end reads were generated in the Illumina NovaSeq-6000 platform (S1 100 cycle) at an output to ensure ~50 million reads/sample. Reads were aligned to the hg38 assembly of the human genome using *STAR* (Dobin et al., 2013). Gene expression was quantified by *featureCounts* (Liao et al., 2014). Quality control metrics were generated by *RNA-SeQC* (DeLuca et al., 2012). Count data was normalized Count data was normalized using TMM normalization from edgeR ; logCPM values were generated using the *voomWithQualityWeights* function from *limma* (Ritchie et al., 2015). FPKM values were calculated using *rpkm* function from *edgeR* (McCarthy et al., 2012; Robinson et al., 2010). Genes were ranked by FPKM to determine percentile of expression. BAM files for Y1 RNA-seq were generated according to the same pipeline from fastq files downloaded from DDBJ/EMBL/GenBank DRA000853 aligned to mm10.

850k array. gDNA from three replicates of cultured NCI-H295R was extracted as described in **Chapters 4 – 5** and prepared for evaluation by Illumina 850k array according to standard Illumina protocols. *MethylAid* (van Iterson et al., 2014) was used on 850k array data to assess quality control, and *minfi* (Aryee et al., 2014) was used to perform functional normalization, and generate table of beta values. Table was filtered for probe sets of interest. PRC2 target probes were probes that fall in the promoters of genes included in the BENPORATH_PRC2_TARGETS set deposited in GSEA (Ben-Porath et

al., 2008; Liberzon et al., 2011; Subramanian et al., 2005). Copy number inference was performed using *conumee* (Hovestadt and Zapatka, 2020).

Targeted gene expression analysis. cDNA synthesis was performed on extracted mRNA according to manufacturer's protocol using the iScript cDNA Synthesis Kit (Bio-Rad, Cat. No. 1708841). qPCR was performed as described in **Chapter 4** using primers in **Table 3.3**, Power SYBR Green qPCR Mastermix (Invitrogen, Cat. No. 4367659), and *Actb* as the housekeeping gene.

Table 3.3. Primers and sequences used for qPCR.

Species	Gene	Orientation	Sequence (5'-3')
Mus musculus	*Nr5a1*	Forward	TGCAGAATGGCCGACCAG
Mus musculus	*Nr5a1*	Reverse	TACTGGACCTGGCGGTAGAT
Mus musculus	*Cyp11b1*	Forward	GCCATCCAGGCTAACTCAAT
Mus musculus	*Cyp11b1*	Reverse	CATTACCAAGGGGGTTGATG
Mus musculus	*Vsnl1*	Forward	CTGCAAAAAGCGACCCTTCC
Mus musculus	*Vsnl1*	Reverse	GTGTGCAGTCCATAGCATCG
Mus musculus	*Mc2r*	Forward	GTAAGTCAACGGCAAACACC
Mus musculus	*Mc2r*	Reverse	GTGTCATTGGTGTGTTCATACG
Mus musculus	*Lef1*	Forward	CTGAAATCCCCACCTTCTACC
Mus musculus	*Lef1*	Reverse	TGGGATAAACAGGCTGACCT
Mus musculus	*G0s2*	Forward	CACCCTAGGCCCAGCCA
Mus musculus	*G0s2*	Reverse	ACACTGCCCAGCACGTATAG
Mus musculus	*Actb*	Forward	CACTGTCGAGTCGCGTCC
Mus musculus	*Actb*	Reverse	TCATCCATGGCGAACTGGTG
Mus musculus	*Hsd3b1*	Forward	GAAGCTGCCCCTGATCTTTTC
Mus musculus	*Hsd3b1*	Reverse	GACAGTGGGAGCTGGTATGAT
Mus musculus	*Axin2*	Forward	GCAGGAGCCTCACCCTTC
Mus musculus	*Axin2*	Reverse	TGCCAGTTTCTTTGGCTCTT
Mus musculus	*Wnt4*	Forward	CTGGACTCCCTCCCTGTCTT
Mus musculus	*Wnt4*	Reverse	ATGCCCTTGTCACTGCAAA
Mus musculus	*Ctnnb1*	Forward	GCAGCAGCAGTTTGTGGA
Mus musculus	*Ctnnb1*	Reverse	TGTGGAGAGCTCCAGTACACC

Targeted G0S2 methylation analysis. Extracted gDNA was subject to targeted assessment of *G0S2* methylation by EpiTect as described in **Chapter 4**.

Cellular fractionation. Protein extracts were prepared using the ActiveMotif Nuclear Complex Co-IP Kit (ActiveMotif, Cat. No. 54001) according to manufacturer's protocol with the following modifications: supernatant from spin after hypotonic lysis was saved as cytoplasmic fraction, and enzymatic digests were performed at 4°C for 90 minutes.

Protein quantification, SDS-PAGE and western blot. Performed as described in **Chapter 5**, with samples prepared in 2X reducing buffer.

CHAPTER 4. Development of a Biomarker Strategy to Translate ACC Subtypes

4.1. Disclosure of relevant publications

Portions of this work have been published:

> **Mohan DR***, Lerario AM*, Else T, Mukherjee B, Almeida MQ, Vinco M, Rege J, Mariani BMP, Zerbini MCN, Mendonca BB, Latronico AC, Marie SKN, Rainey WE, Giordano TJ, Fragoso MCBV^, Hammer GD^. Targeted Assessment of *G0S2* Methylation Identifies a Rapidly Recurrent, Routinely Fatal Molecular Subtype of Adrenocortical Carcinoma. *Clinical Cancer Research*. 2019 Jun 1;25(11):3276-3288. *,^ equal contribution

4.2. Introduction

As discussed in **Chapter 3**, ACC is frequently aggressive with 35% 5-year survival (Else et al., 2014a). Therapies for metastatic ACC are often palliative, limited to administration of adrenolytic drug mitotane and/or cytotoxic chemotherapy (Else et al., 2014a). Patients with locoregional ACC routinely receive surgery and adjuvant mitotane, but 50-70% recur and develop metastases even after complete (R0) resection (Else et al., 2014b; Glenn et al., 2018). Retrospective studies suggest adjuvant mitotane prolongs recurrence free survival (Berruti et al., 2017; Terzolo et al., 2007), but its efficacy is limited by its poor pharmacokinetic properties and dose-limiting toxicities. Obtaining therapeutic serum levels of mitotane may take several months to achieve if at all (Terzolo et al., 2013). Furthermore, there is a substantial proportion of ACC patients who experience rapid

recurrence (<12 months) (Else et al., 2014b; Glenn et al., 2018; Kim et al., 2016), whose aggressive disease course may preclude response to mitotane. These patients may instead benefit from more rapidly acting therapies; however, prospectively identifying this subgroup remains challenging.

Histological grade based on cellular proliferation is the strongest predictor of recurrence following R0 resection in ACC; high grade disease is associated with higher risk of recurrence (Beuschlein et al., 2015; Giordano, 2011; Weiss et al., 1989). Despite its clinical utility, significant caveats complicate interpretation of grade on an individual basis. Evaluation of grade is prone to high inter-rater variability (Papathomas et al., 2016), and outcomes of patients with low and high grade disease remain heterogeneous, with rapidly recurrent patients in both strata (Beuschlein et al., 2015; Miller et al., 2010). While some studies indicate clinical factors may be predictive of recurrence (Kim et al., 2016; Scollo et al., 2016), molecular profiling studies suggest biomarkers may better resolve this heterogeneity by identifying patients with homogeneously dismal outcomes.

We and others have shown that transcriptomes of aggressive ACC are characterized by pronounced cell cycle activation (Giordano et al., 2009), and a score based on mRNA levels of mitotic regulator *BUB1B* (BUB1 Mitotic Checkpoint Serine/Threonine Kinase B) and mitochondrial kinase *PINK1* (PTEN Induced Putative Kinase 1) discriminates uniformly favorable from poor clinical outcomes (de Reynies et al., 2009; Fragoso et al., 2012). Recent studies have implicated aberrant epigenetic patterning in ACC pathogenesis, highlighting that aggressive carcinomas bear widespread promoter CpG island hypermethylation (Assie et al., 2014; Barreau et al.,

2013). Notably, ACC-TCGA similarly identified that rapidly recurrent ACC is distinguished by a CpG island hypermethylation phenotype, CIMP-high (Zheng et al., 2016).

While these studies have illuminated molecular programs core to aggressive ACC biology, clinical translation of "big data"-derived biomarkers remains challenging. Thresholds for continuous data, e.g. mRNA-based biomarkers, vary across patient cohorts (de Reynies et al., 2009; Fragoso et al., 2012), compromising biomarker utility for prospective clinical management of a rare malignancy. Furthermore, while targeted assessment of DNA methylation appears promising for prognosticating ACC (Barreau et al., 2013; Jouinot et al., 2017), measurement strategies frequently rely on several genomic loci, complicated data normalization procedures, and reference benign lesions (Jouinot et al., 2017). Finally, it remains unclear if validated biomarkers identify uniform ACC molecular subtypes amenable to clinical assessment of subtype-specific therapeutic approaches. It is therefore not surprising that mRNA- and DNA methylation-based biomarkers have yet to be successfully translated clinically to prognosticate ACC, and highlights a strong need for identifying novel biomarkers with simplified, binary readouts and therapeutic import.

Here, we present a new analysis of ACC-TCGA data in which we demonstrate that CIMP-high ACC is a unique, rapidly recurrent ACC molecular subtype, bearing upregulation of cell cycle- and DNA damage-associated cellular programs. We identify that uniform hypermethylation and silencing of the gene *G0S2* (G0/G1 Switch 2) is largely exclusive to CIMP-high ACC. We show in an independent cohort that targeted assessment of *G0S2* methylation using an overnight assay independently identifies a

subgroup of ACC patients with rapidly progressive or fatal disease course. Our data demonstrates that *G0S2* methylation status is essentially binary, and thereby has high potential to enable clinicians to prospectively identify ACC patients unlikely to exhibit durable response to standard adjuvant therapy. We also propose that rapidly acting adjuvant cytotoxic agents may benefit patients with this ACC subtype. Finally, our study demonstrates the utility of comprehensive databases like TCGA, and illustrates a pipeline to identify and test clinically relevant biomarkers for ACC that may be extended to other cancers.

4.3. CIMP-high ACC is a rapidly recurrent and routinely fatal molecular subtype

In ACC-TCGA, comprehensive DNA methylome profiling of 79 treatment-naive primary ACC using the Illumina 450k platform clustered ACC into three DNA-methylation-based subtypes: CIMP-low, CIMP-intermediate, and CIMP-high (Zheng et al., 2016). While patients with CIMP-low and CIMP-intermediate carcinomas exhibited indistinguishable disease course (log-rank p=0.22 for disease-free survival of CIMP-low vs. CIMP-intermediate), patients with CIMP-high carcinomas characteristically exhibited rapidly recurrent or deadly disease course with median disease-free survival (DFS) following R0/RX resection of 13.6 months (**Figure 4.1**) and median overall survival (OS) of 36 months (**Figure 4.2**).

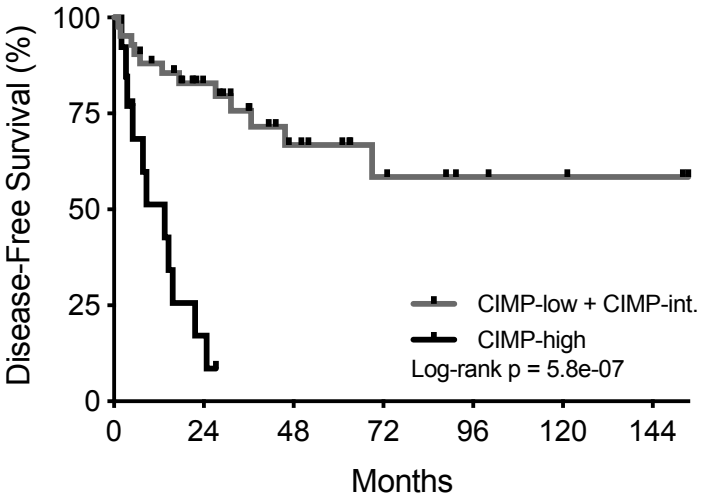

No. at risk	0	24	48	72	96	120	144
CIMP-low + CIMP-int.	42	25	13	7	4	3	2
CIMP-high	13	2	0	0	0	0	0

Figure 4.1. Patients with CIMP-high ACC from ACC-TCGA have rapidly recurrent disease course.
ACC-TCGA reveals that disease-free survival (DFS) of ACC patients with locoregional disease following R0/RX resection can be stratified by CpG island methylator phenotype ("CIMP") status. Patients with CIMP-high carcinoma status have dismal outcomes, with median DFS of 13.6 months compared to failure to achieve median DFS in CIMP-low + CIMP-intermediate group.

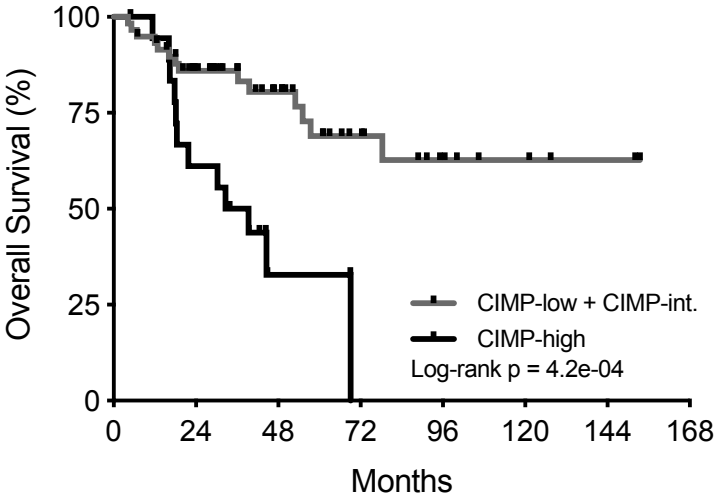

No. at risk	0	24	48	72	96	120	144
CIMP-low + CIMP-int.	59	42	25	13	7	4	2
CIMP-high	19	11	2	0	0	0	0

Figure 4.2. Patients with CIMP-high ACC have deadly disease course.
ACC-TCGA reveals that patients with CIMP- high tumor status have routinely fatal ACC, with median overall survival (OS) of 36 months compared to failure to achieve median OS in CIMP-low + CIMP-intermediate group.

Given the striking clinical phenotype associated with the CIMP-high signature, we sought to determine if other molecular classes and somatic alterations identified by ACC-TCGA were associated with this epigenetic program. We performed association tests between CIMP status and ACC-TCGA-defined transcriptome class (mRNA group), somatic copy number alteration profile (SCNA group), or somatic alterations. We observed that CIMP-high carcinomas were distinguished by a transcriptional signature featuring increased expression of steroidogenic and proliferative machinery ("Steroid-high + prolif." transcriptional program), and a chromosomally "noisy" genomic landscape with numerous arm-level breaks and focal copy number gains and losses (**Figure 4.3**). CIMP-high ACC also frequently bore somatic alterations leading to activation of the cell cycle; however, CIMP-high status was not associated with an increased incidence of alterations leading to activation of Wnt signaling, present in ~40% of ACC (Zheng et al., 2016) (**Figure 4.3**).

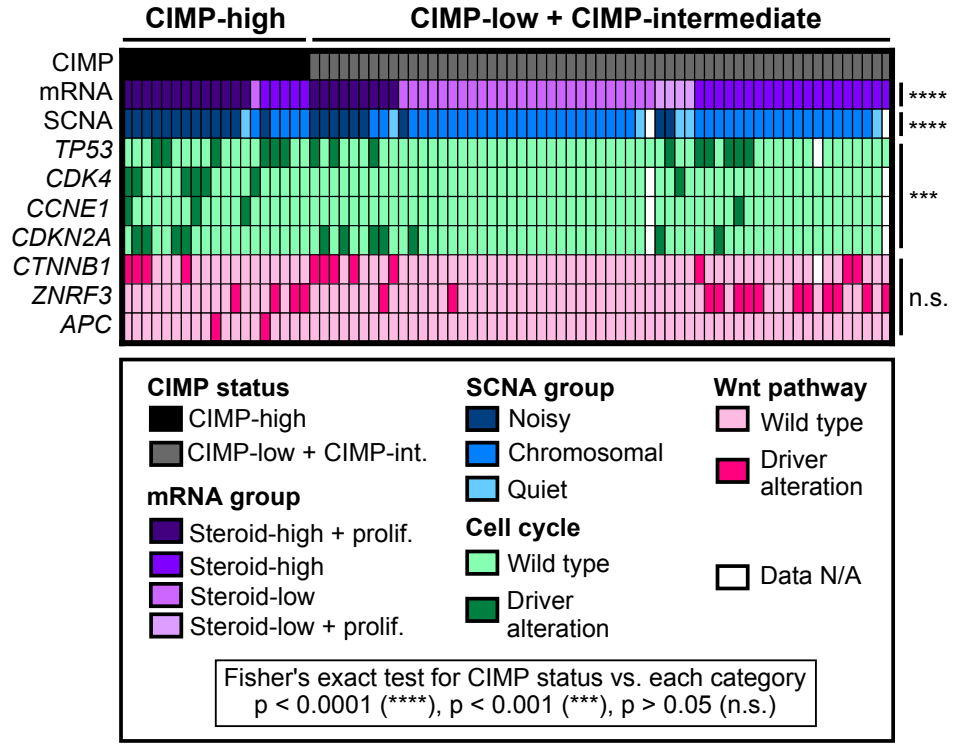

Figure 4.3. ACC-TCGA reveals CIMP-high ACC is a distinct molecular subtype.
CIMP-high ACC is associated with "Steroid-high + prolif" transcriptional program (mRNA group), "Noisy" chromosomal landscape with frequent focal copy number gains and losses (SCNA group), and higher incidence of somatic alterations leading to constitutive cell cycle activation. Notably, CIMP-high ACC is not associated with an increased incidence of somatic alterations leading to activation of the Wnt pathway, but Wnt pathway alterations are prevalent in this class.

We next analyzed RNA-seq data (n=78) from ACC-TCGA to identify differentially expressed genes in CIMP-high compared to non-CIMP-high (CIMP-low + CIMP-intermediate) carcinomas (Supplementary Table S1 published in (Mohan et al., 2019)). We performed gene ontology analysis on differentially expressed genes and identified that CIMP-high ACC exhibited transcriptional upregulation of numerous cell cycle- and DNA damage-associated biological processes, consistent with the enrichment of cell cycle-activating somatic alterations and chromosomal “noisiness” in this subgroup (**Figure 4.4**, left panel). Intriguingly, CIMP-high carcinomas exhibited transcriptional

downregulation of a wide array of immunological processes (**Figure 4.4**, right panel), suggesting that CIMP-high ACC are relatively immune poor. The convergence of this unique transcriptional program, somatic alterations targeting the cell cycle, and “noisy” chromosomal landscape in CIMP-high carcinomas demonstrates that CIMP-high status defines a distinct molecular subtype of ACC characterized by rapidly recurrent or fatal disease course. Therefore, prospectively identifying CIMP-high carcinomas using targeted molecular markers may have strong clinical utility.

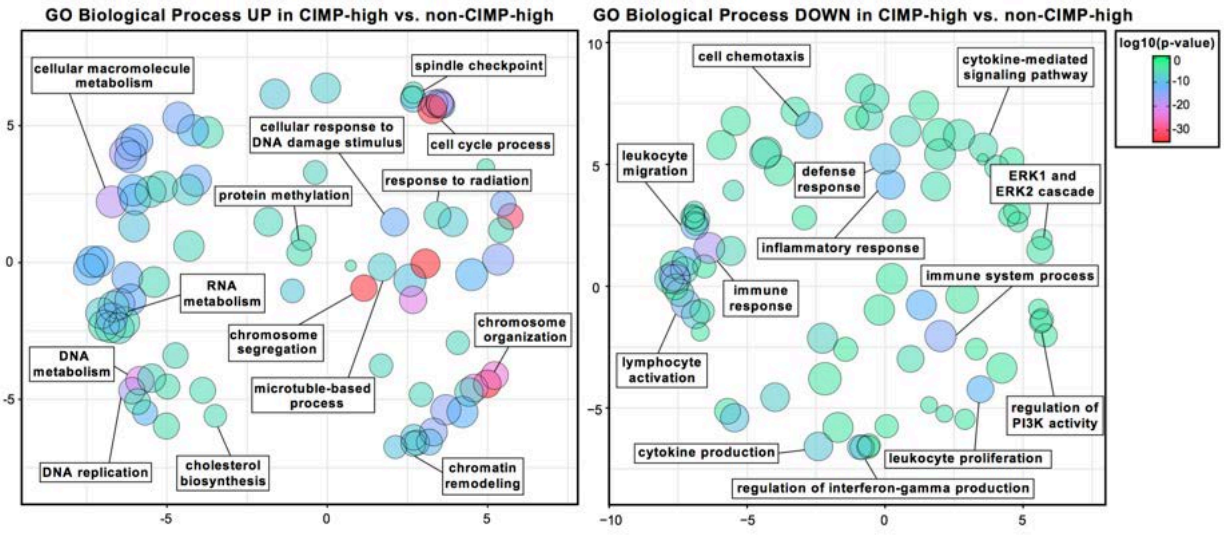

Figure 4.4. Gene ontology (GO) analysis of differentially expressed genes in CIMP-high vs. non-CIMP-high ACC.
Gene ontology (GO) analysis of 3,558 differentially expressed genes (1688 up, 1870 down; Benjamini-Hochberg FDR-corrected p-value <0.05) in CIMP-high vs. CIMP-low + CIMP-intermediate ("non-CIMP-high") ACC reveals that CIMP-high carcinomas bear transcriptional activation of several pharmacologically targetable cell cycle- and DNA damage-associated biological processes (left panel). Interestingly, several immunological processes are concordantly downregulated in CIMP-high ACC (right panel). 200 most significant biological processes up (left panel) or down (right panel) were plotted using REVIGO (Supek et al., 2011). Circle size indicates set size and color indicates p-value according to legend right; axes units are arbitrary, but smaller distance between circles reflects higher degree of semantic similarity (measured by simRel score) between sets.

4.4. ACC-TCGA nominates *G0S2* hypermethylation as a CIMP-high biomarker

We sought to identify a single biomarker with strong discriminatory power between CIMP-high and non-CIMP-high ACC, straightforward to measure and interpret without reference samples or extensive data manipulation. We were therefore interested in genomic loci that are methylated and silenced exclusively in CIMP-high ACC. We analyzed DNA methylation data from ACC-TCGA to identify regions hypermethylated in CIMP-high compared to non-CIMP-high carcinomas (Supplementary Table S2 published in (Mohan et al., 2019)). Among the top ten most hypermethylated regions in our analysis was a 2kb region on chromosome 1 (chr1:209847618-209849445, hg19; **Figure 4.5**), encompassing 13 contiguous 450k probes and spanning the *G0S2* gene locus (non-CIMP-high v. CIMP-high: max beta fold-change -0.709, mean beta fold-change -0.508, Stouffer-corrected p-value 4.32×10^{-134}).

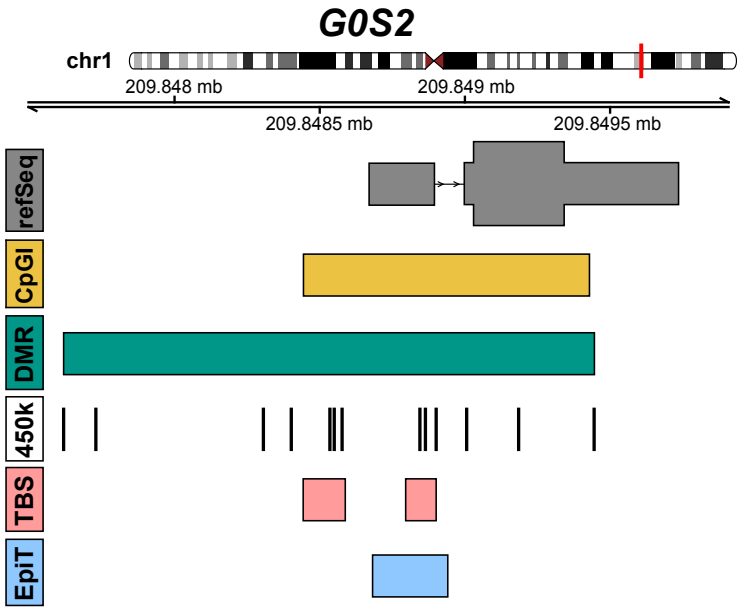

Figure 4.5. Schematic of the *G0S2* locus.
Schematized in this figure is the G0S2 locus including: the gene model and hg19 coordinates ("refSeq"), the *G0S2*-associated CpG island ("CpGI"), the region of the locus differentially methylated in CIMP-high ACC called by DMRcate ("DMR"), Illumina 450k array probes associated with the *G0S2* locus ("450k"), the region of the *G0S2* CpG island captured lature in this study by targeted bisulfite sequencing ("TBS"), and the region of the *G0S2* CpG island captured later in this study by EpiTect ("EpiT").

Our analysis of differentially expressed genes in CIMP-high compared to non-CIMP-high ACC also revealed *G0S2* was among the top five down-regulated genes, nearly silenced in CIMP-high carcinomas (CIMP-high v. non-CIMP-high: log2 fold change -5.21, Benjamini-Hochberg FDR-corrected p-value 2.31×10^{-10}), and highly predictive of CIMP-high status (logistic regression coefficient -0.925, p-value 2.10×10^{-5}); Supplementary Table S1 published in (Mohan et al., 2019). These results suggested *G0S2* is silenced by hypermethylation in a subgroup of ACC as reported in a smaller ACC cohort (Barreau et al., 2013), and that low *G0S2* expression and hypermethylation predict CIMP-high status. This observation was particularly intriguing as analysis of GTEx RNA-

seq data (Carithers et al., 2015) revealed *G0S2* is highly expressed in the physiological adrenal gland (**Figure 4.6**).

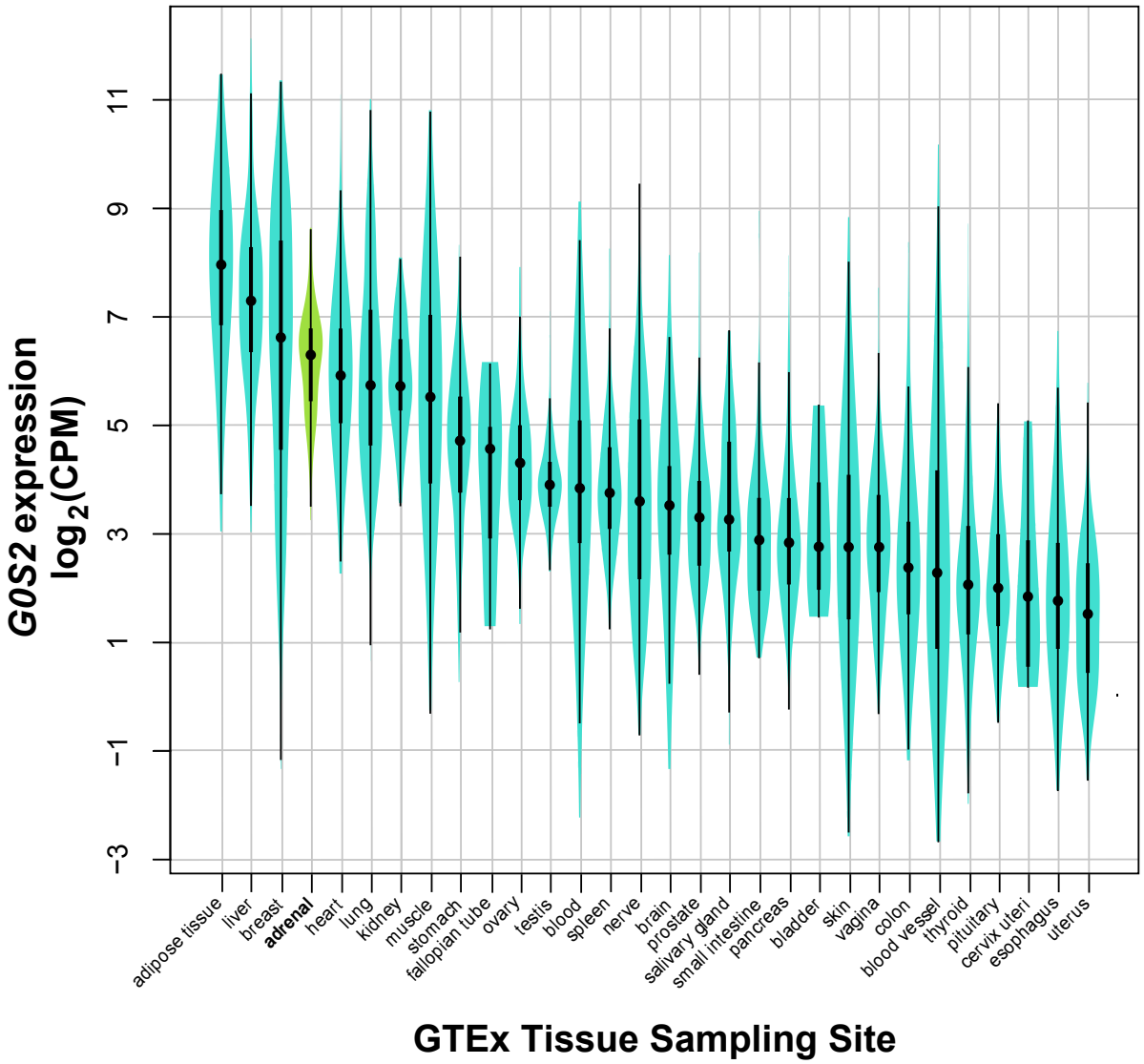

Figure 4.6. *G0S2* is highly expressed in the human adrenal gland.
Violin plots depicting expression of *G0S2* by RNA- seq across 30 different human tissues from the GTEx portal ranked by median *G0S2* expression. Shown in light green, the adrenal gland is among tissues with the highest expression of *G0S2*, ranked fourth. Median is represented by the dot, interquartile range is represented by the thick line, and minimum to maximum range (excluding outliers) is represented by the thin line. Total range and frequency distribution is depicted by the length and width of each violin, respectively. Count data was downloaded from the GTEx portal and normalized and converted to $\log_2$(CPM) using the *voom* function of *limma* in R.

We then plotted all 450k probes spanning the *G0S2* locus in each tumor sample from ACC-TCGA, ranked by decreasing *G0S2* expression. Strikingly, tumors exhibited an "all or none," binary pattern of methylation, with uniform hypermethylation (probe beta value>0.5) across the gene locus nearly restricted to CIMP-high carcinomas, and associated with reduced *G0S2* expression (**Figure 4.7**).

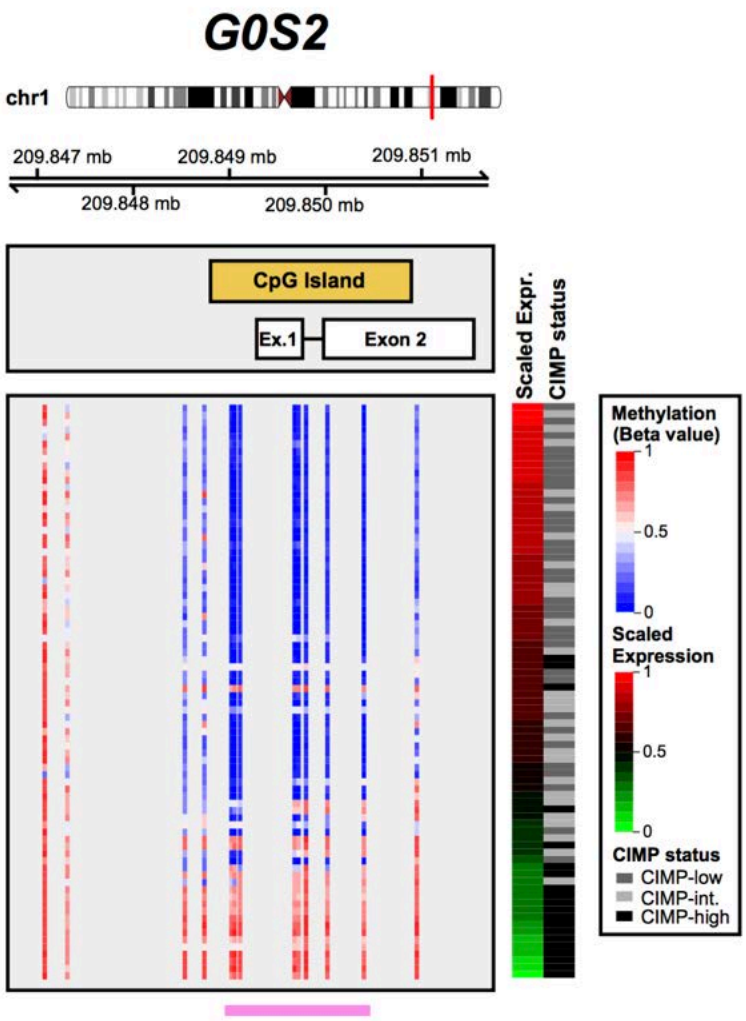

Figure 4.7. *G0S2* exhibits an all or none pattern of methylation in CIMP-high ACC, and locus methylation is associated with gene silencing.
Methylation level (beta values reflecting % methylation) of all CpG dinucleotides spanning the *G0S2* locus including 2 distal CpGs (Illumina Infinium HumanMethylation450 BeadChip, "450k"), and scaled *G0S2* expression data (RNA-seq) from ACC-TCGA (n = 78) are plotted. Coordinates along chromosome 1 are hg19. Each row represents a sample, and samples are ranked in decreasing order of *G0S2* expression (displayed as "Scaled Expression"; RNA-seq CPM scaled to fall in the range of 0-1), with assignment to CIMP status indicated right. Note that hypermethylation of the entire *G0S2* locus is largely exclusive to CIMP-high ACC, and that hypermethylation is associated with reduced or absent expression of G0S2 transcript. Indicated by the pink bar at the bottom of the figure are probes lying within the G0S2-associated CpG island.

Indeed, average methylation level of probes residing in the *G0S2* CpG island is significantly higher in CIMP-high compared to non-CIMP-high ACC ($p<0.0001$, Kruskall-Wallis with Dunn's multiple comparisons test; **Figure 4.8**), expression of *G0S2* is

significantly lower in CIMP-high compared to non-CIMP-high ACC ($p<0.0001$, Kruskall-Wallis with Dunn's multiple comparisons test; **Figure 4.9**), and both metrics are strongly inversely correlated ($p<2.2x10^{-16}$, $r=-0.82$, $R^2=0.68$, Pearson correlation; **Figure 4.10**). The inverse correlation between *G0S2* methylation and expression in ACC-TCGA suggested that measurement of *G0S2* methylation (or expression in the absence of genomic DNA) can enable identification of CIMP-high ACC.

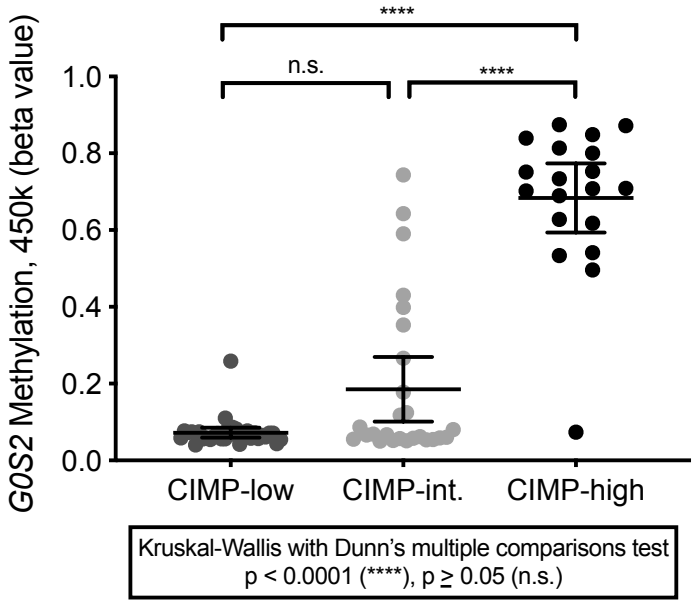

Figure 4.8. *G0S2* methylation is significantly higher in CIMP-high compared to non-CIMP-high ACC. Dot plot displaying average beta value of probes indicated in pink from **Figure 4.7** in ACC-TCGA samples by CIMP group demonstrates that methylation of the *G0S2* CpG island distinguishes CIMP-high ACC, and is significantly higher in CIMP-high ACC (clustered at >0.5) compared to CIMP-low or CIMP-intermediate ACC (clustered close to 0).

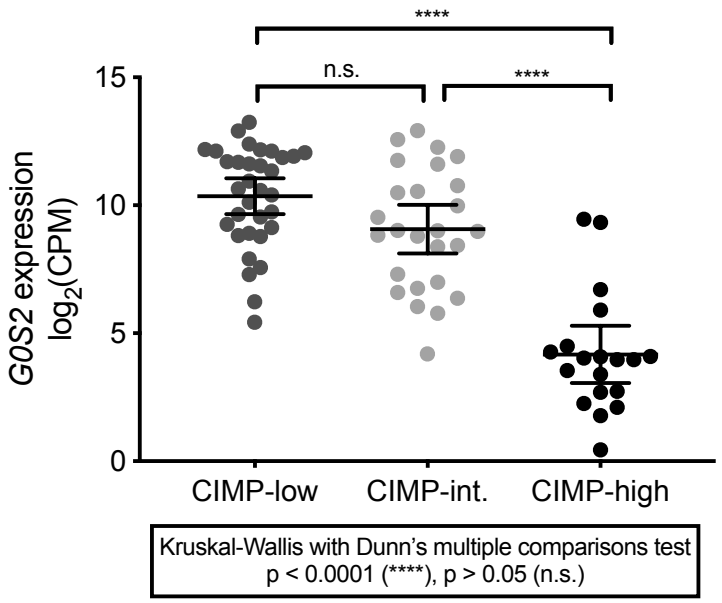

Figure 4.9. Reduced *G0S2* expression is a striking feature of CIMP-high ACC.

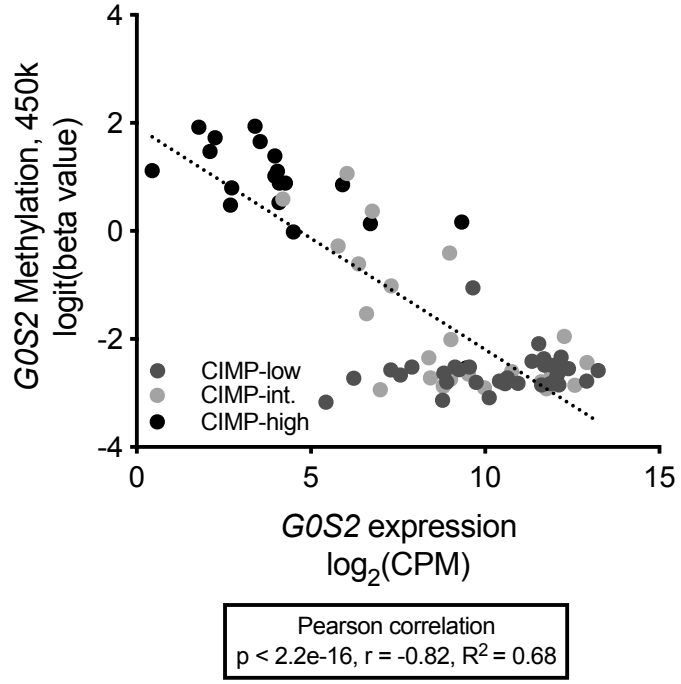

Figure 4.10. *G0S2* methylation and expression are inversely correlated in ACC.
Scatterplot displaying the relationship between logit-transformed average beta value from **Figure 4.8** and *G0S2* expression from **Figure 4.9** demonstrates that *G0S2* methylation and expression are inversely correlated, with CIMP-high ACC bearing the highest levels of *G0S2* methylation and lowest levels of *G0S2* expression.

Finally, we sought to evaluate the ability of *G0S2* methylation alone to classify ACC-TCGA samples by CIMP status. We performed unsupervised hierarchical clustering analysis using the logit-transformed beta values of 450k probes lying within the *G0S2* CpG island (**Figure 4.11**). This analysis identified two distinct clusters of samples: one cluster with samples bearing either no or low levels of *G0S2* methylation ("*G0S2* Unmethylated") corresponding to 2/3 of ACC-TCGA, and one with samples bearing high levels of uniform or heterogeneous *G0S2* methylation ("*G0S2* Methylated") corresponding to 1/3 of ACC-TCGA. The *G0S2* Methylated cluster was strongly enriched for CIMP-high ACC ($p<0.0001$, Fisher's exact test), capturing 18/19 CIMP-high samples.

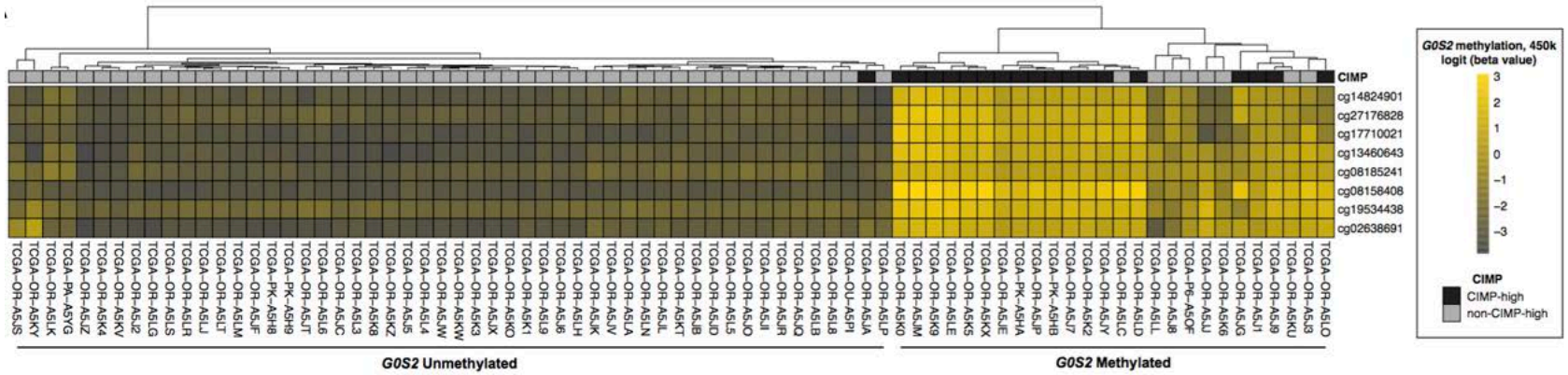

Figure 4.11. Unsupervised hierarchical clustering of *G0S2* CpG island methylation enables identification of CIMP-high ACC.
In ACC-TCGA, *G0S2* CpG island methylation is "all or none," with few samples bearing heterogeneous methylation of the locus. Unsupervised complete hierarchical clustering using Euclidean distance on logit- transformed beta values from 450k array probes lying in the *G0S2* CpG island (n=78) reveals two prominent clusters of samples: one cluster capturing ~2/3 of ACC-TCGA samples, bearing no or low levels of *G0S2* methylation ("*G0S2* Unmethylated," left), and one cluster capturing ~1/3 of ACC-TCGA samples, bearing high levels of uniform or heterogeneous *G0S2* methylation ("*G0S2* Methylated," right). CIMP-high samples are strongly enriched in the *G0S2* Methylated cluster ($p<0.0001$, Fisher's exact test), with 18/19 CIMP-high samples falling in this group. Unsupervised clustering was performed with *pheatmap* in R.

To evaluate the performance of a logistic regression model utilizing *G0S2* methylation to discriminate CIMP-high from non-CIMP-high ACC, we performed an internal k-fold cross validation (k=5, 20 repeats) on the average of the logit-transformed beta values of probes residing in the *G0S2* CpG island. Our fitted logistic regression model is described in **Table 4.1,** and the ROC curve (ROC AUC=0.928, 95% CI: 0.8235 to 1) is depicted in **Figure 4.12**. At average *G0S2* methylation >0.5200819 (measured by 450k array), we can predict assignment to CIMP-high using *G0S2* methylation alone at 94.87% accuracy, with 94.74% sensitivity, 94.92% specificity, 85.71% positive predictive value and 98.25% negative predictive value. This analysis demonstrates that *G0S2* hypermethylation has high discriminatory power to distinguish CIMP-high from non-CIMP-high ACC, and shows that unsupervised clustering of *G0S2* CpG island methylation enables reliable identification of CIMP-high samples. Taken together, our analysis of ACC-TCGA suggests that assessment of *G0S2* methylation and/or expression can reliably identify CIMP-high ACC without comprehensive DNA methylome data.

Table 4.1. *G0S2* hypermethylation predicts CIMP-high.

Resampling parameters and results				
Cross-validated (5 fold, repeated 20 times)				
N (total # of samples)	78			
Accuracy	0.9437738			
Kappa	0.8533003			
***G0S2*/CIMP-high fitted logistic regression model**				
	Estimate	**Std. Error**	**z value**	**Pr(>|z|)**
(Intercept)	-0.1027	0.4607	-0.223	0.824
Average logit (*G0S2* methylation beta value)	-1.459	0.3047	-4.788	1.68E-06
Null deviance	86.608 on 77 degrees of freedom			
Residual deviance	29.773 on 76 degrees of freedom			
AIC	33.773			
Number of Fisher Scoring iterations	12			
Confusion matrix and performance on dataset at optimal cutoff				
Average *G0S2* methylation cutoff (measured by 450k array)	0.5200819			
	Actual CIMP status			
Predicted CIMP status	CIMP-high		non-CIMP-high	
CIMP-high	18		3	
non-CIMP-high	1		56	
Accuracy	0.9487			
95% CI	(0.8739, 0.9859)			
No Information Rate	0.7564			
P-Value [Acc > NIR]	6.36E-06			
Kappa	0.8656			
Sensitivity	0.9474			
Specificity	0.9492			
Positive Predictive Value	0.8571			
Negative Predictive Value	0.9825			
Prevalence	0.2436			
Detection Rate	0.2308			
Detection Prevalence	0.2692			
Balanced Accuracy	0.9483			

NOTE. Optimal cutoff was chosen to maximize the Youden index of the ROC curve in **Figure 4.12**, maximizing both sensitivity and specificity in the fitted logistic regression model.

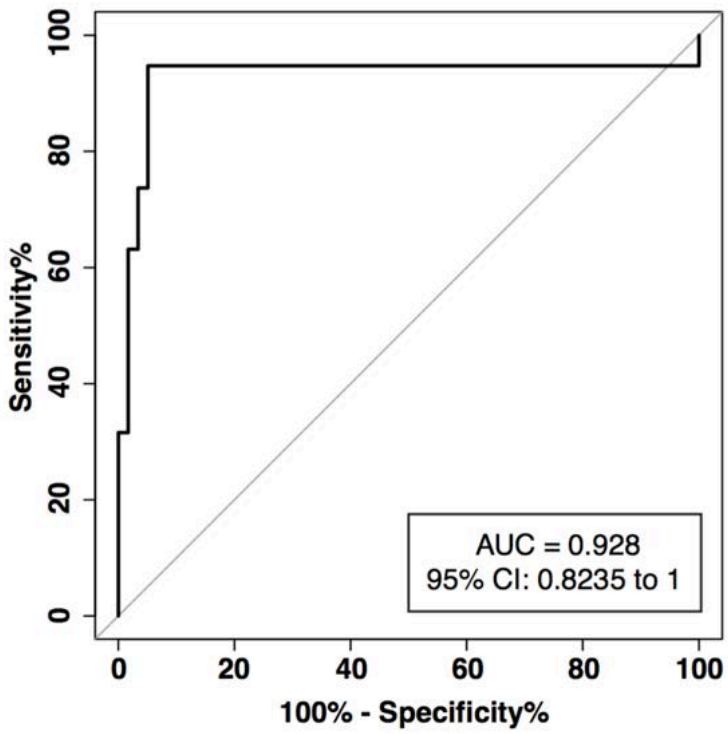

Figure 4.12. *G0S2* methylation has strong discriminatory power to distinguish CIMP-high ACC. To evaluate the performance of a logistic regression model utilizing *G0S2* methylation to discriminate CIMP-high from non-CIMP-high ACC, we performed an internal k-fold cross validation (k=5, 20 repeats) on the averaged logit-transformed beta values of probes depicted in **Figure 4.11**. ROC curve of the fitted logistic regression model demonstrates that *G0S2* methylation has strong discriminatory power in distinguishing CIMP-high from non-CIMP-high ACC. At average *G0S2* methylation >0.520 measured by 450k array, we could classify samples as CIMP-high with 94.87% accuracy. k-fold cross validation in was performed using *caret* in R.

4.5. Hypermethylation and silencing of the *G0S2* locus is exclusive to ACC

We sought to evaluate *G0S2* methylation in an independent ACC cohort, and determine if physiological tissues and ACA exhibit *G0S2* methylation. We collected genomic DNA (gDNA) and mRNA from a retrospective cohort of 80 treatment-naive primary ACC, 22 ACA, and 12 non-naive/non-primary ACC, summarized in **Table 4.2**.

Table 4.2. Clinical characteristics of FMUSP+UM ACC and ACA Cohorts.

FMUSP+UM Primary ACC Cohort, N = 80	
Age (years)	
Median, Range	45.4, 15.4 to 83.3
Sex	
Male / Female	32 (40.0%), 48 (60.0%)
Hormone secretion	
Cortisol-secreting	53 (66.3%)
Other-secreting	6 (7.5%)
Silent	21 (26.2%)
Stage at diagnosis	
ENSAT I	5 (6.2%)
ENSAT II	31 (38.8%)
ENSAT III	22 (27.5%)
ENSAT IV	22 (27.5%)
Grade	
Low grade	44 (55.0%)
High grade	25 (31.2%)
Unknown	11 (13.8%)
Tumor size (cm)	
Median, Range	12.0, 2.5 to 25.0
Unknown	5 (6.2%)
Resection status	
R0	40 (50.0%)
R1	9 (11.2%)
R2	2 (2.5%)
RX	7 (8.8%)
No attempt at curative resection	22 (27.5%)
Recurrence	
Yes	21 (26.2%)
No	26 (32.5%)
N/A	33 (41.3%)
History of metastasis	
Yes	52 (65.0%)
No	27 (33.8%)
Unknown	1 (1.2%)
Death	
Yes	43 (53.8%)
No	37 (46.2%)
DFS after R0/RX (months)	
Median (Kaplan-Meier)	29.0
OS (months)	
Median (Kaplan-Meier)	28.3
Follow up (months)	
Median, Range	21.3, 0.2 to 183.2
Institution	
FMUSP	42 (52.5%)
UM	38 (47.5%)
Molecular data	
Methylation data	70 (87.5%)
Expression data	76 (95.0%)

FMUSP+UM Non-Primary/Neoadjuvant ACC Cohort, N = 12	
Age (years)	
Median, Range	49.0, 23.7 to 80.4
Sex	
Male / Female	2 (16.7%), 10 (83.3%)
Stage at diagnosis	
ENSAT I	0 (0.0%)
ENSAT II	7 (58.3%)
ENSAT III	2 (16.7%)
ENSAT IV	2 (16.7%)
Unknown	1 (8.3%)
Stage at procurement	
ENSAT IV	12 (100.0%)
Sample site	
Adrenal after neo. EDP+M	1 (8.3%)
Adrenal recurrence	2 (16.7%)
Other	8 (66.7%)
Unknown	1 (8.3%)
Death	
Yes	5 (41.7%)
No	6 (50.0%)
Unknown	1 (8.3%)
Follow up (months)	
Median, Range	54.4, 0.7 to 176.9
Institution	
FMUSP	4 (33.3%)
UM	8 (66.7%)
Molecular data	
Methylation data	12 (100.0%)
Expression data	12 (100.0%)

FMUSP+UM ACA Cohort, N = 22	
Age (years)	
Median, Range	44.0, 19.3 to 79.5
Sex	
Male / Female	1 (4.5%), 21 (95.5%)
Hormone secretion	
Cortisol-secreting	18 (81.8%)
Aldosterone-secreting	4 (18.2%)
Institution	
FMUSP	14 (63.6%)
UM	8 (36.4%)
Molecular data	
Methylation data	22 (100.0%)
Expression data	13 (59.1%)

NOTE. "ACC" = adrenocortical carcinoma, "ACA" = adrencortical adenoma. In the "Institution" category, "FMUSP" = Faculdade de Medicina da Universidade de Sao Paulo and "UM" = University of Michigan. Grade is calculated on the basis of mitotic counts, where ≤20 mitoses/50 high-powered fields (HPF) is "Low grade" and >20/50 HPF is "High grade." "EDP+M" = etoposide, doxorubicin, cisplatin, and mitotane. “DFS” = disease-free survival. “OS” = overall survival. In any category, "Unknown" refers to number of samples for which this data point was not available.

We also collected gDNA from extra-adrenal tissues, microdissected adult adrenal cortex, and total adult adrenal cortex. We performed targeted bisulfite sequencing of *G0S2* and determined that uniform hypermethylation throughout the locus is pathological, exclusive to a subset of primary ACC and non-primary/recurrent ACC (**Figure 4.13**); Supplementary Table S5 published in (Mohan et al., 2019) details bisulfite sequencing results. We also demonstrate that physiological tissue and benign adrenocortical tumors cluster with *G0S2* Unmethylated ACC, while only ACC with high levels of uniform or heterogeneous *G0S2* methylation reside in the *G0S2* Methylated cluster. The association of physiological adrenal cortex samples with *G0S2* Unmethylated ACC is consistent with the high expression of *G0S2* in the physiological adrenal gland (**Figure 4.6**).

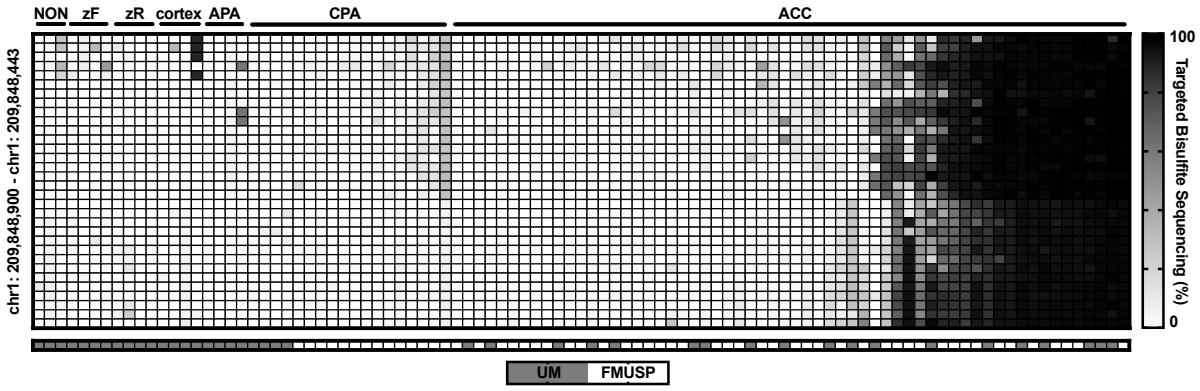

Figure 4.13. Hypermethylation of the *G0S2* locus is binary and exclusive to a subset of ACC.
Heatmap depicting results of bisulfite sequencing of the *G0S2* locus in physiologic tissues and adrenal tumors. Each row is a CpG position in the *G0S2* locus. Each column is a sample; "NON" refers to human extra-adrenal tissues (from left: kidney, lung, and corpus luteum); "zF" refers to the cortisol-secreting zona fasciculata layer of the adrenal cortex, microdissected from adult adrenal cortex; "zR" refers to the androgen-secreting zona reticularis layer of the adrenal cortex, microdissected from adult adrenal cortex; "cortex" refers to an entire adult adrenal cortex; "APA" refers to an aldosterone-producing adrenocortical adenoma (ACA) and "CPA" refers to a cortisol-producing ACA. Only treatment-naive primary ACC samples are shown here. All tumor samples in this panel are from FMUSP+UM ACA and Primary ACC Cohorts. The *G0S2* locus is unmethylated in extra-adrenal tissues, the physiologic adrenal cortex and ACA evaluated here. Hypermethylation of the entire *G0S2* locus is exclusive to a subset of ACC.

The uniform pattern of *G0S2* methylation in ACC-TCGA and our cohort indicated that locus methylation may be accurately measured by methylation-sensitive restriction digestion/qPCR-based methods instead of bisulfite-based approaches. We evaluated *G0S2* methylation using one such approach, EpiTect (Qiagen, USA). EpiTect and targeted bisulfite sequencing were highly concordant (**Figure 4.14, Figure 4.15**), demonstrating that ACA have no measurable *G0S2* methylation, while ACC have a bimodal distribution (**Figure 4.16**; 40% of ACC in FMUSP+UM Primary ACC Cohort have *G0S2* hypermethylation).

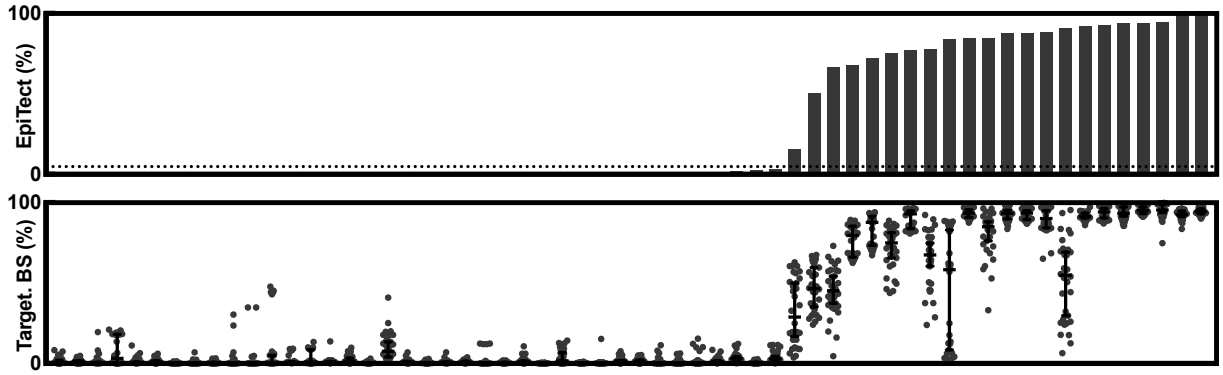

Figure 4.14. Targeted assessment of *G0S2* by EpiTect recapitulates targeted bisulfite sequencing. Targeted assessment of *G0S2* methylation by EpiTect (Qiagen, USA; upper panel) in treatment-naive primary ACC (n = 60) recapitulates results of bisulfite sequencing (lower panel; each dot represents the methylation level of a single CpG, and median and 95% CI are represented by bar and whiskers, respectively). We performed an internal k-fold cross-validation (k = 5, 20 repeats) on all samples with paired EpiTect and targeted bisulfite sequencing data (n = 74; 14 ACA, 60 ACC) to identify the appropriate EpiTect cutoff to classify a sample as bearing *G0S2* hypermethylation (**Figures 4.17**, **4.18** and **Table 4.3**). This analysis established a threshold of >4.696% methylation by EpiTect as a cutoff for pathologic hypermethylation of the *G0S2* locus, which is depicted here by the dotted line.

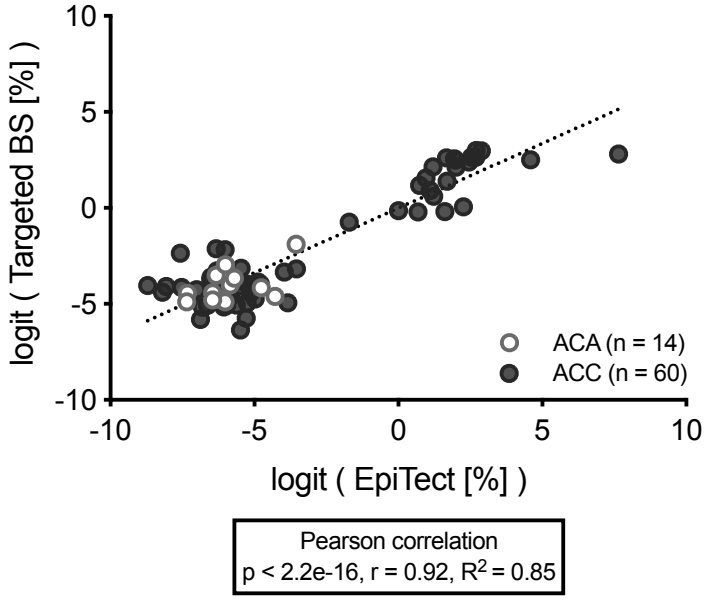

Figure 4.15. Targeted bisulfite sequencing and EpiTect are strongly correlated. Scatterplot displaying relationship between logit-transformed average targeted bisulfite sequencing methylation level and logit-transformed EpiTect methylation level demonstrates that both measures of *G0S2* methylation are strongly correlated.

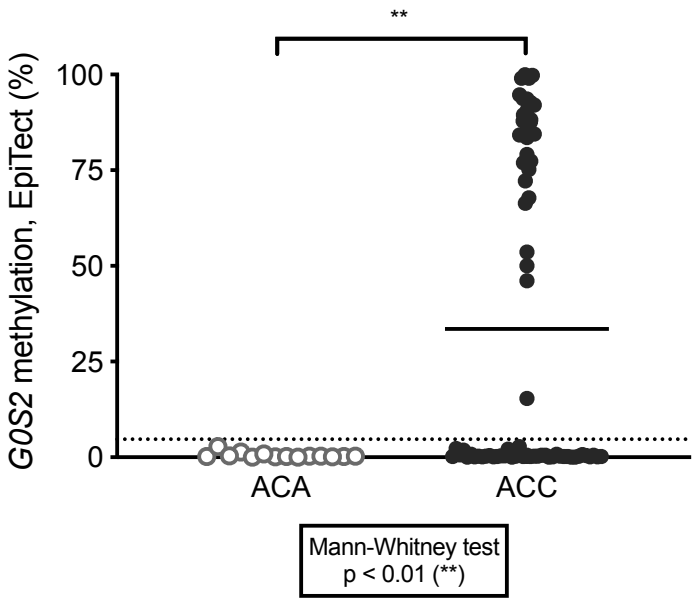

Figure 4.16. *G0S2* methylation is bimodally distributed in ACC.
Dot plot displaying distribution of *G0S2* methylation as measured by EpiTect in FMUSP+UM Primary ACC and ACA Cohorts demonstrates that *G0S2* methylation is clustered at 0% in ACA (n=14) and is bimodally clustered at 0% and >50% in ACC (n=70) with few intermediate values, consistent with ACC-TCGA. Mean of each group is indicated by the bar, and EpiTect cutoff is indicated by the dotted line.

We then sought to evaluate the concordance between EpiTect and binary *G0S2* methylation status defined by unsupervised hierarchical clustering analysis (**Figure 4.17**). For all samples with paired EpiTect and targeted bisulfite sequencing data (n=74; 60 ACC, 14 ACA), we performed an internal k-fold cross validation (k=5, 20 repeats) to evaluate a logistic regression model utilizing EpiTect measurements to discriminate these two classes. Our fitted logistic regression model is described in **Table 4.3** and ROC curve (ROC AUC=1) depicted in **Figure 4.18**, and enables us to obtain a perfect classification with an EpiTect cutoff of 4.696%. These analyses demonstrate that EpiTect enables accurate assessment of binary *G0S2* methylation status defined by gold-standard targeted bisulfite sequencing, reinforcing its potential clinical utility.

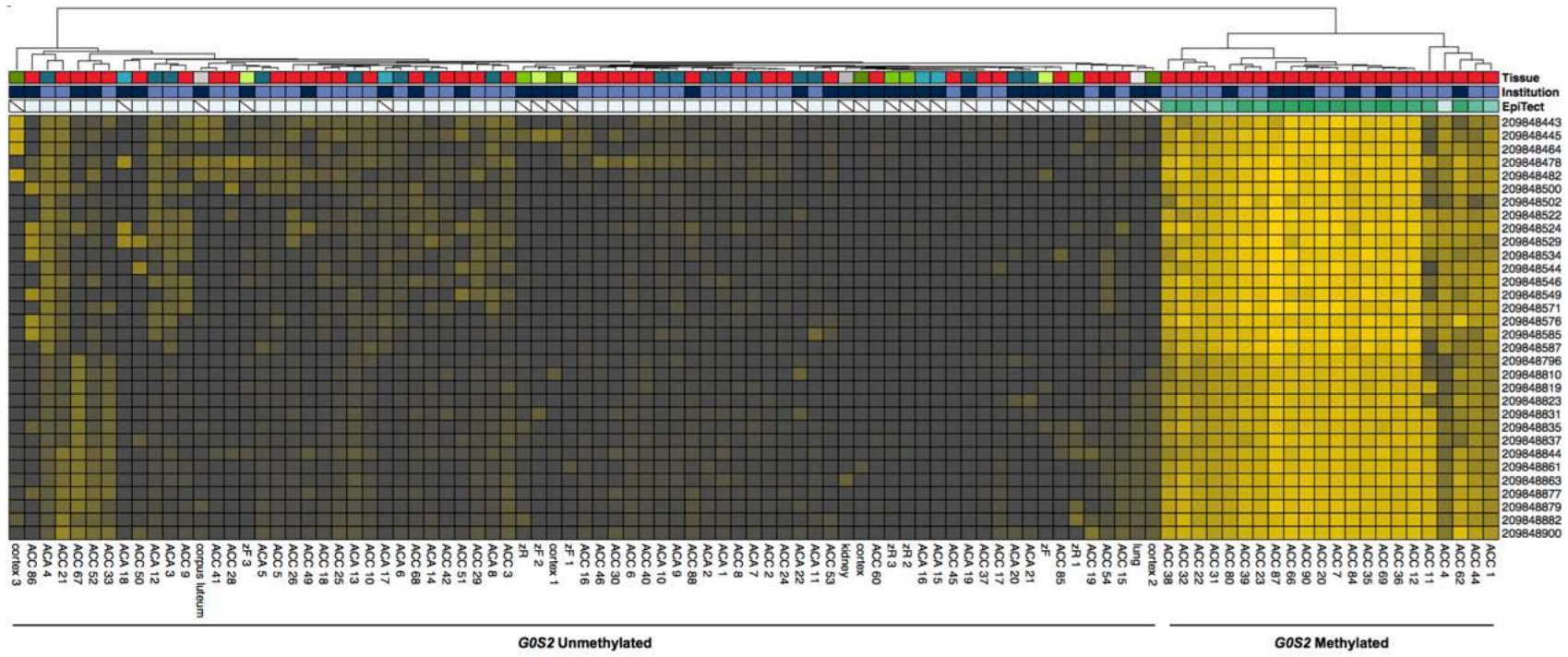

Figure 4.17. *G0S2* Unmethylated and *G0S2* Methylated tumors can be reliably captured by EpiTect.
Unsupervised complete hierarchical clustering using Euclidean distance on logit-transformed targeted bisulfite sequencing data from physiological tissue, benign adrenocortical tumors, and ACC (n=97) reveals two prominent clusters of samples – "*G0S2* Unmethylated" (left) and "G0S2 Methylated" (right) – analogous to the two clusters identified in ACC-TCGA (**Figure 4.11**, same scale). Notably, physiological tissues and benign adrenocortical tumors cluster with ~60% of ACC in the "G0S2 Unmethylated" group, while the "G0S2 Methylated" group is comprised exclusively of ~40% of ACC. G0S2 Methylated tumors are equally distributed across contributing institutions (p=0.2341; Fisher's exact test). EpiTect measurement (indicated for all samples with paired EpiTect and targeted bisulfite sequencing data) is higher in G0S2 Methylated samples as expected.

Table 4.3. EpiTect accurately measures binary *G0S2* methylation status.

Resampling parameters and results				
Cross-validated (5 fold, repeated 20 times)				
N (total # of samples)	74			
Accuracy	0.9865476			
Kappa	0.9650679			
EpiTect/*G0S2* M v. UM fitted logistic regression model				
	Estimate	**Std. Error**	**z value**	**Pr(>|z|)**
(Intercept)	-5.170	1.626	-3.181	0.00147
EpiTect (% *G0S2* Methylation)	35.881	14.200	2.527	0.01151
Null deviance	90.0664 on 73 degrees of freedom			
Residual deviance	1.7816 on 72 degrees of freedom			
AIC	5.7816			
Number of Fisher Scoring iterations	43			
Confusion matrix and performance on dataset at optimal cutoff				
EpiTect cutoff	0.04696157 (4.696%)			
	Actual *G0S2* methylation status			
Predicted *G0S2* methylation status	*G0S2* Unmethylated		*G0S2* Methylated	
G0S2 Unmethylated	52		0	
G0S2 Methylated	0		22	
Accuracy	1			
95% CI	(0.9514, 1)			
No Information Rate	0.7027			
P-Value [Acc > NIR]	4.58E-12			
Kappa	1			
Sensitivity	1			
Specificity	1			
Positive Predictive Value	1			
Negative Predictive Value	1			
Prevalence	0.2973			
Detection Rate	0.2973			
Detection Prevalence	0.2973			
Balanced Accuracy	1			

NOTE. Optimal cutoff was chosen to maximize the Youden index of the ROC curve in **Figure 4.18**, maximizing both sensitivity and specificity in the fitted logistic regression model.

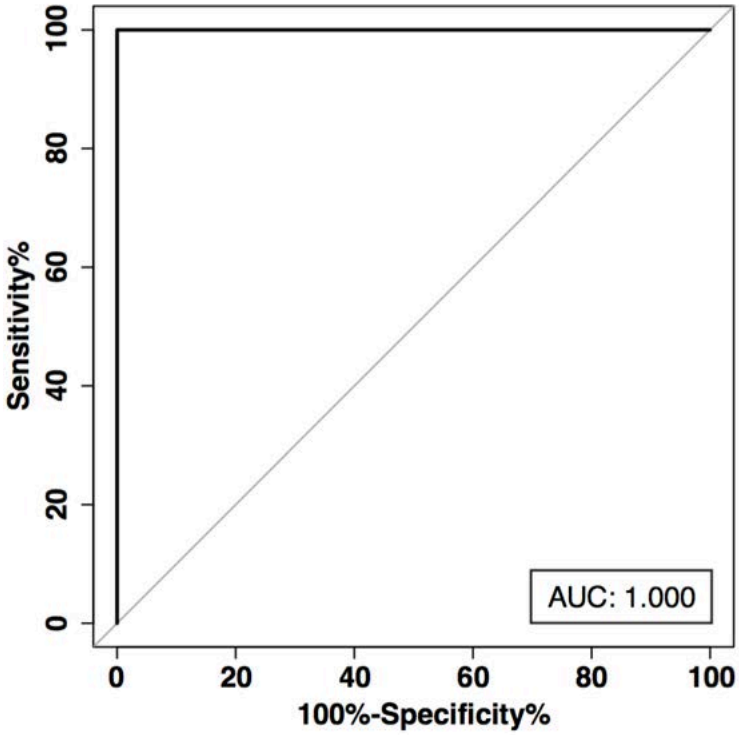

Figure 4.18. EpiTect accurately captures *G0S2* methylation status.

As in ACC-TCGA, tumors with *G0S2* hypermethylation have minimal transcript expression compared to ACA or ACC without *G0S2* methylation (**Figure 4.19**).

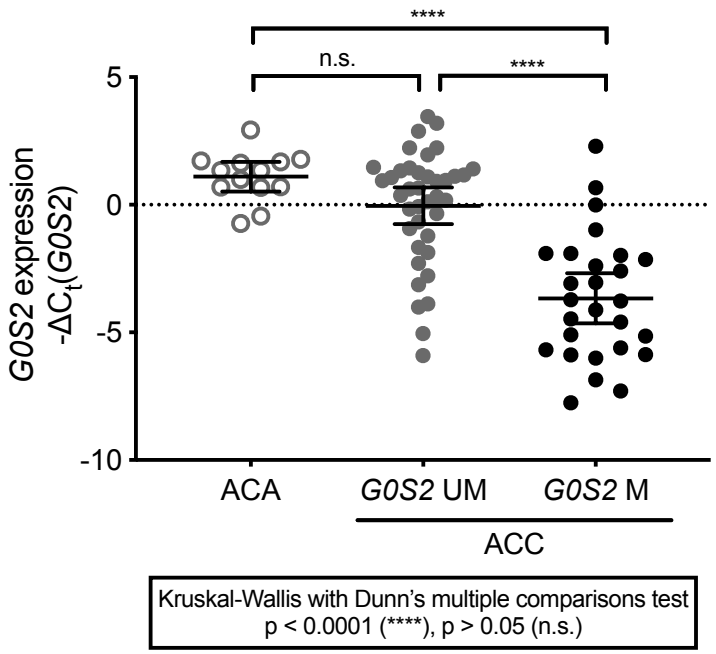

Figure 4.19. *G0S2* methylation is associated with gene silencing in an independent cohort. Evaluation of *G0S2* methylation in ACA and primary ACC without methylation of the *G0S2* locus ("*G0S2* UM") or with hypermethylation of the *G0S2* locus ("*G0S2* M") demonstrates that *G0S2* Methylated tumors have lower expression of *G0S2* compared to other adrenocortical tumors, consistent with ACC-TCGA. Note that plot depicts $-\Delta C_t$(*G0S2*), so a smaller value indicates lower expression. Mean and 95% CI of the mean are represented by bar and whiskers, respectively.

Interestingly, non-primary/non-naive ACC also exhibited the *G0S2* methylation/expression inverse relationship (**Table 4.4**). Finally, we used ROC curve analysis to identify a threshold of *G0S2* expression that reliably predicts *G0S2* hypermethylation (ROC AUC=0.8557, p<0.0001; **Figure 4.20**). At ΔC_t(*G0S2*)>3.944, we could predict *G0S2* hypermethylation with 92.31% specificity (95% CI: 79.13-98.38%) and 48.15% sensitivity (95% CI: 28.67-68.05%); we used this cutoff to infer *G0S2* methylation status of 10 primary ACC for which gDNA was unavailable. Together with ACC-TCGA, these data illustrate that uniform *G0S2* hypermethylation and silencing is exclusive to a subset of ACC, and that *G0S2* methylation can be accurately measured using restriction

digest/qPCR-based methods or inferred from *G0S2* expression when gDNA is unavailable.

Table 4.4. Hypermethylation and silencing of *G0S2* is heterogeneous in recurrent, metastatic, and non-treatment-naive carcinomas.

Tumor ID	Inst.	Stage at diag.	Time to rec. (mo)	Sample site	*G0S2* exp. $-\triangle C_t$ (*G0S2*)	% *G0S2* Meth. EpiTect	% *G0S2* Meth. TBS	Death
ACC 27	FMUSP	Unk	N/A	Unknown metastasis	1.135	0.19%	4.64%	Unk.
ACC 14	FMUSP	ENSAT II	14.00	Adrenal recurrence	-5.553	76.3%	63.7%	No
ACC 34	FMUSP	ENSAT II	6.63	Adrenal recurrence	-4.056	86.9%	32.1%	Yes
ACC 61	UM	ENSAT II	13.70	Peritoneum	-3.144	0.18%	0.38%	No
ACC 59	UM	ENSAT II	23.20	Liver or retrocaval mass	-0.645	48.8%	N/A	No
ACC 63	UM	ENSAT II	23.20	Retroperitoneal soft tissue	-1.293	0.43%	0.76%	No
ACC 64	UM	ENSAT II	14.85	Retrocaval	-1.916	0.74%	0.24%	No
ACC 65	UM	ENSAT II	14.85	Liver	-2.890	0.14%	0.8%	No
ACC 89	UM	ENSAT III	13.77	Peritoneum	-4.730	100.0%	96.6%	Yes
ACC 91	UM	ENSAT III	20.50	Retroperitoneum	-0.356	0.24%	1.99%	Yes
ACC 92	UM	ENSAT IV	N/A	Lymph node	-1.481	0.09%	1.57%	Yes
ACC 13	FMUSP	ENSAT IV	N/A	Adrenal after neoadjuvant EDP+M	0.329	0.56%	3.79%	Yes

NOTE. All samples procured when patients had progressed to ENSAT IV. ACC 59 and ACC 63 are recurrent tumors from the same patient. ACC 64 and ACC 65 are recurrent tumors from the same patient. “Inst.” = institution. “diag.” = diagnosis. “rec.” = recurrence. “exp.” = expression. “Meth.” = methylation. "EDP+M" = etoposide, doxorubicin, cisplatin, and mitotane. "Targeted BS" = Targeted bisulfite sequencing. “Unk” = Unknown. Complete table published as Supplementary Table S7 in (Mohan et al., 2019)

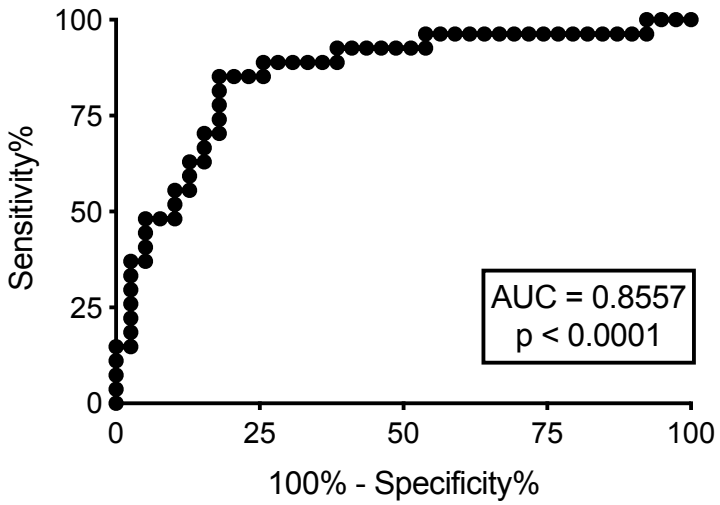

Figure 4.20. *G0S2* expression/methylation ROC curve.
We performed ROC curve analysis on n=66 primary ACC with paired *G0S2* expression and methylation data (gDNA evaluated by EpiTect and mRNA by qPCR) to identify a threshold of ΔC_t(*G0S2*) that reliably predicts *G0S2* hypermethylation (*G0S2* methylation >4.696% by EpiTect). At ΔC_t(*G0S2*)>3.944, we could predict *G0S2* hypermethylation with 92.31% specificity (95% CI: 79.13-98.38%) and 48.15% sensitivity (95% CI: 28.67-68.05%); we used this cutoff to infer G0S2 methylation status of 10 primary ACC for which mRNA was available in the absence of gDNA.

4.6. *G0S2* hypermethylation is an independent predictor of rapid recurrence and death

High histological grade is an established predictor of dismal outcomes in ACC (Beuschlein et al., 2015; Giordano, 2011; Weiss et al., 1989). In the FMUSP+UM Primary ACC Cohort, patients with high grade tumors accordingly exhibited rapidly recurrent disease following R0/RX resection (median DFS of 7.8 months). However, 3/10 of patients with high grade tumors remain disease free after >48 months follow-up and 11/32 patients with low grade disease exhibited recurrence, demonstrating that proliferation-based grade alone stratifies patients into heterogeneous groups (**Figure 4.21**).

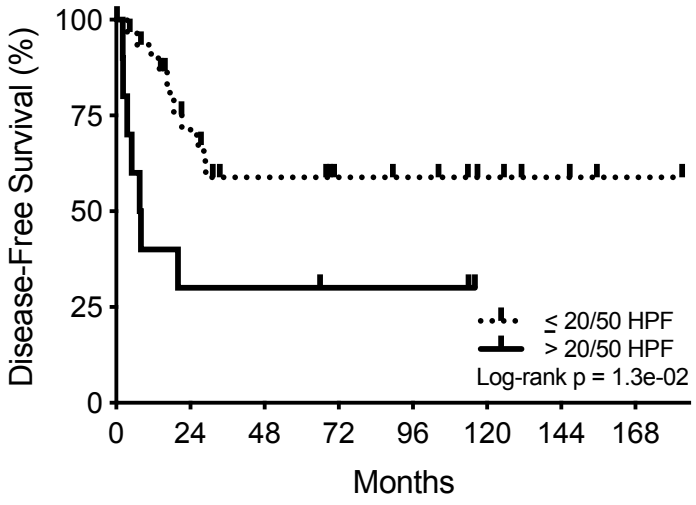

No. at risk	0	24	48	72	96	120	144	168
≤ 20/50 HPF	32	18	12	9	8	5	3	1
> 20/50 HPF	10	3	3	2	2	0	0	0

Figure 4.21. Stratification by histological grade identifies two heterogeneous subgroups of ACC. Stratification of carcinomas from FMUSP+UM Primary ACC Cohort by grade (mitotic counts, where <20 mitotic counts/50 high-powered fields [HPF] is "low grade" and >20/50 HPF is "high grade") identifies two subgroups of carcinomas with failure to achieve median disease-free survival (low grade) and median disease-free survival of 7.8 mo (high grade) following R0/RX resection.

In striking contrast, stratification by *G0S2* methylation (measured by EpiTect or inferred from *G0S2* expression when gDNA unavailable) demonstrates that patients with tumors bearing *G0S2* hypermethylation homogeneously exhibited rapidly recurrent or fatal disease course (median DFS following R0/RX resection of 14 months and median OS of 17 months; **Figures 4.22-4.23**).

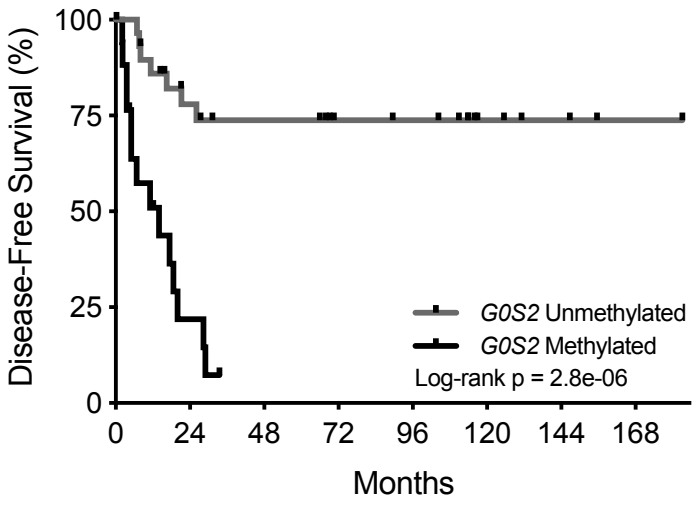

No. at risk	0	24	48	72	96	120	144	168
G0S2 Unmethylated	30	19	16	12	11	5	3	1
G0S2 Methylated	17	3	0	0	0	0	0	0

Figure 4.22. Hypermethylation of the *G0S2* locus predicts rapid recurrence in an independent ACC cohort.
Stratification of primary ACC by measured or inferred *G0S2* methylation status demonstrates that patients with *G0S2* Methylated carcinomas have rapid recurrence and median disease-free survival (DFS) of 14 months following R0/RX resection. In contrast to patients with *G0S2* Unmethylated carcinomas that fail to achieve median DFS, only 1 patient in the *G0S2* Methylated group remains disease-free at >24 months, consistent with CIMP-high/*G0S2* Methylated carcinomas from ACC-TCGA.

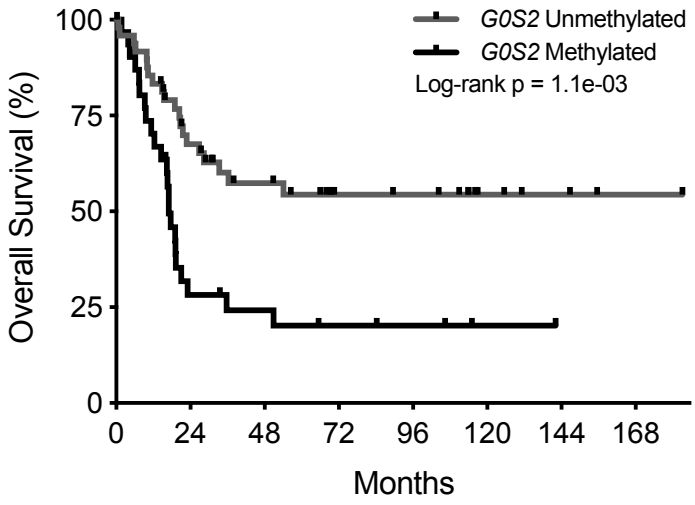

No. at risk	0	24	48	72	96	120	144	168
G0S2 Unmethylated	49	29	20	12	11	5	3	1
G0S2 Methylated	31	8	6	4	3	1	0	0

Figure 4.23. Hypermethylation of the *G0S2* locus predicts death in an independent ACC cohort. Stratification of primary ACC by measured or inferred *G0S2* methylation status demonstrates that patients with *G0S2* Methylated carcinomas have dismal OS outcomes, with median OS of 17 months compared to failure to achieve median OS in the *G0S2* Unmethylated group.

Remarkably, *G0S2* hypermethylation was identified at comparable frequency in low and high grade tumors (p=0.076, Fisher's exact test), with *G0S2* hypermethylation in 13/44 low grade tumors (**Figure 4.24**), suggesting that *G0S2* hypermethylation identifies aggressive disease in tumors inadequately stratified by tumor grade. Finally, carcinomas with *G0S2* hypermethylation were identified at comparable frequency in patients with localized ACC (ENSAT I-II), localized ACC with locoregional invasion or lymph node involvement (ENSAT III), and ACC with distal metastases (ENSAT IV) at diagnosis (p=0.31, Chi-square test; **Figure 4.25**). Notably, among 17 ENSAT I-III patients with R0/RX resection and *G0S2* hypermethylation, only 1 patient remains disease free at >24 months.

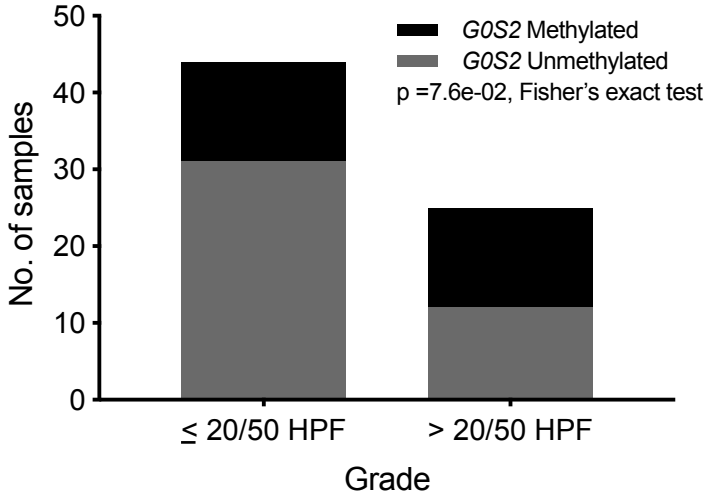

Figure 4.24. *G0S2* Methylated carcinomas are comparably prevalent in low and high grade disease.
G0S2 Methylated primary carcinomas were identified at statistically comparable frequency in patients with high grade disease (13/25) and in patients with low grade disease (13/44).

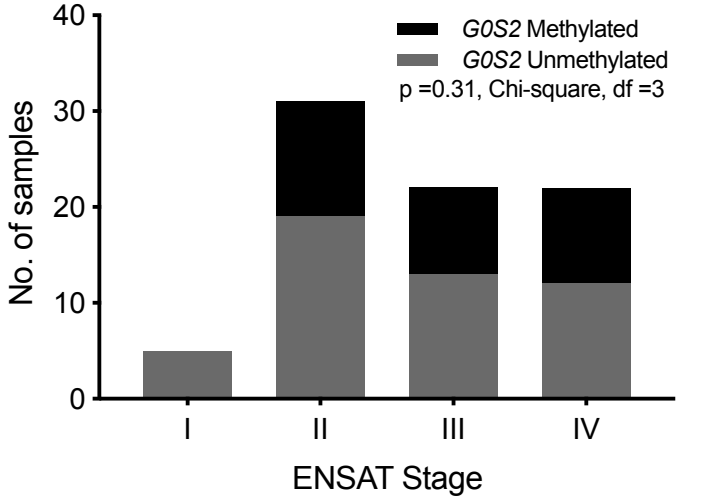

Figure 4.25. *G0S2* Methylated carcinomas are comparably prevalent in localized and disseminated disease.
G0S2 Methylated primary carcinomas were identified in patients with ENSAT II-IV disease at diagnosis without predilection for late stage disease.

We performed Cox proportional hazards regression analysis to evaluate the significance of *G0S2* hypermethylation at predicting recurrence and death compared to other clinical metrics in the FMUSP+UM Primary ACC Cohort (**Table 4.5**). High grade

and *G0S2* hypermethylation were the only variables that significantly predicted recurrence as univariates (high grade v. low grade hazard ratio [HR]=3.15, *G0S2* Methylated v. Unmethylated HR=6.91). In contrast, cortisol secretion, ENSAT IV, tumor size, tumor weight, high grade, and *G0S2* hypermethylation all significantly predicted death as univariates (cortisol-secreting v. non-cortisol-secreting HR=2.86, ENSAT IV v. II & I HR=5.26, tumor size [cm] HR=1.16, tumor weight [g] HR=1.0007, high grade v. low grade HR=3.42, *G0S2* Methylated v. Unmethylated HR=2.65). *G0S2* hypermethylation remained significant in all multivariate models (**Table 4.5**). These observations demonstrate that *G0S2* hypermethylation independently predicts rapidly recurrent disease course prior to detection of macroscopic disease spread, and routinely fatal disease course in the setting of disseminated disease.

Table 4.5. Hypermethylation of the *G0S2* locus independently predicts poor clinical outcomes.

Recurrence				Death			
Variable (Univariable model)	**HR**	**95% CI**	**p-value**	**Variable (Univariable model)**	**HR**	**95% CI**	**p-value**
Male v. Female (N = 47)	0.560	0.216 to 1.45	0.233	Male v. Female (N = 80)	0.852	0.450 to 1.61	0.622
Cortisol-secreting v. Non-cortisol-secreting (N = 47)	2.58	0.996 to 6.66	0.0509	Cortisol-secreting v. Non-cortisol-secreting (N = 80)	2.86	1.36 to 5.99	5.45 e-3
Stage at diagnosis (N = 47)				Stage at diagnosis (N = 80)			
ENSAT III v. II & I	1.49	0.602 to 3.70	0.388	ENSAT III v. II & I	2.09	0.937 to 4.66	0.0718
				ENSAT IV v. II & I	5.26	2.52 to 11.0	1.03 e-5
Tumor size (cm) (N = 45)	1.09	0.992 to 1.20	0.0739	Tumor size (cm) (N = 75)	1.16	1.08 to 1.24	7.71 e-5
Tumor weight (g) (N = 36)	1.0003	0.9995 to 1.0011	0.444	Tumor weight (g) (N = 55)	1.0007	1.0003 to 1.0011	4.59 e-4
High grade v. Low grade (N = 42)	3.15	1.21 to 8.16	0.0183	High grade v. Low grade (N = 69)	3.42	1.74 to 6.74	3.80 e-4
G0S2 M v. UM (N = 47)	6.91	2.74 to 17.5	4.31 e-5	*G0S2* M v. UM (N = 80)	2.65	1.45 to 4.86	1.60 e-3
Variable (Multivariable model)	**HR**	**95% CI**	**p-value**	**Variable (Multivariable model)**	**HR**	**95% CI**	**p-value**
(N = 47)				(N = 80)			
Cortisol-secreting v. Non-cortisol-secreting	2.51	0.964 to 6.53	0.0594	Cortisol-secreting v. Non-cortisol-secreting	2.43	1.14 to 5.16	0.0208
G0S2 M v. UM	6.88	2.71 to 17.5	5.02 e-5	*G0S2* M v. UM	2.27	1.23 to 4.20	9.00 e-3
(N = 47)				(N = 80)			
ENSAT III v. II & I	1.11	0.440 to 2.78	0.830	ENSAT III v. II & I	1.80	0.804 to 4.04	0.153
				ENSAT IV v. II & I	5.44	2.57 to 11.5	9.30 e-6
G0S2 M v. UM	6.81	2.67 to 17.4	5.98 e-5	*G0S2* M v. UM	2.77	1.48 to 5.19	1.39 e-3
(N = 45)				(N = 75)			
Tumor size (cm)	1.09	0.982 to 1.20	0.108	Tumor size (cm)	1.17	1.09 to 1.26	3.72 e-5
G0S2 M v. UM	6.95	2.71 to 17.8	5.33 e-5	*G0S2* M v. UM	3.53	1.85 to 6.75	1.36 e-4
(N = 36)				(N = 55)			
Tumor weight (g)	1.0005	0.9997 to 1.0012	0.208	Tumor weight (g)	1.0009	1.0005 to 1.0013	2.78 e-5
G0S2 M v. UM	7.10	2.55 to 19.8	1.78 e-4	*G0S2* M v. UM	4.51	2.01 to 10.1	2.48 e-4
(N = 42)				(N = 69)			
High grade v. Low grade	3.38	1.27 to 8.98	0.0147	High grade v. Low grade	3.10	1.56 to 6.17	1.25 e-3
G0S2 M v. UM	7.90	2.86 to 21.8	6.69 e-5	*G0S2* M v. UM	3.05	1.54 to 6.05	1.43 e-3

NOTE. Hazard ratios (HR) and 95% confidence intervals (95% CI) were determined by Cox proportional hazards regression using available clinical and molecular data from all tumors in the FMUSP+UM Primary ACC Cohort. In each category, N is number of samples included in each univariable or multivariable model. The p-value is calculated from the Wald statistic using a chi-squared distribution. Grade is based on mitotic counts, where $\leq$ 20 mitoses/50 high-powered fields (HPF) is "Low grade" and > 20/50 HPF is "High grade." "G0S2 M. v. UM" = G0S2 Methylated v. Unmethylated.

4.7. *G0S2* hypermethylation facilitates stratification of ACC into homogeneous groups in combination with validated molecular biomarkers

Though *G0S2* hypermethylation independently predicts uniformly dismal disease course, patients without *G0S2* methylation exhibited heterogeneous outcomes (**Figures 4.24-4.25**). We sought to determine if alternative molecular predictors could resolve this heterogeneity by separating patients with certain favorable prognosis from those with intermediate recurrence risk. We and others have shown that a score derived from expression of *BUB1B* and *PINK1* (*BUB1B-PINK1*) can stratify ACC into "good prognosis" and "bad prognosis" groups (de Reynies et al., 2009; Fragoso et al., 2012). The disease course of "good prognosis" ACC has been likened to that of patients with ACA, as patients were primarily cured by surgery. Interestingly, "good prognosis" ACC had *BUB1B-PINK1* indistinguishable from ACA (de Reynies et al., 2009).

We evaluated *BUB1B-PINK1* in FMUSP+UM Primary ACC and ACA Cohorts. We then performed an internal k-fold cross validation (k=5, 20 repeats) on *BUB1B-PINK1* score to evaluate the performance of a logistic regression model predicting any history of metastasis in *G0S2* Unmethylated ACC (**Figure 4.26** depicts fitted logistic regression model ROC curve with ROC AUC 0.840, 95% CI: 0.7177 to 0.9619; model is described in **Table 4.6**).

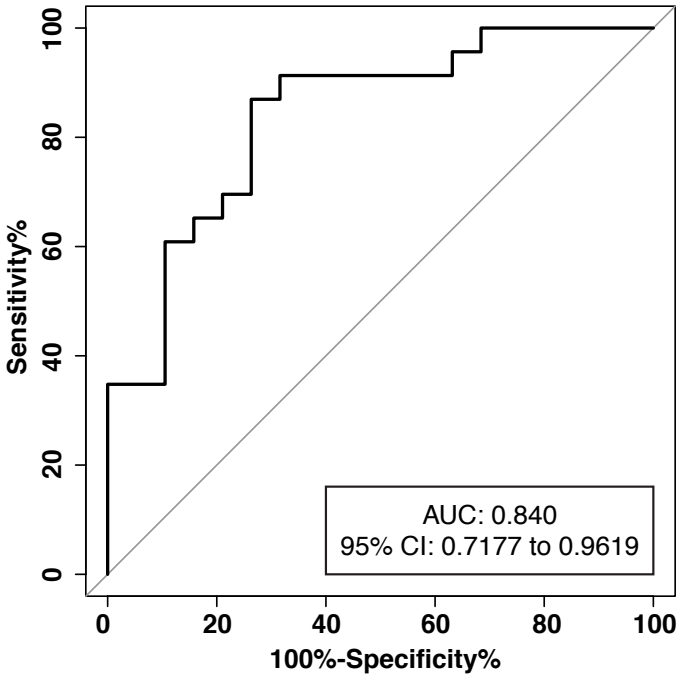

Figure 4.26. *BUB1B-PINK1* score can predict metastasis in *G0S2* Unmethylated ACC.
To evaluate the performance of a logistic regression model predicting any history of metastasis in *G0S2* Unmethylated ACC utilizing *BUB1B-PINK1* score, we performed an internal k-fold cross validation (k=5, 20 repeats) on *BUB1B-PINK1* score (n=42). We considered patients as "metastasis free" if they had no recorded history of metastasis and follow-up time >24 mo. ROC curve of the fitted logistic regression model demonstrates that *BUB1B-PINK1* has strong discriminatory power in distinguishing *G0S2* Unmethylated tumors with any history of metastasis from *G0S2* Unmethylated tumors with no history of metastasis. At *BUB1B-PINK1*<5.200, we had 100% sensitivity to predict any history of metastasis. k-fold cross validation was performed using *caret* in R.

Table 4.6. *BUB1B-PINK1* can predict any history of metastasis in patients with *G0S2* Unmethylated ACC.

Resampling parameters and results				
Cross-validated (5 fold, repeated 20 times)				
N (total # of samples)	42			
Accuracy	0.7580357			
Kappa	0.5121646			
***BUB1B-PINK1* fitted logistic regression model**				
	Estimate	**Std. Error**	**z value**	**Pr(>|z|)**
(Intercept)	2.5605	0.8707	2.941	0.00327
BUB1B-PINK1	-0.7706	0.2421	-3.184	0.00145
Null deviance	57.843 on 41 degrees of freedom			
Residual deviance	38.448 on 40 degrees of freedom			
AIC	42.448			
Number of Fisher Scoring iterations	13			
Confusion matrix and performance on dataset at optimal cutoff				
***BUB1B-PINK1* cutoff**	5.200273			
	Actual history of metastasis			
Predicted history of metastasis	No		Yes	
No	6		0	
Yes	13		23	
Accuracy	0.6905			
95% CI	(0.5291, 0.8238)			
No Information Rate	0.5476			
P-Value [Acc > NIR]	0.0425656			
Kappa	0.3358			
Sensitivity	1			
Specificity	0.3158			
Positive Predictive Value	0.6389			
Negative Predictive Value	1			
Prevalence	0.5476			
Detection Rate	0.5476			
Detection Prevalence	0.8571			
Balanced Accuracy	0.6579			

NOTE. Optimal cutoff was chosen to maximize sensitivity for capturing any history of metastasis in the fitted logistic regression model depicted by the ROC curve in **Figure 4.26**.

At *BUB1B-PINK1*<5.200, we predicted metastasis in patients with *G0S2* Unmethylated carcinomas with 100% sensitivity and 31.58% specificity. We assigned carcinomas from the FMUSP+UM Primary ACC Cohort to three groups: ACC I (*G0S2* Unmethylated, *BUB1B-PINK1*>5.200), ACC II (*G0S2* Unmethylated, *BUB1B-PINK1*<5.200), and ACC III (*G0S2* Methylated). ACA and ACC I tumors had no difference in *BUB1B-PINK1* ($p>0.05$, Kruskal-Wallis with Dunn's multiple comparisons test), while ACC II and ACC III had different *BUB1B-PINK1* from ACA ($p<0.0001$) and ACC I (II v. I: $p<0.005$, III v. I: $p<0.0001$). ACC II and ACC III had indistinguishable *BUB1B-PINK1* ($p>0.05$), suggesting *BUB1B-PINK1* cannot further stratify *G0S2* Methylated carcinomas (**Figure 4.27**). Using this combination of *BUB1B-PINK1* and *G0S2* methylation status, we stratified the FMUSP+UM Primary ACC Cohort into three groups with variable risk of recurrence (**Figure 4.28**) and death (**Figure 4.29**). In patients with *G0S2* Unmethylated carcinomas, we could now distinguish those who remain disease free and alive (ACC I) from those with history of recurrence and death (ACC II). All clinical and molecular data are summarized in Supplementary Table S9 published in (Mohan et al., 2019).

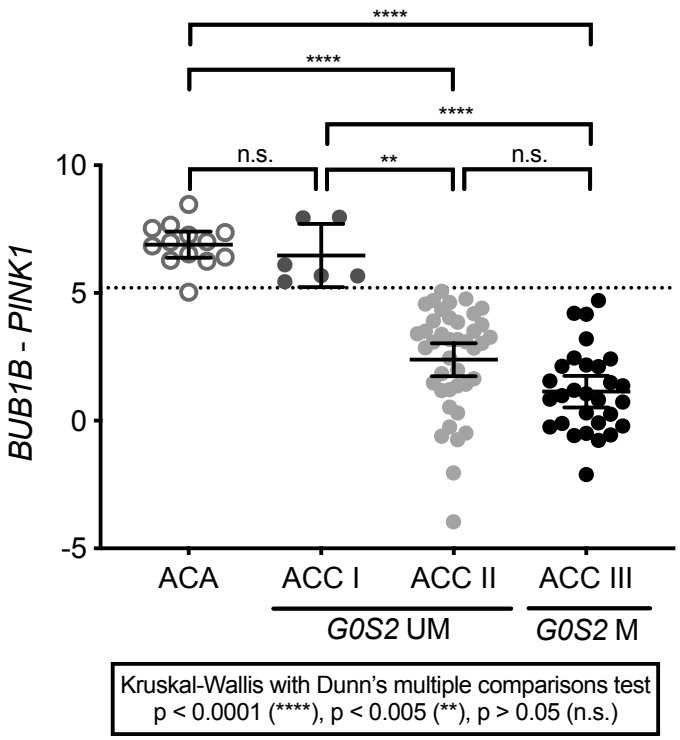

Figure 4.27. *BUB1B-PINK1* score identifies ACA-like ACC but fails to discriminate between remaining *G0S2* Unmethylated and *G0S2* Methylated ACC.
Application of an internal k-fold cross validation (k = 5, 20 repeats) to *BUB1B-PINK1* score in *G0S2* unmethylated primary samples from FMUSP+UM cohort enabled identification of a *BUB1B-PINK1* score threshold (*BUB1B-PINK1*<5.200; **Figure 4.26**, **Table 4.6**) with 100% sensitivity to identify any history of recurrence or metastatic disease. *G0S2* Methylated carcinomas were assigned to ACC III. *G0S2* Unmethylated carcinomas with *BUB1B-PINK1* score above threshold were classified as ACC I, and below threshold were classified as ACC II. Importantly, ACC I carcinomas have BUB1B-PINK1 score indistinguishable from ACA. ACC II and ACC III (*G0S2* Methylated) carcinomas have indistinguishable *BUB1B-PINK1* scores. Mean and 95% CI of the mean are represented by bar and whiskers, respectively.

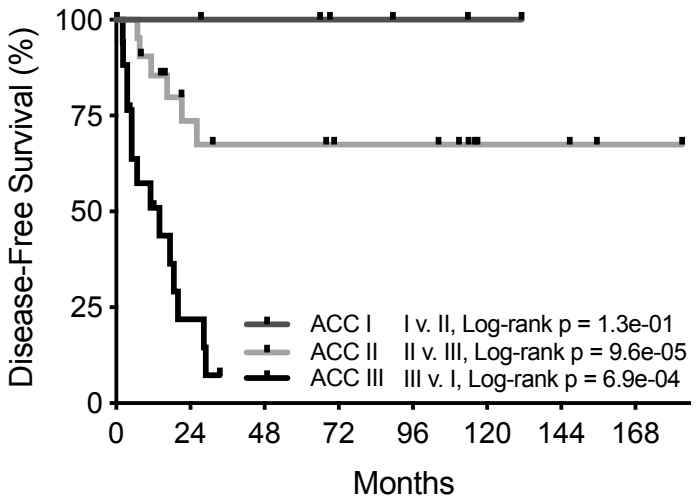

No. at risk	0	24	48	72	96	120	144	168
ACC I	6	6	5	3	2	1	0	0
ACC II	22	12	10	8	8	3	3	1
ACC III	17	3	0	0	0	0	0	0

Figure 4.28. Hypermethylation of the *G0S2* locus facilitates stratification of ACC into good, intermediate, and poor prognostic groups in terms of recurrence when combined with *BUB1B-PINK1* score.

Combined assessment of BUB1B-PINK1 score and G0S2 methylation facilitates stratification of ACC into three groups by disease-free survival (DFS). Patients with ACC I carcinomas have no known history of recurrence, patients with ACC II carcinomas have heterogeneous outcomes (fail to achieve median DFS following R0/RX resection), and patients with ACC III (G0S2 Methylated) carcinomas have rapidly recurrent disease (median DFS of 14 months following R0/RX resection).

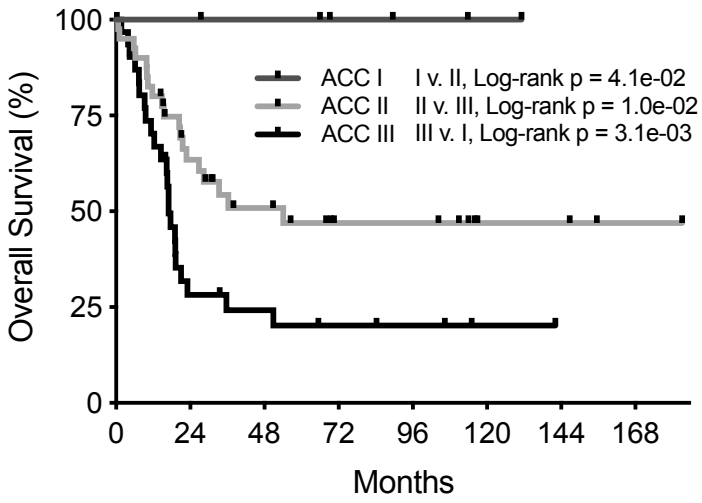

No. at risk	0	24	48	72	96	120	144	168
ACC I	6	6	5	3	2	1	0	0
ACC II	41	22	14	8	8	3	3	1
ACC III	31	8	6	4	3	1	0	0

Figure 4.29. Hypermethylation of the *G0S2* locus facilitates stratification of ACC into good, intermediate, and poor prognostic groups in terms of death when combined with *BUB1B-PINK1* score.
Combined assessment of *BUB1B-PINK1* score and *G0S2* methylation also facilitates stratification of ACC into three groups by overall survival (OS). Patients with ACC I carcinomas have no known history of mortality at the time of this study, patients with ACC II carcinomas have median OS of 36.3 months, and patients with ACC III carcinomas have median OS of 17 months.

These results demonstrate the combined utility of *G0S2* methylation and *BUB1B-PINK1* score in stratifying patients into three groups, two of which have uniformly favorable or dismal outcomes. These data illustrate a strategy for implementing molecular biomarkers in series to precisely define risk categories in ACC, with high potential to impact clinical management.

4.8. CIMP-high status is amenable to targeted assessment in archival material

G0S2 methylation is a powerful biomarker that enables rapid assessment of CIMP-high status in ACC tissue. However, the studies described in sections **4.3** – **4.7** were

performed on nucleic acids extracted from high quality frozen specimen, which are not routinely available. We therefore sought to extend the application of *G0S2* methylation to readily available archival material, including formalin-fixed, paraffin-embedded (FFPE) tissues. We first assembled a small pilot cohort of FFPE tissues where we had already evaluated *G0S2* methylation status in counterpart high quality gDNA, and sought to evaluate *G0S2* methylation by EpiTect in FFPE-derived gDNA. An important feature that distinguishes FFPE-derived gDNA from high quality gDNA obtained from frozen tissue is that FFPE-derived gDNA is highly fragmented and often degraded; gel electrophoresis on FFPE-derived gDNA demonstrates a smear of gDNA lengths ranging from <100 bp to >40 kb, rather than a single, intact, high molecular weight band (**Figure 4.30** – **4.31**)

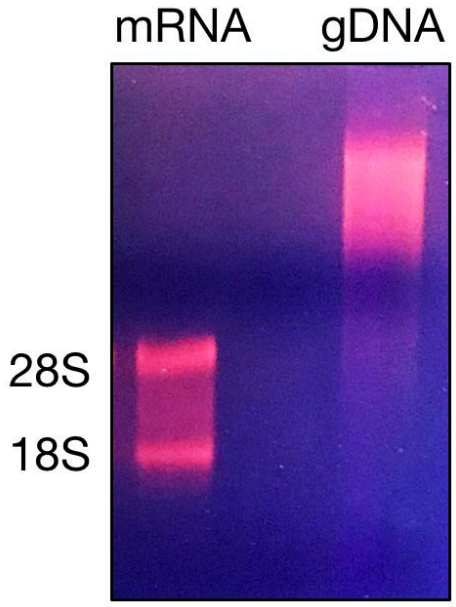

Figure 4.30. High quality gDNA is uniformly high molecular weight.
All mRNA and some gDNA extracted for studies described in sections **4.3** – **4.7** were subject to agarose gel electrophoresis under nuclease-free conditions to evaluate sample quality/purity as described in section **4.10**. Example image from a gel is shown here, demonstrating characteristic 18S and 28S bands in mRNA lane and single, intact, high molecular weight band in gDNA lane. The 28S band characteristically runs at just under 4 kb while the 18S band runs at 1-2 kb. Extracted gDNA is therefore well over 4 kb in length.

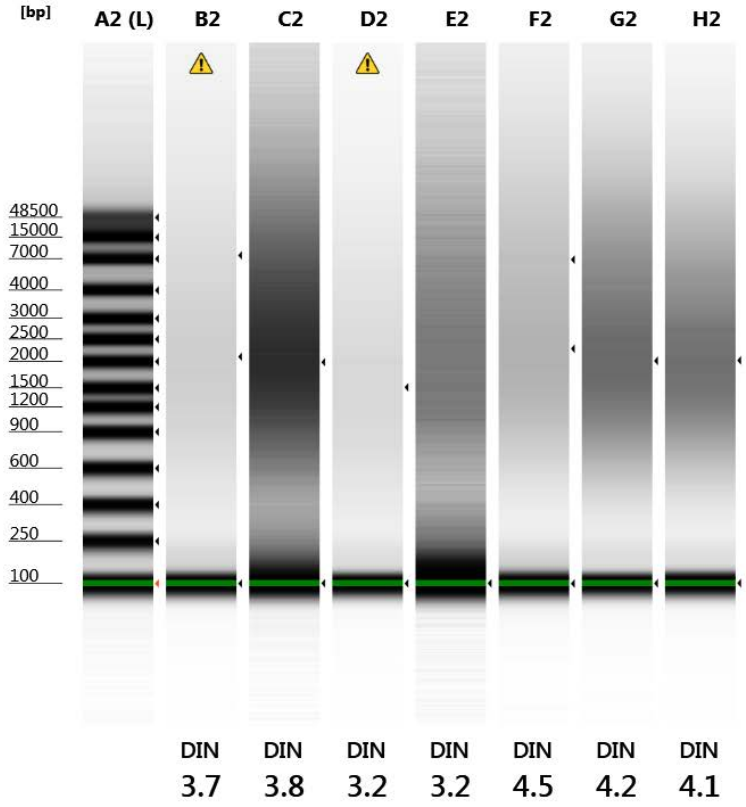

Figure 4.31. FFPE-derived gDNA is heavily fragmented.
gDNA extracted from FFPE tissues was analyzed using the Agilent Genomic DNA ScreenTape by the University of Michigan Advanced Genomics Core. Ladder is shown in lane A2 and samples are loaded in lanes B2-H2 with a 100 bp standard. Virtually all gDNA samples possess a broad range of sizes, evidenced by the broad smear and absence of intact genomic band and low DIN values (perfect DIN = 10).

Given our success in using EpiTect on gDNA extracted from frozen tissues, we first attempted to use EpiTect on FFPE-derived gDNA. As detailed in section **4.10**, EpiTect is a restriction digest-based approach, and one of the control steps is to perform qPCR using primers directed to the *G0S2* locus on "mock" digested gDNA, that is gDNA that was not incubated with any restriction enzymes. The C_t yielded from the mock digest represents the total amount of intact genomic DNA at the *G0S2* locus included in the restriction digestion, and is the lowest possible C_t value. As expected given the

degradation pattern (**Figure 4.31**), qPCR on mock digested FFPE gDNA yielded very high C_t values, and in 1/7 cases, a C_t could not be determined (**Figure 4.32**).

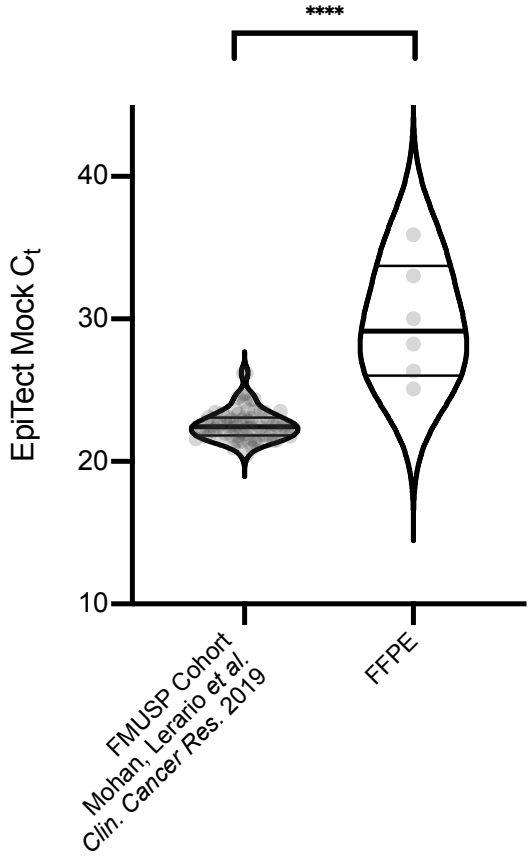

	FMUSP Cohort Mohan, Lerario *et al. Clin. Cancer Res.* 2019	FFPE
Number of values	74	6
Minimum	20.41	25.09
25% Percentile	21.82	26.04
Median	22.43	29.13
75% Percentile	23.09	33.74
Maximum	26.21	35.91
Range	5.797	10.81
Mean	22.59	29.77
Std. Deviation	1.098	4.101
Std. Error of Mean	0.1276	1.674

Mann Whitney test
$p < 0.0001$ (****)

Figure 4.32. FFPE-derived gDNA possess less intact gDNA at the *G0S2* locus compared to samples included in the study presented in sections 4.3 – 4.7.
Left, FFPE-derived gDNA have a significantly higher C_t for qPCR evaluating the *G0S2* locus in mock-digested samples ($p < 0.0001$, Mann Whitney test) compared to samples that were utilized in the study presented in sections **4.3** – **4.7**. Right, descriptive statistics for each group.

2/7 samples in this pilot failed the EpiTect assay (either due to high mock C_t value or inadequate restriction digestion), but we obtained EpiTect estimates of *G0S2* methylation in the remaining 5/7 samples. Frozen and FFPE *G0S2* methylation calls were largely concordant in samples that passed EpiTect (**Table 4.7**).

Table 4.7. EpiTect results from FFPE pilot.

Tumor ID	ACC 47	ACC 60	ACC 83	ACC 62	ACC 88	ACC 66	ACC 89
EpiTect FFPE	FAIL	FAIL	31.60%	81.52%	1.51%	22.81%	95.00%
EpiTect Frozen	79.14%	0.10%	0.25%	90.54%	0.30%	93.66%	99.99%
FFPE *G0S2* status	FAIL	FAIL	M	M	UM	M	M
Frozen *G0S2* status	M	UM	UM	M	UM	M	M

NOTE. "M" = *G0S2* Methylated; "UM" = *G0S2* Unmethylated.

From this pilot, we concluded that the low success rate of EpiTect in FFPE-derived gDNA (concordant classification obtained in 4/7 samples) precludes routine application of this assay to FFPE archival material at this time. The nature of FFPE-derived gDNA (**Figure 4.31**) suggested we may obtain superior test performance using an alternative probe- or NGS-based approach in which only small intact fragments of gDNA which are less sensitive to DNA degradation are required to determine *G0S2* methylation status. For an ongoing study seeking to identify molecular predictors of response to targeted therapies in ACC (**Appendix A**), we assembled an international cohort of FFPE samples (n = 34) including samples more than a decade old. We then submitted these samples for targeted bisulfite sequencing of the *G0S2* locus (as in **Figures 4.13, 4.17**, and detailed in section **4.10** with the exception that samples without an intact gDNA band were still sequenced). Gel electrophoresis analysis of samples included for targeted bisulfite sequencing analysis is depicted in **Figure 4.33**.

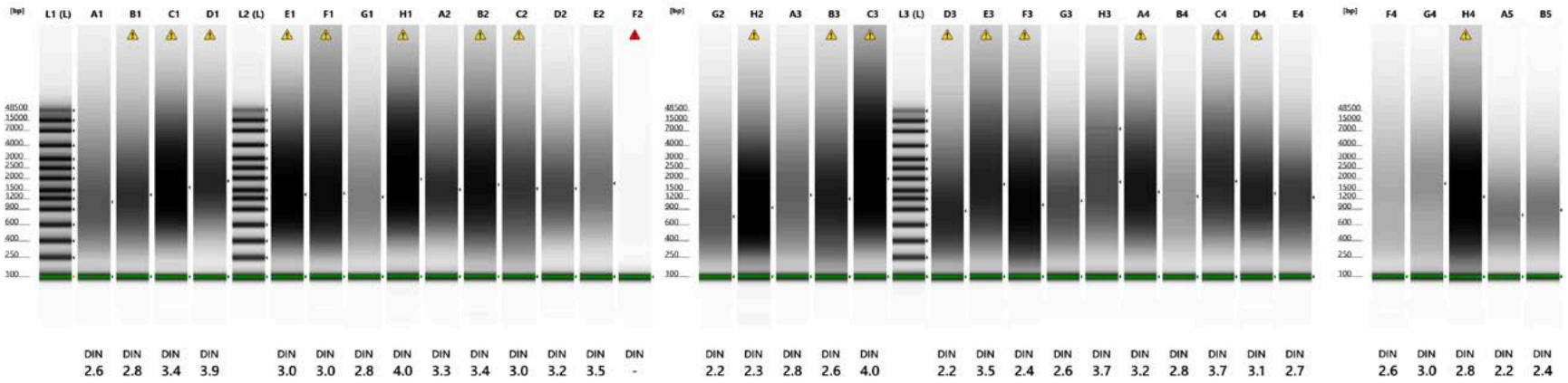

Figure 4.33. Agilent Genomic DNA ScreenTape analysis on FFPE gDNA submitted for targeted *G0S2* bisulfite sequencing.
Markers are loaded in lanes L1 (L), L2 (L), and L3 (L). All other lanes contain samples loaded with a 100 bp standard. DIN values are low and comparable to DIN values of samples analyzed in **Figure 4.31**. Analysis performed by Zymo Research Co.

We could obtain useable bisulfite sequencing data from all samples submitted for sequencing. We then performed unsupervised hierarchical clustering on targeted bisulfite sequencing data as in **Figures 4.11** and **4.17**. We could identify two distinct classes of *G0S2* Methylated and *G0S2* Unmethylated tumors, suggesting targeted assessment of *G0S2* methylation in FFPE-derived gDNA captures two classes of ACC akin to targeted assessment of *G0S2* methylation in frozen tissue (**Figure 4.34**).

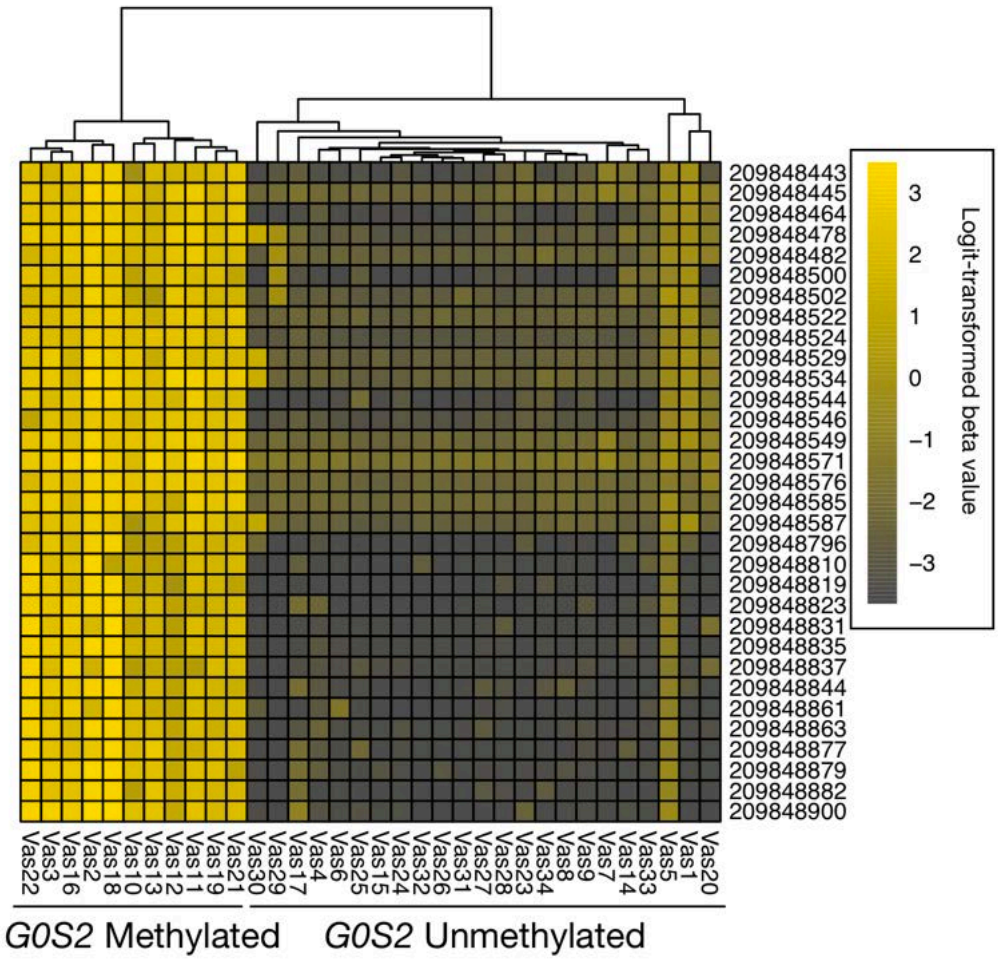

Figure 4.34. *G0S2* methylation status can be obtained from archival material.
Unsupervised complete hierarchical clustering using Euclidean distance on logit-transformed targeted bisulfite sequencing data from FFPE ACC samples (n=34) reveals two prominent clusters of samples – "*G0S2* Methylated" (left) and "G0S2 Unmethylated" (right) – analogous to the two clusters identified in ACC-TCGA and our independent cohort (**Figure 4.11**, **Figure 4.17**, same scale).

Finally, to verify that *G0S2* methylation status measured from FFPE-derived gDNA is indeed capturing CIMP status, we profiled two samples (Vas16 and Vas23) using the 850k array platform. As predicted by *G0S2* methylation status, Vas16 is CIMP-high while Vas23 is not (**Figure 4.35**).

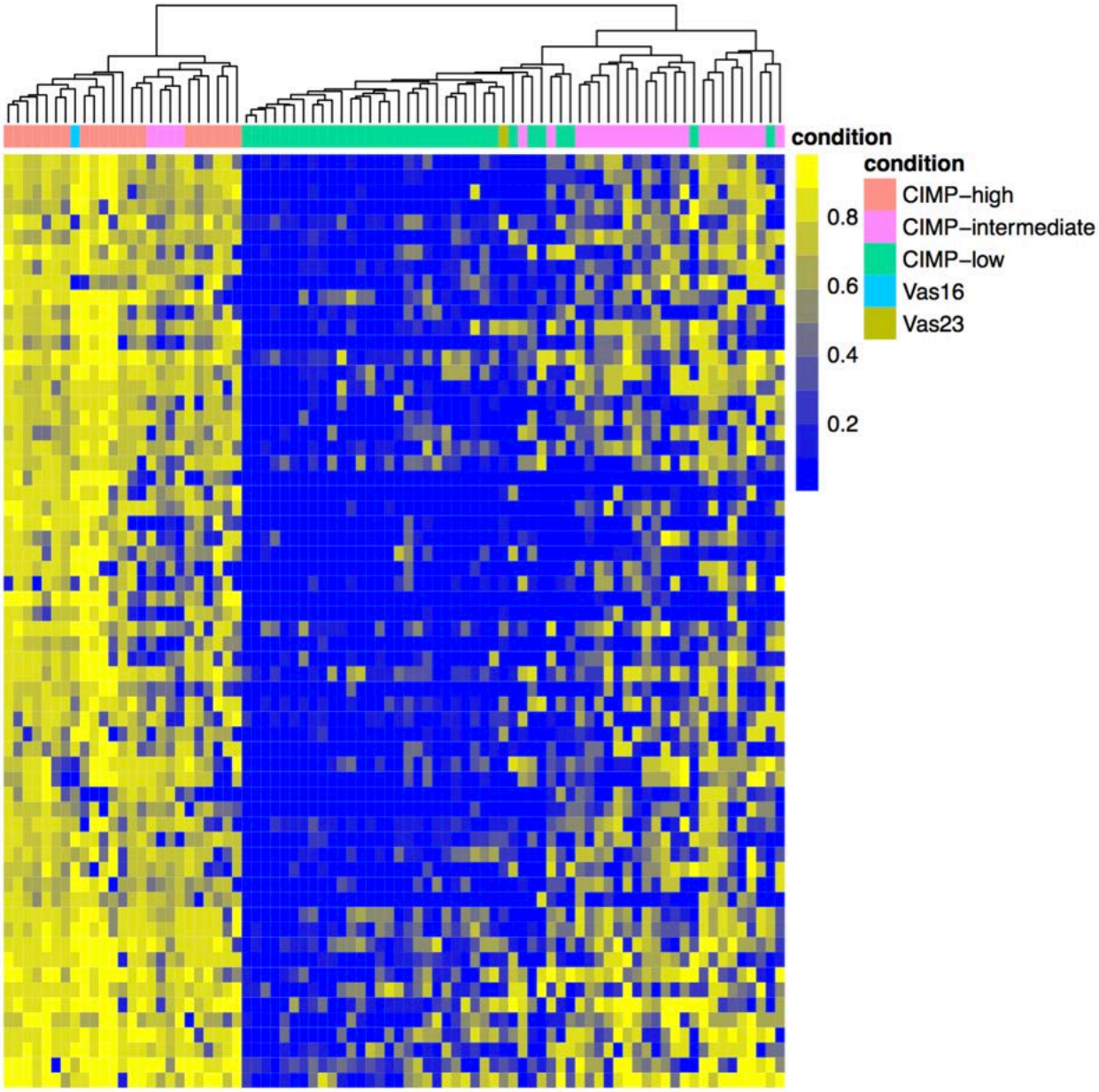

Figure 4.35. *G0S2* methylation status recapitulates genome-wide CIMP status in archival material. Heatmap depicting methylation status at CIMP-defining probes from ACC-TCGA (Zheng et al., 2016) demonstrates that the DNA methylation landscape of Vas16 clusters CIMP-high while that of Vas23 clusters with CIMP-low, as predicted by *G0S2* methylation status.

Taken together, these data expand the application of *G0S2* methylation to routinely available archival material and enable fast and inexpensive acquisition of CIMP-status for any patient with ACC worldwide.

4.9. Discussion

ACC is a rare cancer with variable outcomes inadequately stratified by clinical and histological metrics. ACC-TCGA identified 3 molecular subtypes of ACC and posited that clinical heterogeneity arises from unique transcriptional and epigenetic programs driving each class (Zheng et al., 2016). We noted that the genomes of rapidly recurrent carcinomas are characterized by aberrant methylation directed to promoter CpG islands, "CIMP-high." In this study, we also identified that CIMP-high carcinomas comprise a distinct molecular subtype of ACC, bearing upregulation of cell cycle- and DNA damage-associated cellular programs. However, prospective assessment of this complex signature is infeasible for routine molecular diagnostics.

Here, we identified that hypermethylation and silencing of *G0S2* is a hallmark of ACC-TCGA CIMP-high carcinomas. In an independent cohort, we determined that *G0S2* hypermethylation is restricted to 40% of ACC, absent from ACA and physiological tissues. We then demonstrated that measurement of *G0S2* methylation using a straightforward, overnight assay independently identifies a homogeneous subgroup of ACC patients with rapidly recurrent and fatal disease course. *G0S2* methylation is essentially binary (carcinomas are either *G0S2* Methylated or *G0S2* Unmethylated), subverting a requirement for complicated analytical strategies and reference samples. *G0S2*

hypermethylation almost invariably predicts rapidly recurrent and fatal disease in patients with localized, locoregional and disseminated ACC, including one third of patients with low grade disease. Interestingly, we observed only one patient with tumor *G0S2* hypermethylation who remains disease free >24 months following R0/RX resection. Given that adjuvant mitotane therapy is the standard of care at FMUSP and UM, our data suggests that *G0S2* hypermethylation predicts short-lived remission regardless, reinforcing the need to develop improved adjuvant therapies for high risk patients.

Expert opinion proposes that adjuvant cytotoxic chemotherapy should be considered as alternative to mitotane in high risk patients (Fassnacht et al., 2018; Varghese and Habra, 2017). However, a precise definition of "high risk" is lacking, relying on histological grade and subjective clinical assessment. Our study suggests that prospective assessment of *G0S2* methylation would objectively identify uniformly high risk patients. Additionally, we illustrated that *G0S2* methylation can be combined in series with validated biomarkers (*BUB1B-PINK1*) to stratify ACC into three groups, with uniformly favorable (recurrence free), intermediate, and uniformly dismal (inevitable recurrence) clinical outcomes. Such a strategy could dramatically improve clinical management and direct future trials on adjuvant therapies (**Figure 4.36**). The major ongoing clinical trial evaluating the efficacy of adjuvant mitotane in low-intermediate risk ACC ("ADIUVO," NCT00777244) defines risk using grade; our study suggests this criterion is inadequate, as up to one third of these patients will have tumor *G0S2* hypermethylation and likely recur on adjuvant mitotane. As new clinical trials are designed

to evaluate adjuvant therapies in high risk patients, we propose assessment of *G0S2* methylation to determine risk as in **Figure 4.36**.

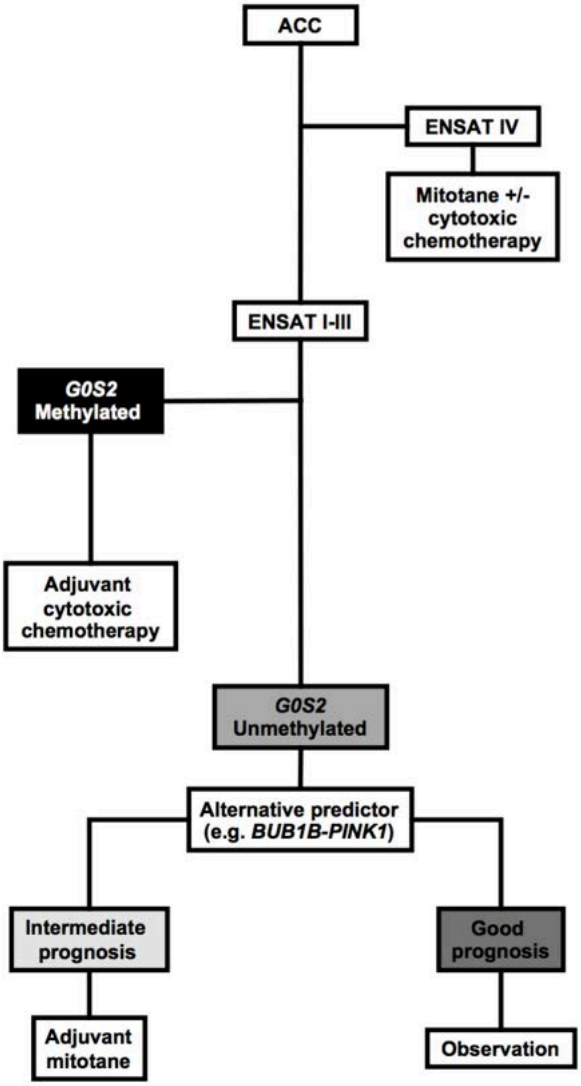

Figure 4.36. Proposed stratification and treatment workflow incorporating *G0S2* methylation and other molecular markers.
Patients with *G0S2* Methylated carcinomas have homogenously dismal outcomes, and are unlikely to exhibit durable response to adjuvant mitotane therapy. We therefore propose the evaluation of adjuvant cytotoxic chemotherapy in this subgroup. Alternative predictors such as *BUB1B-PINK1* facilitate stratification of patients with *G0S2* Unmethylated carcinomas, and enable identification of a subgroup with uniformly favorable prognosis. We propose observation for this subgroup of patients, restricting adjuvant mitotane to patients with intermediate prognosis. Proposed treatment decisions for patients with ENSAT I-III ACC will need to be evaluated in prospective clinical trials prior to incorporation into clinical practice.

High risk CIMP-high/*G0S2* Methylated ACC is associated with a unique transcriptional, copy number and mutational landscape in ACC-TCGA, suggesting a common biological program underlies this aggressive ACC subtype (Zheng et al., 2016). We demonstrated that CIMP-high carcinomas are chromosomally noisy, frequently bear somatic alterations leading to activation of cell cycle, and exhibit a transcriptional program characterized by increased expression of steroidogenic enzymes, proliferation machinery, and genes coordinating DNA damage-associated processes. Cell cycle and DNA damage-associated genes upregulated in CIMP-high ACC include *MELK, AURKB*, *CDK6*, *PLK1*, and *TOP2A* which have been successfully targeted in preclinical and translational models of ACC (Borges et al., 2017; Bussey et al., 2016; Fiorentini et al., 2018; Hadjadj et al., 2017; Kiseljak-Vassiliades et al., 2018b), and may even predict clinical responsiveness to combination therapy with etoposide, doxorubicin, cisplatin and mitotane (Roca et al., 2017). While there is currently little data to support a clinical trial evaluating utility of demethylating agents alone in ACC (Liu et al., 2004; Suh et al., 2010), studies in other solid tumors demonstrate that epigenetic priming with demethylating agents may increase efficacy of cytotoxic therapies and targeted DNA repair inhibitors (Matei et al., 2012; Matei et al., 2018; Pulliam et al., 2018). Together, these observations suggest that therapies targeting the cell cycle, DNA repair, and epigenetics may be efficacious in patients with CIMP-high/*G0S2* Methylated ACC and warrant future study.

The molecular mechanisms driving CpG island hypermethylation in *IDH1/2*-wild type cancers including CIMP-high ACC are poorly understood (Miller et al., 2016). One possible mechanism driving aberrant CpG island hypermethylation is evaluated **Chapter**

5. Our data and studies identifying *G0S2* hypermethylation in other cancer types (Chang et al., 2010; Tokumaru et al., 2004) suggest that methylation of this locus is driven by the same unknown molecular programs supporting hypermethylation in other regions of the CIMP-high cancer genome. However, the high expression of *G0S2* in lipid-rich tissues including the adrenal gland (**Figure 4.6**) suggests that *G0S2* may have tissue-specific tumor suppressor roles. While *G0S2* has been best characterized as a regulator of lipid metabolism (Yang et al., 2010), studies have demonstrated that methylation-dependent silencing of *G0S2* in breast cancer augments oncogenic PI3K/mTOR signaling (Yim et al., 2017) and MYC transcriptional activity (Yim et al., 2016). These studies suggest that *G0S2* may have important roles in adrenocortical biology, including a similar tumor suppressor function worthy of future investigation.

In conclusion, our study is the first to reduce the complex genome-wide CpG island hypermethylation signature from ACC-TCGA to a single, binary molecular marker, amenable to targeted assessment using routine molecular diagnostics. Assessing *G0S2* methylation as we have here is inexpensive, straightforward, compatible with a timeline feasible for clinical decision-making, and will enable the direction of efficacious adjuvant therapies for patients with uniformly aggressive ACC. Our ongoing and future studies are directed towards evaluating *G0S2* methylation prospectively, in circulating tumor DNA, and in readily available clinical samples including FFPE tissues (see section **4.8**).

4.10. Materials and methods

Data mining from ACC-TCGA. We downloaded the ACC-TCGA RNA-seq count table and raw data (IDAT files) from the Infinium HumanMethylation450 BeadChip ("450k") platform from the GDC legacy archive (https://portal.gdc.cancer.gov/legacy-archive). We used R (Team, 2016)/Bioconductor packages *limma* (Ritchie et al., 2015) and *minfi* (Aryee et al., 2014) to obtain $\log_2$-normalized counts per million (CPM) values for gene expression and beta and M values for methylation arrays. We used *limma* to nominate differentially expressed genes (Benjamini-Hochberg FDR-corrected p-value<0.05) between CIMP-high and non CIMP-high ACC. We used *goana* (Ritchie et al., 2015; Young et al., 2010) to identify gene ontology terms enriched among differentially expressed genes in CIMP-high vs. non-CIMP-high ACC. REVIGO (Supek et al., 2011) is an online tool that enables non-redundant visualization of large sets of GO terms based on semantic similarity. We used REVIGO with SimRel semantic similarity algorithm to plot the 200 most significant biological processes up (ranked by increasing P.Up, P.Up<0.05) or down (ranked by increasing P.Down, P.Down<0.05) in **Figure 4.4**. We used DMRcate (Peters et al., 2015) to interrogate differentially methylated regions (Stouffer-corrected p-value<0.05) across groups. We used logistic regression on the RNA-seq data to identify transcripts predictive of CIMP-high status. We used *pheatmap* (Kolde, 2018) to perform unsupervised complete hierarchical clustering, and *caret* (Kuhn et al., 2018) to perform k-fold cross validation.

Patients. Our study includes 114 adrenocortical tumors evaluated from 1989-2017. 42 treatment-naive primary ACC, 1 primary ACC from a patient who received neoadjuvant etoposide/doxorubicin/cisplatin+mitotane, 3 non-primary ACC, and 14 cortisol-secreting adrenocortical adenomas (ACA) are from Faculdade de Medicina da Universidade de São Paulo (FMUSP), São Paulo, Brazil; 38 primary ACC, 8 non-primary ACC, 4 aldosterone-secreting ACA, and 4 cortisol-secreting ACA are from the University of Michigan (UM), Ann Arbor, MI, USA. Diagnosis of ACA/ACC was established by expert pathological assessment (M.C.N.Z., T.J.G.) of surgical specimen using Weiss criteria (Weiss et al., 1989). Diagnosis of ACA or ACC was assigned to samples with Weiss score <3 or ≥ 3, respectively. Informed consent was obtained from all participants, and studies were conducted in accordance with the Declaration of Helsinki with study protocols approved by FMUSP and UM Institutional Review Boards. Clinical, hormonal, and demographic data were collected retrospectively.

Tissue processing, nucleic acid extraction, and quantification of gene expression from frozen samples.

FMUSP: Immediately following surgical resection, samples were collected by an institutional pathologist and snap frozen in liquid nitrogen. Frozen tumor tissue was cryotome sectioned (6 µm) under RNase-free conditions to acquire ≥ 30 mg tissue per sample. ≥ 3 random non-contiguous sections from each tumor were prepared for rapid hematoxylin and eosin (H&E) staining to evaluate sample quality and tumor purity. Samples with >50% acellular material in >2/3 sections were excluded from downstream

processing. Slides from samples included in downstream processing were assessed by T.J.G. to confirm typical ACC histology. Genomic DNA (gDNA) and total RNA were simultaneously extracted with AllPrep DNA/RNA Mini Kit (Qiagen, USA; Cat. No. 80204) and optional on-column RNase A (Qiagen, USA; Cat. No. 19101) and DNase I (RNase-free DNase Set, Qiagen, USA; Cat. No. 79254) digests, respectively.

UM: Samples collected immediately following surgical resection were snap frozen in liquid nitrogen, embedded in OCT freezing media (Miles Scientific, USA), cryotome sectioned (5 µm), and evaluated by routine H&E by surgical pathologists. When possible, corresponding H&E sections from paraffin blocks were also evaluated. Areas of pure tumor (≥70% tumor cells) were selected for nucleic acid extraction. gDNA and RNA were extracted using one of the following methods: TRIzol (Invitrogen/Thermo Fisher Scientific, USA; Cat. No. 15596026) with acid-phenol:chloroform cleanup, RNeasy Mini Kit (Qiagen, USA; Cat. No. 74104) or DNeasy Blood and Tissue Kit (Qiagen, USA; Cat. No. 69504), or AllPrep DNA/RNA/Protein Mini Kit (Qiagen, USA; Cat. No. 80004).

For all samples, RNA integrity was evaluated by agarose gel electrophoresis; purity (260/280, 260/230 ratios) and quantity of gDNA and RNA were measured by spectrophotometry (NanoDrop 2000 Spectrophotometer, Thermo Fisher Scientific, USA; Cat. No. ND-2000). cDNA was synthesized (High-Capacity cDNA Reverse Transcription Kit with RNase Inhibitor, Applied Biosciences/Thermo Fisher Scientific, USA; Cat. No. 4374966) from high integrity and high quality RNA (visual 28S:18S rRNA ratio 2:1 and

260/280 ratio≥2.00). Quantitative real-time polymerase chain reaction (qPCR) was performed in the QuantStudio 3 Real-Time PCR System (Applied Biosciences/Thermo Fisher Scientific, USA; Cat. No. A28136), using TaqMan Fast Advanced Master Mix (Applied Biosciences/Thermo Fisher Scientific, USA; Cat. No. 4444557) and FAM-MGB-labeled TaqMan Gene Expression Assays (Applied Biosciences/Thermo Fisher Scientific, USA) to evaluate expression of *G0S2* (Hs00274783_s1), *BUB1B* (Hs01084828_m1), *PINK1* (Hs00260868_m1), and housekeeping gene *GUSB* (Hs00939627_m1). TaqMan Gene Expression Assays were performed in triplicate. Gene expression levels were calculated using the ΔC_t method where $\Delta C_t(X)=C_t(X)-C_t(GUSB)$, and *BUB1B-PINK1* score calculated as $\Delta C_t(BUB1B)-\Delta C_t(PINK1)$.

Measurement of G0S2 methylation.

Targeted bisulfite sequencing: Assessment of *G0S2* methylation by targeted bisulfite sequencing in physiological tissues, ACA, and ACC was performed by Zymo Research Corporation, Irvine, CA, USA. Zymo Research Co. designed/validated primers to amplify the G0S2 locus, chr1:209,848,443-chr1:209,848,900 (hg19), using a proprietary pipeline. Submitted gDNA with 260/280≥1.7, intact genomic band (≥5 kb) by gel electrophoresis, and sufficient quantity (≥100 ng) was subject to bisulfite conversion, targeted amplification, next generation sequencing library indexing, and sequencing on Illumina MiSeq. Sequence data was demultiplexed and assessed for bisulfite conversion rate, read coverage, mapping efficiency, and CpG coverage. Bisulfite conversion rate was

≥99% for all samples. Average CpG coverage ranged from 5,000-50,000X. Methylation at each CpG was calculated from the ratio of methylated to total CpG count.

Methylation-sensitive restriction digest/qPCR: Available gDNA from ACC and ACA was subject to methylation-sensitive restriction digestion using EpiTect II DNA Methylation Enzyme Kit (Qiagen, USA; Cat. No. 335452). This kit contains two enzymes: Methylation Sensitive Enzyme A (cannot cleave gDNA in the presence of CpG methylation in the proprietary restriction site) and Methylation Dependent Enzyme B (can cleave gDNA only in the presence of CpG methylation in the proprietary restriction site). Per manufacturer protocol, gDNA from each tumor was subject to four digests: "mock" digest (M_o, containing no restriction enzymes), methylation-sensitive digest (M_s, containing only Enzyme A), methylation-dependent digest (M_d, containing only Enzyme B), and double digest (M_{sd}, containing both enzymes). To measure intact gDNA following overnight restriction digestion, gDNA was amplified by qPCR using the EpiTect Methyl II PCR Primer Assay for Human G0S2 (Qiagen, USA; Cat. No. EPHS101235-1A) and RT² SYBR Green ROX qPCR Mastermix (Qiagen, USA; Cat. No. 330521). Percent *G0S2* methylation was calculated arithmetically from M_o, M_s, M_d, and M_{sd} C_t values according to manufacturer instructions, using a Microsoft Excel spreadsheet provided by Qiagen.

Tissue processing and genomic DNA extraction from FFPE samples.

Tissue processing and gDNA extraction: FFPE blocks were microtome sectioned, with first few sections discarded. Either 4 x 20 µm scrolls (for pilot study depicted in **Figures**

4.31 – 4.32, Table 4.7) or 4 x 10 µm scrolls (for study described in **Figures 4.33 – 4.35**) were collected in a microcentrifuge tube and stored at 4°C until nucleic acid extraction. Pilot study samples were processed for gDNA extraction using the Quick-DNA FFPE Kit (Zymo, USA; Cat. No. D3067) with overnight Proteinase K digestion and without use of isopropanol. Other samples were processed for simultaneous gDNA/mRNA extraction using the Qiagen AllPrep DNA/RNA FFPE Kit (Qiagen, USA; Cat. No. 80234) using xylene for deparaffinization and optional on-column RNase A (Qiagen, USA; Cat. No. 19101) and DNase I (RNase-free DNase Set, Qiagen, USA; Cat. No. 79254) digests.

***Measurement of* G0S2 *methylation and CIMP status from FFPE samples*.**

Methylation-sensitive restriction digest/qPCR: Assessment of *G0S2* methylation by the EpiTect system (Qiagen, USA) was performed as previously described.

Targeted bisuflite sequencing: Assessment of *G0S2* methylation by targeted bisulfite sequencing was performed by Zymo Research Corporation, Irvine, CA, USA as previously described.

850k array profiling: Extracted FFPE-derived gDNA was submitted to Diagenode Epigenomic Services, Denville, NJ, USA for FFPE restoration and 850k array profiling. DNA was deaminated using EZ-96 DNA Methylation Kit (Zymo Research) following Illumina recommendations. Bisulfite conversion was controlled by qPCR as follows: one assay targeting a methylated region of *DNAJC15* and two assays targeting *GNAS* (one

assay for the unmethylated allele and one assay for the methylated allele) were used for quality control. Deaminated DNA derived from blood were amplified in parallel, and a sample passed quality control when the measured C_t for the two *GNAS* loci or *DNAJC15* is within 5 C_t of the positive control. Data was analyzed as described in **Chapter 3**.

Statistical analysis. We used Chi-square test to evaluate associations between categorical variables, Mann-Whitney test or Pearson correlation to compare continuous data from 2 groups, and Kruskal-Wallis with Dunn's multiple comparisons test to compare continuous data from >2 groups. We used *pheatmap* (Kolde, 2018) to perform unsupervised complete hierarchical clustering. We used *caret* (Kuhn et al., 2018) to perform k-fold cross validation. We used receiver operating characteristic (ROC) curve analysis to estimate a cutoff of G0S2 expression that predicts methylation. We used Kaplan-Meier analysis with pairwise log-rank test to compare overall survival (OS) and disease-free survival (DFS), and Cox proportional hazards regression models to estimate hazard ratios for clinical/molecular variables. p-value<0.05 was significant for all analyses. Statistical analyses were performed in GraphPad Prism, MedCalc, and R (Team, 2016).

CHAPTER 5. DNA Hypermethylation is Directed to PRC2 Targets and Propagated Independently of PRC2 in CIMP-high ACC

5.1. Disclosure of relevant publications

Portions of this work are being prepared for publication:

> **Mohan DR**, Borges KS, Finco I, LaPensee CR, Solon A, Rege J, Little III DW, Else T, Almeida MQ, Apfelbaum A, Vinco M, Wakamatsu A, Mariani BMP, Latronico AC, Mendonca BB, Zerbini MCN, Fragoso MCBV, Lawlor ER, Ohi R, Rainey WE, Venneti S, Marie SKN, Giordano TJ, Breault DT, Lerario AM*, Hammer GD*. A differentiation program coordinated by SF1/β-catenin is a targetable epigenetic vulnerability in aggressive adrenocortical carcinoma. In preparation. *co-senior author
>
> Lerario AM*, **Mohan DR***, Rege J, Rainey WE, Hammer GD. Meta-analysis of adrenocortical tumors identifies cell of origin programs derailed in tumorigenesis and malignancy. In preparation. *co-first author

5.2. Introduction

CpG island hypermethylation (CIMP-high status) defines a homogeneous molecular subtype of ACC with uniformly dismal clinical outcomes (**Chapter 4**). After developing a biomarker-based strategy enabling prospective identification of CIMP-high (**Chapter 4**), we sought to better understand the molecular programs supporting aberrant epigenetic patterning. Here, we describe our efforts to investigate the etiology of the CIMP-high, through profiling a spectrum of adrenocortical tumors and taking advantage of the NCI-H295R cell line as a definitive *in vitro* model of this molecular subtype (**Chapter**

3). We identify that DNA hypermethylation is directed to PRC2 targets in a cancer-specific manner, refute the long-standing model that PRC2 is coordinating DNA hypermethylation (Viré et al., 2006), and present work suggesting that DNA hypermethylation of these regions instead disrupts PRC2 recruitment genome-wide. PRC2 catalytic activity is preserved in CIMP-high ACC, and required for NCI-H295R viability and sustained proliferation. EZH2 inhibition derepresses PRC2 targets, but surprisingly induces profound changes in the epigenetic landscape and cellular transcriptome. These data ultimately converge on the idea that the functional requirement for PRC2 members and catalytically active PRC2 in CIMP-high ACC may extend far beyond canonical PRC2 functions.

5.3. DNA hypermethylation in CIMP-high ACC is directed to PRC2 targets

To better understand the mechanisms supporting aberrant DNA methylation, we performed Gene Set Enrichment Analysis (GSEA, (Mootha et al., 2003; Subramanian et al., 2005)) on genes whose promoters are targeted for hypermethylation in CIMP-high vs. non-CIMP-high ACC (obtained by annotating DMRcate regions from **Chapter 4**). As is the case for many CIMP-high cancers given the nature of CpG islands (**Chapter 1**) We identified a significant enrichment for promoters bound by PRC2 in embryonic and neural precursor cells (**Figure 5.1**). Indeed, CIMP-high hallmark gene *G0S2* is also an embryonic PRC2 target (**Figure 5.2**).

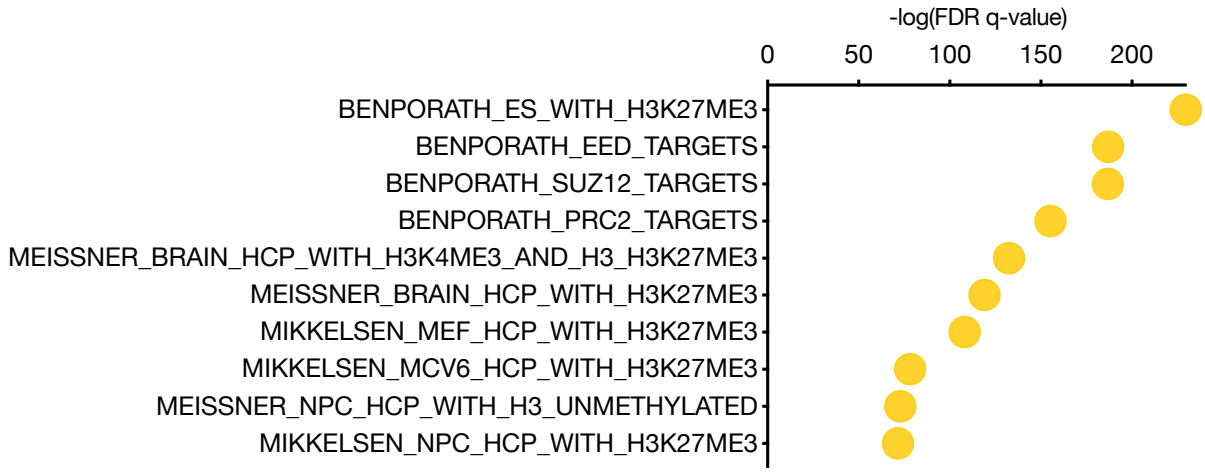

Figure 5.1. Hypermethylation is directed to PRC2 targets in CIMP-high ACC.
Annotated significant (FDR-corrected p-value < 0.05) DMRcate regions (from **Chapter 4**) were filtered to include only regions overlapping with promoters. Regions were ranked by descending mean difference in DNA methylation (beta fold change), and top 2084 gene identifiers (1994 NCBI Entrez Gene IDs, the maximum) were evaluated for enrichment with curated collections in GSEA (Mootha et al., 2003; Subramanian et al., 2005). Top ten most significant gene sets shown, revealing overlap of hypermethylated regions in CIMP-high ACC with promoter CpG islands bound by PRC2 in embryonic and neural precursor cells. HCP = high-CpG-density promoter.

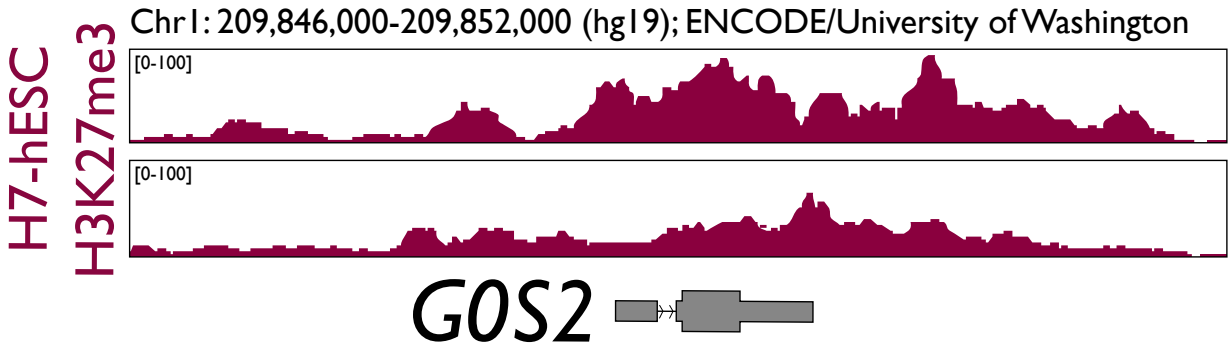

Figure 5.2. *G0S2* is a PRC2 target in human embryonic stem cells.
Examination of H3K27me3 signal at the *G0S2* locus in ChIP-seq from H7 human embryonic stem cells (H7-hESC) deposited in ENCODE demonstrates a broad and rolling H3K27me3 domain encompassing *G0S2* locus and CpG island. The precise location of the *G0S2* CpG island relative to the transcript is depicted in **Figure 4.5.**

Given the possibility that PRC2 has highly tissue-specific roles (**Chapters 1 – 2**) and that these roles may influence DNA methylation patterns (Yagi et al., 2020), we wanted to determine if differential PRC2 target methylation could be explained by tumor

cell type heterogeneity. However, ACC are among the most stromally poor cancers in ACC-TCGA (average purity ~80%; (Zheng et al., 2016)) and CIMP-high and non-CIMP-high ACC are comparably pure (**Figure 5.3**), suggesting that PRC2 target methylation reflects a cancer cell-specific program.

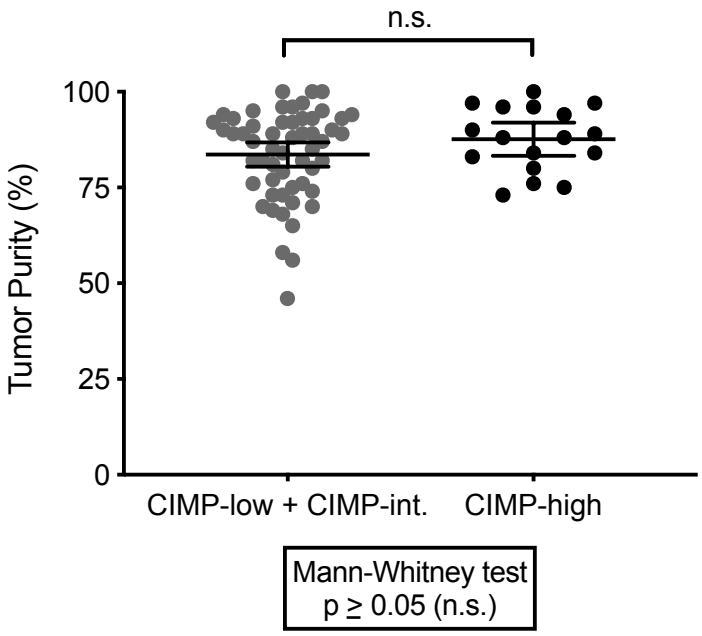

Figure 5.3. CIMP-high and non-CIMP-high ACC are comparably pure.
ACC-TCGA tumor purity plotted by CIMP status (Zheng et al., 2016) reveals CIMP-high and non-CIMP-high ACC are comparably pure. Mean and 95% confidence interval of the mean represented by the line and bars, respectively.

We then speculated that aberrant DNA methylation in CIMP-high ACC may serve a primary role of silencing gene expression (as is true for the *G0S2* locus, **Chapter 4**), and that DNA methylation may potently silence PRC2 targets to maintain sustained proliferation potential (**Chapter 1**, **Table 1.7**). We plotted the fold change in methylation of differentially methylated promoters between CIMP-high and non-CIMP-high ACC versus the corresponding change in gene expression (**Figure 5.4**).

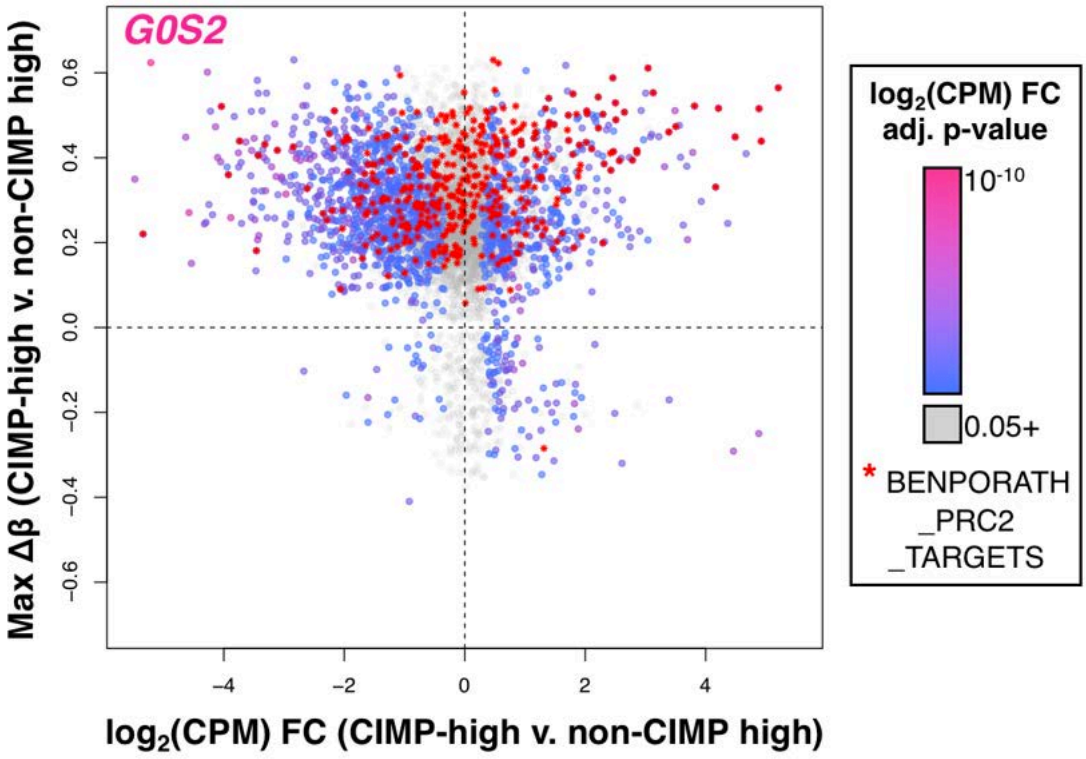

Figure 5.4. Promoter CpG island hypermethylation does not coordinate gene expression as a general mechanism in CIMP-high ACC.
Scatterplot depicts max change in DNA methylation (max beta fold change) between CIMP-high and non-CIMP-high ACC at promoter DMRcate regions (queried by GSEA in **Figure 5.1**) versus corresponding $\log_2$ of the fold change in gene expression (measured by counts per million, CPM) between CIMP-high and non-CIMP-high ACC, color-coded by the p-value for the fold change in gene expression. Genes that were not differentially expressed appear as grey dots. PRC2 targets (from BENPORATH_PRC2_TARGETS set (Ben-Porath et al., 2008) deposited in GSEA) are indicated by the red stars on the plot. *G0S2*, the left-corner-most point in the top left quadrant, is among few genes in which promoter CpG island hypermethylation completely shuts down gene expression.

This analysis revealed that, as expected, the vast majority of differentially methylated promoters in CIMP-high ACC are hypermethylated. Intriguingly, despite the strong discriminatory power of *G0S2* methylation/silencing in identifying CIMP-high ACC (**Chapter 4**), promoter CpG island hypermethylation was not uniformly correlated with decreased gene expression. This was also true of embryonic PRC2 targets, which were invariably targeted for hypermethylation but had variable (if any) change in gene

expression. Considering that, physiologically, many PRC2 targets should be repressed by the PRC2 and expressed at low levels in somatic cells (**Chapter 1**), these data are consistent with the idea that PRC2 target DNA methylation may have induced an epigenetic class switch (for example, H3K27me3 is now exchanged for alternative repressive markers, e.g. DNA methylation and H3K9me3 (Gal-Yam et al., 2008; Ohm et al., 2007)), or that PRC2 collaborates with DNA methyltransferases to write DNA methylation (Viré et al., 2006) at sites of the genome that already exhibit PRC2-dependent repression. What this analysis does not rule out, however, is the possibility that somatic adrenocortical tissue acquire profound DNA methylation of PRC2 targets and that PRC2 target methylation in CIMP-high ACC is simply a cell-of-origin phenomenon. Indeed, PRC2 targets may gain methylation passively in physiological and premalignant tissues (Tao et al., 2019; Vaz et al., 2017) despite that these regions are evolutionarily protected from hypermethylation (Long et al., 2016). We suspected that somatic adrenocortical PRC2 target hypermethylation was unlikely given that *G0S2* methylation was exclusive to malignant tissue and absent from non-CIMP-high ACC with putative adult adrenocortical origin (**Chapter 4**). However, to address this question more completely, we profiled the DNA methylation landscape of a small cohort of fetal adrenal and adult adrenal cortex and examined the DNA methylation of PRC2 target promoter CpG islands (**Figure 5.5**).

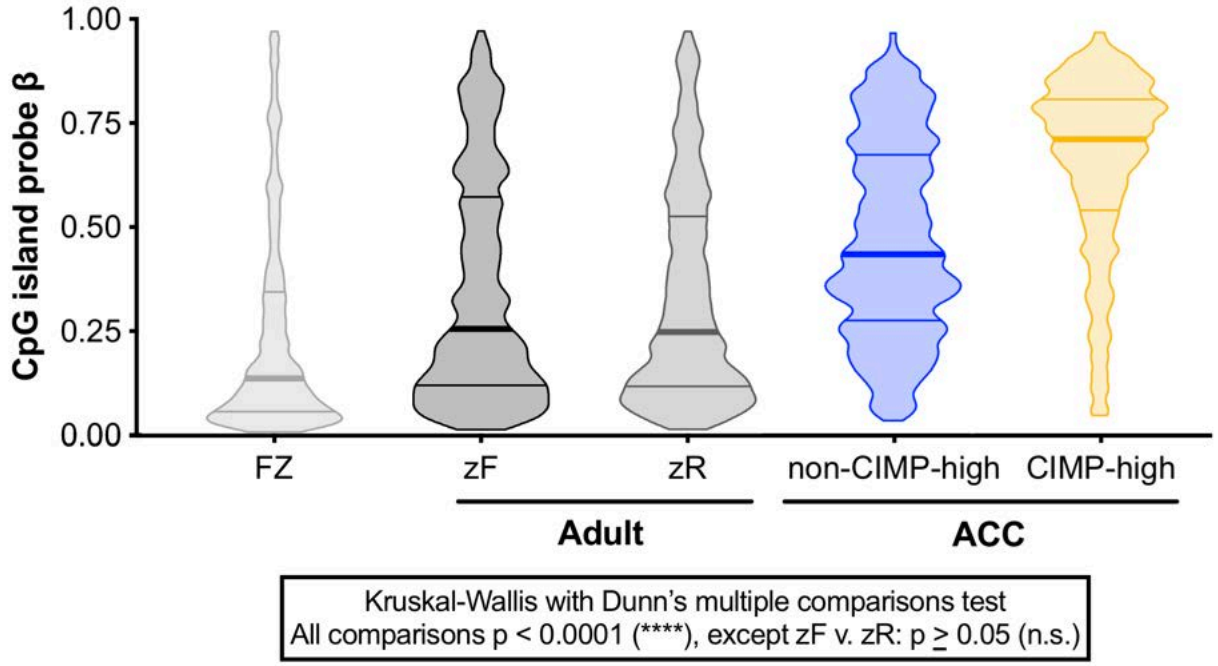

Figure 5.5. DNA hypermethylation of PRC2 targets reverses physiological adrenal epigenetic programming.
Violin plot depicting distribution of PRC2 target CpG methylation measured by Illumina 850k or 450k methylation array in fetal adrenal (n = 3), adult adrenal (zF, zR; n = 4 each) and ACC from ACC-TCGA (n=79, (Zheng et al., 2016)) reveals that PRC2 targets are protected from methylation in physiology and targeted for methylation in CIMP-high ACC.

This study demonstrated that most PRC2 targets gain small amounts of passive methylation in adult tissue, but as a class are still protected from methylation in physiological adrenal cortex. In contrast, PRC2 targets are deprotected in non-CIMP-high ACC and are uniformly targeted for methylation in CIMP-high tumors. These data suggest that, similarly to *G0S2* methylation, global PRC2 target hypermethylation in CIMP-high ACC is a cancer-specific phenomenon likely mediated by cancer-specific programs (such as those proposed in **Table 1.7**). Cancer-specific CpG island hypermethylation may be directed by catalytically active PRC2 (Viré et al., 2006) or act as a mechanism to disrupt PRC2 function (Bayliss et al., 2016). Furthermore, cell-cycle-dependent upregulation of EZH2 might lead to a novel EZH2 function (**Table 1.7**). We therefore next asked if EZH2

is upregulated and engaged in canonical programs in CIMP-high ACC, and then sought to determine if catalytically active PRC2 directs or is disrupted by DNA methylation.

5.4. EZH2 is nuclear, upregulated in CIMP-high ACC and coupled to H3K27me3

We evaluated expression of *EZH2* mRNA and cell cycle markers in ACC-TCGA and an independent cohort of benign and malignant tumors (same cohort as is described in **Chapter 4**) stratified by CIMP-status (**Figure 5.6**).

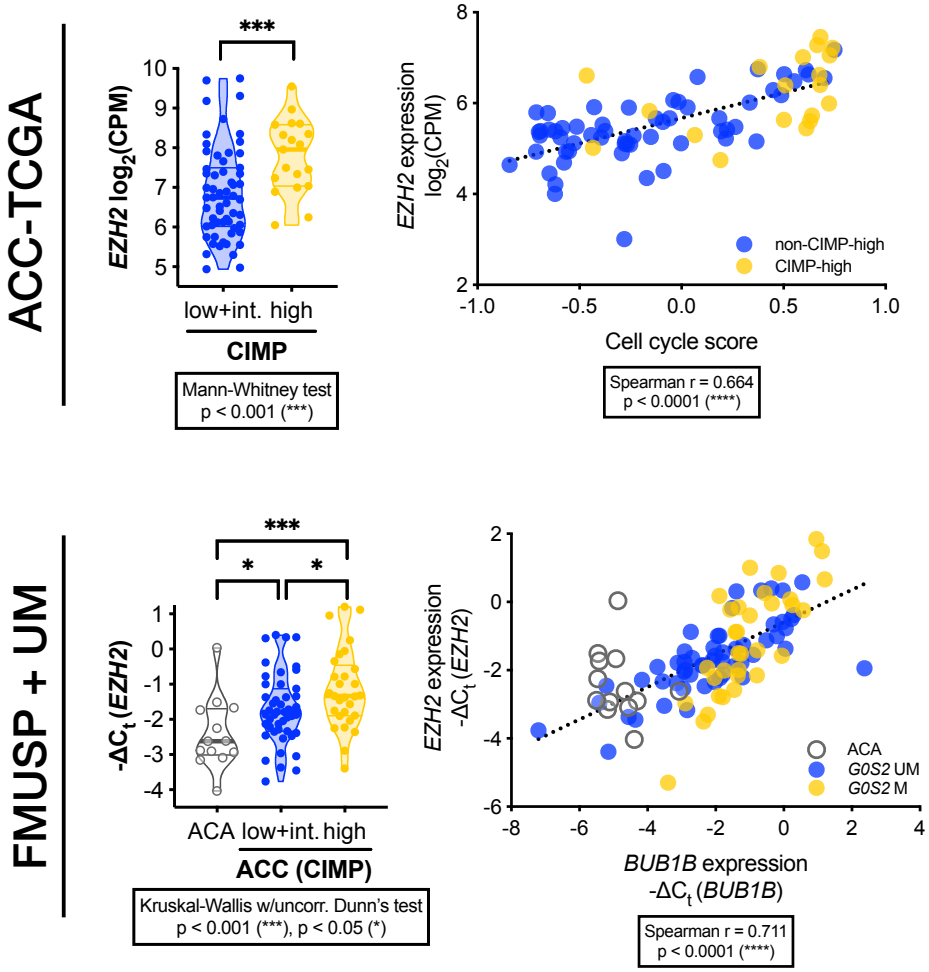

Figure 5.6. *EZH2* is upregulated in a cell-cycle-dependent manner in CIMP-high ACC.
Evaluation of *EZH2* expression in ACC-TCGA (n = 78, (Zheng et al., 2016) top row, left column) and our independent cohort (n = 102, FMUSP+UM, bottom row, left column; this is the same cohort as described in **Chapter 4**) reveals that *EZH2* is upregulated in CIMP-high ACC compared to non-CIMP-high ACC and benign adrenocortical tumors (ACA). *EZH2* expression in ACC-TCGA samples is strongly correlated to cell cycle score, a signature of co-regulated cell cycle dependent genes that we identified by Independent Component Analysis (Biton et al., 2014) on ACC-TCGA data (described in more detail in the caption for **Figure 6.6**). *EZH2* expression is also strongly correlated to the expression of cell cycle gene *BUB1B* in the FMUSP+UM cohort (**Chapter 4**). These findings are not necessarily surprising, as CIMP-high tumors frequently possess cell cycle alterations (**Chapters 3 – 4**) and *EZH2* is correlated with cell cycle activation across TCGA (**Figure 1.3**).

As expected given the proliferative programs that prevail CIMP-high tumors (**Chapters 3 – 4**), *EZH2* was expressed higher in CIMP-high ACC than in non-CIMP-high ACC and benign lesions. *EZH2* expression was also highly cell-cycle-dependent,

consistent with known mechanisms of regulation of *EZH2* (Bracken et al., 2003) and other epigenetic modifiers across all TCGA (**Figure 1.3**). To determine if EZH2 was participating in canonical PRC2-dependent functions in ACC, we evaluated expression of EZH2 and H3K27me3 by IHC in a tissue microarray of benign and malignant adrenocortical tumors. We also evaluated expression of Ki-67, a classical proliferation marker used to stratify ACC (Beuschlein et al., 2015). We observed that EZH2 was nuclear, upregulated in ACC, correlated with Ki-67, and predictive of poor clinical outcomes, consistent with higher expression of EZH2 in CIMP-high tumors (data not shown). We also observed that high EZH2 (above median for ACC, which was also higher than the EZH2 expression we observed in benign tissue) was coupled to high levels of H3K27me3 (**Figure 5.7**). Taken together, these data suggest that EZH2 is catalytically active on histone substrates in CIMP-high ACC, despite PRC2 target DNA hypermethylation. Given that EZH2 requires incorporation into the core PRC2 to possess catalytic activity (**Table 1.5**), this data also suggested that a major role of EZH2 in ACC is PRC2-dependent, contrary to reports with fewer or no patient samples (Drelon et al., 2016a; Tabbal et al., 2019).

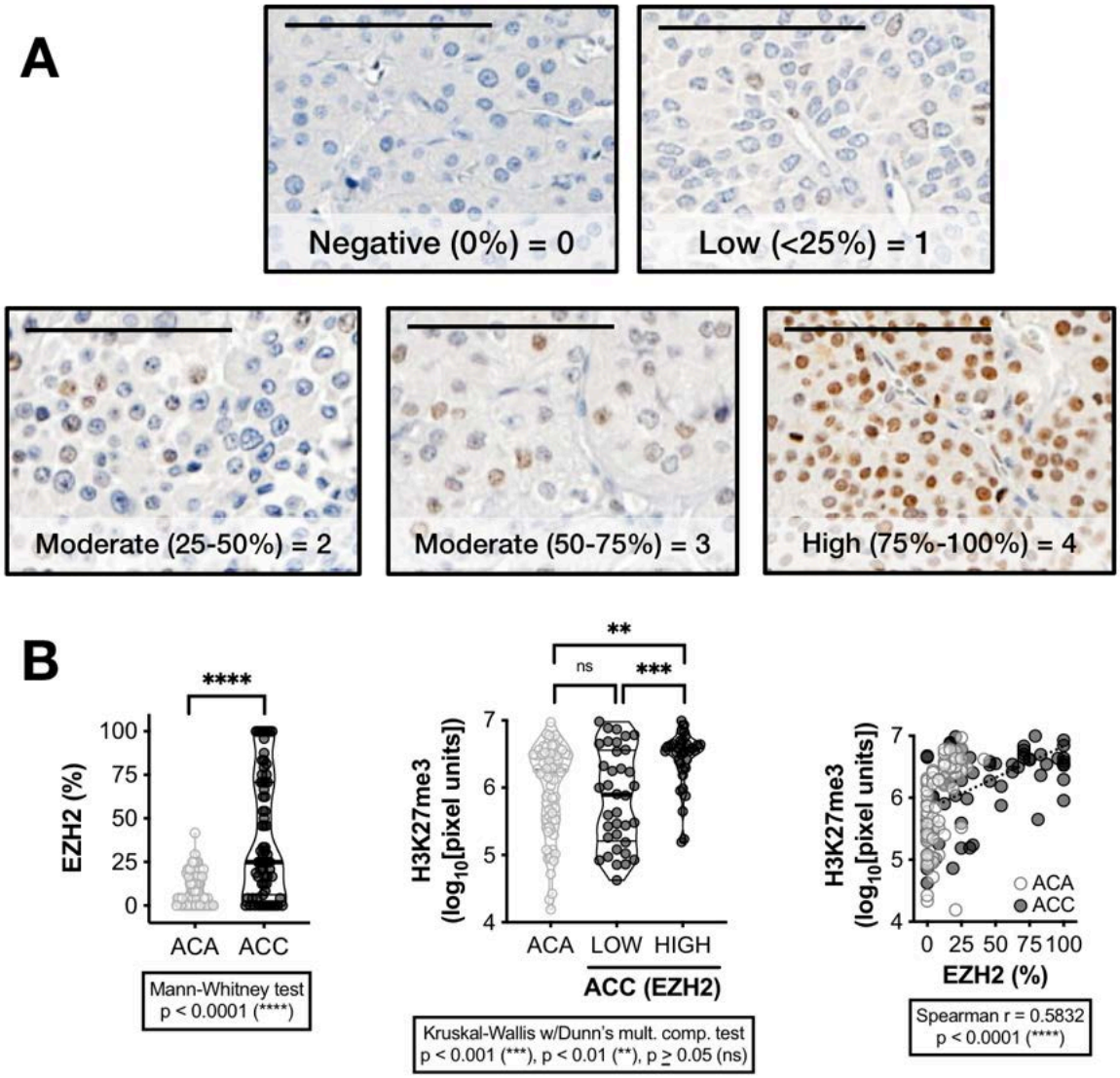

Figure 5.7. High EZH2 expression is coupled to H3K27me3 in ACC.
Tissue microarray of benign (ACA, n = 74) and malignant (n = 74) adrenocortical tumors (3 replicates per sample) was stained for EZH2 and H3K27me3. EZH2 was quantified on a 0-4 scale based on % positive nuclei by two independent observers (A) and averaged across replicates. EZH2 is expressed at much higher levels in ACC compared to ACA (B, left). H3K27me3 staining was quantified by MATLAB as in (Bayliss et al., 2016). H3K27me3 was higher in ACC with above median EZH2 positivity (B, middle), and was strongly correlated to EZH2 positivity (B, right). Not shown, *EZH2* mRNA/protein are correlated ($r = 0.5117$, $p < 0.01$; Spearman). Bar in panel A = 100 µm.

5.5. Inhibition of EZH2 catalytic activity is associated with dose-dependent loss of viability and diminishes sustained proliferation potential

We then sought to evaluate if EZH2 and its catalytic activity were required for sustained proliferation in CIMP-high ACC, taking advantage of the NCI-H295R cell line as our model system (**Chapter 3**). We first treated NCI-H295R with a variety of SAM-competitive and allosteric EZH2/PRC2 inhibitors (EZH2i) for a duration corresponding to approximately 1.5 doublings and observed that all EZH2 inhibitors induced loss of viability in a dose-dependent manner, preceded by a reduction in H3K27me3. In contrast, siRNA-dependent near complete knockdown of *EZH2* for a duration corresponding to 2.5 doublings induced only a mild reduction in viability and H3K27me3, suggesting that PRC2, and not EZH2 is essential for cellular proliferation, **Figure 5.8**.

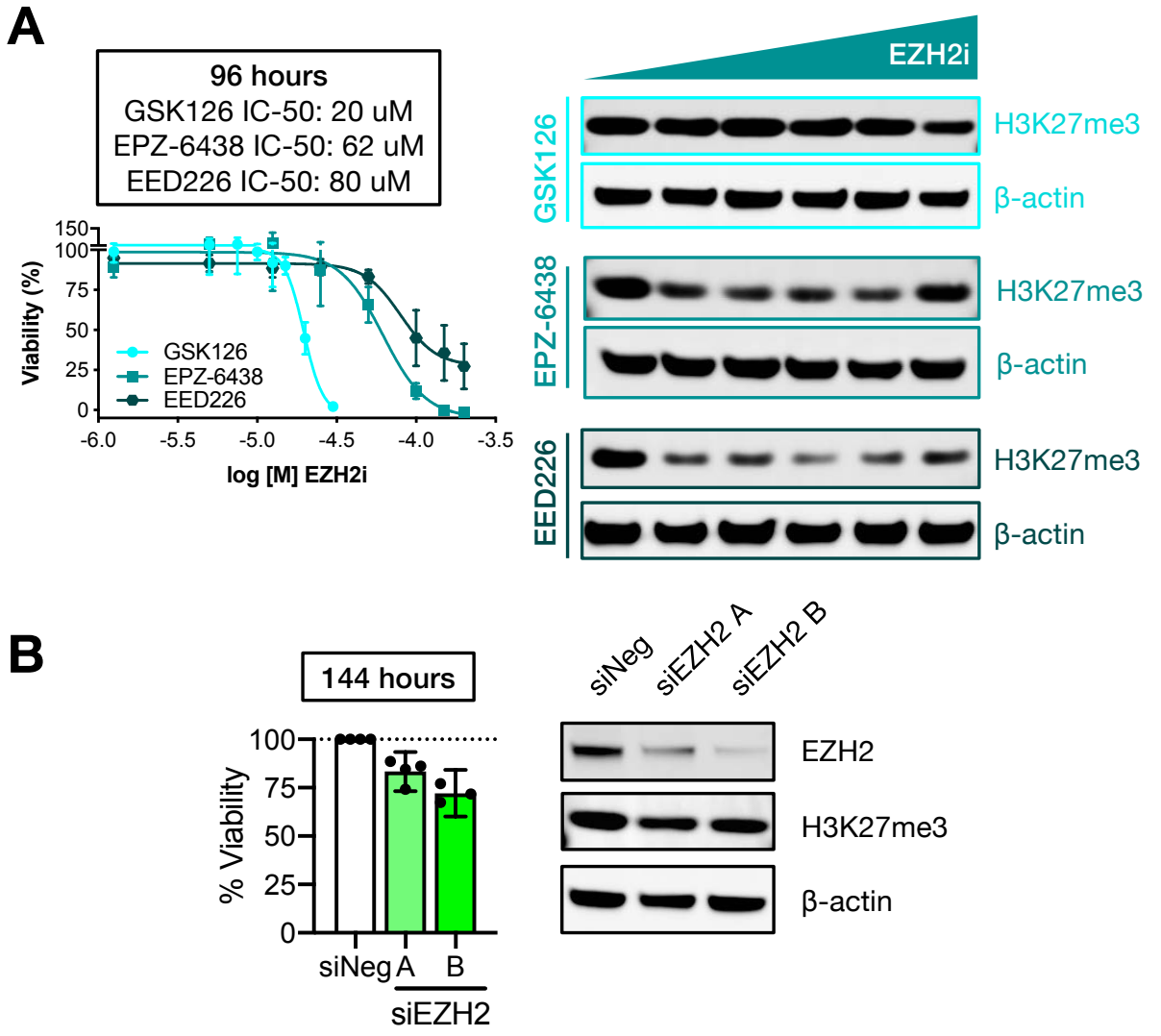

Figure 5.8. Inhibition of PRC2 catalytic activity induces dose-dependent reduction in NCI-H295R viability.

A. NCI-H295R were treated with different classes of EZH2i for 96 hours (EPZ-6438 and GSK126 are SAM-competitive EZH2i, and EED226 is an allosteric EZH2i), and harvested for measurement of viability by alamarBlue (n = 4) or evaluation of H3K27me3 by western blot. 96 hour EZH2i causes a dose-dependent reduction in viability preceded by depletion of H3K27me3. For western blot, right, increasing doses of EZH2i were tested up to the IC-50 dose. The doses tested from left to right are as follows. GSK126: 0, 1.25 μM, 5 μM, 7.5 μM, 15 μM, 20 μM (IC-50); EPZ-6438: 0 μM, 1.25 μM, 12.5 μM, 25 μM, 50 μM, 62 μM (IC-50); EED226: 0 μM, 1.25 μM, 12.5 μM, 25 μM, 50 μM, 80 μM (IC-50). B. NCI-H295R were transfected at 0 hrs and 72 hrs with siRNA directed against *EZH2* (siEZH2) or scrambled negative control (siNeg), and harvested at 144 hours for assessment of viability by alamarBlue (left, n ≥ 3) and EZH2/H3K27me3 by western blot (right). Left, mean is represented by the height of the bar and 95% confidence interval of the mean is represented by the whiskers. For both A and B, β-actin serves as a loading control. Representative western blots shown, n ≥ 2. Note, NCI-H295R doubling time is ~60 hours (consistent with literature, experiments, and estimated from baseline G1/S/G2/M cell cycle distribution, data not shown). Time points selected are adequate to measure replication dilution of H3K27me3.

To determine if PRC2 coordinates a heritable epigenetic program required for sustained proliferation, we plated equal numbers of EZH2i-pre-treated viable cells for a two-dimensional colony forming assay in complete medium without EZH2 inhibitors. Colony forming assays are a classical experiment to examine two key hallmarks of cancer – the ability to survive low density plating, and sustained proliferation potential (Franken et al., 2006; Hanahan and Weinberg, 2000, 2011). In such an experiment, low numbers of cells are plated at single-cell density, such that the progeny of only one cell gives rise to one colony; therefore, colony size and number are indicative of both colony plating efficiency and proliferation capacity. We observed, strikingly, that EZH2i pretreatment, even at doses that do not induce loss of viability, diminished colony formation and survival in a dose-dependent manner for at least one month after drug administration (**Figure 5.9**). These data suggest that EZH2i induces heritable changes in the cellular epigenome that disrupt sustained proliferation potential in this *in vitro* model of CIMP-high ACC.

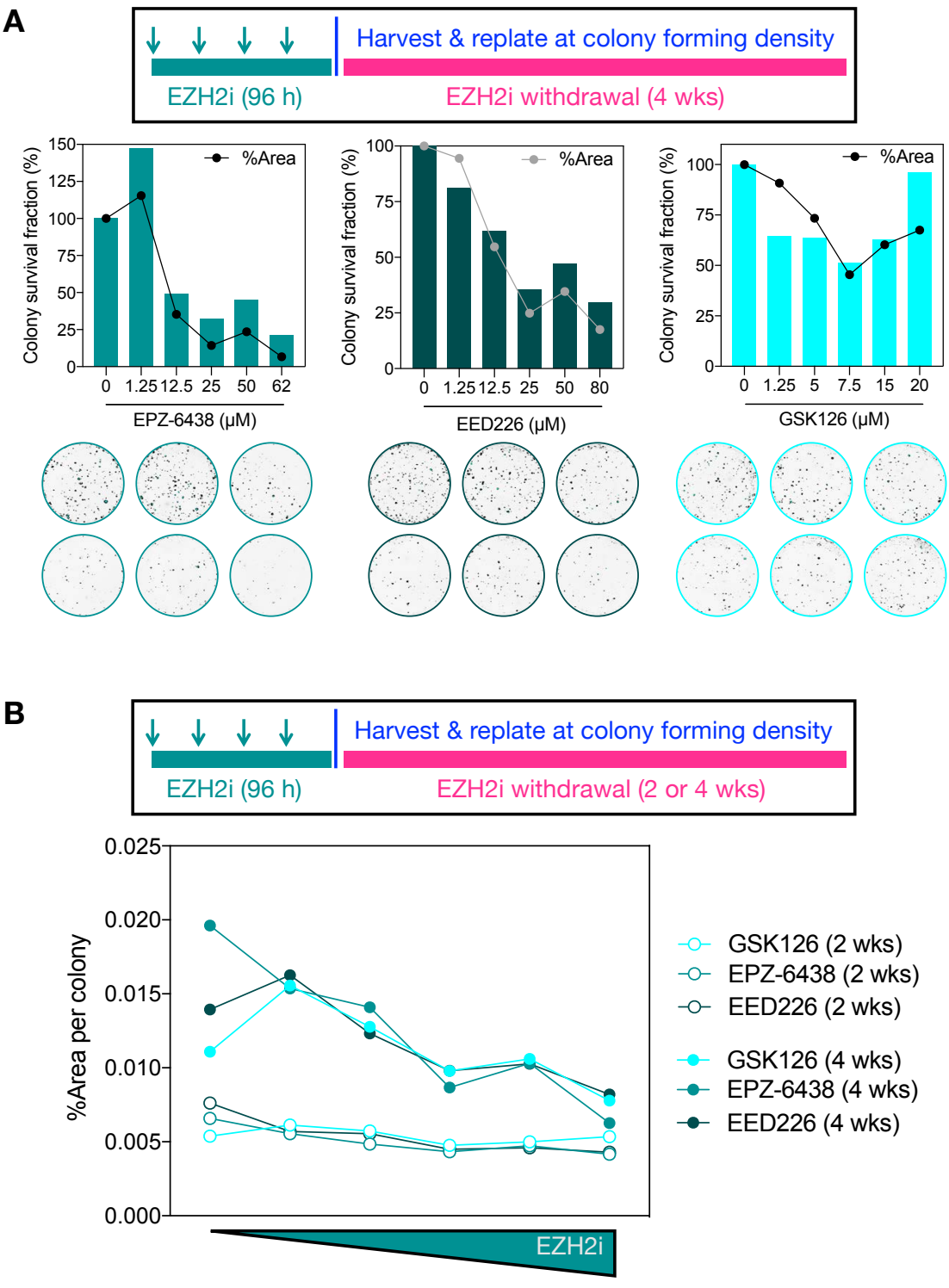

Figure 5.9. EZH2i induces heritable changes in colony formation and survival.
NCI-H295R were pre-treated with different classes of EZH2i for 96 hours at increasing doses, where the maximum doses tested were the determined IC-50 for each class of drugs. Following EZH2i administration, equal numbers of viable cells were plated at colony forming density in medium free of EZH2i. Colonies were grown out for 2 or 4 weeks. In A, EZH2i pre-treatment resulted in a dramatic reduction in colony survival

fraction (number of colonies in drug treatment vs. corresponding vehicle) and total plate area covered by colonies at 4 weeks, even at doses that were well below the IC-50 for all three drugs. Well images are shown below each bar graph (maximum administered concentration in bottom right corner and vehicle in top left corner). In B, 2 weeks following EZH2i, minimal changes in colony size could be observed. However, at 4 weeks following EZH2i, dose-dependent reductions in colony size in EZH2i-pretreated cells were evident, again even at doses well below the IC-50. These data suggest that EZH2i disrupts clonogenic survival and sustained proliferation potential. Representative experiment shown (n = 2).

5.6. Inhibition of EZH2 catalytic activity does not alter the CIMP-high methylome, and EZH2 assembles in methylation-sensitive PRC2.1

Given the concentration of CIMP-high methylation on PRC2 targets, we then sought to determine if the DNA hypermethylation landscape is directed by catalytically active PRC2 as reported in seminal studies on cancer-specific roles of this complex (Viré et al., 2006). We evaluated DNA methylation of the *G0S2* locus after EZH2i and after *EZH2* knockdown. We also measured DNA methylation genome-wide after EZH2i. EZH2i and *EZH2* knockdown induced virtually no changes in DNA methylation at the *G0S2* locus or genome-wide (**Figure 5.10**).

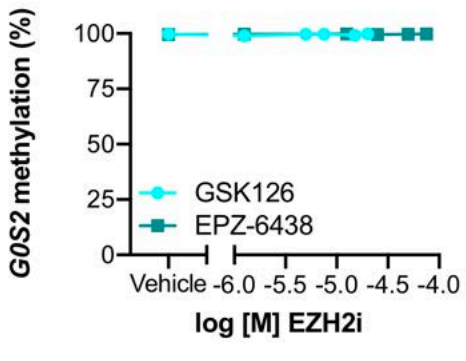

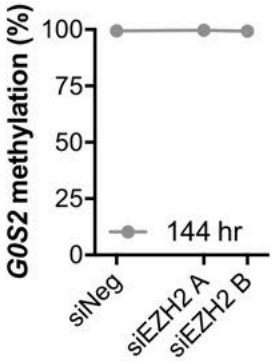

EPZ-DMS	# of probes
Down	2
Not significant	832496
Up	0

Figure 5.10. EZH2i and EZH2 depletion fail to disrupt CIMP-high DNA methylation.
G0S2 methylation was evaluated following 96 hour EZH2i (n = 3, left) or after 144 hr EZH2 knockdown (n = 1, middle) by EpiTect. gDNA extracted from cells treated for 96 hours with vehicle or the IC-50 concentration of EPZ-6438 (62 μM) was submitted for DNA methylome profiling by 850k array. This study identified no differentially methylated regions and only 2 differentially methylated probes, ruling out the possibility that EZH2 coordinates CIMP-high DNA methylation through catalytic activity.

These data convincingly demonstrate that EZH2 catalytic activity is not required for maintenance of CIMP-high DNA methylation *in vitro*. However, PRC2 may direct DNA methyltransferase activity through protein-protein interactions (Viré et al., 2006) rather than through its catalytic activity. This is the case in embryonic stem cells, in which Dnmt3l, a catalytically inactive DNMT, competes with Dnmt3a/b for binding to PRC2 to mediate PRC2 target protection from methylation (Neri et al., 2013). We therefore performed EZH2-directed complex immunoprecipitation paired with mass spectrometry (IP-MS) and DNMT1-directed IP-MS on nuclear lysates from NCI-H295R. We proceeded with DNMT1 because this is the dominant DNMT expressed in NCI-H295R, as EZH2 is the dominant H3K27 methyltransferase (**Figure 5.11**).

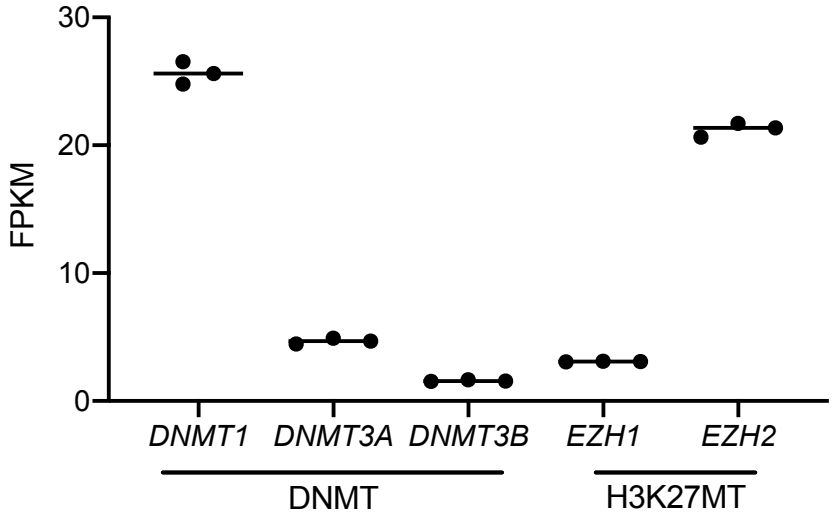

Figure 5.11. *DNMT1* and *EZH2* are the dominant DNA and H3K27 methyltransferases expressed in NCI-H295R.
RNA-seq data from baseline NCI-H295R demonstrates high expression of *DNMT1* and H3K27 methyltransferase (H3K27MT) *EZH2* relative to other enzymes of the same respective classes.

DNMT1 also exhibits cell-cycle-dependent upregulation in ACC (**Figure 5.12**) like many TCGA cancers (**Figure 1.3**).

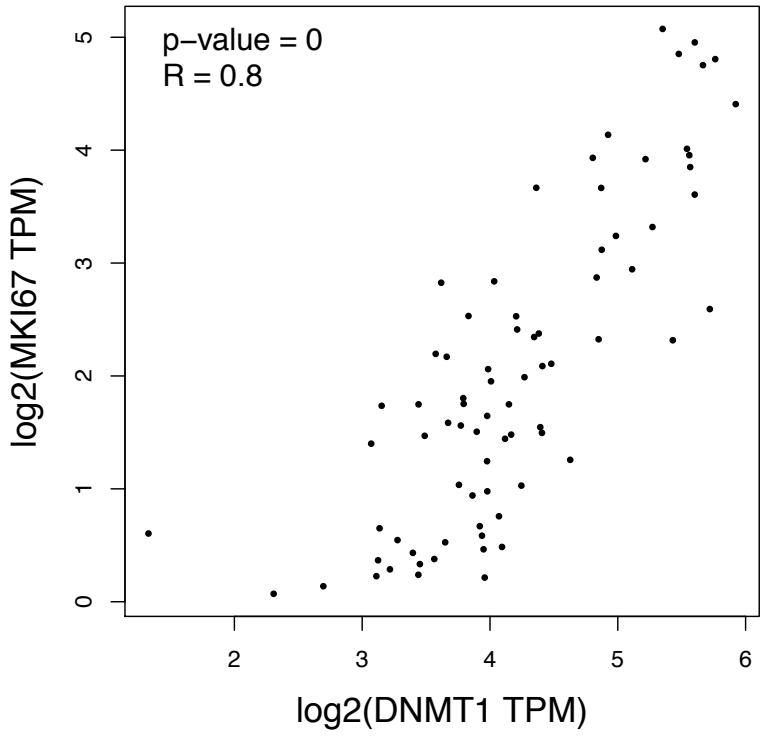

Figure 5.12. *DNMT1* is strongly correlated to prototype cell cycle marker *MKI67* in ACC.
GEPIA (Tang et al., 2017) was used to mine expression data from ACC-TCGA (Zheng et al., 2016).

EZH2- and DNMT1-directed IP-MS revealed that EZH2/PRC2 and DNMT1 do not interact, though DNMT1 binds many chromatin-bound proteins, including non-PRC2 chromatin modifiers like the HP1 family of H3K9me readers. DNMT1 binding to H3K9me readers represents an evolutionarily conserved mode of DNMT1 action (Catania et al., 2020), suggests that DNA methyltransferases may exhibit crosstalk with H3K9me, and is consistent with the H3K27me3 to H3K9me3 epigenetic class-switching model of CIMP-high (Ohm et al., 2007). We also identified that EZH2 is assembled in PRC2.1 and binds no DNA methyltransferases, and that there is virtually no overlap between the EZH2/DNMT1 interactomes (**Figure 5.13**). The PCL proteins that define PRC2.1 have

exceedingly low affinity for methylated CpGs and preferentially bind unmethylated DNA (**Table 1.5**, (Li et al., 2017)).

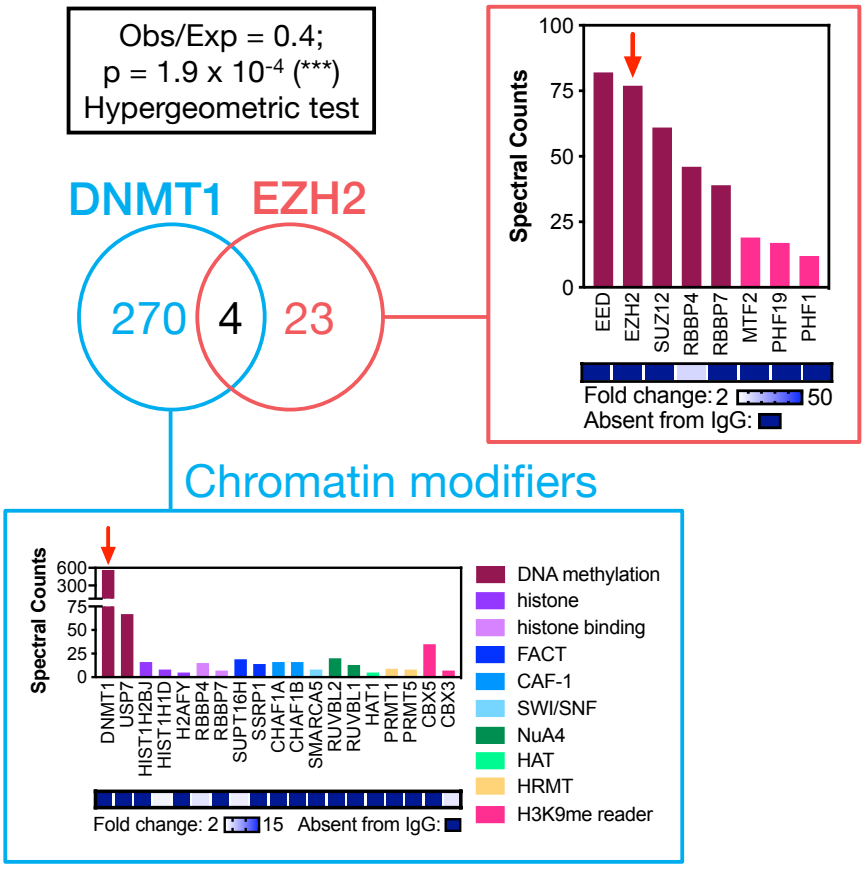

Figure 5.13. EZH2 and DNMT1 interactomes suggest H3K27me3 deposition and DNA methylation are mutually exclusive.
Mass spectrometry (MS) of EZH2- and DNMT1-directed NCI-H295R nuclear co-IP reveals almost no overlap between EZH2 and DNMT1 interactomes; 4 overlapping interactors are general histone-binding proteins, a kinesin and splicing machinery (not shown). Regarding canonical PRC2 binding partners, we identified that EZH2 is assembled in PRC2.1, and no spectra mapping to PRC2.2 accessory proteins (for example, JARID2 or AEBP2) or DNMT machinery was identified. DNMT1 had many binding partners, a subset of which could be classified as chromatin modifiers. We observed that DNMT1 interacts with the HP1 family of H3K9me readers (CBX5, CBX3) consistent with known mechanisms by which DNMT1 interfaces with histone modifications, and suggesting that DNA methylation may instead be instructed by H3K9me (Ohm et al., 2007). Proteins identified by MS are considered true interactors if >5 spectral counts and absent from IgG IP-MS or >2-fold enrichment over IgG IP-MS.

Taken together, these studies suggest that DNA methylation in CIMP-high ACC is propagated independently of the PRC2, and furthermore, that CIMP-high DNA

methylation may disrupt PRC2 recruitment to those sites. Our observation that EZH2 is still assembled in canonical PRC2.1 suggests that the major actions of EZH2 on the epigenome are indeed through its canonical activity. This is also supported by our observation that high EZH2 expression is associated with higher levels of H3K27me3 in ACC (**Figure 5.7**). However, it is possible that non-stoichiometric, excess EZH2 produced by sustained cell cycle activation may have non-canonical roles on chromatin, for example, functioning as a nuclear receptor coactivator (Xu et al., 2012). We did not identify any interaction between EZH2 and SF1 (the core nuclear receptor defining the adrenal cortex, **Chapter 2**) either by EZH2- or SF1- directed IP-MS (this data will later be described in **Figures 6.1** and **6.11**). However, as this data is suggestive but not conclusive regarding EZH2's role on chromatin, we then sought to examine EZH2 recruitment genome-wide.

5.7. EZH2 is retained at non-methylated PRC2 target sites genome-wide

We performed ChIP-seq on NCI-H295R to evaluate the genomic distribution of EZH2, H3K27me3, and H3K27ac at baseline. We also evaluated chromatin accessibility genome-wide by ATAC-seq. We observed that H3K27me3 and H3K27ac deposition was largely mutually exclusive (as expected, and reinforcing the specificity of the antibodies we used for ChIP-seq), and that most EZH2 peaks co-localized with broad and inaccessible H3K27me3 domains (**Figure 5.14**).

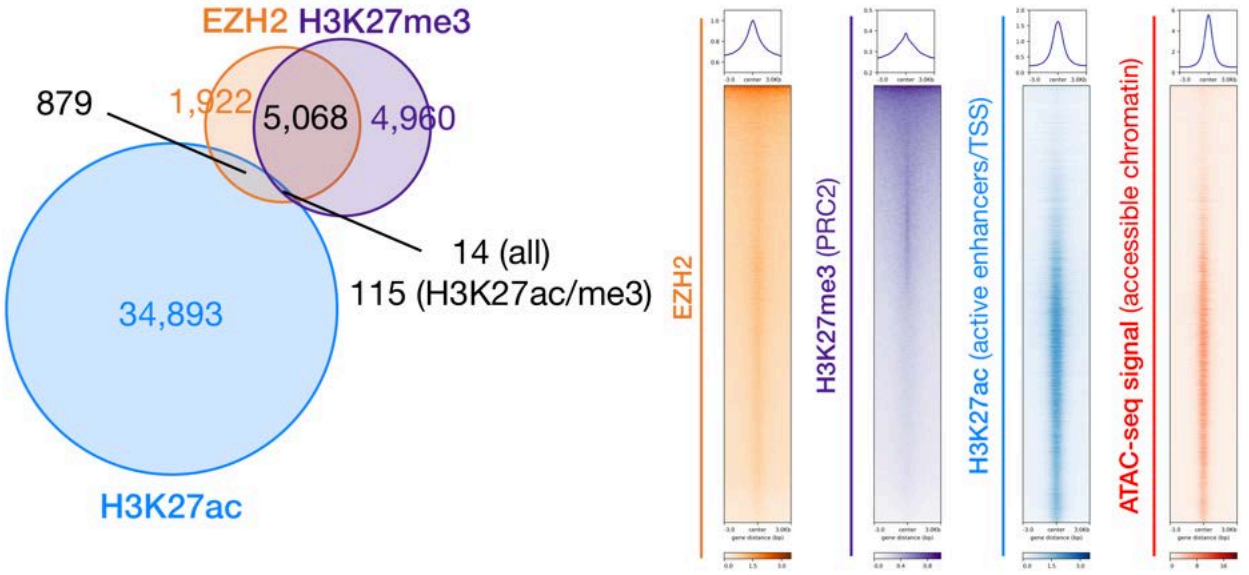

Figure 5.14. EZH2 co-localizes primarily with inaccessible H3K27me3 deposition genome-wide. Left, Venn diagram depicting overlap between peak calls for EZH2, H3K27me3, H3K27ac on ChIP-seq from NCI-H295R demonstrates that EZH2 overlaps primarily with H3K27me3 and not H3K27ac. Interestingly, EZH2 does bind some sites of the genome that do not contain either histone mark. Right, heatmap of EZH2, H3K27me3, H3K27ac, and chromatin accessibility (ATAC-seq) signal at the union peak set of H3K27me3 and H3K27ac, illustrating that EZH2/H3K27me3 domains are inaccessible while H3K27ac peaks are accessible.

These data are consistent with retention of EZH2's canonical and PRC2-dependent catalytic activity on chromatin despite cell-cycle-dependent EZH2 upregulation. We then sought to evaluate H3K27me3 and H3K27ac deposition in NCI-H295R at regions of the genome that are targeted for hypermethylation in CIMP-high ACC (hereafter referred to as hypermethylated DMRs). We observed that, as expected, hypermethylated DMRs show minimal overlap with H3K27ac (data not shown). These regions also showed minimal overlap with H3K27me3, consistent with our IP-MS data suggesting that DNA methylation and H3K27me3 are mutually exclusive. Consistent with this observation, the average DNA methylation levels of H3K27me3 peaks were substantially lower than the methylation levels of hypermethylated DMRs (**Figure 5.15**).

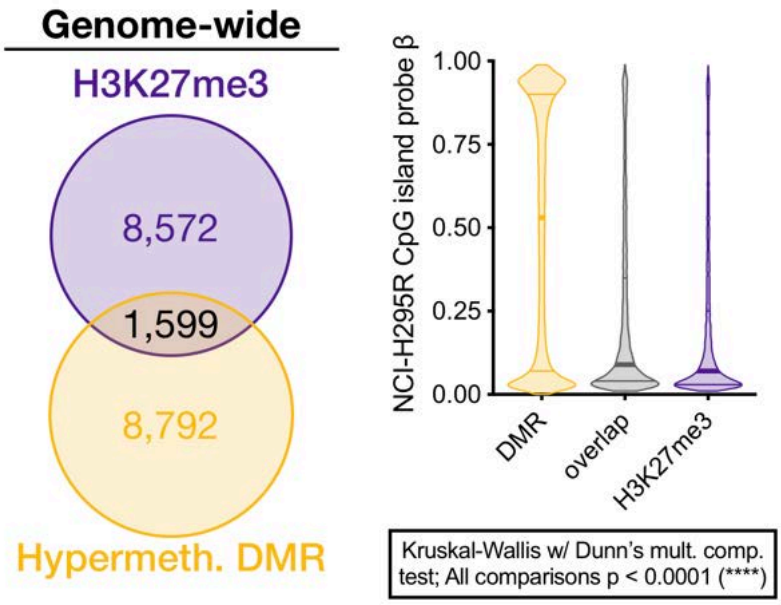

Figure 5.15. DNA methylation excludes H3K27me3 deposition in NCI-H295R.
H3K27me3 is excluded from regions of the genome recurrently targeted for DNA hypermethylation in CIMP-high ACC (hypermethylated DMRs). In NCI-H295R, an *in vitro* model of CIMP-high ACC, hypermethylated DMRs overlapping with CpG islands possess high levels of DNA methylation (measured by probe beta value) as expected. However, DNA methylation is largely excluded from H3K27me3 peaks in NCI-H295R, whether that genomic region was annotated as a hypermethylated DMR (overlap) or was a pure H3K27me3 peak.

It is also possible that these regions of the genome are not targeted for H3K27me3 deposition in the physiological adrenal cortex. We believed that this was unlikely given our DNA methylation data in fetal and adult adrenal cortex demonstrating that PRC2 binding sites are largely protected from methylation (**Figure 5.5**). To get closer to definitively ruling this possibility out, we examined the H3K27me3 signal in physiological adrenal tissue ChIP-seq deposited in ENCODE at NCI-H295R H3K27me3 peaks and hypermethylated DMRs. We observed strong H3K27me3 deposition in physiological fetal and adult adrenal tissues at hypermethylated DMRs, and reduced H3K27me3 deposition at regions annotated as NCI-H295R H3K27me3 peaks (**Figure 5.16**).

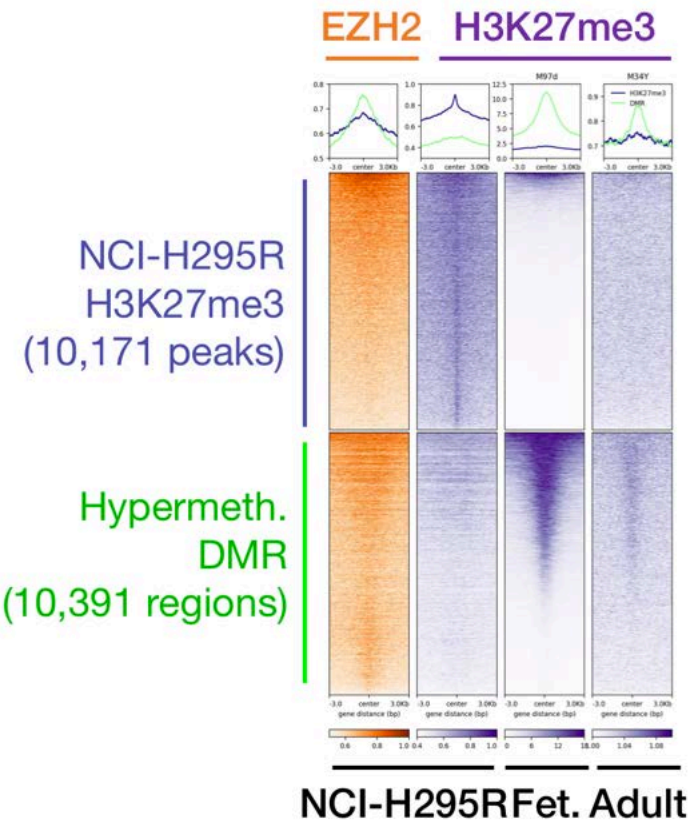

Figure 5.16. CIMP-high DNA hypermethylation reverses physiological H3K27me3 deposition, and leads to "*de novo*" H3K27me3 deposition in NCI-H295R.
Heatmap depicts EZH2 (first column) and H3K27me3 signal (second column) in NCI-H295R at H3K27me3 peaks and hypermethylated DMRs. As expected (**Figure 5.15**), NCI-H295R H3K27me3 signal is substantially lower at hypermethylated DMRs than at annotated H3K27me3 peaks. Interestingly, EZH2 deposition appears broader at H3K27me3 peaks, and present but more focal at hypermethylated DMRs. These data suggest that EZH2 may still be recruited to hypermethylated DMRs but is stalled, and cannot spread H3K27me3 marks. We then wanted to examine the H3K27me3 status of regions annotated as NCI-H25R H3K27me3 peaks and hypermethylated DMRs in fetal and adult H3K27me3 ChIP-seq data deposited in ENCODE (right two columns). In contrast, we observed that both fetal and adult tissue have stronger H3K27me3 signal at hypermethylated DMRs than at regions annotated as H3K27me3 peaks in NCI-H295R. These data suggest that DNA hypermethylation in CIMP-high ACC reverses physiological H3K27me3 deposition and may lead to aberrant PRC2 recruitment at novel or low affinity sites.

These observations suggest that DNA hypermethylation in CIMP-high ACC leads to epigenetic class switching, PRC2 eviction and recruitment to novel genomic sites. We then decided to investigate genome-wide consequences of EZH2i, and if these novel H3K27me3 sites are sensitive to EZH2i.

5.8. EZH2i disrupts EZH2 recruitment, wipes H3K27me3, and restores expression of PRC2 targets

We treated NCI-H295R with EZH2i (EPZ-6438) for 96 hours at the IC-50 dose established in **Figure 5.8**). ChIP-seq after EZH2i demonstrated global reductions in H3K27me3 and EZH2 recruitment at baseline H3K27me3 sites, and restoration of chromatin accessibility at these regions. Surprisingly, after EZH2i, EZH2 was recruited to several novel sites on the genome despite no new H3K27me3 deposition. These sites overlapped substantially with regions that possess H3K27ac after EZH2i (**Figure 5.17**).

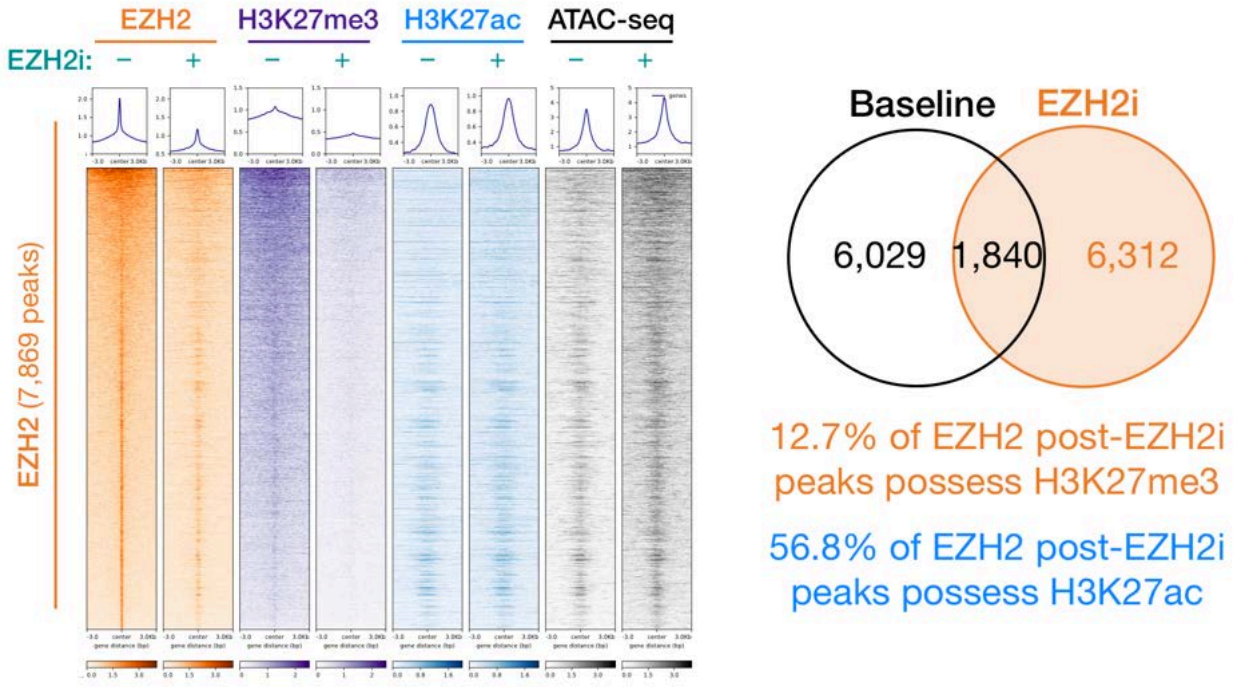

Figure 5.17. EZH2i wipes H3K27me3 and disrupts EZH2 recruitment genome-wide.
Heatmap (left) depicts impact of EZH2i administration on EZH2, H3K27me3, H3K27ac, and chromatin accessibility (ATAC-seq) signal at baseline EZH2 peaks. EZH2i evicts EZH2 from >75% of baseline peaks. We were surprised to observe many novel peaks emerging after EZH2i (right). Only a minority of new EZH2 peaks possesses H3K27me3; in contrast, more than half of new EZH2 peaks bear H3K27ac. These data suggest EZH2 may have ubiquitous chromatin binding properties, and demonstrate the potent impact of EZH2i on EZH2 recruitment genome-wide.

We also performed RNA-seq after EZH2i. As expected, we observed that EZH2i restored expression of PRC2 targets, and that the average FPKM of genes that were upregulated after EZH2i was significantly lower than the average FPKM of all genes in the transcriptome (Mann-Whitney, $p < 0.0001$). This is consistent with the model that catalytically active EZH2 restrains gene expression in CIMP-high ACC. Though we observed baseline H3K27me3 at several novel, non-physiological genomic sites (**Figures 5.16 – 5.17**), EZH2i also derepressed more than half of the genes that are upregulated in a mouse model of adrenocortical *Ezh2* deficiency (discussed in section **2.6**,(Mathieu et al., 2018)) (**Figure 5.18**). EZH2i failed to restore expression of genes that are hypermethylated in CIMP-high ACC, like *G0S2*, which was undetectable by RNA-seq in vehicle and EZH2i-treated cells (data not shown).

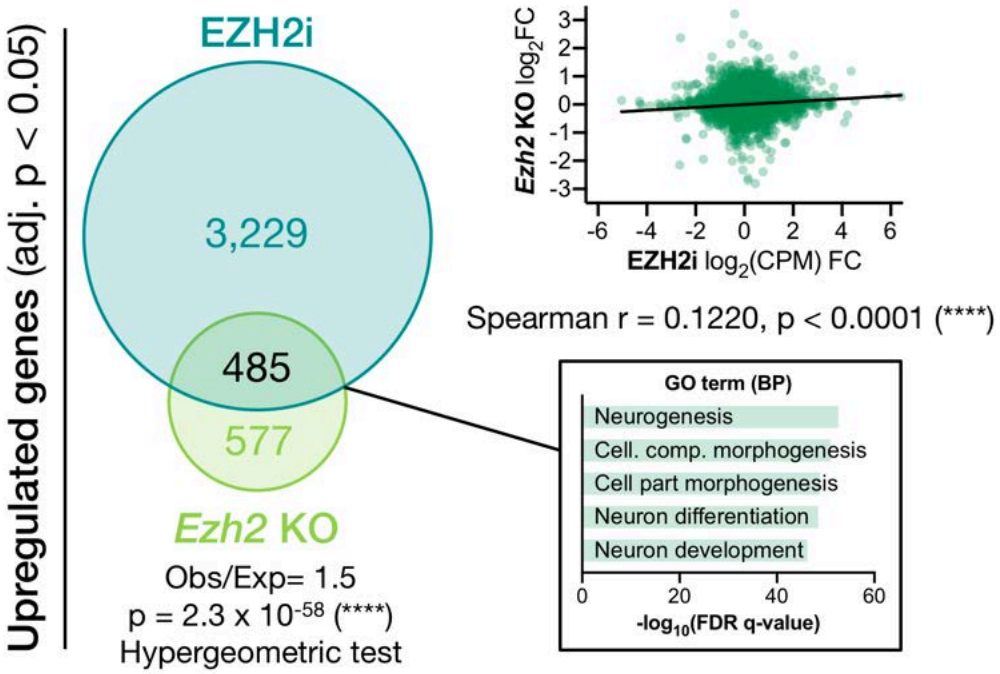

Figure 5.18. EZH2i depresses stem/progenitor programs restrained by EZH2 in the physiological adrenal cortex.
Comparison of genes that were upregulated following EZH2i in NCI-H295R with genes that were upregulated in a mouse model of SF1-driven *Ezh2* deficiency (*Ezh2* KO) demonstrates substantial overlap (left). GSEA (Mootha et al., 2003; Subramanian et al., 2005) for overlap genes using the GO (Biological Processes) gene set identifies several developmental programs coordinated by PRC2. Differentially expressed genes were also positively correlated (top right corner).

EZH2i induced expression of many genes (**Figure 5.18**), and a volcano plot depicting the differentially expressed genes between EZH2i-treated and vehicle-treated cells revealed that the transcriptome following EZH2i was broadly disrupted, with more than half of the transcriptome classified as differentially expressed (**Figure 5.19**).

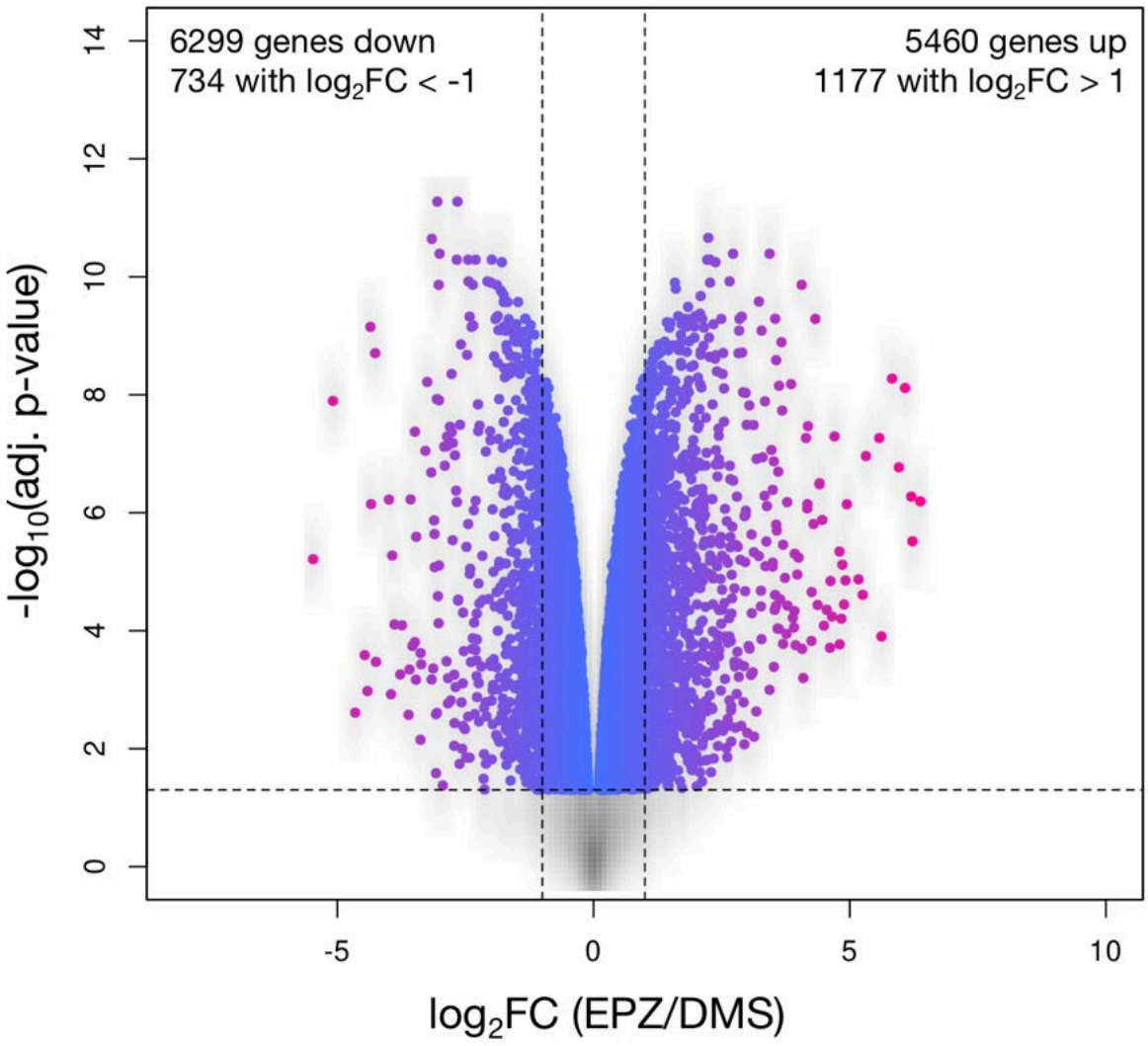

Figure 5.19. Volcano plot of gene expression following EZH2i reveals broad disruption of the transcriptome.
Volcano plot depicts -$\log_{10}$(p-value) for differential gene expression vs. $\log_2$(CPM) fold change of gene expression between EZH2i-treated cells vs. vehicle.

This data suggests that EZH2i may be targeting a broader epigenetic program required for sustained proliferation (**Figure 5.9**) than that classically coordinated by the PRC2. Our investigation of these profound consequences of EZH2i, and the physiological program this pharmacological intervention is targeting, is the focus of **Chapter 6**.

5.9. Discussion

In this chapter, we perform extensive profiling of patient samples and the *in vitro* CIMP-high ACC model, NCI-H295R. We show that the DNA hypermethylation landscape of CIMP-high ACC is directed to embryonic PRC2 targets (**Figures 5.1 – 5.2**) and represents a cancer-specific program (**Figure 5.5**; this is also supported by data presented in **Chapter 4**). CIMP-high ACC possess higher expression of *EZH2*, and high EZH2 expression is coupled to its catalytic activity on histones (**Figures 5.6 – 5.7**, **5.14**). PRC2 target hypermethylation is associated with PRC2 LOF in other cancers (Bayliss et al., 2016). However, here, we identify that PRC2 is assembled in the methylation-sensitive PRC2.1 complex (**Figure 5.13**), and that H3K27me3 (possibly through PRC2.1 targeting) is shuttled away from regions of the genome that are targeted for DNA hypermethylation to new or previously lower affinity genomic sites (**Figures 5.15 – 5.16**). Despite the fundamental disruption of PRC2 recruitment induced by CIMP-high methylation, adequately targeted H3K27me3 is required for sustained proliferation (**Figure 5.9**) and EZH2 inhibition induces profound changes in the epigenome and transcriptome (**Figures 5.17 – 5.19**). Taken together, these data support a model in which PRC2-independent repression of CIMP-high targets in ACC confers a shift in PRC2 targeting properties, inducing a PRC2 GOF and/or neomorph state.

Why CIMP-high ACC would continue to possess and rely on high PRC2 catalytic activity when other tissues use this as one of several mechanisms to select for PRC2 LOF with malignancy (**Table 1.7**, (Bayliss et al., 2016)) is not totally clear. Cancer cells (particularly those with invariable potential for metastasis, like CIMP-high ACC, **Chapter**

4) necessarily exhibit the cellular plasticity to adapt and proliferate through diverse challenges that accompany a rapidly shifting cancer microenvironment. More recently, this quality has been appreciated as a new hallmark of cancer (Hanahan and Weinberg, 2011), likely achieved through any of the numerous metabolic or genetic mechanisms by which cancer cells disrupt epigenetic programming (**Figure 1.3**, **Table 1.7**). The use of epigenetics, rather than transient shifts in intracellular signaling programs, to mediate cellular plasticity enables cancer cells to acquire and pass through a series of meta-stable transcriptional states (Chang et al., 2008) that may facilitate the selection of novel and advantageous oncogenic hits. Considering the spectrum of modules mammalian cells evolved to write, read, and erase epigenetic programs (**Chapter 1**), which tool among many a cancer cell may wield is likely heavily influenced (if not determined) by the existing chromatin environment and therefore the tissue of origin (Corces et al., 2018).

The DNA hypermethylation program that characterizes CIMP-high ACC is uniform, with many loci possessing binary and complete methylation of CIMP-high/PRC2 targets (**Figures 3.3**, **4.35**, **5.5**; **Chapter 4**). These data, consistent with literature examining the etiology and emergence of CIMP-high (Tao et al., 2019; Vaz et al., 2017), suggest that acquisition of this signature is an early and favorable selection event in adrenocortical carcinogenesis. Across different cancer types, CIMP-high has diverse functional consequences for global EZH2/PRC2 catalytic activity (**Table 1.7**). We have identified that CIMP-high comprises a distinct ACC molecular subtype (**Chapter 4**) with concordant hyperactivation of key transcriptional programs (this will be detailed in **Chapter 6**) and several layers of abnormal epigenetic patterning (this chapter). These data suggest that

retention of high EZH2 expression/catalytic activity despite methylation-sensitive PRC2 complex assembly (**Figure 5.13**) and DNA hypermethylation of PRC2 targets (**Figures 5.1 – 5.2**, **5.5**) may be required to stabilize selection of transcriptional programs turned on in CIMP-high ACC and its cell-of-origin.

We postulated that the first cell seeding CIMP-high ACC is a partially zF-differentiated transit-amplifying cell residing at the zG/zF boundary (**Figure 2.6**, concepts discussed in **Chapters 2 – 3**), necessarily predicated on the idea that physiological epigenetic programs facilitating adrenocortical differentiation are perverted and/or co-opted during transformation. How epigenetic programs coordinate adrenocortical development and homeostasis is still incompletely understood (**Chapter 2**). zG to zF lineage conversion is likely epigenetically mediated (**Figure 2.7**), and EZH2 is apparently a critical regulator of this process both in development and ACTH-dependent homeostasis (**Chapter 2**, **Figures 2.8 – 2.9**, (Mathieu et al., 2018)). ACC cells also possess the ability to traverse the spectrum of zG to zF differentiation in response to differentiation cues (**Chapter 3**, will be shown for NCI-H295R in **Chapter 6**). This observation is particularly striking in light of decades of work demonstrating that physiological adrenocortical homeostasis and zonation are tightly controlled by a balance between endocrine and paracrine signaling (**Chapter 2**), and implicates steroidogenic differentiation plasticity as key for malignant transformation and carcinogenesis in the adrenal cortex. The physiological role of EZH2 (**Chapter 2, Figures 2.8 – 2.9**, (Mathieu et al., 2018)) and our data in this chapter (particularly **Figure 5.18**) suggest that CIMP-high reliance on intact PRC2/EZH2 catalytic activity may be partially influenced by the

adrenocortical context. This is supported by our data identifying a surprising and nuanced role of PRC2/EZH2 in coordination of adrenocortical differentiation in ACC – the focus of **Chapter 6**.

5.10. Materials and methods

Analysis of ACC-TCGA. Performed as described in **Chapter 3**, **Chapter 4**.

Patient/donor samples. Patient/donor samples were obtained with informed consent from the University of Michigan (UM) and Faculdade de Medicina da Universidade de Sao Paulo (FMUSP), and extraction of nucleic acids for 850k array profiling, and measurement of *BUB1B* expression, *GUSB* housekeeping gene expression, and *G0S2* methylation was performed and previously reported (**Chapters 3 – 4**). In this study, *EZH2* expression was measured by TaqMan Gene Expression Assays (Applied BioSciences/Thermo Fisher Scientific, Cat No. hs00544830_m1). *EZH2* expression levels were calculated using the ΔC_t method as previously described (**Chapter 4**).

Tissue microarrays. Tissue microarray (TMA) of adrenocortical tumors from FMUSP was stained for EZH2 and H3K27me3 in triplicate. EZH2 staining was performed with 1:100 EZH2 (Cell Signaling Technology, Cat. No. 5246S) using standard IHC paraffin protocols and the NovoLink Max Polymer Detection System (Leica Biosystems, Newcastle Ltd, Cat. No. RE7 159) with the following modifications: All washes were performed with PBS. Antigen retrieval was performed using boiling Tris-EDTA, pH 9.0

(Spring Bioscience, Cat. No. PMB4-235) for 35 minutes, endogenous peroxidase activity was quenched for 10 minutes at room temperature with 6% H_2O_2 in methanol. Blocking was performed for 10 minutes at 37°C with Cas Block (Invitrogen, Cat. No. 00-8120). Slides were incubated with primary antibody diluted in 1% BSA, 0.1% sodium azide in PBS for in a humidity chamber for 30 minutes at 37°C followed by 18 hours (overnight) at 4°C. H3K27me3 staining was performed as previously described (Bayliss et al., 2016). EZH2 expression levels was quantified on 0-4 scale based on % positive nuclei per section and averaged across two independent observers as described in **Figure 5.7**. H3K27me3 levels were quantified by MATLAB as previously described (Bayliss et al., 2016).

Nucleic acid extraction and quantification. Performed as described in **Chapters 3 – 4**.

Targeted DNA methylation analysis. Extracted gDNA was subject to targeted assessment of *G0S2* methylation by EpiTect as described in **Chapter 4**.

Cell culture. Performed as described in **Chapter 3**.

Pharmacological experiments (not including ChIP-seq experiment). NCI-H295R cells were plated at a density of 400,000 or 800,000 cells/well in 6 well plates. Alternatively, fewer cells were plated at the same density (corrected by surface area) in

24 well plates or 12 well plates. 18-24 hours after plating, media was changed for media containing EPZ-6438, EED226, GSK126, or vehicle (DMSO). The concentration of vehicle was kept constant for all wells in a given experiment. Media was changed and replaced as described every 24 hours. After 96 hours of drug treatment, cells were harvested for RNA, protein or cell viability.

siRNA experiments. NCI-H295R were plated at a density of 800,000 cells per well in 6 well plates (or cell number scaled accordingly for plating in 12 well or 24 well plates) in antibiotic-free media. 18-24 hours after plating, media was changed for fresh antibiotic-free media containing 50 nM siRNA (Negative Control #1, s4916 or s4917 from Thermo Fisher) and transfection reagent (TransitX2, Mirus Cat. No. MIR 6000) prepared according to manufacturer instructions. Transfection was repeated 72 hours after first transfection and cells were harvested at 144 hours after first transfection for desired endpoint readouts.

Viability assays and calculations. Viability was measured using alamarBlue (Invitrogen, Cat. No. DAL1025) according to manufacturer's instructions. Briefly, at endpoint, media was changed to media containing alamarBlue at a concentration of 60 µL alamarBlue/600 µL media. Plate was incubated under standard culture conditions with protection from light for 2-4 hours (or until desired dye development was visible), and 100 µL of media was transferred in triplicate to a 96 well plate. Absorbance was measured using VersaMax tunable microplate reader (Molecular Devices) at 570 nm using 600 nm

as a reference wavelength. % viability (%V) was calculated as follows. For vehicle or each treatment concentration, AR = $(\varepsilon_{OX,600})(A_{570}– B_{570}) – (\varepsilon_{OX,570})(A_{600}– B_{600})$, where $\varepsilon_{OX,600}$ = 117,216, $\varepsilon_{OX,570}$ = 80,586, A_{570} = absorbance of treatment well at 570 nm, B_{570} = absorbance of blank well (well containing no cells, only media and alamarBlue) at 570 nm, A_{600} = absorbance of treatment well at 600 nm, and B_{600} = absorbance of blank well at 600 nm. %V = $100*AR_{treatment}/AR_{vehicle}$.

Protein extraction and quantification. At endpoint, cells were washed with ice cold PBS and incubated for 10 minutes on ice with ice cold whole-cell nuclear lysis buffer (50 mM Tris-HCl pH 8.1, 10 mM EDTA, 1% SDS in ultrapure H2O, adapted from (Drelon et al., 2016a)), supplemented with protease inhibitors (cOmplete, Mini, EDTA-Free, Roche, Cat. No. 04693159001) and phosphatase inhibitors (PhosSTOP, Roche, Cat. No. 04906845001) according to manufacturer's instructions. Cells were scraped off plate in lysis buffer and transferred to microcentrifuge tubes. Samples were sonicated for 10 seconds each, 3x per sample at setting 70-80; samples were placed on ice between sonication cycles. After sonication, lysates were stored on ice for 10 minutes. Lysates were then centrifuged at 14,000xg at 4°C for 15 minutes to remove insoluble debris, and supernatants were collected in fresh tubes. Alternatively, cells were washed with PBS containing phosphatase inhibitors (prepared using reagents provided in ActiveMotif, Cat. No. 54001), scraped into microcentrifuge tubes, pelleted by centrifugation at 1200xg for 5 minutes, frozen at -80°C, and later extracted for protein using complete whole-cell nuclear lysis buffer as stated above. Alternatively, cells washed with PBS, incubated on

ice with complete whole-cell nuclear lysis buffer, scraped into microcentrifuge tubes, frozen at -80°C and protein extraction was later resumed as stated above. Prior to downstream processing, lysates and protein standards were quantified by BCA (Thermo Scientific, Cat. No. PI23227) in duplicate in 96 well plates. Briefly, 2 mg/mL standards were used to generate a 32 µg to 0 µg dilution series (in 50 µL); 2-5 µL of sample was diluted in 50 µL water. 200 µL of working reagent (prepared according to manufacturer instructions) were added to each well, plate was incubated at 37°C protected from light for 30 minutes, and absorbance was read at 562 nm using a VersaMax tunable microplate reader (Molecular Devices). Absorbance values of standard curve were used to determine sample concentration.

SDS-PAGE and western blot. Samples were prepared by boiling at 95°C for 6 minutes in lysis buffer supplemented with 4x Laemmli Sample Buffer (Bio-Rad, Cat. No. 161-0747, with 355 mM 2-mercaptoethanol freshly added) according to manufacturer's instructions. Alternatively, samples were boiled at 95°C for 5 minutes in 2X reducing buffer (130 mM Tris pH 6.8, 4% SDS, 0.02% bromophenol blue, with 0.1 M DTT freshly added) with 16.7% glycerol. Samples and a size marker (Bio-Rad, Cat. No. 1610374) were loaded onto NuPage 4-12% Bis-Tris gels (Invitrogen, Cat. Nos. NP0323, NP0322) and run using the MOPS (Invitrogen, Cat. No. NP0001) or MES (Invitrogen, Cat. No. NP0002) buffer systems. Following SDS-PAGE, gels were coomassie stained or transferred onto a PVDF membrane (Thermo Scientific 88520) using a traditional wet transfer system and NuPage Transfer Buffer (Invitrogen NP0006) supplemented with up to 20% methanol according

to manufacturer instructions. Uniform transfer efficacy was verified by coomassie staining of SDS-PAGE gel after transfer. Western blot was performed according to standard protocols, which typically consisted of 1 hour room temperature block, overnight primary antibody incubation at 4°C, 4x5 minute washes, 1 hour secondary incubation at room temperature protected from light, 4x5 minute washes, 5 minute rinse, and visualization using the LI-COR Odyssey imaging system at 700 nm and/or 800 nm. Odyssey (TBS) Blocking Buffer (LI-COR, discontinued) or Intercept (TBS) Blocking Buffer (LI-COR, Cat. No. 927-60003) was used for blocking. Primary or secondary antibodies were diluted in blocking buffer + 0.1% Tween 20. TBS + 0.1% Tween 20 was used for wash steps, and TBS alone for the final rinse. The following antibodies were used for western blot: 1:1000 EZH2 (Cell Signaling Technology, Cat. No. 5246S), 1:1000 SUZ12 (Cell Signaling Technology, Cat. No. 3737), 1 µg/mL SUZ12 (R&D, Cat. No. MAB4184), 1:1000 active β-catenin (Cell Signaling Technology, Cat. No. 8814), 1:1000 β-catenin (Invitrogen, Cat. No. MA1-2001), 1:500-1:2000 H3K27me3 (EMD Millipore, Cat. No. 07-449), 1:1000 H3K27ac (ActiveMotif, Cat. No. 39133), 1:2000 SF1 (custom in-house antibody, RRID AB_2716716), 1-2 µg/mL SF1 (Invitrogen, Cat. No. 434200/N1665), 1:5000 β-actin (Sigma-Aldrich, Cat. No. A-5441).

Coomassie staining. Coomassie staining was performed using Imperial Protein Stain (Thermo, Cat. No. 24615) according to manufacturer instructions. Briefly, SDS-PAGE gel was washed for 15 minutes with gentle shaking in ultrapure water. Gels were incubated with Imperial Protein Stain for 1-2 hours at room temperature with gentle shaking. Stain

was discarded and replaced with ultrapure water and a folded Kimwipe Tissue. After overnight destaining, gels were imaged using the LI-COR Odyssey imaging system protein gel setting at 700 nm.

Nuclear complex immunoprecipitation (co-IP). Nuclear co-IP was performed using the Nuclear Complex Co-IP Kit (ActiveMotif, Cat. No. 54001) and Protein G Agarose Columns (ActiveMotif, Cat. No. 53039) according to manufacturer's protocol with the following modifications: enzymatic digests were performed at 4°C for 90 minutes, and all co-IPs were performed at a concentration of 3.5 µg antibody/275 µg nuclear lysate using IP Low Buffer (ActiveMotif, Cat. No. 37511) for incubation and wash steps with no additional salts or detergents. Anywhere from 150-500 µg of nuclear lysate was used for IP, and antibody concentration was scaled up or down accordingly to maintain 3.5 µg antibody/275 µg nuclear lysate. Nuclear lysate concentration was quantified by BCA prior to setting up co-IP. Any of the following antibodies were used for Co-IP: EZH2 (Cell Signaling Technology, Cat. No. 5246S), SUZ12 (Cell Signaling Technology, Cat. No. 3737), SUZ12 (Bethyl, Cat. No. A302-407A), active β-catenin (Cell Signaling Technology, Cat. No. 8814), SF1 (custom in-house antibody, RRID AB_2716716), negative control IgG (EMD Millipore, Cat. No. 12-370). Co-IPs were evaluated by mass spectrometry (IP-MS), or were eluted and evaluated by coomassie staining and/or western blot.

Immunoprecipitation/mass spectrometry (IP-MS) and data processing. NCI-H295R cells were cultured as described and plated in 10 cm dishes. To minimize biological

variability, 3 ~80% confluent plates of 3 independent passages of exponentially growing cells (total 9 plates) were harvested and pooled for nuclear co-IP using the Nuclear Complex Co-IP Kit (Active Motif 54001) and Protein G Agarose Columns (Active Motif 53039). Nuclear co-IP was performed as described using aforementioned antibodies against EZH2, active β-catenin, SF1, DNMT1, or negative control IgG with the following modifications: 500 µg of pooled nuclear lysate was used for each co-IP (antibodies scaled accordingly), and co-IPs were not eluted. Instead, after final wash in IP wash buffer without BSA, samples were centrifuged at 1200xg at 4°C for 3 minutes. For a final rinse to remove residual wash buffer, 500 µL of PBS was added to each IP, samples were centrifuged at 1200xg at 4°C for 30 seconds, and Protein G columns were stored in new 1.5 mL microcentrifuge tubes and frozen at -80°C. Samples were delivered on dry ice to MS Bioworks, Ann Arbor, MI for mass spectrometry analysis using the IP-works platform.

Samples were prepared and analyzed by MS Bioworks as follows. The resin was suspended in 60 µL of 1.5X loading buffer and columns were heated to 90°C for 2 min. The column bottom plugs were removed and the boiled eluate was recovered by centrifugation at 3,000 x g for 1 min. Half of each submitted sample was processed by SDS-PAGE using a NuPAGE 10% Bis-Tris gel (Invitrogen, Cat. No. NP0301) with the MES buffer system (Invitrogen, Cat. No. NP0002). The gel was run 2 cm. The gel lane was excised into 10 equal sized segments and in-gel digestion was performed on each using a robot (ProGest, DigiLab) with the following protocol: Washed with 25mM ammonium bicarbonate followed by acetonitrile. Reduced with 10mM dithiothreitol at 60°C followed by alkylation with 50mM iodoacetamide at RT. Digested with sequencing

grade trypsin (Promega) at 37°C for 4 hours. Quenched with formic acid and the supernatant was analyzed directly without further processing.

Half of each digest was then analyzed by nano LC-MS/MS with a Waters NanoAcquity HPLC system interfaced to a ThermoFisher Q Exactive. Peptides were loaded on a trapping column and eluted over a 75 μm analytical column at 350 nL/min; both columns were packed with Luna C18 resin (Phenomenex). The mass spectrometer was operated in data-dependent mode, with the Orbitrap operating at 70,000 FWHM and 17,500 FWHM for MS and MS/MS respectively. The fifteen most abundant ions were selected for MS/MS. 5 hours of instrument time was used per sample.

Data were searched using a local copy of Mascot (Matrix Science) with the following parameters: Enzyme – Trypsin/P, Database – SwissProt Human (concatenated forward and reverse plus common contaminants), Fixed modification – Carbamidomethyl (C), Variable modifications – Oxidation (M), Acetyl (N-term), Pyro-Glu (N-term Q), Deamidation (N/Q), Mass values – Monoisotopic, Peptide Mass Tolerance – 10 ppm, Fragment Mass Tolerance – 0.02 Da, Max Missed Cleavages – 2. Mascot DAT files were parsed into Scaffold (Proteome Software) for validation, filtering and to create a non-redundant list per sample. Data were filtered using at 1% protein and peptide FDR and requiring at least two unique peptides per protein. Known contaminants and reverse hits were excluded from downstream analysis.

In this study, a protein was considered an interactor if it met the following criteria: $\geq$ 5 spectral counts in target co-IP and either not detected in IgG co-IP or at least 2-fold enrichment over IgG in target co-IP based on dividing spectral count values. Prior to

submission of co-IPs for IP-MS, co-IP efficacy was verified by Coomassie staining and evaluation of *bona fide* protein interactions reported in the literature by western blot (e.g. EZH2/SUZ12, DNMT1/PCNA). The 2-fold cutoff for enrichment was determined based on the minimum threshold required to capture *bona fide* protein interactors (supported by the literature).

2D Clonogenicity. At experiment endpoint, cells were washed twice with warm PBS, trypsinized, and viable cells (identified by Trypan blue exclusion) were counted using a hemocytometer. 3,000 viable cells/well or 1,000 viable cells/well were plated in 6 well plates in 3 mL standard media. Cells were maintained under standard conditions with no media changes. 2 or 4 weeks after plating, respectively, plates were washed with twice with PBS and fixed for 15 minutes with 4% PFA in PBS at room temperature, protected from light, with gentle agitation. Plates were washed four times with water, stained for 15 minutes at room temperature with gentle agitation in crystal violet staining solution (0.1% crystal violet in 5% ethanol in water), washed four times with water, and inverted over a paper towel to dry overnight. The next day, plates were imaged using the LI-COR Odyssey imaging system using the microplate setting at 700 nm. Colonies were counted in plate images using the "Analyze Particles" tool in Fiji (Schindelin et al., 2012).

RNA-seq. Performed and analyzed as described in **Chapters 3 – 4**.

ATAC-seq. ATAC-seq was performed as previously described with modifications (Corces et al., 2017). Specifically, 50,000 cells were resuspended in 500 µL resuspension

buffer (10 mM Tris-HCl pH 7.4, 10 mM NaCl, and 3 mM MgCl2 in water). Cells were centrifuged at 50xg for 10 min in a pre-chilled (4°C) fixed-angle centrifuge. Lysis and transposition were performed simultaneously by resuspending cells in 25 µL tagmentation mix (12.5 µL 2xTD buffer [Illumina, Cat. No. 15027866], 1.25 µL Tn5 enzyme [Illumina, Cat. No. 15027865], 9.25 µL PBS, 0.5 µL 1% digitonin, 0.5 µL Tween-20, 0.5 µL NP40, and 0.5 µL 100x protease inhibitors), and incubating at 37°C for 30 min in a thermomixer with shaking at 1,000 rpm. Tn5 transposase-tagged DNA was amplified by PCR and purified using AMPure XP magnetic beads. ATAC-seq reads were sequenced 2x150 bp using a NovaSeq 6000.

For analysis of ATAC-seq data, we used *bowtie2* (Langmead and Salzberg, 2012) to align the reads to the hg38 version of the human genome. Reads overlapping with blacklisted regions (defined by ENCODE), and reads with a mapping score < 20 were filtered. For ATAC-seq peak calling, we used *genrich* (Gaspar, 2018). For differential peak calling we used *diffbind* (Ross-Innes et al., 2012; Stark and Brown, 2011).

ChIP-seq. NCI-H295R were plated in standard culture medium in 10 cm dishes at a density of 2.4 million cells per plate. To best account for biological variability, this experiment was performed using 24 plates of cells total, where 16 plates were reserved for EZH2i administration at the IC-50 dose (62 µM EPZ-6438) and 8 plates were reserved for vehicle administration (equivalent volume of DMSO). 24 hours after plating and daily thereafter, media was changed for media containing IC-50 EZH2i or vehicle. After approximately 96 hours of drug administration (120 hours post-plating), cells were

harvested for ChIP-seq with *Drosophila* histone spike-in for all epitopes according to Active Motif's Epigenetic Services ChIP Cell Fixation protocol. Briefly, media was supplemented with 1/10 media volume of freshly prepared Formaldehyde Solution (11% formaldehyde, 0.1 M NaCl, 0.5 M EDTA pH 8.0, 1 M HEPES pH 7.9 in nuclease-free water), and plate was agitated for 15 minutes at room temperature. Fixation was stopped with addition of 1/20 volume of Glycine Solution (2.5 M Glycine, MW 75 in nuclease-free water) and incubating at room temperature for 5 minutes. Cells were then scraped, collected into a conical tube, and pelleted at 800xg at 4°C for 10 minutes. Supernatant was aspirated and each tube of cells was re-suspended in 10 mL chilled PBS-Igepal (0.5% Igepal CA-630 in PBS). Cell were pelleted again, supernatant aspirated, and cells resuspended in 10 mL chilled PBS-Igepal supplemented with 100 µL of 100 mM PMSF in ethanol. Cells were pelleted again, supernatant aspirated, snap frozen on dry ice, stored at -80°C, and shipped on dry ice to Active Motif Services (Carlsbad, CA) for chromatin preparation and ChIP-seq.

In brief, chromatin was isolated by the addition of lysis buffer, followed by disruption with a Dounce homogenizer. Lysates were sonicated and DNA sheared to an average length of 300-500 bp. Genomic DNA (Input) was prepared by treating aliquots of chromatin (pooled from all submitted samples) with RNase, proteinase K and heat for de-crosslinking, followed by ethanol precipitation. Pellets were resuspended and the resulting DNA was quantified on a NanoDrop spectrophotometer. Extrapolation to the original chromatin volume allowed quantitation of the total chromatin yield.

An aliquot of chromatin (30 µg) was precleared with protein A agarose beads (Invitrogen). Genomic DNA regions of interest were immunoprecipitated using the following antibodies: EZH2 (Active Motif, Cat. No. 39901; concentration 8 µL Ab/30 µg chromatin), H3K27me3 (ActiveMotif, Cat. No. 39155; concentration 4 µg Ab/30 µg chromatin), H3K27ac (ActiveMotif, Cat. No. 39133; concentration 4 µg Ab/30 µg chromatin). Complexes were washed, eluted from the beads with SDS buffer, and subjected to RNase and proteinase K treatment. Crosslinks were reversed by incubation overnight at 65°C, and ChIP DNA was purified by phenol-chloroform extraction and ethanol precipitation. Quantitative PCR (QPCR) reactions to verify ChIP efficacy were carried out in triplicate on specific positive control genomic regions using SYBR Green Supermix (Bio-Rad).

Illumina sequencing libraries were prepared from the ChIP and Input DNAs by the standard consecutive enzymatic steps of end-polishing, dA-addition, and adaptor ligation. Steps were performed on an automated system (Apollo 342, Wafergen Biosystems/Takara). After a final PCR amplification step, the resulting DNA libraries were quantified and sequenced on Illumina's NextSeq 500 (75 nt reads, single end).

We used *bowtie2* (Langmead and Salzberg, 2012) to align the reads to the hg38 version of the human genome. Reads overlapping with blacklisted regions (defined by ENCODE), and reads with a mapping score < 20 were filtered. BAM files were down-sampled to account for *Drosophila* spike-in control, enabling quantitative comparison of epitopes accounting for net chromatin recruitment across treatment conditions. To perform ChIP-seq peak calling, we used *SPAN* and the *JBR* browser (JetBrains Research

BioLabs). These tools allow for empirical parameter adjustment after visual inspection of the peaks to obtain the best possible signal-to-noise ratio (FRIP). We used *manorm* (Shao et al., 2012) to perform differential peak call between conditions. We used the *annotatePeak* function from the R/Bioconductor package *ChipSeeker* (Yu et al., 2015) to annotate the peaks according to distance to TSS and overlapping features. For motif enrichment analysis we used *HOMER* (Heinz et al., 2010). We used *bedtools* (Quinlan and Hall, 2010) for identifying intersects of interest across different epitopes. For visualization and quantification of the intensity of the signal across peaks of interest we used *deepTools 2.0* (Ramírez et al., 2016).

850k arrays. 850k array data was generated and analyzed as described in **Chapters 3 – 4**. In the case of EZH2i-/vehicle-treated samples, 850k array data was generated from extracted gDNA by Diagenode without FFPE restoration treatment. Additionally, statistical analysis was performed using *limma* (Ritchie et al., 2015) to assess probe-specific differential methylation.

CHAPTER 6. A Differentiation Program Coordinated by SF1/β-catenin is a Targetable Epigenetic Vulnerability in CIMP-high ACC

6.1. Disclosure of relevant publications

Portions of this work are being prepared for publication:

> **Mohan DR**, Borges KS, Finco I, LaPensee CR, Solon A, Rege J, Little III DW, Else T, Almeida MQ, Apfelbaum A, Vinco M, Wakamatsu A, Mariani BMP, Latronico AC, Mendonca BB, Zerbini MCN, Fragoso MCBV, Lawlor ER, Ohi R, Rainey WE, Venneti S, Marie SKN, Giordano TJ, Breault DT, Lerario AM*, Hammer GD*. A differentiation program coordinated by SF1/β-catenin is a targetable epigenetic vulnerability in aggressive adrenocortical carcinoma. In preparation. *co-senior author
>
> Lerario AM*, **Mohan DR***, Rege J, Rainey WE, Hammer GD. Meta-analysis of adrenocortical tumors identifies cell of origin programs derailed in tumorigenesis and malignancy. In preparation. *co-first author

6.2. Introduction

Our studies in **Chapter 5** suggest a critical role for PRC2/EZH2 in CIMP-high ACC and closed on data revealing that EZH2i induced a broad disruption of the adrenocortical transcriptome, including genes repressed by EZH2 in the physiological adrenal cortex **Figures 5.18 – 5.19**). These findings are not readily explained by the baseline genome-wide recruitment profile of EZH2, which was largely restricted to recruitment at H3K27me3 domains outside of physiological binding sites (**Figures 5.14**, **5.16**). We therefore sought to determine if EZH2 is engaged in other, non-classical PRC2 programs.

Here, we identify that EZH2 has several context- and tissue-specific binding partners, including p.S45P β-catenin. We also generate data suggesting that the EZH2/β-catenin complex is off-chromatin and PRC2-independent. Deepening the understanding of the roles of β-catenin in physiology and ACC (**Chapters 2 – 3**), we identify that on a molecular level, β-catenin complexes with master transcriptional regulator SF1 to coordinate an adrenocortical differentiation program at proximal and distal CREs. This demonstrates that β-catenin has a major tissue-specific role, and the presence of an EZH2/β-catenin complex provides EZH2 the opportunity to access a tissue-specific differentiation program. We identify that both EZH2- and SF1-containing β-catenin complexes are conserved in mouse models of physiology and adrenocortical carcinogenesis, and that EZH2i disrupts SF1/β-catenin recruitment genome-wide, reversing adrenal differentiation and proliferation, presumably through a novel squelching role of off-chromatin and/or catalytically inactive EZH2. Taken together, these data nominate EZH2 as a critical and pharmacologically targetable mediator of the differentiation signature that paradoxically prevails this rapidly recurrent, routinely fatal molecular subtype of ACC.

6.3. EZH2 has novel context-specific binding partners

The observation that EZH2i disrupted a broad spectrum of transcriptional programs (**Figure 5.19**), including those governed by EZH2 in the physiological adrenal cortex (**Figure 5.18**), led us to explore if the consequences of EZH2i on transcriptional programming may be partially determined by an off-chromatin, non-PRC2 and perhaps

tissue-specific role of EZH2. We revisited our EZH2 IP-MS data and identified that EZH2 had several novel partners, including non-SF1 nuclear receptors known to regulate adrenocortical biology (Bassett et al., 2004), and β-catenin, which possesses the p.S45P mutation and is constitutively active in NCI-H295R (**Figure 6.1**).

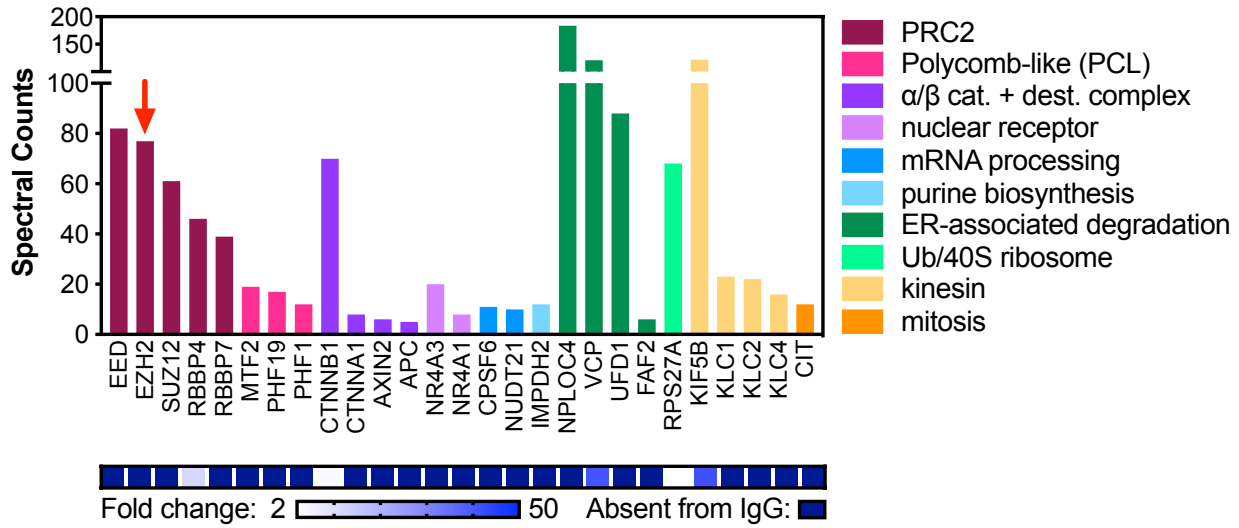

Figure 6.1. Complete EZH2 interactome reveals novel context- and tissue-specific binding partners. Complete proteome from MS of EZH2-directed nuclear co-IP reveals that EZH2 interactome is comprised predominantly of classical PRC2 and PCL proteins, complexes implicated in DNA repair, and novel binding partners critical for adrenocortical differentiation and cancer (notably: NR4A3, NR4A1, and p.S45P β-catenin). y-axis depicts spectral counts (SpC). EZH2 binding to p.S45P β-catenin was validated by targeted nuclear co-IP ($n \geq 5$, data not shown).

Given its abundance in the EZH2 interactome (**Figure 6.1**) and the well-established role of β-catenin in zG to zF lineage conversion and tumorigenesis (**Chapters 2 – 3**), we elected to focus our studies on the EZH2/β-catenin interaction. Several groups have identified an interaction between EZH2/β-catenin in other tissues, though not in the context of the p.S45P mutation (Anwar et al., 2018; Hoffmeyer et al., 2017; Zhu et al., 2016). In embryonic stem cells, Wnt-dependent induction of mesoderm differentiation may rely on simultaneous β-catenin-dependent activation of Wnt targets genes with β-

catenin/PRC2-dependent gene repression (Hoffmeyer et al., 2017). We therefore investigated if β-catenin is incorporated into the PRC2 directly, or if EZH2/β-catenin are a separate complex. Efforts to perform β-catenin-directed IP-MS were unsuccessful at identifying β-catenin transcription partners in NCI-H295R, secondary to the exceedingly high protein expression of β-catenin and high affinity of this protein for adherens junctions that contaminate nuclear lysates ((Yakulov et al., 2013), NCI-H295R active β-catenin-directed IP-MS, data not shown). We therefore sought to evaluate β-catenin's incorporation into the PRC2 by performing a PRC2-directed nuclear co-IP. While EZH2-directed nuclear co-IP consistently and successfully retrieved both SUZ12 and β-catenin, SUZ12-directed nuclear co-IP did not retrieve β-catenin. Furthermore, EZH2/H3K27me3/β-catenin possess only minimal overlap on chromatin, suggesting EZH2/β-catenin is a nuclear but off-chromatin complex (**Figure 6.2**).

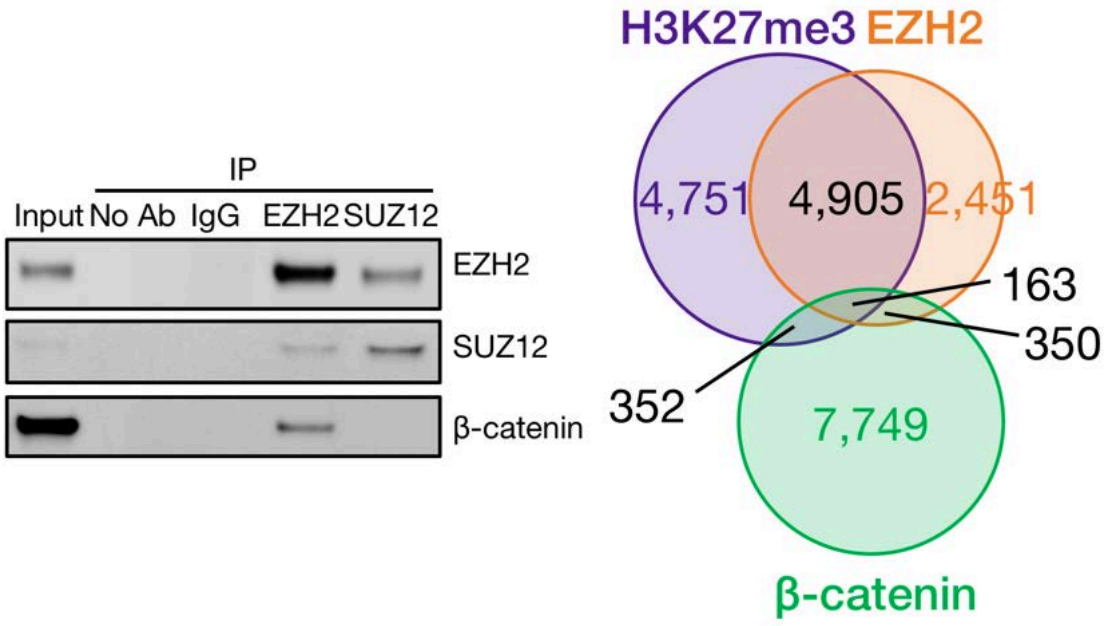

Figure 6.2. EZH2/β-catenin binding is likely PRC2 independent and off-chromatin.
Left, EZH2-directed nuclear co-IP consistently retrieves SUZ12 and β-catenin, while SUZ12-directed nuclear co-IP only retrieves EZH2. These data suggest EZH2/β-catenin interact in an off-chromatin complex. Representative western blot shown, $n \geq 2$. On top row, Input = 10% input, No Ab = IP performed with no antibody, IgG = IP performed with negative control IgG, EZH2 = IP performed with antibody against EZH2, SUZ12 = IP performed with antibody against SUZ12. Right, consistent with our nuclear co-IP results, overlap of NCI-H295R baseline H3K27me3, EZH2, β-catenin peaks reveals β-catenin only minimally interacts with PRC2 and EZH2 on chromatin.

Mutations in exon 3 of *CTNNB1* (like p.S45P) prevent β-catenin turnover and degradation, and mutant β-catenin therefore accumulates at exceeding high levels in cells expressing the mutation. In the case of NCI-H295R, transcription of *CTNNB1* is exclusively from the mutant allele, despite the presence of both wild type and mutant *CTNNB1* in the genome (data not shown). It is therefore possible that β-catenin binding to EZH2 reflects the abundance of this protein in a cancer cell expressing the mutation and may be non-specific or irrelevant for adrenocortical biology. Lack of specificity is unlikely given our criteria for calling protein-protein interactors (detailed in section **5.10**) and that we observed no interaction between β-catenin and SUZ12 or DNMT1 (β-

catenin/DNMT1 evaluated by IP-MS). However, evaluating an EZH2/β-catenin interaction in adrenal tissue would be ultimately required to support relevance for adrenal biology. This is challenging given the restricted population of adrenocortical cells that express nuclear β-catenin (**Chapter 2**), the large amount of tissue required to perform even one co-IP, and the relatively low sensitivity of this methodology. Our efforts to affinity purify an EZH2/β-catenin complex out of adrenal tissue were unsuccessful, though we could purify PRC2 by EZH2-directed co-IP on nuclear lysate prepared from 20 flash frozen mouse adrenals (**Figure 6.3**).

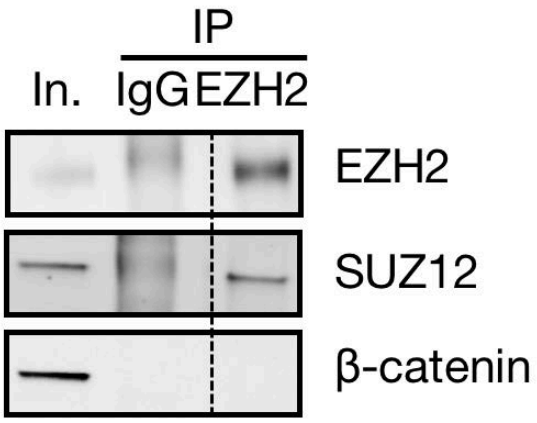

Figure 6.3. EZH2-directed nuclear co-IP on murine adrenal tissue identifies PRC2 but not EZH2/β-catenin.
Nuclear lysate was prepared from 20 flash frozen adrenals from male mice 2.5 months of age, which yielded limited material. Across the top of the image, In. = 10% input, IgG = IP with negative control Rb IgG, EZH2 = IP with EZH2. Western blot was performed to detect proteins shown right. In, IgG, and EZH2 were run on the same gel and epitopes were probed on the same membrane; irrelevant lanes are cropped at the dash line. Each mouse has 2 adrenals; preparing nuclear lysate for co-IP of two epitopes (IP for a second, irrelevant epitope cropped at the dashed line) and IgG would therefore require a minimum of 10 mice.

To evaluate a role for this complex in the adrenal cortex *in vivo*, we therefore sought an alternative approach that required relatively little amounts of tissue and could identify protein-protein interactions in less abundant cell populations. We optimized a technique that enables detection of protein-protein interactions *in situ* via proximity

ligation assay (PLA). PLA allows us to determine zonal and sub-cellular localization of endogenous protein-protein complexes on slides prepared from thin sections of FFPE tissue; each protein-protein interaction (proximity between antibodies detecting proteins can be a maximum of 40 nm apart) is visualized as a dot. PLA on the murine adrenal cortex identified EZH2/β-catenin complexes were nuclear and zonally distributed, with highest abundance in the adrenocortical zG/upper zF and following the Wnt signaling gradient (**Figure 6.4**).

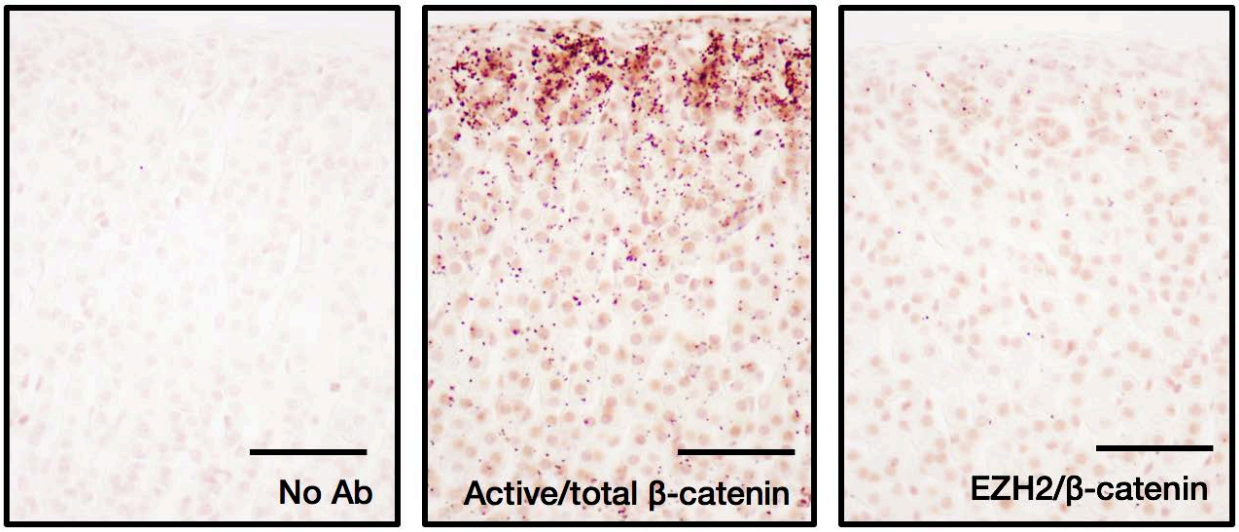

Figure 6.4. EZH2/β-catenin complex is present in the nucleus of adrenocortical zG/upper zF cells. PLA was performed on murine adrenals to examine EZH2/β-catenin binding *in vivo*. PLA was performed with no antibodies (negative control, left), two antibodies against β-catenin (positive control, middle), or antibodies recognizing EZH2 and β-catenin (right). The images in this figure are from a ~7 week old female that has undergone ACTH-dependent adrenal regeneration and experienced complete cortical renewal. Bar = 100 μm. PLA signal (reddish/pink dots, sub-nuclear in size) for EZH2/β-catenin is present, nuclear, and stronger in the zG/upper zF, mirroring the Wnt/β-catenin gradient (middle). No antibody is a standard negative control for PLA; additional studies not shown here show little to no signal when slides are incubated with antibodies only from a single species. Sections are shown with capsule aligned to the top of the field, analogous to **Figure 2.1**.

These data suggest that nuclear EZH2/β-catenin may be relevant for adrenocortical biology. Given that EZH2's interactions with its partners are preserved

even after EZH2i (**Figure 6.5**), it is possible that this EZH2/β-catenin complex even participates in the cellular response to EZH2 inhibition.

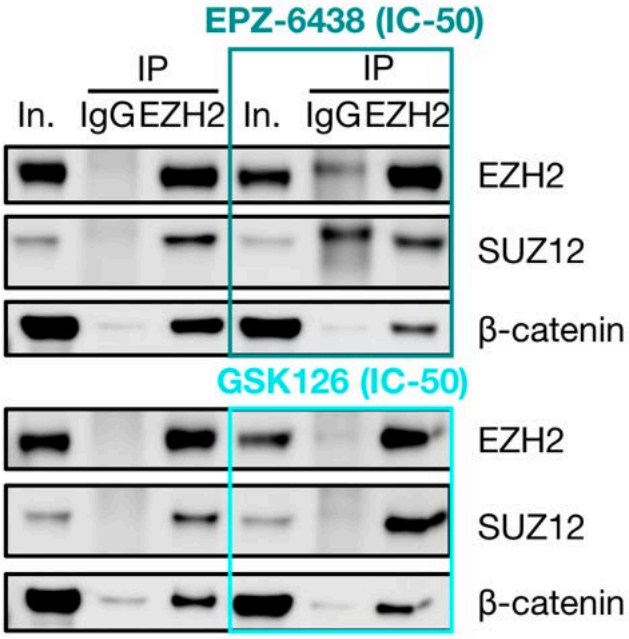

Figure 6.5. EZH2/SUZ12 and EZH2/β-catenin are preserved even after EZH2i.
EZH2-directed nuclear complex co-IP in vehicle- (left) or EZH2i-treated (right, boxed for each drug) cells demonstrates the persistence of EZH2/SUZ12 and EZH2/β-catenin complexes even after EZH2i. Representative experiment shown (n = 2 biological replicates). On top row, In = 10% input, IgG = IP with negative control Rb IgG, EZH2 = IP with EZH2. Band in EPZ-6438 IgG EZH2/SUZ12 blots is a non-specific band that occasionally emerges at this weight when using rabbit antibodies for IP and western detection and does not represent bona fide EZH2/SUZ12 signal.

6.4. Inhibition of EZH2 catalytic activity disrupts physiological differentiation programs

Our identification of a zonally distributed EZH2/β-catenin complex and the overlap between programs targeted by EZH2i with physiology (**Figure 5.18**) led us to ask if EZH2i was disrupting adrenocortical differentiation. In the mouse model of SF1-cre-driven *Ezh2* deficiency, mice develop profound defects in zonation, culminating ultimately in a failure of zG to zF lineage conversion, zF hypoplasia, and glucocorticoid insufficiency (Mathieu

et al., 2018). Human ACC and ACC cell lines exhibit a spectrum of zF differentiation, Wnt/β-catenin-dependent programming and proliferation, with CIMP-high ACC at the maxima of these three poles (**Chapters 3 – 4**, **Figure 6.6**).

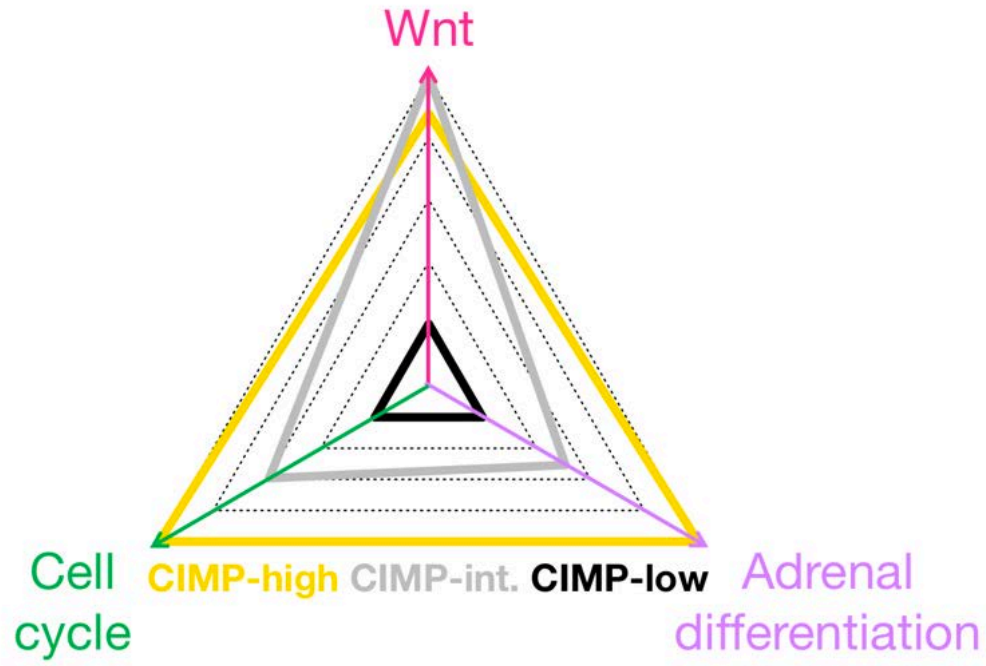

Figure 6.6. CIMP-high ACC possess hyperactivation of zF differentiation, Wnt/β-catenin-dependent programming, and proliferation.
GSVA (Hänzelmann et al., 2013) was used to calculate the expression score of genes that define adrenal differentiation (Zheng et al., 2016) or genes which were identified by Independent Component Analysis (ICA,(Biton et al., 2014)) to be regulated in a cell-cycle- or Wnt-dependent manner across ACC-TCGA (supported by significantly higher component score [$p < 0.05$, Mann Whitney] in tumors with driver alterations in the cell cycle or Wnt pathway components). The average score for CIMP-low, CIMP-int, and CIMP-high tumors along each axis is plotted in this radar plot, with values mapped onto an arbitrary scale of 1-5 dictating position along each axis. CIMP-low tumors have uniformly low expression of adrenal differentiation, Wnt programming and cell cycle activation. CIMP-intermediate tumors have relatively higher activation of these programs, and maximize Wnt signaling. CIMP-high tumors have the highest activation of all three programs.

To evaluate if EZH2i disrupted zF differentiation, we wanted to compare the transcriptome of zF-differentiated to EZH2i-treated NCI-H295R. We treated the NCI-H295R with zF differentiation agent forskolin and profiled the transcriptome by RNA-seq. Despite that CIMP-high as a class is at the zF differentiation maximum across human

ACC (**Figure 6.6**), the presence of mutant *CTNNB1* in this cell line and high levels of nuclear β-catenin are likely to enable faithful responsiveness to forskolin and refractory response to Wnt/β-catenin stimulants, analogously to the Y1 cell line (**Chapter 3**). Indeed, forskolin administration increased expression of zF differentiation genes, shut down expression and chromatin accessibility of zG/canonical Wnt target genes, and potently induced expression of steroidogenic enzymes in NCI-H295R (**Figure 6.7**).

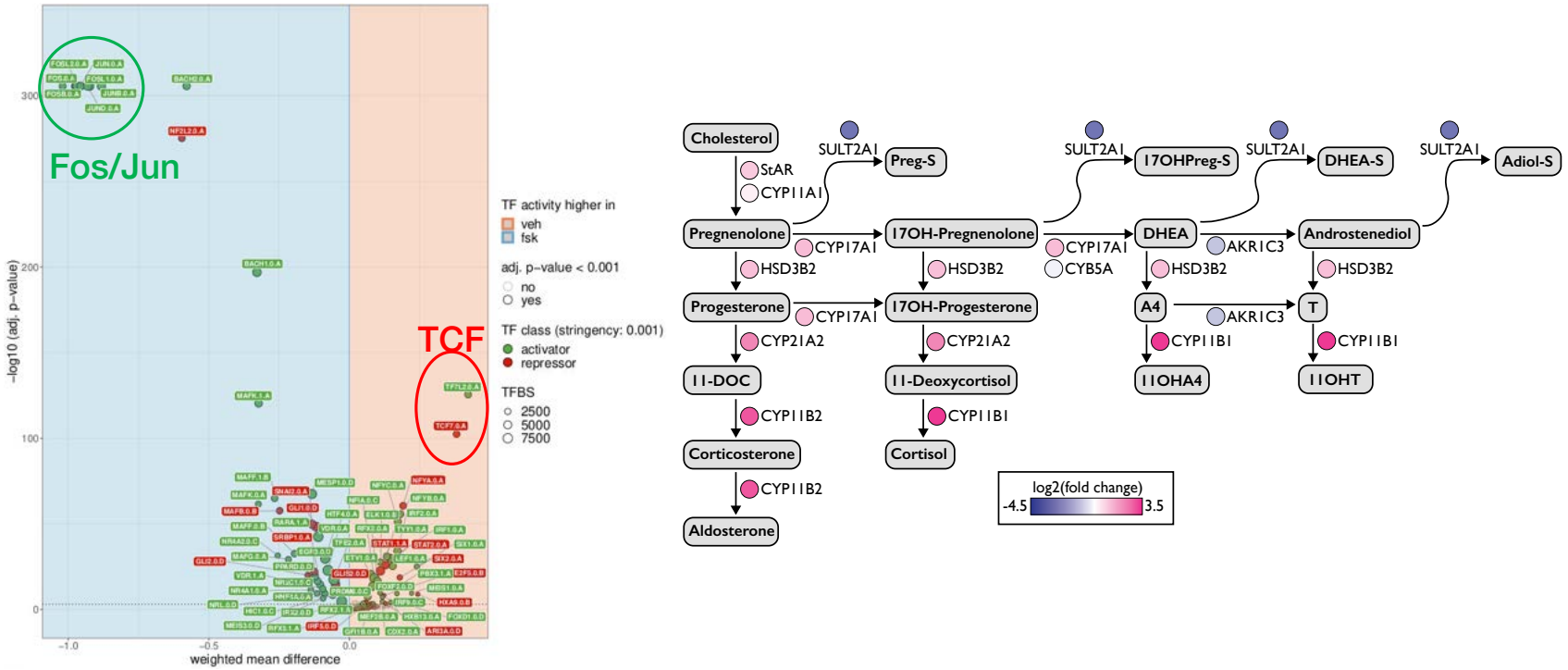

Figure 6.7. Forskolin induces faithful zF differentiation and steroidogenesis in NCI-H295R.
Left, *diffTF* analysis integrating RNA-seq and ATAC-seq data from NCI-H295R treated with forskolin for 48 hours vs. vehicle control reveals that forskolin induces a prominent induction of immediate early response programs (Fos/Jun) at the expense of shutting down endogenous Wnt/β-catenin signaling (TCF). The induction of immediate early response programs is consistent with known mechanisms of action of PKA (**Figure 2.4**). Right, also consistent with known roles of PKA signaling, forskolin potently induced expression of steroidogenic enzymes, consistent with induction of faithful zF differentiation in NCI-H295R.

Strikingly, comparison of RNA-seq data from EZH2i and forskolin-treated cells revealed that EZH2i disrupted roughly 70% of genes differentially expressed following forskolin administration, and potently suppressed expression of steroidogenic enzymes. EZH2i-induced suppression of steroidogenic enzymes was dose-dependent and observed with two different classes of EZH2i. Moreover, pretreatment of NCI-H295R with EZH2i prior to forskolin administration diminished forskolin-induced silencing of canonical Wnt targets and induction of steroidogenic enzymes (**Figure 6.8**).

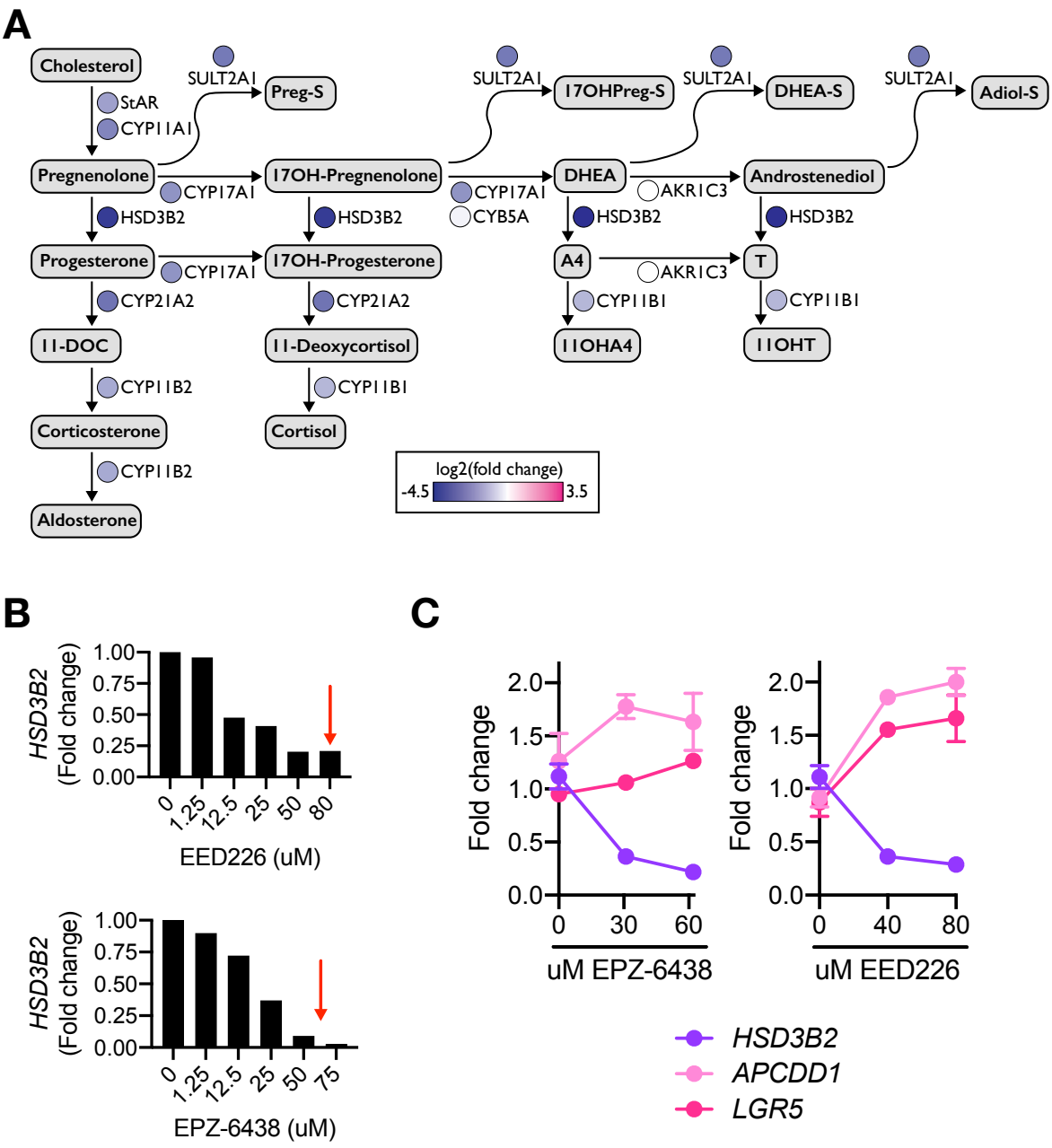

Figure 6.8. EZH2i reverses zF differentiation.
A. RNA-seq from NCI-H295R treated with EZH2i demonstrates that EZH2i represses expression of steroidogenic enzymes induced by forskolin (**Figure 6.7**) and indicative of steroidogenic differentiation. B. Two classes of EZH2i repress *HSD3B2* in a dose-dependent manner, prior to the IC-50 (indicated by the red arrow; in the case of EPZ-6438 IC-50 is at 62 μM which was not tested in this experiment). Representative experiment shown, n ≥ 3. C. NCI-H295R were pretreated with EZH2i for 96 hours at the indicated doses (either the IC-50 or half of the IC-50). After EZH2i, media was changed for media containing 10 μM forskolin. After 48 hours of forskolin stimulation, cells were harvested for analysis of gene expression by qPCR. For both EZH2i, EZH2i pre-treatment disrupted forskolin's induction of steroidogenic enzymes (*HSD3B2*) and repression of canonical Wnt targets (*APCDD1, LGR5*). n ≥ 2.

These observations are consistent with a role for EZH2 in programming cellular response to PKA (Mathieu et al., 2018), though likely not through the proposed mechanism of disruption of expression of PKA signaling components given EZH2i induces broad disruption of the transcriptome (**Figure 5.19**). Indeed, we observed that EZH2i reversed all three core transcriptional modules of CIMP-high ACC, while forskolin could only induce differentiation at the expense of proliferation and Wnt-dependent programming (**Figure 6.9**).

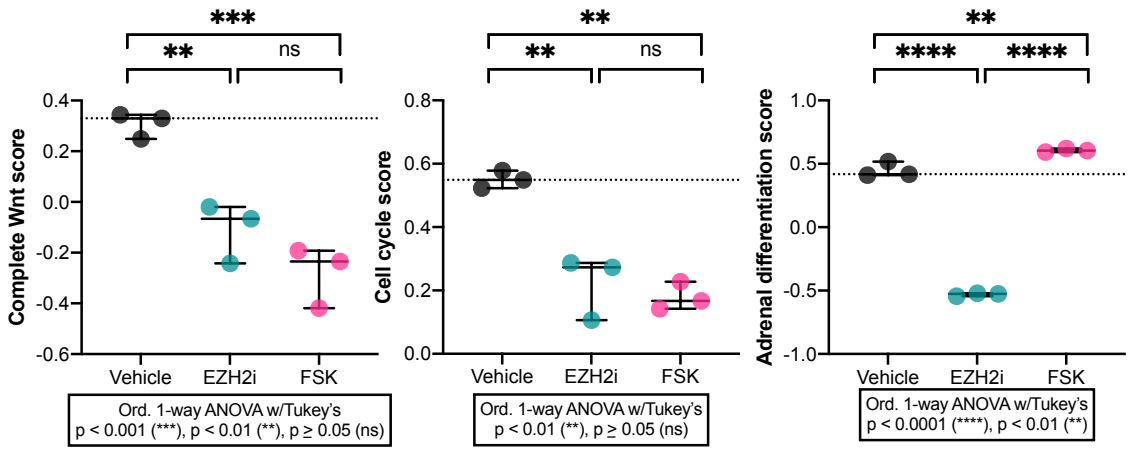

Figure 6.9. EZH2i reverses the core transcriptional features of CIMP-high ACC.
Wnt, cell cycle, and adrenal differentiation scores in NCI-H295R were quantified from RNA-seq derived from baseline (Vehicle) NCI-H295R or after EZH2i or forskolin (FSK) administration using GSVA as in **Figure 6.6**, and demonstrates that EZH2i reverses all three CIMP-high defining programs, while forskolin increases adrenal differentiation at the expense of Wnt signaling and cellular proliferation.

In addition to diminishing clonogenic potential (**Figure 5.9**) and despite failing to modulate the DNA methylome (**Chapter 5**), EZH2i had a potent impact on transcriptional programs that define CIMP-high ACC (**Figure 6.9**). This data suggests that EZH2 coordinates a chromatin landscape that stabilizes the differentiated and Wnt-active CIMP-high transcriptional state that enables sustained proliferation. Given that part of this

transcriptional state reflects Wnt/β-catenin transcriptional activity and that β-catenin is a major binding partner of EZH2 not disrupted by EZH2i (section **6.3**), we next sought to investigate β-catenin's role on chromatin.

6.5. An epigenetic program coordinated by SF1/β-catenin regulates adrenal differentiation

We performed ChIP-seq for β-catenin in NCI-H295R at baseline, and identified that, as expected, β-catenin principally binds active and accessible chromatin regions. We performed motif enrichment for β-catenin peaks and were surprised to observe a substantial enrichment for the SF1 motif, enriched even more significantly than motifs corresponding to canonical Wnt/β-catenin transcription factors TCF/LEF (**Figure 6.10**).

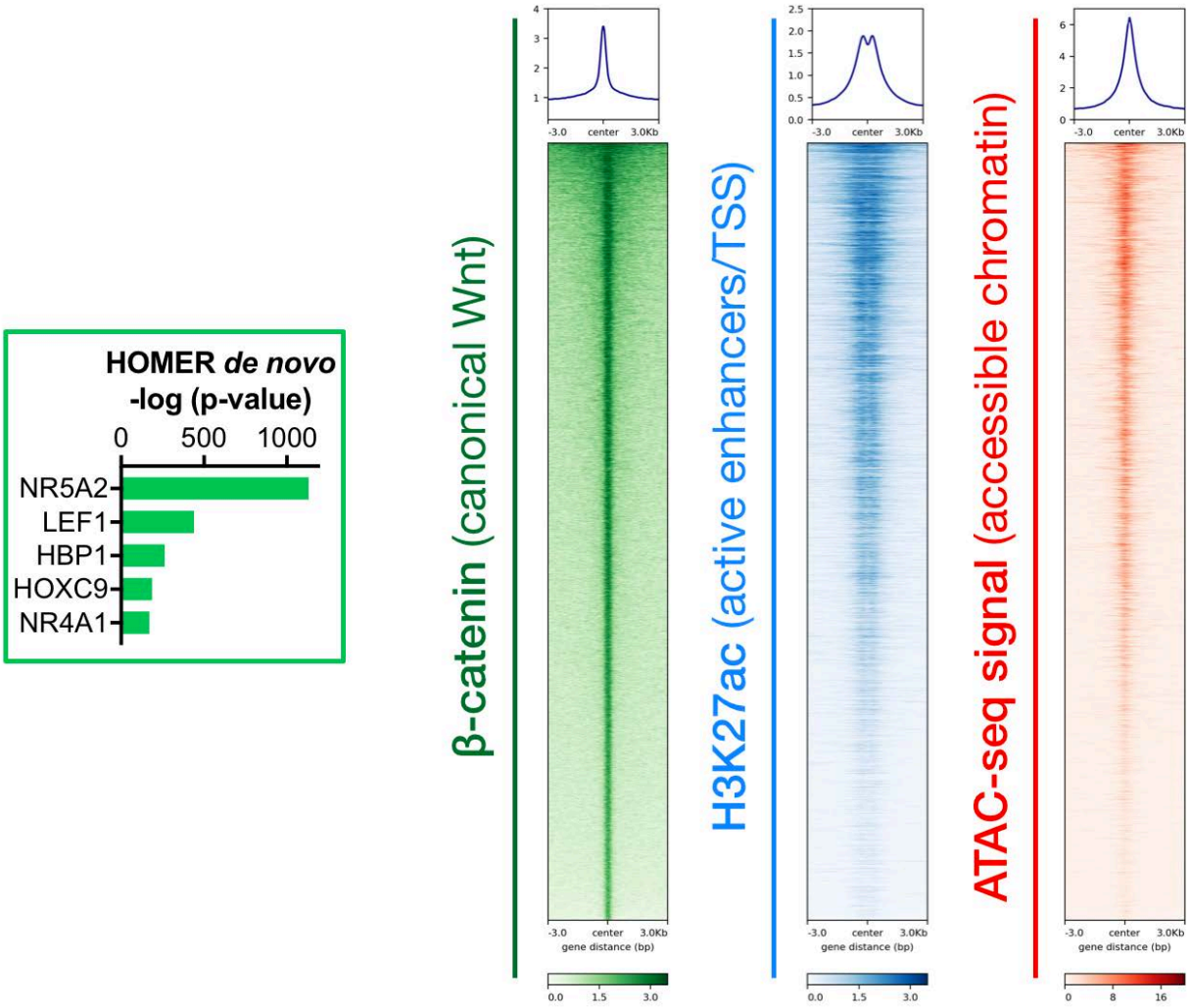

Figure 6.10. β-catenin binds SF1 and TCF/LEF motifs at active and accessible chromatin genome-wide.
Measurement of genome-wide distribution of β-catenin, H3K27ac, and chromatin accessibility at baseline β-catenin binding sites (8,164 peaks) in NCI-H295R reveals that the vast majority of β-catenin peaks are decorated with H3K27ac and are also accessible. Strikingly, motif enrichment for β-catenin identified a highly significant enrichment for regions bearing the SF1 motif (depicted in the bar graph, left, as NR5A2), far exceeding the enrichment for regions bearing canonical LEF motifs. This data suggested β-catenin may co-regulate SF1-dependent the transcriptional landscape.

We had previously performed SF1-directed IP-MS and had observed that p.S45P β-catenin is also a major binding partner of SF1 in NCI-H295R (**Figure 6.11**).

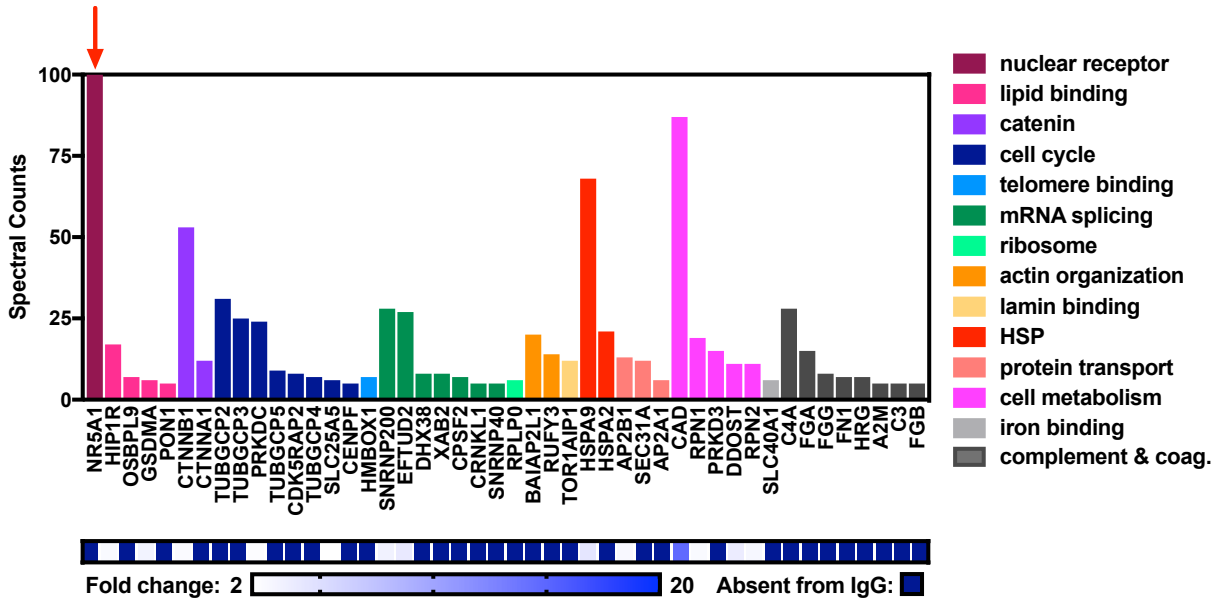

Figure 6.11. SF1-directed IP-MS identifies β-catenin as the dominant binding partner.
Complete proteome from MS of SF1-directed nuclear co-IP identifies β-catenin as a dominant binding partner. y-axis depicts spectral counts (SpC). SF1 binding to β-catenin was validated by targeted nuclear co-IP (n = 2, data not shown). SF1 antibody used for IP-MS is a custom polyclonal antibody purified from rabbit sera. Iron binding and complement/coagulation components (grey) likely reflect contaminants present in the antibody solvent.

An SF1/β-catenin interaction in the Y1 cell line and adrenal cortex has been previously reported by our group (Gummow et al., 2003), and is thought to regulate gene expression in a context-specific manner (Mizusaki et al., 2003). We could also demonstrate the presence of zonally distributed SF1/β-catenin complexes in the murine adrenal cortex by PLA (**Figure 6.12**).

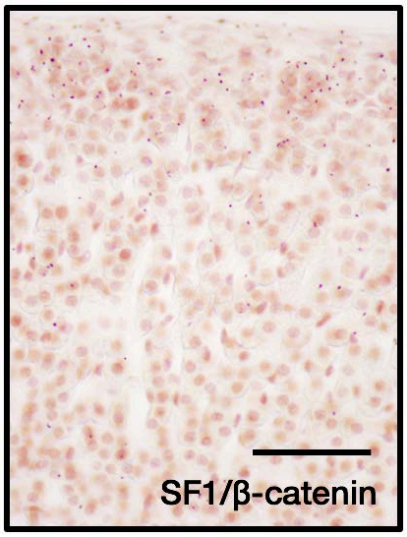

Figure 6.12. SF1/β-catenin is zonally distributed in the murine adrenal cortex.
PLA was performed on murine adrenals to examine SF1/β-catenin binding *in vivo*. PLA was performed with no antibodies, two antibodies against β-catenin, antibodies recognizing EZH2 and β-catenin (**Figure 6.4**), or antibodies recognizing SF1 and β-catenin (above). The images in this figure are from the same ~7 week old female that has undergone ACTH-dependent adrenal regeneration and experienced complete cortical renewal in **Figure 6.4**. Bar = 100 μm. PLA signal (reddish/pink dots, sub-nuclear in size) for SF1/β-catenin is abundant, nuclear, and stronger in the zG/upper zF, mirroring the Wnt/β-catenin gradient (**Figure 6.4**). Sections are shown with capsule aligned to the top of the field, analogous to **Figure 2.1**.

The interaction interface between SF1/β-catenin has been mapped and is believed to reside in the C-terminus of β-catenin, and hence not disrupted by modifications to exon 3 (Mizusaki et al., 2003). An interaction between SF1 and p.S45P β-catenin has not previously been described, nor is it well understood if SF1/β-catenin effect global coordination of gene expression programs or simply co-occupy few loci. We then performed ChIP-seq for SF1, and identified that, as expected, SF1 binds accessible and active chromatin regions (data not shown). There was also substantial overlap between SF1 and β-catenin binding sites (**Figure 6.13**), and SF1/β-catenin sites encompassed predominantly distal CREs (**Figure 6.14**). Given the strong overlap of SF1 and β-catenin with H3K27ac and accessible chromatin, these data suggest that SF1/β-catenin

coordinate transcriptional programming genome-wide, predominantly through enhancer programming.

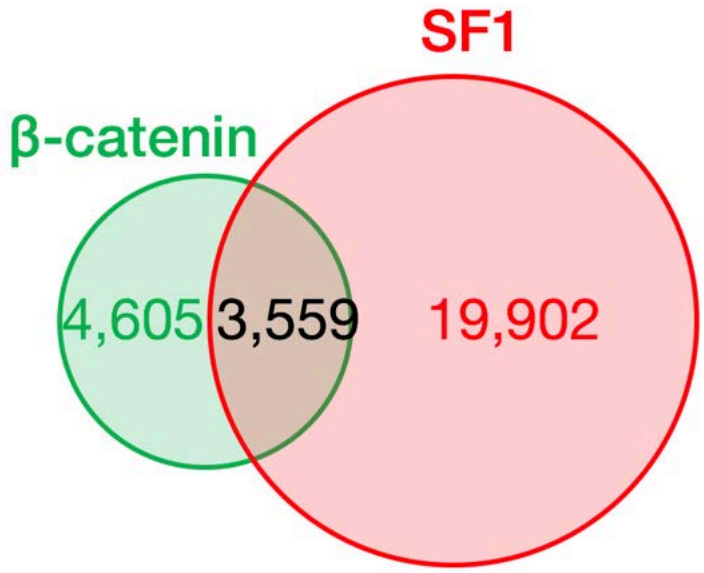

Figure 6.13. SF1/β-catenin overlap genome-wide.
SF1 occupies many sites in the NCI-H295R genome, with >20,000 peaks. β-catenin's binding profile is more restricted, and nearly half of all β-catenin peaks colocalize with SF1.

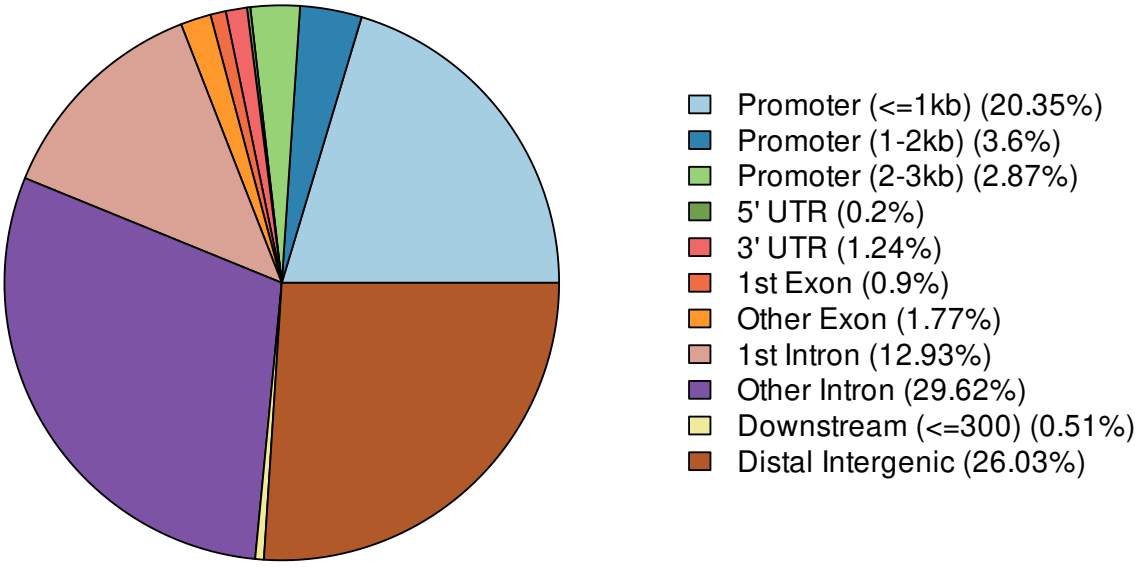

Figure 6.14. SF1/β-catenin predominantly occupy distal CREs.
Characteristics of SF1/β-catenin binding sites identifies that 65% of peaks are >1000 bp away from a TSS and are therefore distal.

Enhancers serve as critical nodes for regulation of gene expression, as a single enhancer may coordinate the expression of many promoters, and therefore many genes (**Table 1.1**). A special class of enhancers, super-enhancers (SE), with high density occupancy of Mediator (a complex that bridges enhancer/promoter contacts, (Kagey et al., 2010)) has been implicated in lineage-specific programming (Hnisz et al., 2013; Sabari et al., 2018; Whyte et al., 2013; Zamudio et al., 2019). SEs also possess high density deposition of H3K27ac and occupancy of lineage-defining transcription factors, and drive pervasive cell-of-origin transcriptional programs in development and disease (Hnisz et al., 2013; Hnisz et al., 2015; Whyte et al., 2013). Bioinformatically, SEs can be identified by "stitching" nearby enhancers and ranking them by H3K27ac density (Lovén et al., 2013; Pott and Lieb, 2015; Whyte et al., 2013). We wanted to determine if SE programming in CIMP-high ACC is coordinated by SF1/β-catenin, and if this coordination reflects physiological programming or is cancer specific. We performed SE analysis on NCI-H295R ChIP-seq, and compared NCI-H295R SE to physiological adrenal SE. >90% of adrenal SE retain H3K27ac deposition in NCI-H295R, but ~70% of these enhancers are demoted from SE status in this cell line. ~80% of SE in NCI-H295R are novel, and ~70% of all NCI-H295R SE are bound by both SF1 and β-catenin. This data suggests SF1/β-catenin together are coordinating a master switch of adrenal differentiation in NCI-H295R, and represents a major departure from SE regulation in the physiological adrenal gland, wherein only ~30% of SE possess SF1/β-catenin occupancy in NCI-H295R (**Figure 6.15**).

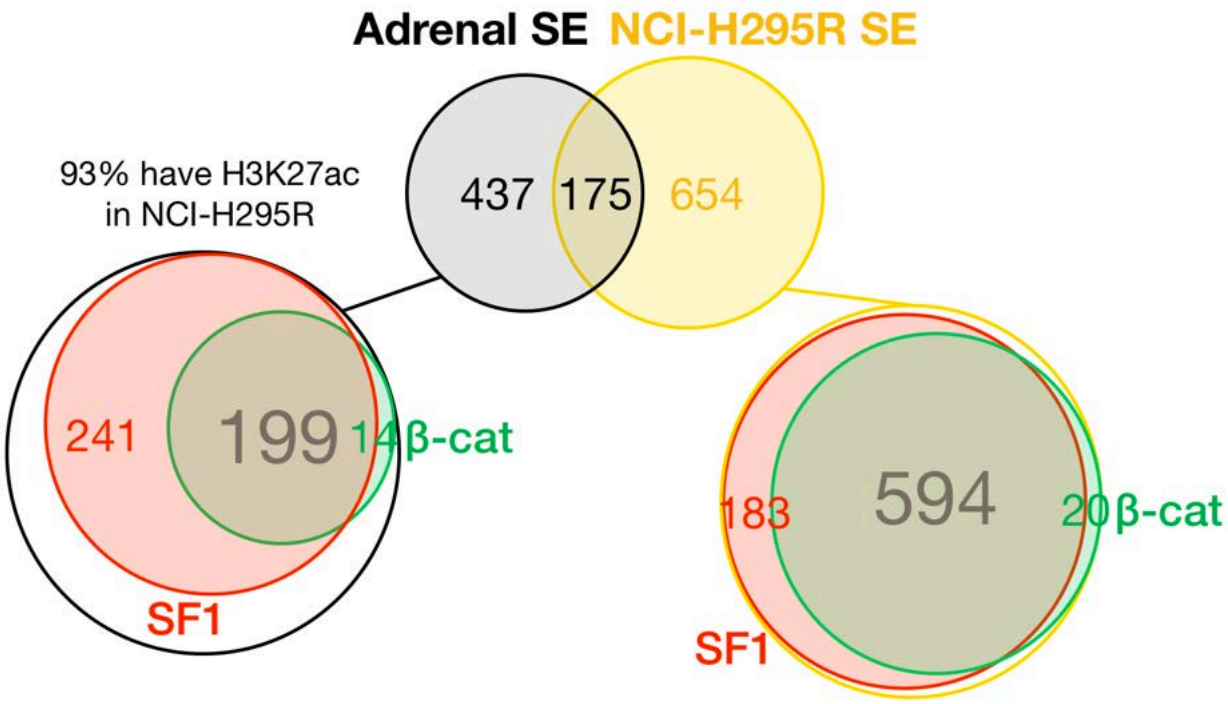

Figure 6.15. SF1/β-catenin coordinate lineage-defining super-enhancers in NCI-H295R.
Comparison of NCI-H295R SE (identified using *ROSE*) and physiological adrenal SE (obtained from 3DIV analysis on ENCODE samples (Kim et al., 2020; Yang et al., 2018)) identifies many novel SE in NCI-H295R. Despite the small overlap between adrenal SE and NCI-H295R SE, 93% of adrenal SE still retain H3K27ac in NCI-H295R, suggesting that adrenal SE are downgraded in NCI-H295R but not totally decommissioned. Evaluation of SF1/β-catenin occupancy at NCI-H295R reveals that 72% of NCI-H295R SE are regulated by both SF1 and β-catenin. This is in striking contrast to adrenal SE, in which only 32% possess SF1 and β-catenin in NCI-H295R. These data suggest that SF1/β-catenin in NCI-H295R are monopolizing machinery required for SE establishment (for example CBP) at the expense of other transcriptional programs.

As expected considering the predicted tissue-defining roles of SEs (Hnisz et al., 2013; Sabari et al., 2018; Whyte et al., 2013; Zamudio et al., 2019), SF1/β-catenin SEs regulate expression of many genes that are critical for adrenocortical and steroidogenic identity, including *HSD3B2* and *NR5A1* itself (data not shown here, but these SEs will be later explored in **Figure 6.22**). These SEs are also present in the physiological adrenal gland.

Finally, to extend this analysis to ACC more broadly, we sought to determine if SF1/β-catenin sites are differentially accessible across CIMP classes in ACC-TCGA, as

would be expected given the augmentation of both Wnt/β-catenin and adrenocortical differentiation in these tumors (**Figure 6.6**). Though there are only few ACC-TCGA samples with ATAC-seq profiling and our analyses are indeed preliminary, we observed a significant increase in accessibility of SF1/β-catenin co-targets in CIMP-high tumors (**Figure 6.16**).

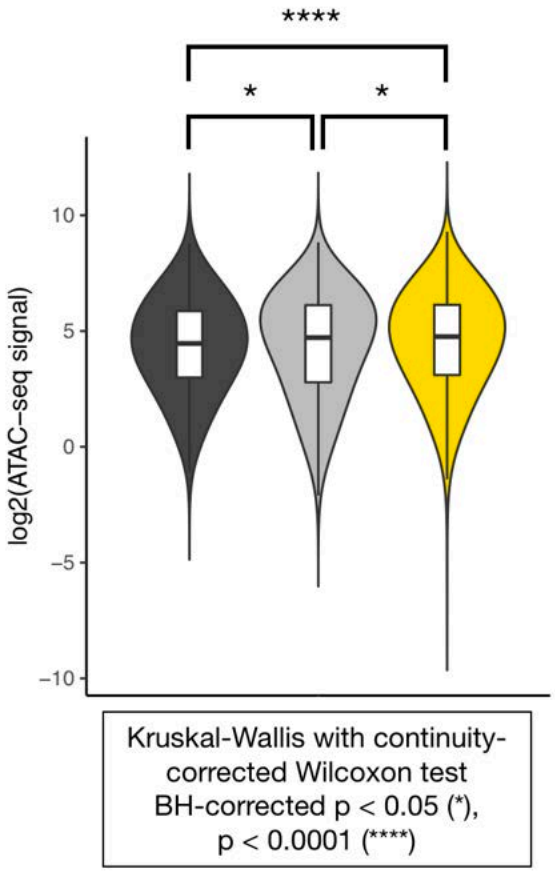

Figure 6.16. SF1/β-catenin co-targets are more accessible in CIMP-high ACC.
Chromatin accessibility signal at SF1/β-catenin co-targets was measured in ACC-TCGA samples with ATAC-seq data (n = 9, from (Corces et al., 2018)), sorted by CIMP status. Though only few ACC-TCGA samples have ATAC-seq data, this analysis revealed that SF1/β-catenin co-targets are increasingly accessible in CIMP-intermediate and CIMP-high ACC.

Taken together, our studies in NCI-H295R identify a novel SF1/β-catenin-dependent differentiation axis that exists in physiological tissue and is augmented in

CIMP-high ACC. Identifying SF1/β-catenin-dependent SE in physiological adrenal as well as zonally distributed SF1/β-catenin and EZH2/β-catenin suggests that these complexes may be present prior to or in early stages of carcinogenesis and are selected for through dysplasia and malignancy. We therefore next investigated if SF1/β-catenin and EZH2/β-catenin accompany adrenocortical carcinogenesis.

6.6. EZH2/β-catenin and SF1/β-catenin are conserved in mouse models of adrenocortical carcinogenesis

Our collaborators recently developed an autochthonous mouse model of β-catenin/p53-driven dysplasia to metastatic glucocorticoid-producing ACC derived from definitive adrenocortical cells expressing CYP11B2 ((Borges et al., 2020), **Table 2.4**). The genetic and endocrine features of this model render it comparable to COC3/CIMP-high ACC (**Chapter 3**) and enable visualization of the full spectrum of carcinogenesis. We used PLA to measure the abundance of EZH2/β-catenin and SF1/β-catenin complexes during hyperplasia (**Figure 6.17**), carcinoma formation (**Figure 6.18**), and metastasis (**Figure 6.19**), and observed the hyperplastic transformation and metastatic seeding of cells uniformly expressing EZH2/β-catenin and SF1/β-catenin complexes.

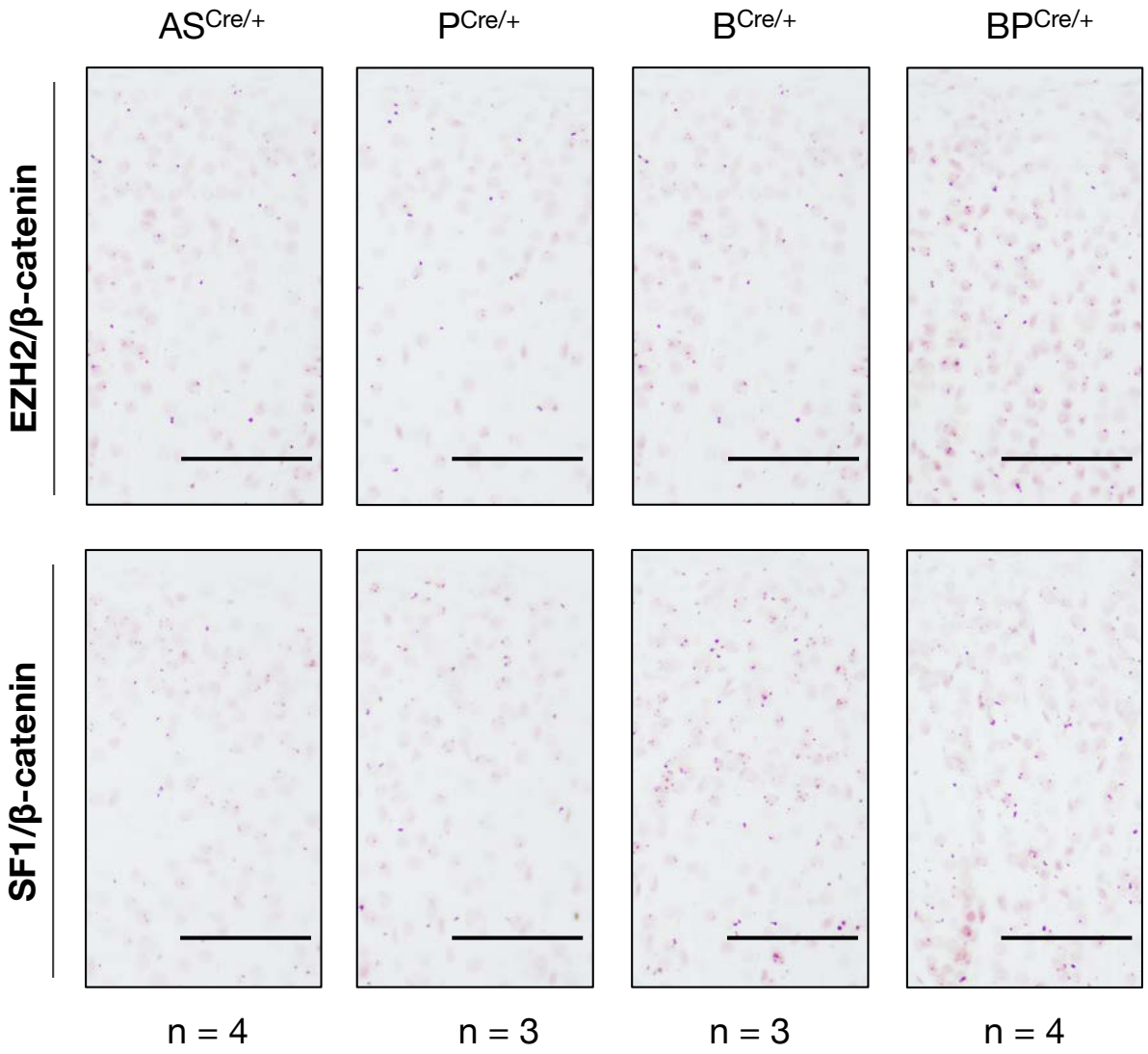

Figure 6.17. EZH2/β-catenin and SF1/β-catenin complexes increase across β-catenin/p53-dependent hyperplasia.

3 month old mice from β-catenin/p53-driven mouse model were evaluated for the presence of adrenocortical EZH2/β-catenin and SF1/β-catenin complexes as in **Figures 6.4** and **6.12.** No antibody negative control was also performed (not shown). At this stage in tumorigenesis, all mice with both β-catenin GOF and p53 deletion possess adrenocortical hyperplasia and have not yet developed malignancy. $AS^{Cre/+}$ = control mice, age matched, $B^{Cre/+}$ = $AS^{Cre/+}$ $Ctnnb1^{fl(ex3)/+}$, $P^{Cre/+}$ = $AS^{Cre/+}$ $Trp53^{fl/fl}$, $BP^{Cre/+}$ = $AS^{Cre/+}$ $Ctnnb1^{fl(ex3)/+}$ $Trp53^{fl/fl}$. PLA demonstrates an increase in abundance in EZH2/β-catenin complexes in $BP^{Cre/+}$, consistent with an induction in *Ezh2* expression in these mice at this timepoint (data not shown), suggesting formation of EZH2/β-catenin may be rate limited by *Ezh2* expression. PLA also demonstrates an increase in SF1/β-catenin complexes in both $B^{Cre/+}$ and $BP^{Cre/+}$ mice, suggesting that the formation of SF1/β-catenin may be rate limited by nuclear β-catenin. Number of biological replicates indicated below each panel of images. Bar = 100 μm. Sections are shown with capsule aligned to the top of the field, analogous to **Figures 6.4** and **6.12**.

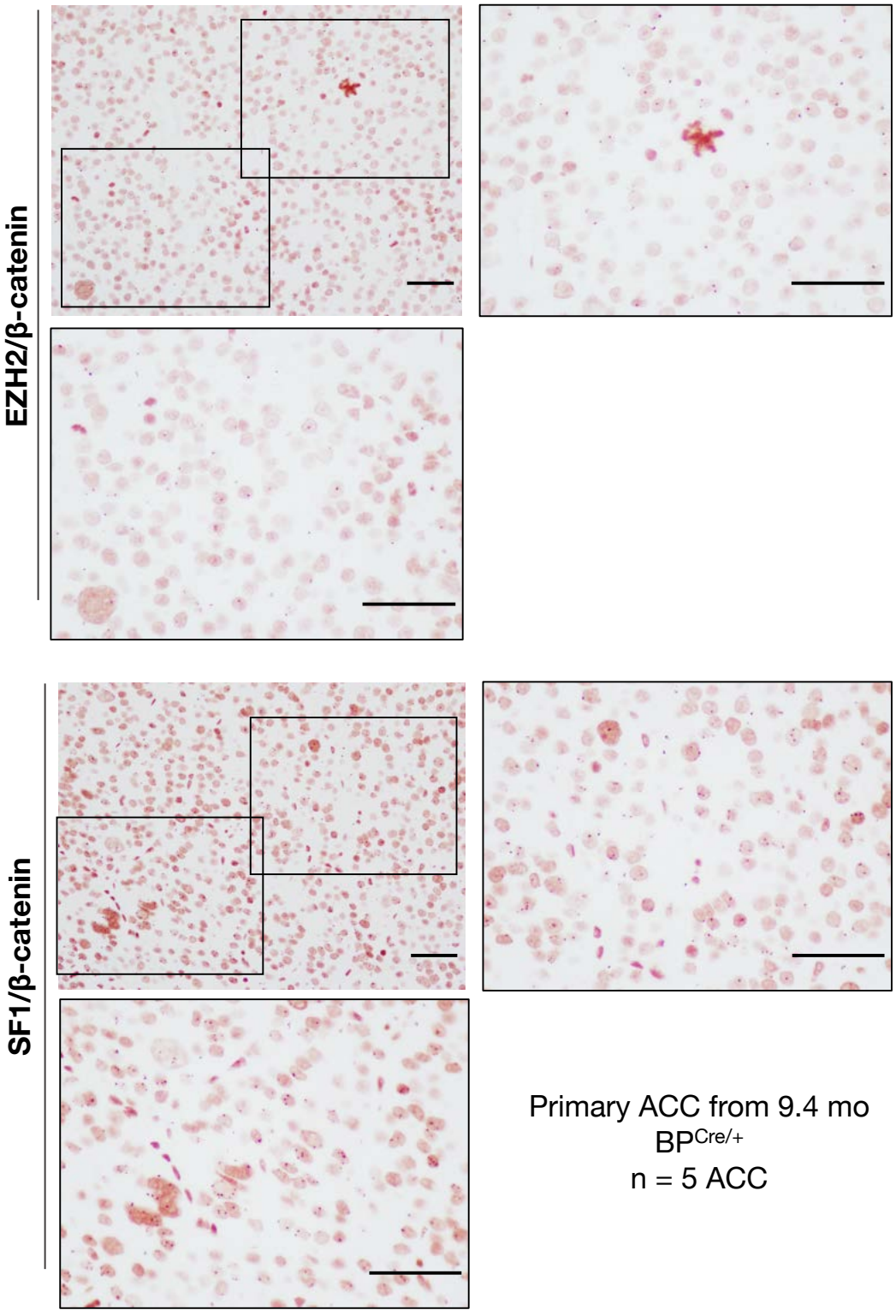

Figure 6.18. EZH2/β-catenin and SF1/β-catenin complexes persist through β-catenin/p53-dependent malignant transformation.
Lower magnification image in the top left corner of each set. Boxes are drawn to indicate location of higher magnification images located to the right and below each low magnification image. Bar = 100 μm.

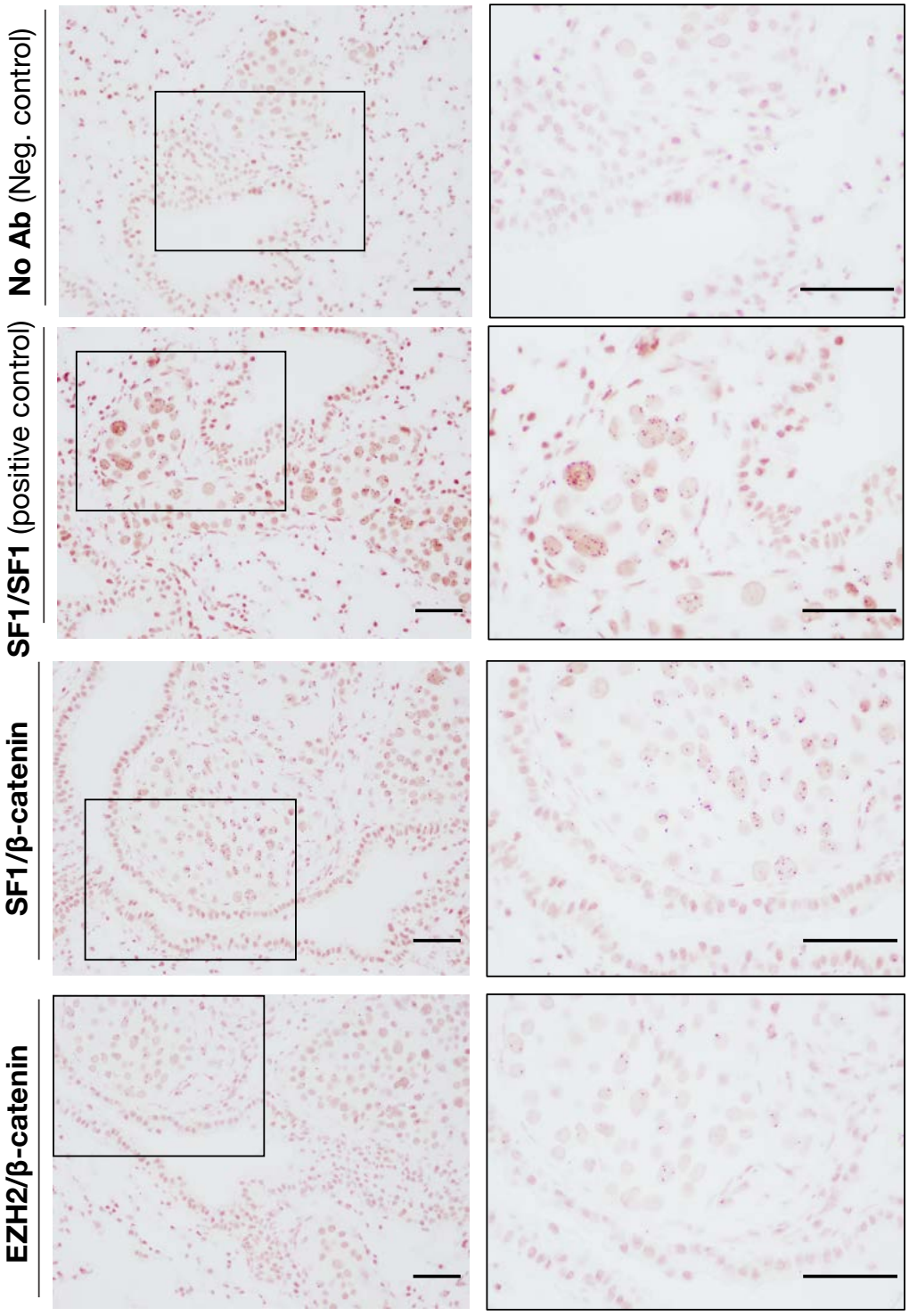

Figure 6.19. EZH2/β-catenin and SF1/β-catenin complexes persist at distal metastases.
EZH2/β-catenin and SF1/β-catenin complexes can be visualized in tissue that resemble tumor tissue (pleomorphic nuclei, abnormal location, etc.) and are largely excluded from normal-appearing adjacent respiratory epithelium. Bar = 100 μm.

These data demonstrate that persistence of EZH2/β-catenin and SF1/β-catenin complexes is conserved across human and murine carcinogenesis, and strongly suggest that the programs correlated with or perhaps directly coordinated by these complexes are subject to positive selection through all phases of COC3/CIMP-high-like adrenal cancer evolution.

6.7. EZH2i erases SF1/β-catenin-dependent CRE programming

The presence of EZH2/β-catenin and SF1/β-catenin *in vivo* was compelling, given our observation that EZH2/β-catenin is an off-chromatin complex that persists with EZH2i (section **6.3**). We also identified that EZH2i reverses adrenal differentiation in CIMP-high ACC (section **6.4**), which is likely nearly entirely coordinated by SF1/β-catenin (section **6.5**). Furthermore, many genes that are regulated by SF1/β-catenin enhancers are repressed by EZH2i (**Figure 6.20**).

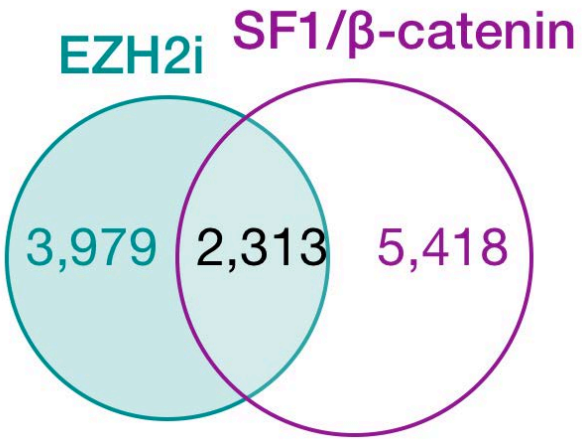

Figure 6.20. EZH2i represses expression of genes putatively regulated by SF1/β-catenin enhancers. Genes putatively targeted by active SF1/β-catenin enhancers were identified by overlapping human adrenal promoter capture Hi-C contact tables (Jung et al., 2019) with H3K27ac signal as in **Chapter 2** and then overlapping enhancers with the consensus SF1/β-catenin peak set. More than a third of all genes downregulated with EZH2i are putatively regulated by SF1/β-catenin enhancers. Bearing in mind the

profound differences between enhancer programming in ACC and physiology (**Figure 6.15**), it is possible that this number would be even higher if we had Hi-C data from human ACC to overlap peaks with.

These data led us to suspect that EZH2i may disrupt SF1/β-catenin recruitment genome-wide, which we evaluated by ChIP-seq. Strikingly, we observed that SF1 and β-catenin were globally evicted at SF1 targets by EZH2i, at the expense of aberrant EZH2 recruitment (**Figure 6.21**).

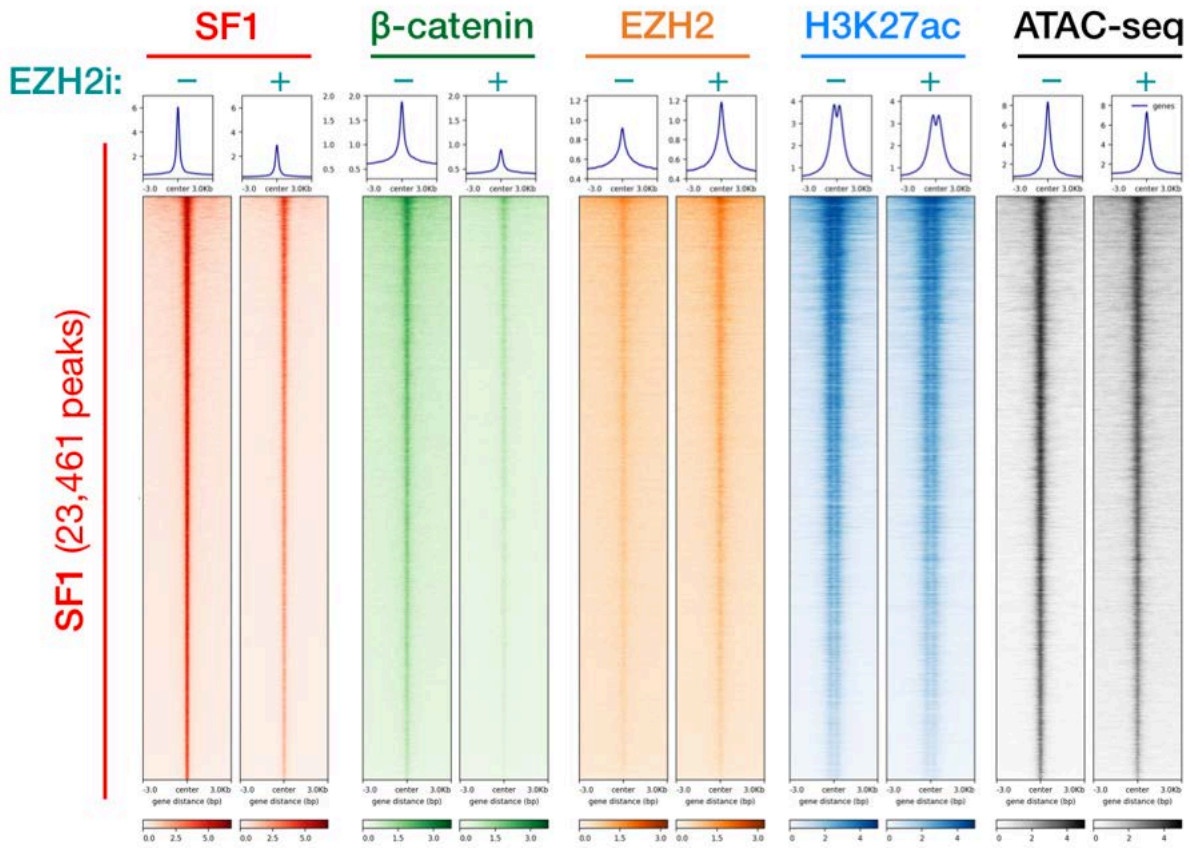

Figure 6.21. EZH2i evicts SF1 and β-catenin genome wide.
Heatmap depicts SF1, β-catenin, EZH2, H3K27ac, and chromatin accessibility (ATAC-seq) signal at baseline SF1 peaks at baseline (-) or with EZH2i (+). EZH2i in NCI-H295R leads to global eviction of SF1 and β-catenin at baseline SF1 binding sites coincident with aberrant recruitment of EZH2 and decreased H3K27ac and chromatin accessibility. Not shown, 56% of baseline β-catenin peaks do not possess SF1, and EZH2i also evicts β-catenin from those sites.

We were struck by the impact of EZH2i on SF1 and β-catenin recruitment. Given the preservation of EZH2/β-catenin following EZH2i (**Figure 6.5**) and the impact of EZH2i on EZH2 recruitment genome-wide (**Figures 6.21**, **5.17**), we speculated that EZH2i expunges β-catenin from chromatin secondary to the "excess" of EZH2 induced by its eviction from H3K27me3 domains. Given that we did not observe a direct interaction between EZH2 and SF1 (**Figures 6.1**, **6.11**), it was difficult to rationalize why EZH2i also disrupted SF1 solo programming. However, inspecting the prototype *NR5A1* and *HSD3B2* SEs before and after EZH2i, we observed that EZH2i disrupted SF1 and β-catenin binding to these loci and this was associated with a decrease in gene expression (**Figure 6.22**).

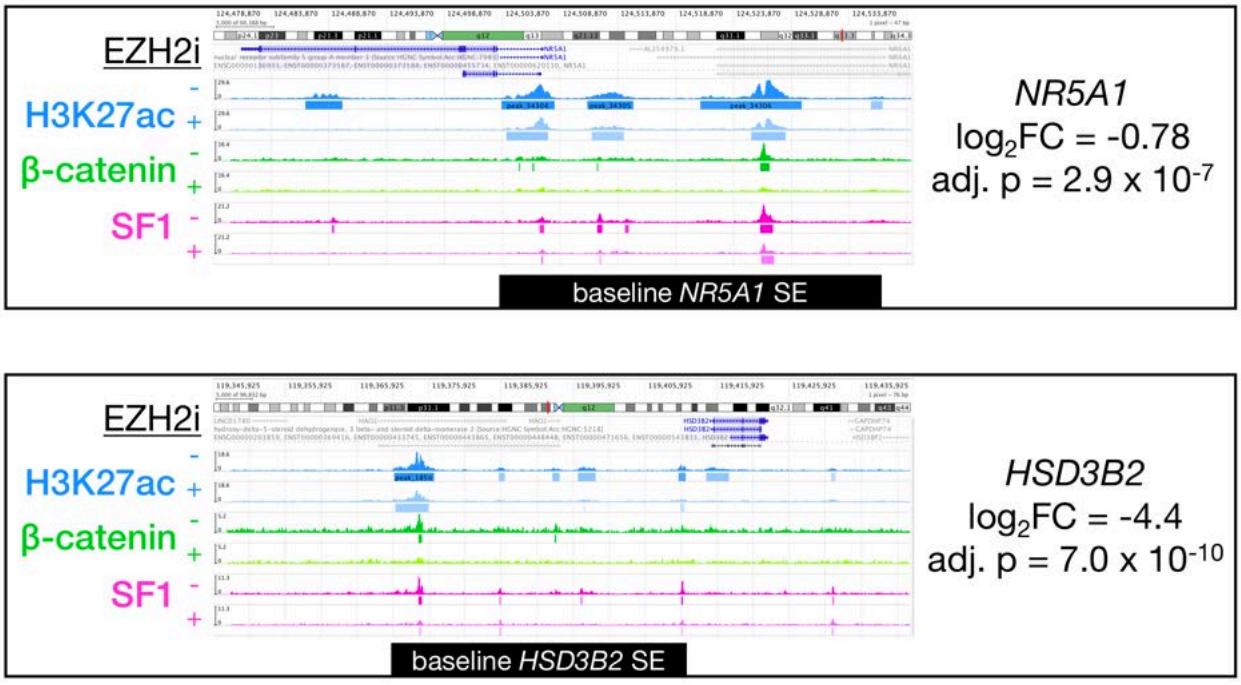

Figure 6.22. SF1/β-catenin recruitment to *NR5A1* and *HSD3B2* super-enhancers is disrupted by EZH2i and associated with a decrease in gene expression.
Genome browser view of H3K27ac, β-catenin, and SF1 signal at baseline (-) or with EZH2i (+) at SE spanning the *NR5A1* (top) or *HSD3B2* (bottom) loci demonstrates diminishing SF1 signal and disappearing β-catenin peaks, associated with a substantial and significant decrease in gene expression (right, from NCI-H295R RNA-seq). SE were identified using *ROSE* and assigned to *NR5A1* and *HSD3B2* by overlapping human adrenal promoter capture Hi-C contact tables (Jung et al., 2019) as in **Chapter 2**.

This suggested that the impact of EZH2i on SF1 recruitment genome-wide may be a consequence of disrupted SE programming. Examining super enhancers more broadly, we observed that EZH2i downgrades nearly half of all SE, and residual SE lose SF1/β-catenin coordinate control (**Figure 6.23**).

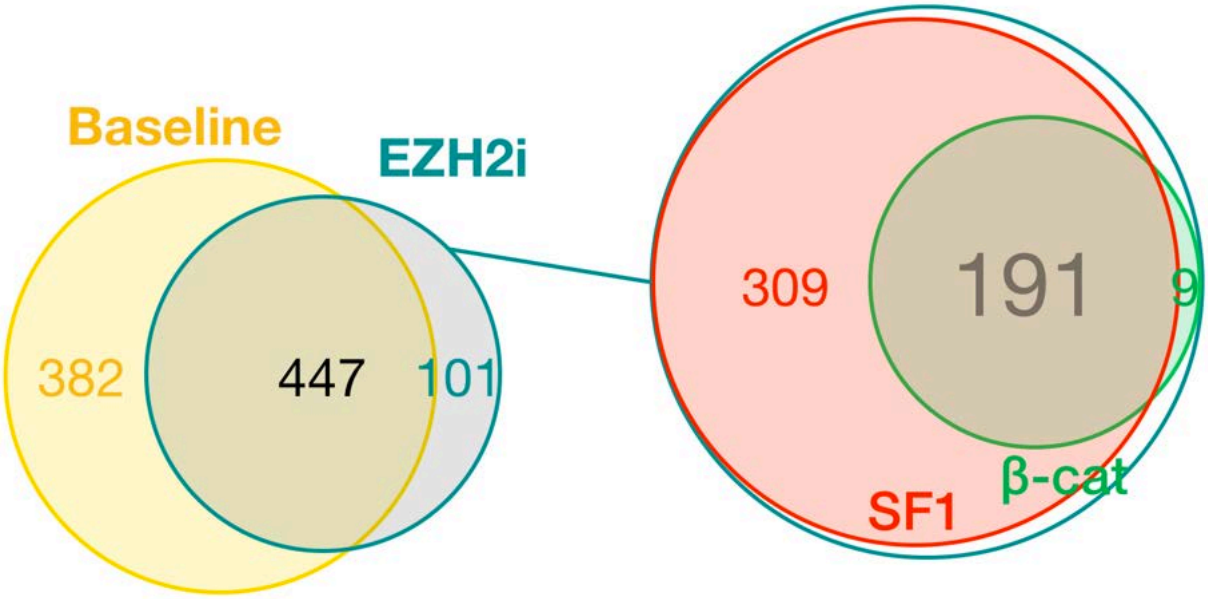

Figure 6.23. EZH2i disrupts global super-enhancer programming.
SE identification before and after EZH2i demonstrates that EZH2i erased nearly 50% of SE, and retained SE lost SF1/β-catenin coordinate control. After EZH2i, only 35% of retained SE are bound by both SF1 and β-catenin.

These data converge on the idea that, through manipulation of the SF1/β-catenin axis, the most direct and immediate consequence of EZH2i is on disruption of SE programming. To evaluate this hypothesis, we treated all ACC cell lines with a specific and irreversible inhibitor of the H3K27 acetyltransferase CBP (PRI-724, reviewed by the investigator who identified this compound in (Kahn, 2014)). CBP regulates H3K27ac deposition genome-wide (**Table 1.2**) including at enhancers, and CBP-dependent H3K27ac deposition is required for enhancer activity (Merika et al., 1998; Raisner et al.,

2018). Cell lines received the CBP inhibitor (CBPi) either alone or combination with EZH2i at the determined IC-50 dose for that cell line. We observed that combination EZH2i/CBPi was synergistic in all ACC cell lines tested, suggesting that these drugs target the same biological program (**Figure 6.24**).

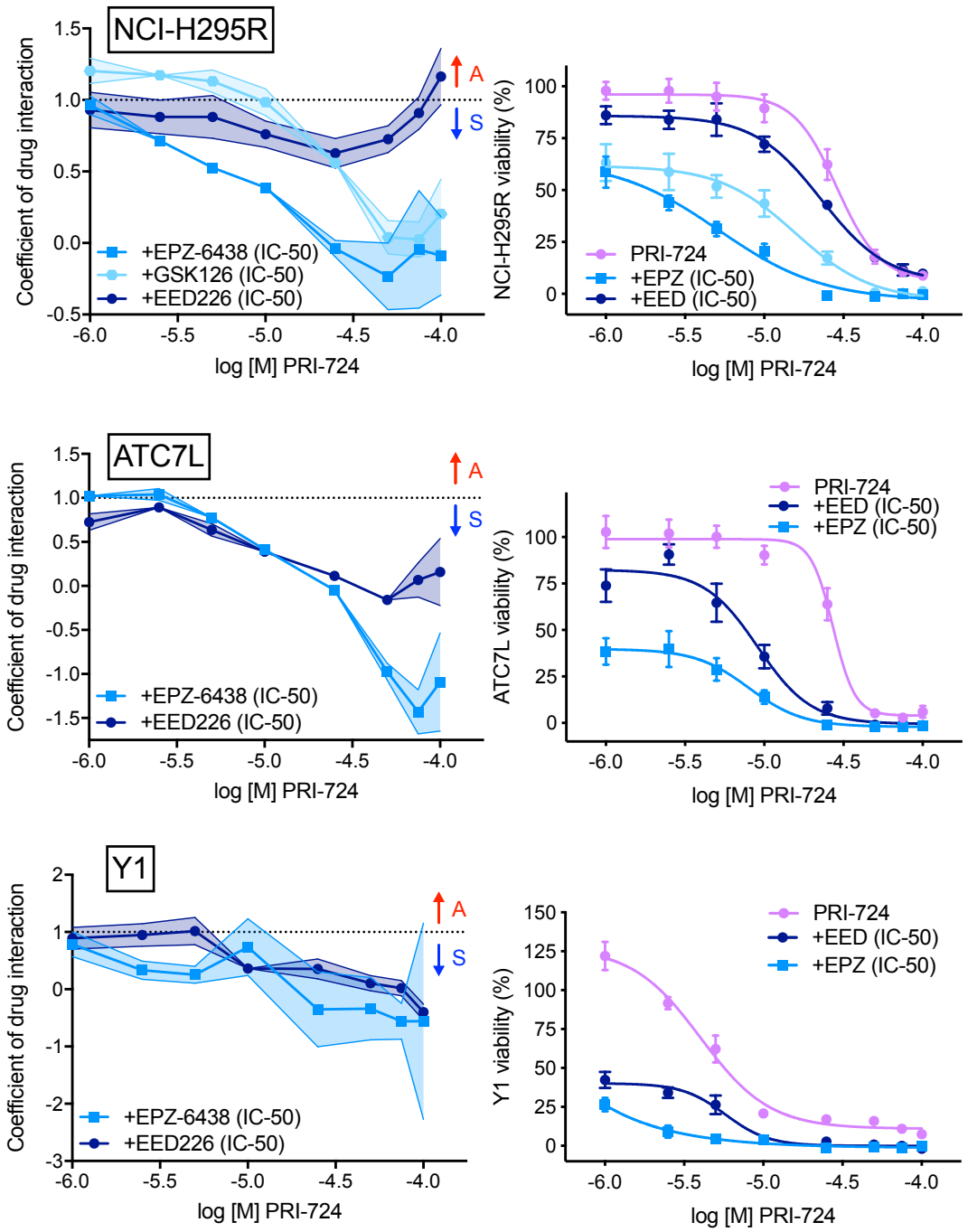

Figure 6.24. EZH2i and CBPi are synergistic in ACC cell lines.
NCI-H295R, ATC7L, and Y1 were treated with increasing doses of CBPi (PRI-724), alone or in combination with EZH2i at the IC-50 dose for each cell line (EZH2i viability curves for ATC7L and Y1 not shown). EZH2i and CBPi induce synergistic (S) loss of viability at increasing doses of CBPi in all ACC cell lines, suggesting that EZH2 and CBP may redundantly coordinate epigenetic programming in ACC.

We then evaluated the NCI-H295R response to CBPi by RNA-seq and compared this to the NCI-H295R response to EZH2i. Strikingly, we observed redundant and highly correlated effects of CBPi and EZH2i on the NCI-H295R transcriptome, including a potent and dose-dependent downregulation of steroidogenic enzymes (**Figure 6.25**). Similarly to EZH2i, CBPi induces downregulation of all core modules that define CIMP-high ACC (**Figure 6.26**).

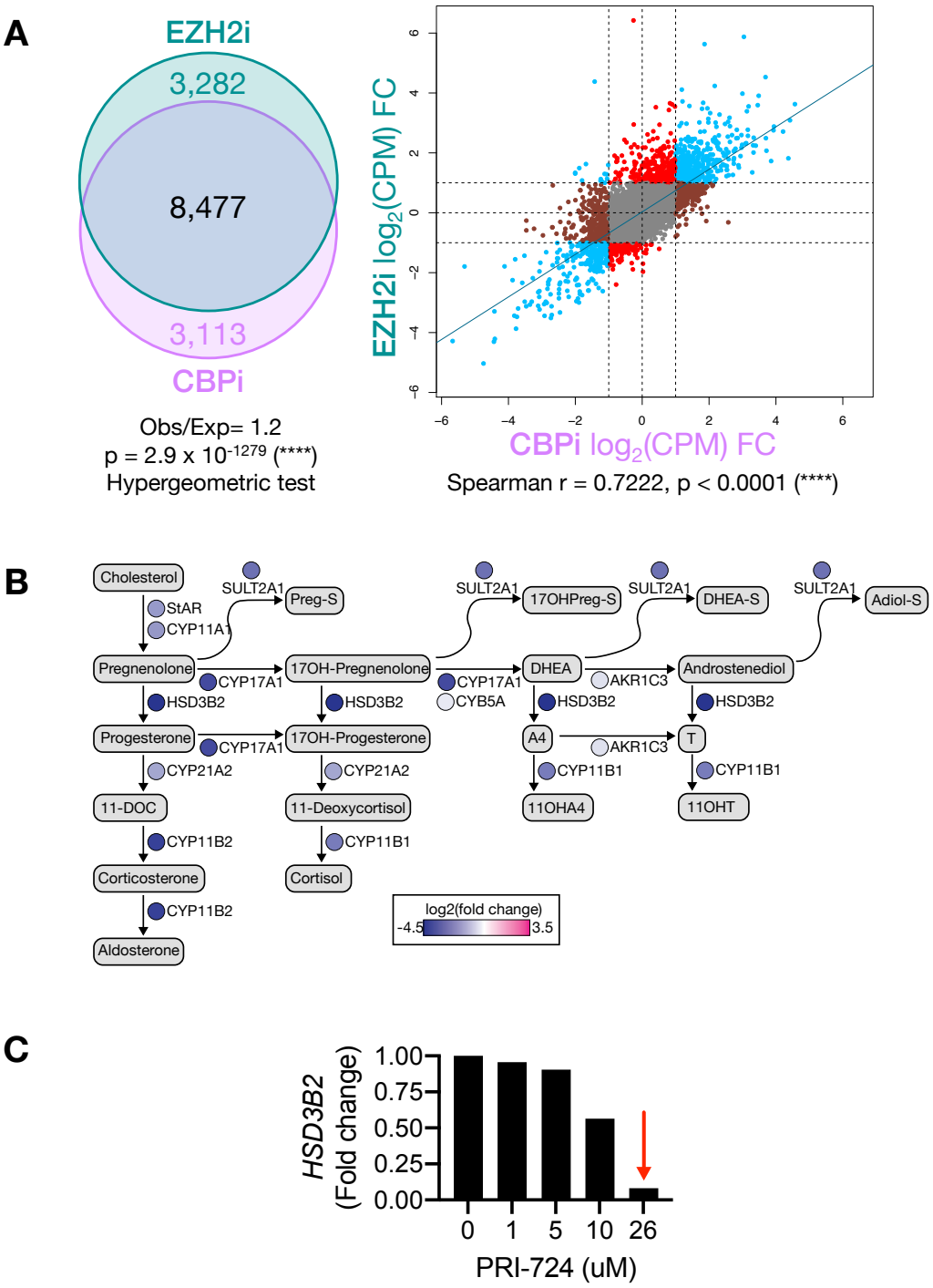

Figure 6.25. EZH2i and CBPi redundantly disrupt the NCI-H295R transcriptome.
A. Left, Venn diagram depicting genes that are differentially expressed following 96-hour IC-50 administration of EZH2i (EPZ-6438) or CBPi (PRI-724) in NCI-H295R reveals highly significant overlap, with ~70% of differentially expressed genes in each set overlapping. Right, gene expression changes induced by EZH2i and CBPi are strongly positively correlated. B. Like EZH2i, CBPi induces potent downregulation of steroidogenesis, consistent with induction of a dedifferentiation program. C. Representative experiment measuring *HSD3B2* expression by qPCR after CBPi administration reveals CBPi induces dose-dependent downregulation of steroidogenic enzymes like *HSD3B2*, even at doses under the IC-50 (indicated by the red arrow).

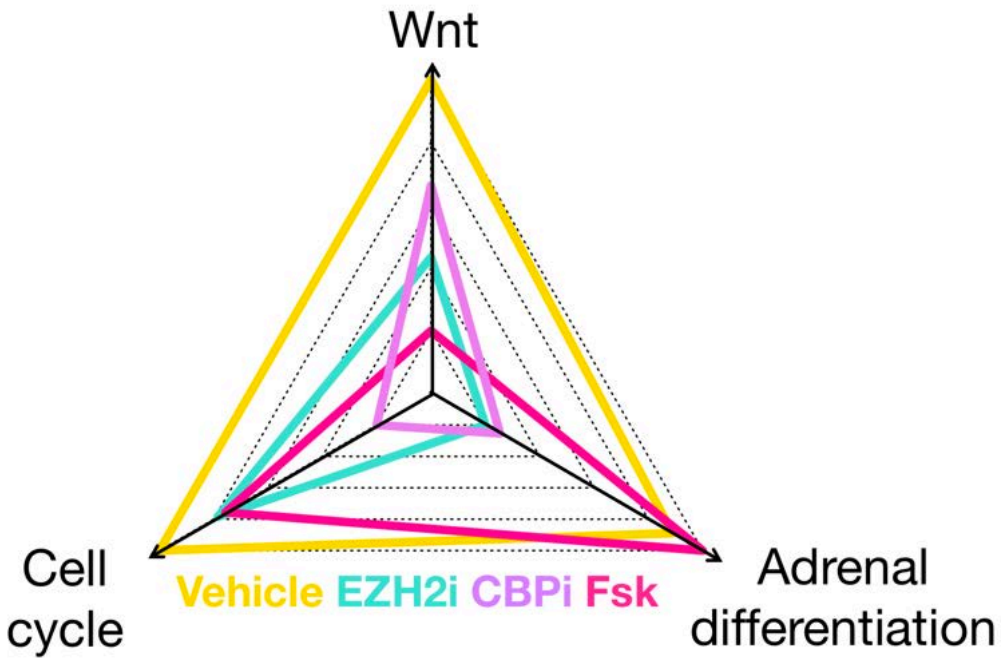

Figure 6.26. CBPi, like EZH2i, reverses CIMP-high-defining transcriptional programs.
Adrenal differentiation, Wnt, and cell cycle scores for CBPi, EZH2i, and forskolin (Fsk) calculated by GSVA (Hänzelmann et al., 2013) and graphed as in **Figures 6.6** and **6.9**.

Evaluation of the impact of EZH2i and CBPi on differentiation genes in the ATC7L and Y1 cell lines are ongoing; however, these data are consistent with the idea that the primary impact of EZH2i is on disrupting SE and enhancer programming. Taken together, our observations point to adrenocortical differentiation as a targetable therapeutic vulnerability selected for in CIMP-high ACC.

6.8. Discussion

CIMP-high is a rapidly recurrent, routinely fatal, and homogeneous molecular subtype of ACC defined by several levels of aberrant epigenetic patterning (**Chapters 3 – 5**, this chapter). The fundamental mechanisms supporting cancer-specific DNA hypermethylation in CIMP-high ACC remain elusive, but our studies have pointed to a

role for this aberrant epigenetic signature in augmenting the function of EZH2/PRC2 and maintaining a reliance of ACC cells on GOF/neomorphic EZH2/PRC2 catalytic activity (**Chapter 5**). Our studies in this chapter reconciled the convergence of SF1-dependent adrenocortical differentiation and activation of Wnt/β-catenin in CIMP-high ACC, by illuminating an SF1/β-catenin program that coordinates lineage fidelity through pervasive control of SE (section **6.5**). We identify a series of protein complexes, EZH2/β-catenin and SF1/β-catenin, that shuttle β-catenin off and on chromatin and consequently switch off and on adrenocortical differentiation states (sections **6.3**, **6.5**, **6.7**). These complexes are conserved in the murine adrenal cortex and models of carcinogenesis (**Figures 6.4**, **6.12**; section **6.6**), suggesting that the transcriptional program coordinated by these factors and stabilized in CIMP-high tumors (**Figures 6.6**, **6.15**) supports conserved mechanisms of cancer evolution. Furthermore, we demonstrate multiple pharmacological strategies to disrupt this program, using inhibitors of EZH2 and/or CBP (section **6.7**).

The Wnt/β-catenin pathway is recurrently selected for somatic alteration in many human cancers and is mutated in >50% of CIMP-high ACC (**Chapters 3 – 4**). Efforts to target this pathway have been unsuccessful, secondary to on-target toxicities in organs with rapid turnover that rely extensively on canonical Wnt signaling, e.g. the colon (Kahn, 2014). Our discovery that the major role of β-catenin-dependent programming in CIMP-high ACC is to stabilize SF1-dependent adrenocortical differentiation opens a novel avenue with a potentially large therapeutic index through which to target this oncogenic program (and is the subject of a pending patent, citation in **Appendix E**). Indeed, the SF1/β-catenin interaction interface maps to a region on β-catenin more proximal to the

C-terminus than its interaction interface with LEF1 (Mizusaki et al., 2003). Is it possible that other tissue-specific nuclear receptors bind to this same site in other cancers, and does this represent a more promising pharmacological strategy through which to shut down oncogenic β-catenin (also the subject of pending patent cited in **Appendix E**)? A new paradigm, in which novel strategies are developed for tissue-specific disruption of oncogenic programs, will be essential to fight cancers that rely on differentiation programs for sustained proliferation and dissemination potential, like ACC.

Repressive epigenetic modifiers like PRC2 are classically modeled as complexes that maintain tissue stemness (**Chapter 1**). Studies in embryonic stem cells and mouse models with global PRC2 deficiency almost invariably identify that PRC2 is critical for embryonic pluripotency and gastrulation (**Table 1.6**), supporting this postulate. Indeed, most studies investigating a role of aberrant PRC2 activity in cancer suggest that this complex ultimately maintains cancer cell stemness (section **1.6**) and sustained proliferation potential (which we demonstrated for ACC in **Figure 5.9**), seemingly in contrast to our work in this chapter (e.g. **Figure 6.8**). A perhaps more nuanced interpretation of this data is that PRC2/H3K27me3 deposition is required to facilitate meta-stable cell state changes that enable accurate and complete differentiation. Indeed, our studies in this chapter reveal that catalytically active PRC2 stabilizes the maintenance of a pro-proliferative differentiation state in CIMP-high ACC, through EZH2's ability to interact with a transcriptional coactivator (β-catenin) core to lineage fidelity (β-catenin control of adrenocortical lineage conversion detailed in **Chapter 2**). The functional consequences of this role of PRC2 are not unlike that identified in *A. thaliana*, in which

PRC2 is required to maintain terminal differentiation of somatic cells (Ikeuchi et al., 2015). A key difference between somatic cells in plants and mammals is that plant somatic cells, despite achieving terminal differentiation, retain totipotency (Steward, 1958). From this perspective, tissue of origin and cancer cell plasticity together may be the ultimate determinants of how and why different epigenetic programs get deployed, thereby encoding tissue-specific therapeutic vulnerabilities across the chromatin landscape.

6.9. Materials and methods

Cell culture. Cell culture was performed as described in **Chapter 3**.

Pharmacological treatments. Pharmacological treatments on NCI-H295R cells were performed as described in **Chapter 5** with the exception that cells were also treated with PRI-724 or forskolin. Pharmacological treatments on Y1 and ATC7L cell lines were performed similarly to those on NCI-H295R with the exception that Y1 and ATC7L cells were plated at a density of 250,000 cells/well in 6 well plates, or scaled accordingly for plating in 12 well or 24 well plates.

Extraction and quantification of nucleic acids and proteins. Performed as described in **Chapters 3 – 5**.

Quantification of gene expression. Performed as described in **Chapters 3 – 5**, with the following primers where *PPIB* is a housekeeping gene:

Table 6.1. Primers and sequences used for qPCR.

Species	Gene	Orientation	Sequence (5'-3')
Homo sapiens	*HSD3B2*	Forward	CTTTTAACAATCTAAGTTACGCCCT
Homo sapiens	*HSD3B2*	Reverse	AGTAGCAGGAAACACTTGCCA
Homo sapiens	*APCDD1*	Forward	CCAGAGGATGTTCTACCGGC
Homo sapiens	*APCDD1*	Reverse	AGGCATGGTCGTGGTTCTTG
Homo sapiens	*LGR5*	Forward	TCCGATCGCTGAATTTGGCT
Homo sapiens	*LGR5*	Reverse	ACGACAGGAGGTTGGACGAT
Homo sapiens	*PPIB*	Forward	GGCCCAAAGTCACCGTCAAG
Homo sapiens	*PPIB*	Reverse	AGCCAAATCCTTTCTCTCCTGTA

SDS-PAGE and western blot. Performed as described in **Chapter 5.**

Nuclear complex co-IP and IP-MS. Performed as described in **Chapter 5.**

Proximity ligation assay (PLA). PLA was performed using the Duolink Detection Reagents Brightfield Kit (Sigma-Aldrich, Cat. No. DUO92012) and associated wash buffers (Sigma-Aldrich, Cat. No. DUO82047-4L) and PLA probes according to manufacturer protocol with the following modifications: blocking was performed for 2 hours at room temperature using a custom blocking buffer which was a 1:1 mixture of blocking buffers prepared from VECTASTAIN Elite ABC-HRP Kit, Peroxidase (Rabbit IgG) (Vector Labs, Cat. No. PK-6101) and the M.O.M. (Mouse on Mouse) Immunodetection Kit – Basic (Vector Laboratories, Cat. No. BMK-2022). Each blocking buffer is prepared at 2x the recommended concentration and combined 1:1 to create this custom blocking buffer. Primary antibodies were diluted in M.O.M. diluent and incubated with slides overnight in a humidified chamber at 4°C. PLA probes were also diluted in M.O.M. diluent. Counterstain step was skipped because counterstain masked signal from

nuclear epitopes. The following antibodies were used for PLA in dysplasia to carcinoma sequence: EZH2 (Cell Signaling Technology, Cat. No. 5246S), β-catenin (BD Biosciences, Cat. No. 610154), SF1 (custom in-house antibody, RRID AB_2716716), SF1 (Invitrogen, Cat. No. 434200/N1665). They were used at the following combinations: EZH2 (1:50)/β-catenin (1:50) to detect EZH2/β-catenin interactions, SF1 (1:500)/β-catenin (1:100) to detect SF1/β-catenin interactions, SF1 (Rb, 1:1500)/SF1 (Mmu, 1:100) to detect SF1+ cells particularly in metastatic lesions, or no antibodies (No Ab) as a negative control. As a positive control (detecting β-catenin) in a small cohort of samples and during PLA optimization, 1:500 Active β-catenin, Cell Signaling Technology, Cat. No. 8814 was paired with varying concentrations of β-catenin (BD Biosciences, Cat. No. 610154) or β-catenin (Invitrogen, Cat. No. MA1-2001).

Viability assays and calculations. Viability assays were performed as described in **Chapter 5**. To evaluate drug interactions, a simplified coefficient of drug interaction (CDI) was calculated as described (Pham et al., 2019). Briefly, CDI between drugs C and D is given by the formula CDI = $\%V_{CD}/(\%V_C * \%V_D)$ where $\%V_{CD}$ is the %V when cells are treated with both drug C at dose x_1 and drug D at dose x_2, $\%V_C$ is the %V when cells are treated with drug C alone at dose x_1, and $\%V_D$ is the %V when cells are treated with drug D alone at dose x_2. CDI>1 signifies antagonism, CDI=1 signifies additivity, and CDI<1 signifies synergy. Negative CDI values are secondary to fluctuations of absorbance around the level of the blank when no viable cells remain in a well, and are consistent

with CDI<1 for a drug that induces loss of viability. An alternative strategy would be to set the values of these conditions to 0.

ChIP-seq. ChIP-seq and analysis was performed as described in **Chapter 5**, using antibodies against SF1 (EMD Millipore, Cat. No. 07-618; concentration 5 µg Ab/30 µg chromatin) or β-catenin (Invitrogen, Cat. No. 71-2700; concentration 4 µg Ab/30 µg chromatin). We identified super-enhancers using *ROSE* (Lovén et al., 2013; Whyte et al., 2013).

RNA-seq. RNA-seq and analysis was performed as described in **Chapters 3 – 5**.

ATAC-seq. ATAC-seq and analysis was performed as described in **Chapter 5**. Integration of RNA-seq and ATAC-seq data was performed using *diffTF* (Berest et al., 2019). ACC-TCGA ATAC-seq BigWig files were downloaded from TCGA Genomic Data Commons (NCI, 2005-2018), and signal at SF1/β-catenin binding sites was measured using *multiBigwigSummary* in *deepTools* (Ramírez et al., 2016).

CHAPTER 7. Summary, Conclusions, and Future Directions

7.1. Disclosure of relevant publications

Portions of this work are being prepared for publication:

> **Mohan DR**, Borges KS, Finco I, LaPensee CR, Solon A, Rege J, Little III DW, Else T, Almeida MQ, Apfelbaum A, Vinco M, Wakamatsu A, Mariani BMP, Latronico AC, Mendonca BB, Zerbini MCN, Fragoso MCBV, Lawlor ER, Ohi R, Rainey WE, Venneti S, Marie SKN, Giordano TJ, Breault DT, Lerario AM*, Hammer GD*. A differentiation program coordinated by SF1/β-catenin is a targetable epigenetic vulnerability in aggressive adrenocortical carcinoma. In preparation. *co-senior author
>
> Lerario AM*, **Mohan DR***, Rege J, Rainey WE, Hammer GD. Meta-analysis of adrenocortical tumors identifies cell of origin programs derailed in tumorigenesis and malignancy. In preparation. *co-first author

7.2. Epigenetic principles and ACC molecular subtypes

Eukaryotic organisms have evolved complex mechanisms to instate versatile, context-specific transcription from a single genome. Epigenetics is one such mechanism that facilitates genome packaging and therefore spatiotemporal compartmentalization of transcriptional networks. Covalent modifications on histones and DNA map this multi-dimensional information onto a unidimensional DNA template and therein participate in transmission of cellular memory across divisions. Enzymes and protein complexes that catalyze deposition of epigenetic marks on histone and DNA substrates exhibit strong evolutionary conservation, and intact function of these enzymes is a uniform requirement

for eukaryotic cell and organism survival (**Chapter 1**). This requirement is particularly compelling given the diverse roles of epigenetic machinery in various cell types and tissues, shaping how genetic alterations manifest in different disease states (**Table 1.3**, section **1.5**, **Chapters 2 – 3**; (Corces et al., 2018)).

Major advances in high-throughput molecular profiling techniques have revolutionized our ability to understand how epigenetic programs participate in health and disease. Such investigations have been particularly fruitful for the studies of cancer, a disease in which inherited and acquired genetic alterations reverse physiological molecular circuits to drive sustained proliferation (sections **1.6 – 1.7**; (NCI, 2005-2018)). More recently, it has become clear that cancers can be defined by multiple dimensions that span somatic alterations, active transcriptional modules, and unique epigenetic patterns. This paradigmatic shift has been especially transformative for ACC, a poorly understood and rare cancer which we now appreciate is driven by three core molecular subtypes with differential activation of pathways required for adrenal homeostasis (**Chapters 2 – 3**).

This dissertation focused on understanding the consequences of aberrant epigenetic patterning in a prevalent, rapidly recurrent, and routinely fatal molecular subtype of ACC, CIMP-high (**Chapters 3 – 4**). Patients with CIMP-high tumors (encompassing 40% of all ACC, more than any single somatic alteration) invariably relapse on standard of care adrenolytic agent mitotane with deadly, incurable metastatic disease (**Chapter 4**). These data suggest patients with this subtype need to be directed to alternative systemic therapies early in disease course, potentially at diagnosis.

Furthermore, CIMP-high ACC is a complex molecular state, driven by aberrant DNA hypermethylation directed to promoter CpG islands, somatic alterations in cell cycle and Wnt/β-catenin pathway components, and relative overexpression of adrenocortical differentiation programs (**Chapters 3 – 6,** especially **Figures 3.3**, **4.3**, **4.4**, **5.1**, **6.6**). The numerous features that define this class illuminate many potential therapeutic targets, but are impossible to disentangle from the multiplicity of potential resistance mechanisms. We have shown here that differentiation plasticity is a hallmark of CIMP-high ACC (section **3.8**, **Chapter 6**), and work by others in our field suggests that this feature my support resistance to mitotane (Seidel et al., 2020). Identifying a central node driving CIMP-high is therefore essential for development of the efficacious therapy that is urgently needed to fight this devastating disease. Here, we demonstrate that the DNA methylation landscape of CIMP-high ACC is one such central node, enabling strategies to diagnose CIMP-high (**Chapter 4**), inducing a cascade of abnormal epigenetic patterning (**Chapter 5**), and reinforcing intrinsic therapeutic vulnerabilities (**Chapter 6**). I will now highlight the major conclusions of these studies and supporting data in sections **7.3 – 7.6**, and will discuss future directions for this work in section **7.7**.

7.3. Targeted assessment of CIMP-high DNA hypermethylation reproducibly identifies aggressive ACC

The discovery that ACC is comprised of distinct molecular subtypes that predict survival outcomes (Zheng et al., 2016) represents a major advance in our understanding of this disease, but poses two major practical challenges: First, how do we prospectively

identify patients with CIMP-high ACC in a timeline that is compatible with clinical decision-making? Second, how should the diagnosis of CIMP-high ACC impact clinical care? To address the first question, we took advantage of publicly available datasets to identify that aberrant DNA methylation is sufficient to capture all core molecular features of CIMP-high ACC, and that the entire DNA methylation landscape can be distilled down to all-or-none methylation of a single locus spanning the *G0S2* CpG island (section **4.4**). We then prove that methylation of this locus alone is sufficient to capture reproducible clinical features of this molecular subtype, including invariable rapid recurrence even if a patient transiently attains macroscopic "disease free" status (section **4.6**). Intriguingly, *G0S2* methylation/CIMP-high status identifies aggressive disease course even in patients with tumors that possess low mitotic activity (**Figure 4.24**, **Table 4.5**). Driver cell cycle alterations are recurrent in ACC and especially frequent in CIMP-high; in contrast to other CIMP-high cancers, ACC do not possess recurrent somatic alterations in metabolic enzymes that drive hypermethylation (**Table 1.7**). These data suggest that fine shifts in cell cycle activation may be the trigger that tips the stoichiometry of epigenetic machinery in favor of propagating the CIMP-high signature (e.g. **Figure 1.3**, **Table 1.7**), though the molecular mechanisms controlling initiation of CIMP-high in the adrenal cortex remain unknown.

We next demonstrated strategies to combine *G0S2* with other molecular markers to stratify ACC into distinct prognostic groups analogous to those identified in ACC-TCGA, enabling identification of invariably good prognosis ACC among patients with non-CIMP-high disease (section **4.7** and pending patent applications cited in **Appendix E**). Finally,

though the bulk of these studies were conducted using gDNA extracted from flash frozen samples, we also developed a method to measure locus methylation in archival material, including FFPE tissues (section **4.8**). Taken together, this work enables rapid molecular subtyping (in as little as 48 hours) of any ACC sample for the first time. Indeed, since publication of the work in **Chapter 4** as (Mohan et al., 2019), the predictive power of our stratification scheme has been reproduced by other groups (Schreiber et al., 2020). Given the rapid and homogeneous metastatic recurrence patterns that characterize CIMP-high ACC, it is likely that patients with this ACC subtype possess microscopic metastases that are unresponsive to standard of care therapies like the adrenolytic agent mitotane (supported by our data in **Chapter 4** and by (Schreiber et al., 2020)). It is therefore crucial that we identify medical therapies capable of arresting growth of disseminated disease, and this is the focus of the remainder of this thesis.

7.4. DNA hypermethylation induces several layers of aberrant epigenetic patterning in CIMP-high ACC

Testing agents that may be effective in CIMP-high ACC requires adequate *in vitro* and *in vivo* models. Here, we identified that the most well established *in vitro* model of human ACC (NCI-H295R) is indeed CIMP-high (section **3.7**), and take advantage of this model to characterize the consequences of aberrant CpG island hypermethylation with the hopes of nominating a novel therapeutic strategy (**Chapters 5 – 6**). CIMP-high ACC is characterized by frequent somatic alterations that drive activation of the Wnt/β-catenin pathway and cell cycle. We also utilized a mouse model possessing constitutive activation

of β-catenin and inactivation of p53 (**Table 2.4**; (Borges et al., 2020)) to characterize the molecular programs that may be selected for in CIMP-high ACC at early and late stages of tumorigenesis (**Chapter 6**).

Given the power of DNA hypermethylation in predicting dismal outcomes in ACC (**Chapter 4**), we first sought to investigate the molecular mechanisms supporting this signature in CIMP-high tumors (**Chapter 5**). We identified that DNA hypermethylation in CIMP-high ACC is directed to EZH2/PRC2 targets, a complete perversion of evolutionarily encoded and physiological epigenetic programming (section **5.3**). The concentration of DNA hypermethylation on PRC2 targets is consistent with early studies identifying this signature in other CIMP-high cancers (section **1.6**). This led us to investigate a long-held model suggesting that DNA hypermethylation is directed by catalytically active EZH2, through a physical interaction between catalytically active PRC2 and DNA methyltransferases (Viré et al., 2006). In striking contrast to this model, we identified that PRC2 does not interact with DNMT machinery, and DNA hypermethylation is propagated independently of the PRC2, rendering these sites PRC2 independent (sections **5.6 – 5.7**). We also identified that DNMT1 does interface with chromatin modifiers, including HP1 family members that read H3K9me (**Figure 5.13**). These data are consistent with an epigenetic class switching model, in which regions of the genome physiologically possessing H3K27me3 now bear DNA methylation and H3K9me3 (**Table 1.7;** (Gal-Yam et al., 2008; Ohm et al., 2007)). We also showed that *EZH2* is upregulated in CIMP-high ACC in a cell-cycle-dependent manner, and coupled to its catalytic activity on histones (section **5.4**). Intact PRC2 catalytic activity is required for sustained

proliferation in CIMP-high ACC (section **5.5**), suggesting a crucial role for EZH2/PRC2 in coordinating programs core to these tumors. DNA hypermethylation disrupts locus-specific PRC2 function by restricting PRC2 recruitment and spreading of H3K27me3 domains, and forcing "excess" PRC2 to target new sites on chromatin (section **5.7**). These data suggest that EZH2/PRC2 adopts a GOF/neomorph state in CIMP-high ACC.

Through studies not described in this thesis, we have also investigated the reversibility of the CIMP-high DNA methylation signature. Our preliminary experiments with prolonged (up to 192 hour) administration of DNA demethylating agents in NCI-H295R fail to induce any demethylation of *G0S2* despite inducing global demethylation elsewhere (e.g. of LINE elements). This, combined with our work demonstrating the persistence of *G0S2* methylation despite systemic therapies (**Table 4.4**), our analyses identifying *G0S2* methylation/silencing at distal ACC metastases (**Table 4.4** and our analysis of gene expression data from metastases [GEO dataset GSE90713], not shown), and our data showing that CIMP-high DNA methylation is refractory to PRC2 inhibition (**Figure 5.10**), suggest that the CIMP-high DNA methylation signature, once acquired, is exquisitely stable. Certainly, this feature of CIMP-high enables *G0S2* methylation to serve as a powerful biomarker (**Chapter 4**), despite that DNA methylation itself has minimal net consequences on gene expression (**Figure 5.4**). However, this also suggests that selection of the DNA methylation program in CIMP-high ACC may be secondary to the consequences of DNA hypermethylation on other epigenetic programs, like those coordinated (directly or indirectly) by the PRC2 (**Chapter 6**).

7.5. Repressive epigenetic programs reinforce adrenocortical differentiation states that favor sustained proliferation in CIMP-high ACC

EZH2 inhibition induced profound changes on the NCI-H295R transcriptome, partially recapitulating the roles of EZH2 in coordinating zG/zF lineage conversion in the physiological adrenal cortex (**Figures 5.18 – 5.19**; section **2.6**; (Mathieu et al., 2018)). This observation enabled us to recognize that the PRC2 GOF/neomorph state reinforces an unanticipated link between this repressive epigenetic complex and adrenocortical differentiation in CIMP-high ACC (**Chapter 6**). We identified that EZH2 binds β-catenin, a transcriptional coactivator rendered constitutively active through recurrent somatic alterations in ACC, in a PRC2-independent and off-chromatin manner (section **6.3**). Unexpectedly, we simultaneously discovered that β-catenin coordinates a genome-wide lineage-defining transcriptional program together with master adrenal transcription factor SF1 at proximal and distal CREs including super-enhancers (SEs), rationalizing the persistence of adrenocortical differentiation in aggressive, Wnt-active ACC (section **6.5**). We then showed that EZH2i, in addition to reversing the H3K27me3 landscape (section **5.8**), reverses SF1/β-catenin-dependent adrenocortical differentiation by evicting these master regulators from the genome (sections **6.4, 6.7**). Given EZH2/β-catenin persists despite EZH2i (**Figure 6.5**), SF1/β-catenin eviction is presumably achieved through an off-chromatin role of EZH2 in squelching β-catenin away from chromatin and compromising SEs that require this coactivator, including a highly sensitive SE coordinating expression of SF1 itself (**Figure 6.22**). The trickle-down effect of EZH2-induced β-catenin offloading is a potent disruption of the differentiation program that

defines CIMP-high ACC and a near complete erasure of definitive adrenocortical identity. Biochemical experiments clearly defining on-chromatin and off-chromatin pools of EZH2-containing complexes would be required to definitively prove this mechanism, and are ongoing.

EZH2/β-catenin and SF1/β-catenin complexes are conserved through the entire hyperplasia to metastasis spectrum of the β-catenin/p53-dependent mouse model of adrenocortical carcinogenesis we investigated in this thesis (section **6.6**; (Borges et al., 2020)). These data, combined with our molecular characterization of these complexes in NCI-H295R (**Chapter 6**) and the prevalence of adrenocortical differentiation/Wnt pathway activation in CIMP-high tumors (**Chapters 3 – 4**, **Figure 6.6**), suggest that SF1/β-catenin-dependent adrenocortical differentiation undergoes positive selection at both early and late stages of cancer evolution. Should off-chromatin EZH2 be the major mechanism for the EZH2i-induced shutdown of the SF1/β-catenin-dependent landscape, as we propose, these data also suggest that the persistence of EZH2/β-catenin throughout tumorigenesis may create an Achille's heel for epigenetic agents that target this axis (e.g. CBPi, EZH2i; **Chapter 6**, **Figure 6.24**). These studies also illuminate a basis for tissue-specific targeting of oncogenic β-catenin, the subject of a pending patent application (citation in **Appendix E**).

Our ongoing studies are focused on characterizing the prevalence of SF1/β-catenin and EZH2/β-catenin complexes across the spectrum of benign and malignant adrenocortical tumors. We predict that SF1/β-catenin will be selective for or more abundant in steroidogenic ACC with frequent Wnt/β-catenin pathway alterations (COC2

and COC3/CIMP-high, **Chapter 3**) and EZH2/β-catenin will be selective for or more abundant in CIMP-high secondary to the high frequency of cell cycle alterations and upregulation of EZH2 in these tumors (**Figure 4.3**, section **5.4**). We are also conducting preclinical studies to evaluate the efficacy of EZH2i and CBPi in shutting down tumor growth *in vivo*, and are investigating additional molecules which may specifically disrupt the SF1/β-catenin-dependent transcriptional program. Combining our approaches to rapid ACC molecular subtyping (**Chapter 4** and pending patent citation in **Appendix E**) with our strategies to co-opt subtype-specific therapeutic vulnerabilities convergent on adrenocortical differentiation (**Chapters 5 – 6** and pending patent citation in **Appendix E**) may ultimately pave avenues for a novel and effective therapeutic schema for patients with CIMP-high disease.

7.6. Final model

Adrenal cancers are defined by differential activation of programs required for adrenocortical homeostasis (**Chapters 2 – 3**). Like many human cancers (**Chapter 1**), ACC take advantage of epigenetic machinery through pathophysiological programming (**Chapter 4**) to stabilize transcriptional programs favorable for sustained proliferation like adrenocortical/steroidogenic differentiation (**Chapter 5 – 6**). Our work has illuminated a new understanding of the molecular underpinnings of a highly aggressive molecular subtype of ACC, CIMP-high. This class of tumors is prevalent and clinically and molecularly homogeneous (**Chapter 4**). Virtually all patients with CIMP-high ACC will relapse with metastases on standard of care, creating an urgent need for the development

of novel systemic therapies. In addition to designing a biomarker-based approach that enables rapid and prospective molecular classification of ACC (**Chapter 4**), we dissected recurrently disrupted epigenetic programs (**Chapter 5**) and consequences of aberrant epigenetic patterning (**Chapter 6**).

We discovered that abnormal DNA methylation, in addition to serving as a pathognomonic marker of this subtype (**Chapter 4**), disrupts physiological epigenetic patterning coordinated by EZH2/PRC2 (**Chapter 5**; schematized in **Figure 7.1A**). The disruption of EZH2/PRC2's canonical function reinforces a physiological role of EZH2 in buffering off-chromatin pools of β-catenin (**Chapter 6**), a transcriptional coactivator frequently stabilized by somatic alteration in CIMP-high ACC (**Chapters 3 – 4**). Simultaneously, we uncovered an unexpected and critical function of β-catenin in binding SF1 and reinforcing SF1-dependent adrenocortical differentiation genome-wide at proximal and distal elements (**Chapter 6**). This EZH2/β-catenin/SF1 triangulation creates or enhances a dependence of SF1/β-catenin programming on PRC2 catalytic activity, and is selected for at early and late stages of tumorigenesis (**Chapter 6**). Taken together, these studies illuminate an intrinsic tissue-specific vulnerability that is a promising, pharmacologically targetable approach for CIMP-high ACC (**Figure 7.1B**), and unearth several new questions (section **7.7**).

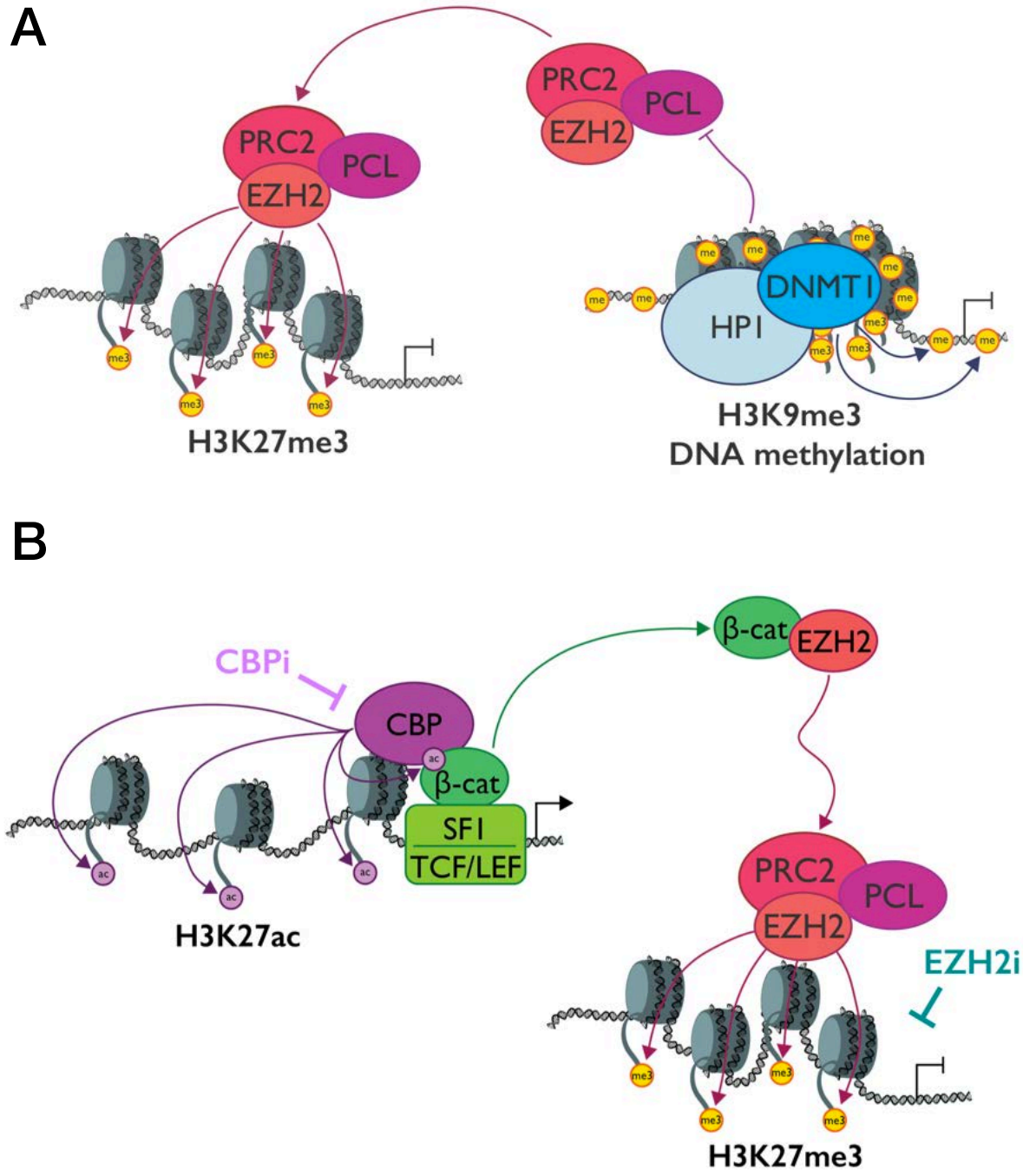

Figure 7.1. Final model: CIMP-high ACC reinforces an adrenocortical differentiation state that favors sustained proliferation through several layers of aberrant repressive epigenetic patterning.
A. CIMP-high ACC is characterized by transcriptional upregulation of Wnt/β-catenin signaling, adrenocortical differentiation, and the cell cycle through recurrent somatic alterations and previously unknown mechanisms (**Chapters 3 – 4, 6**). This is coincident with a homogeneous signature of genome-wide CpG island hypermethylation (**Chapter 4**), notably at PRC2 targets (**Chapter 5**). DNA hypermethylation enabled our development of a powerful clinical strategy to identify CIMP-high ACC (**Chapter 4**). Through our work in **Chapter 5**, we demonstrated that this signature disrupts physiological epigenetic programming established by EZH2/PRC2 through displacement of DNA methylation-sensitive

PRC2.1 (the predominant PRC2 complex in CIMP-high ACC) off of hypermethylated regions (which are now coordinated by DNMT machinery and other chromatin remodelers, like HP1 family members that read H3K9me) and onto new sites. B. β-catenin classically transduces Wnt signaling through TCF/LEF transcription factors, and this canonical program is turned on in ACC with activating Wnt pathway alterations. However, here, we simultaneously identified that the adrenocortical differentiation program turned on in CIMP-high ACC is coordinated by a TCF/LEF-independent SF1/β-catenin complex, and that EZH2/PRC2 gains access to this program through a novel, off-chromatin EZH2/β-catenin complex (**Chapter 6**). Disrupting PRC2 catalytic activity via EZH2i alone or in combination with therapies disrupting enzymes required for SF1/β-catenin-dependent transcriptional activation (e.g. CBPi) nearly completely erases this differentiation signature and diminishes sustained proliferation potential (**Chapters 5 – 6**). Given that SF1/β-catenin and EZH2/β-catenin are selected for through all stages of tumorigenesis (**Chapter 6**), this EZH2/β-catenin/SF1 triangulation reinforces a targetable, intrinsic tissue-specific therapeutic vulnerability in CIMP-high ACC.

7.7. Future directions

Steroidogenesis is a complex, tightly regulated, and energetically expensive biological process. Why steroidogenic differentiation would be selected for in ACC is counterintuitive given the many molecular events cancers originating from other tissues acquire to harness proliferation potential at the expense of differentiation. Our analysis of human adrenal single-cell RNA-seq suggests that partial zF differentiation is a feature of cells with the highest cell cycle activity in the adrenal cortex (**Figure 2.7**). It is therefore possible that the epigenetic programs rerouted in CIMP-high ACC stabilize a transcriptional program that facilitates cell-of-origin-dependent transformation and proliferation.

Glucocorticoids are potent immune suppressants, so effective that they are used routinely to prevent organ rejection in transplant recipients. Steroidogenic and CIMP-high ACC are exquisitely poor in immune cells and most ACC are refractory to immunotherapy, suggesting a physiologically relevant role for the SF1/β-catenin-dependent steroidogenic programs in shaping the tumor microenvironment (**Appendix B**). The persistence of

steroidogenesis may enable exclusion of immune cells from the ACC microenvironment both at the primary tumor and at distal sites (supported by our analysis of gene expression data from metastases [GEO dataset GSE90713], data not shown). Moreover, recent comprehensive single-cell molecular profiling studies of fetal tissues have astonishingly revealed that the adrenal gland is a major site of fetal hematopoiesis (Cao et al., 2020; Domcke et al., 2020) – is it possible that during development, the SF1/β-catenin-expressing definitive adrenal cortex trains developing immune cells? Is this a hierarchy reinstated by steroidogenic ACC?

Along these lines, our work has illuminated several new avenues for investigation in adrenocortical development and homeostasis, specifically with the new paradigm that β-catenin is a master regulator of epigenetic programming. Given the known physiological roles of EZH2 (section **2.6**; (Mathieu et al., 2018)) and the zonal distribution of β-catenin-containing complexes (**Chapter 6**), is it possible that SF1/β-catenin and EZH2/β-catenin together shape zG to zF lineage conversion? Is a balance between SF1/β-catenin and EZH2/β-catenin complexes required to shut down canonical Wnt signaling as cells acquire zF identity? ACTH, the major trigger for zF differentiation, stimulates cell proliferation at the zG/zF boundary – does higher expression of *EZH2* in cycling cells accelerate this transition? Finally, how does SF1/β-catenin participate in the establishment of Wnt signaling in the definitive adrenal cortex? Is this interaction required for definitive cortex formation? Does β-catenin-dependent control of *NR5A1* at the SE we identified (**Figure 6.22**) help restore *NR5A1* expression after it is silenced during development?

Taken together, our studies illuminate how derailed epigenetic programs advantage cancer cells by maintaining a permissive chromatin environment for context-specific sustained proliferation. Understanding precisely how aberrant epigenetic patterning emerges in the adrenal cortex and what components of this cascade are reversible at early and late stages of tumorigenesis will be crucial as we move forward to develop the next generation of therapeutic strategies to fight ACC.

APPENDICES

Appendices A – D describe additional work for which I provided substantial intellectual contribution as either the primary contributor or a major contributor, which do not fit elsewhere in the thesis. **Appendix E** provides additional detail regarding author contributions and research products that include parts of thesis work.

APPENDIX A. Chromosomal "Noisiness" Predicts Linsitinib Resistance in ACC

A.1. Disclosure of relevant publications

This work has not been published, but has provided a basis for two pending patent applications (citation in **Appendix E**) on which Antonio Marcondes Lerario, MD, PhD, Gary D. Hammer, MD, PhD, and I are inventors. Antonio Marcondes Lerario, MD, PhD, and I developed this analysis together, and it is briefly discussed here. The exome sequencing performed in this study was supported by Astellas Pharma.

A.2. Introduction

Overexpression of *IGF2* is the most common molecular abnormality in adrenocortical carcinoma (ACC), reported in up to 90% of tumors (**Chapter 2**). Preclinical studies in the last decade have suggested that pharmacological inhibition of IGF2 signaling through targeting the insulin growth factor receptor 1 (IGF1R) may be a promising therapeutic avenue for advanced ACC (Barlaskar et al., 2009). Disappointingly, phase I-III clinical trials have since demonstrated that IGF1R inhibitors, though well tolerated, have therapeutic efficacy for a limited number of advanced ACC patients (Fassnacht et al., 2015; Haluska et al., 2010; Lerario et al., 2014). Indeed, the recent randomized, placebo-controlled Phase III trial evaluating use of linsitinib in patients with refractory metastatic ACC (Fassnacht *et al.*, *Lancet Oncology* 2015) was widely

considered a “failure” stemming from the result that most patients enrolled in the trial failed to exhibit durable clinical responses. However, up to 10% of patients exhibited clinically relevant responses, including disease stabilization, tumor shrinkage and long-term ACC regression, suggesting that subgroup analysis may illuminate potential responders to IGF1R inhibitors. In this study, we sought to identify somatic alterations that are predictive of response to IGF1R inhibition.

A.3. Patients and methods

We analyzed whole-exome sequencing data available from 12 grade-matched tumors included in the Fassnacht *et al.* study, including tumors from 3 patients who exhibited partial response (shrinkage >20%; PR by RECIST), 3 patients who exhibited disease stabilization (SD), and 6 patients who exhibited disease progression (PD). We performed variant calling with *freebayes* (Garrison and Marth, 2012), with the “pooled continuous” and “pooled discrete” modes activated and minimum alternate fraction set to 5% to enable identification of subclonal populations. We restricted our analysis to exonic and protein coding variants. We used restrictive filtering criteria and filtered out variants present in the population databases gnomAD (Lek et al., 2016) and 1000 Genomes (Auton et al., 2015). We restricted our analysis to genes known to be cancer associated and recurrently mutated in ACC. We manually inspected the region of *ZNRF3* to assess drops in coverage indicating somatic deletion. To generate B-allele frequency profiles, we used *samtools* (Li et al., 2009) *mpileup* to generate pileup files and a home-made *perl* script to extract the allele frequencies from pileup files. After removing homozygous

positions (allele frequency above 95% and below 5%), we smoothened the data using the *smooth* function from R-base (Team, 2016). We next used the function *cpt.mean* from *changepoint* (PELT algorithm) to perform segmentation (Killick and Eckley, 2014). We determined the number of breakpoints for each tumor according to the number of segments identified by *cpt.mean*.

A.4. Results

We identified 4 putative somatic alterations in 3/6 PD patients, including: 2 hotspot mutations in *CTNNB1* (2 PD patients), 1 missense mutation in *MEN1* (1 PD patient) and 1 nonsense mutation in *ATRX* (1 PD patient); and 1 somatic alteration in 1/6 SD/PR patients, including 1 nonsense mutation in *NF1* (1 PR patient). We did not identify any alterations in the *ZNRF3* locus, but these data are consistent with the idea that patients with somatic *CTNNB1* mutations (ACC-TCGA COC2-COC3 (Zheng et al., 2016) do not respond to linisitinib therapy (**Table A.1**). We also identified mutations in *TP53* as detailed in **Table A.1**, though it is unclear if they have pathogenic significance.

Table A.1. Putative somatic alterations in patient tumors reveals that patients with ACC bearing *CTNNB1* mutations progress on linsitinib.

Patient	Response	Mutations identified in tumor
A	Partial Response	None identified
B	Partial Response	None identified
C	Partial Response	*NF1* (nonsense), *TP53* (missense)
D	Stable Disease	*TP53* (missense)
E	Stable Disease	None identified
F	Stable Disease	None identified
G	Progressive Disease	*TP53* (missense), *CTNNB1* (hotspot)
H	Progressive Disease	None identified
I	Progressive Disease	*MEN1* (missense)
J	Progressive Disease	None identified
K	Progressive Disease	None identified
L	Progressive Disease	*ATRX* (nonsense), *CTNNB1* (hotspot)

Using B-allele frequency profiling, we identified different patterns of chromosomal breakpoints between responders (PR, SD patients) and non-responders (PD patients). We identified that patients with PD had a greater number of breakpoints than patients who exhibited PR or SD on linsitinib therapy (**Figure A.1**), suggesting that higher levels of genomic instability may predict intrinsic resistance to linsitinib.

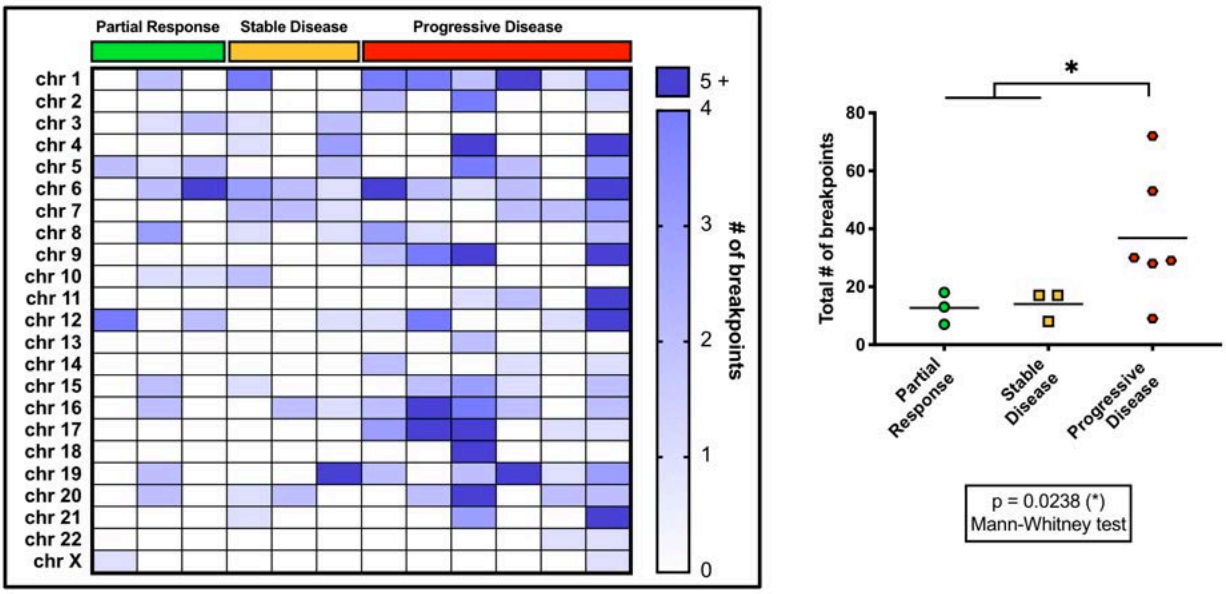

Figure A.1. Patients with PD have a greater number of breakpoints than patients who exhibited either PR or SD on linsitinib therapy.
Number of breakpoints is depicted in each patient sample (columns) by chromosome (rows) in the panel left. In the panel right, we can see that the total number of breakpoints in the tumors of patients with progressive disease is higher than in patients who exhibited a partial response or stable disease in response to linistinib.

Using B-allele frequency profiling, we also identified different patterns of loss of heterozygosity (LOH) between responders and non-responders. While tumors from non-responders bear an intricate pattern of arm-level LOH with several breakpoints and variable minor allele frequencies, tumors from responders bear widespread whole-chromosome LOH with fewer arm-level breakpoints. These results are consistent with tumors from non-responders and responders being comparable to the “noisy” and “chromosomal” groups identified by ACC-TCGA (Zheng et al., 2016), respectively (**Figure A.2**). Taken together, these observations suggest that acquired secondary alterations downstream of IGF2 signaling dictate resistance to IGF1R inhibition, and provide a rationale for developing strategies that may improve responsiveness to IGF1R inhibitors in future trials.

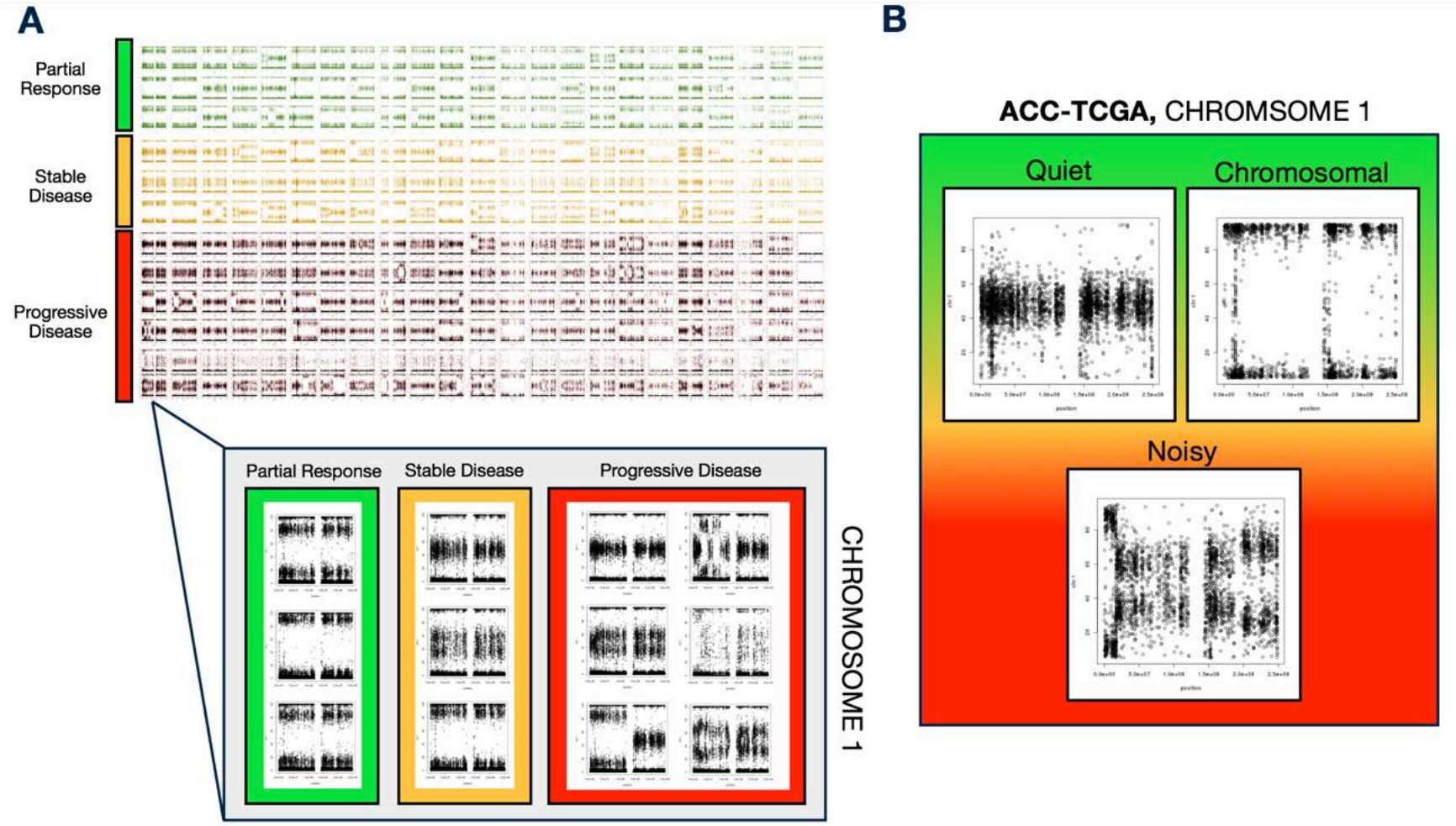

Figure A.2. Patients with chromosomally "noisy" ACC progress on linsitinib.
A. B-allele frequency profiling identifies an ACC-TCGA-like "chromosomal" or "quiet" LOH pattern in tumors of patients with PR/SD following linsitinib treatment, and ACC-TCGA-like "noisy" LOH pattern with in tumors of patients with PD. B. ACC-TCGA somatic copy number alteration profiles depicting chromosome 1 from example quiet, chromosomal, and noisy tumors. Noisy pattern is predictive of an aggressive disease course (rapid recurrence, death) and a hallmark feature of ACC-TCGA COC3 and CIMP-high (Mohan et al., 2019; Zheng et al., 2016).

A.5. Ongoing studies

Resistance to linsitinib is associated with a hallmark feature of a molecular subtype of ACC – chromosomal noisiness (**Figure A.2**), which is synonymous with ACC-TCGA COC3 (Zheng et al., 2016), and has substantial overlap with CIMP-high tumors (**Figure 4.3**, (Mohan et al., 2019)). This is reinforced by our observation that putative somatic *CTNNB1* alterations (prevalent in COC2 and COC3 ACC (Zheng et al., 2016) and frequent in CIMP-high ACC, **Figure 4.3**) were only present in non-responders (**Table A.1**). These data not only allude to a utility for molecular subtyping to identify responders to IGF-targeting therapy, but exemplifies the power of molecular subtyping in predicting intrinsic resistance to certain classes of targeted agents. Our ongoing studies and the subject of our pending patent applications (citation in **Appendix E**) are focused on translating our molecular subtyping strategy described in **Chapter 4** to enable prospective stratification of ACC and direction of targeted therapies to specific ACC subtypes.

APPENDIX B. Evidence for Intra-Tumoral Steroidogenesis as a Novel Mechanism of Immune Evasion in ACC

B.1. Disclosure of relevant publications

This work has not been published, but was part of a grant proposal our team submitted to the United States Department of Defense, which was awarded. Antonio Marcondes Lerario, MD, PhD, and I served as the two lead grant writers for this proposal (see **Appendix E** for grant citation and details). The analysis Dr. Lerario and I performed supporting rationale for this proposal and ongoing studies are briefly described here, and serves as the basis for ongoing work in our group.

B.2. Summary of rationale and ongoing studies

In recent years, studies investigating targeted therapies for a variety of advanced cancers have illuminated a promising role for immunotherapy, a well-tolerated group of therapeutic interventions that promotes cancer cell clearance by the immune system. Cancer cells frequently accumulate somatic alterations in protein-coding genes, giving rise to an abnormal landscape of cancer-specific proteins that act as “neoantigens” (Segal et al., 2008; Wortzel et al., 1983). These neoantigens have the potential to be recognized and cleared by immune system components such as CD8+ cytotoxic T cells (e.g. (Tran

et al., 2016)), a physiological mechanism which is protective for the organism but fatal for tumor formation.

Cancers have therefore developed numerous strategies to evade immune clearance. One such strategy includes cancer cell activation of immune checkpoint proteins, a class of membrane-bound receptors expressed by immune cells that recognize ligands on immune cells or other cell types. Active immune checkpoints act as a security measure against autoimmunity by restricting lymphocyte responsiveness to stimulatory signals in the presence of a "self" antigen (Freeman et al., 2000). Cancer cells take advantage of this immunomodulatory mechanism through upregulation of a variety of ligands that activate immune checkpoints, including the ligand of PD-1, PD-L1 (Azuma et al., 2008; Hamanishi et al., 2007; Nomi et al., 2007; Thompson et al., 2007). Through immune checkpoint activation, cancer cells evade recognition as "non-self" and persist in a protected microenvironment (Blank et al., 2004; Topalian et al., 2016).

Therapeutic approaches to mitigate immune checkpoint signaling have emerged as a remarkably effective strategy to enhance T cell-mediated clearance of cancer cells (Iwai et al., 2002; Leach et al., 1996). Extension of these studies to clinical trials have demonstrated that patients with advanced cancers from a variety of tissues exhibit clinically meaningful responses to PD-1/PD-L1 inhibitors (e.g. (Brahmer et al., 2012; Hamid et al., 2013; Topalian et al., 2012)). However, not all cancers respond to PD-1/PD-L1 inhibition, and numerous investigations into molecular features predictive of therapeutic response are ongoing. Recent studies suggest that, in general, cancers susceptible to PD-1/PD-L1 inhibition use this checkpoint to actively suppress T cell

function. Prior to therapy, susceptible cancers bear higher PD-1+ T cell infiltration, suggestive of active engagement of the PD-1/PD-L1 checkpoint (Vilain et al., 2017). Following therapy, susceptible cancers gain an influx of CD8+ T cells (Sun et al., 2018; Tumeh et al., 2014) commensurate with increased cancer cell expression of PD-L1 (Taube et al., 2014; Vilain et al., 2017). Intriguingly, susceptible cancers also bear high mutational load leading to increased expression of neoantigens (Rizvi et al., 2015). This reliance on high mutational load is further supported by the landmark observation that mismatch-repair deficient solid tumors are particularly responsive to PD-1 inhibitors (Le et al., 2017; Le et al., 2015), resulting in the U.S. Food and Drug Administration (FDA)'s recent Accelerated Approval of anti-PD-1 therapy (pembrolizumab) for treatment of any solid tumor with high microsatellite instability or mismatch repair deficiency, which includes ~5% of ACC (Bonneville et al., 2017; Raymond et al., 2013). This FDA Approval represents a promising addition to the clinical toolkit to fight ACC, evidenced by an ongoing phase II clinical trial evaluating this agent as monotherapy for patients with advanced disease (NCT02673333).

Despite these advances, expert clinicians who care for patients with ACC at our center and at collaborator institutions have observed that few patients with ACC exhibit disease regression following treatment with pembrolizumab (Habra, 2017). This is consistent with the observation that mismatch repair deficiency affects a minority of ACC tumors, but also augmented by our recent observations in ACC-TCGA (Zheng et al., 2016).

In ACC-TCGA, we identified that ACC bears lower expression of immune-specific genes than nearly all TCGA tumor types (Thorsson et al., 2018; Zheng et al., 2016), suggesting that ACC is largely immune poor. However, ACC-TCGA also revealed substantial heterogeneity across tumors. A subset of ACC bear high levels of immune infiltration (measured by immune score, (Yoshihara et al., 2013)), and high PD-1 and PD-L1 expression, suggestive of active suppression of T cell function via the PD-1/PD-L1 checkpoint in these tumors (Vilain et al., 2017). In contrast, the majority of ACC, with the worst clinical outcomes, have a low degree of immune infiltration and low expression of PD-1 and PD-L1, despite bearing a generally higher mutational burden (**Figure B.1**). These observations suggest that monotherapy targeting the PD-1/PD-L1 checkpoint is unlikely to have efficacy in most patients with ACC, and that alternative biological programs other than checkpoint activation impair steady state immune infiltration into these tumors.

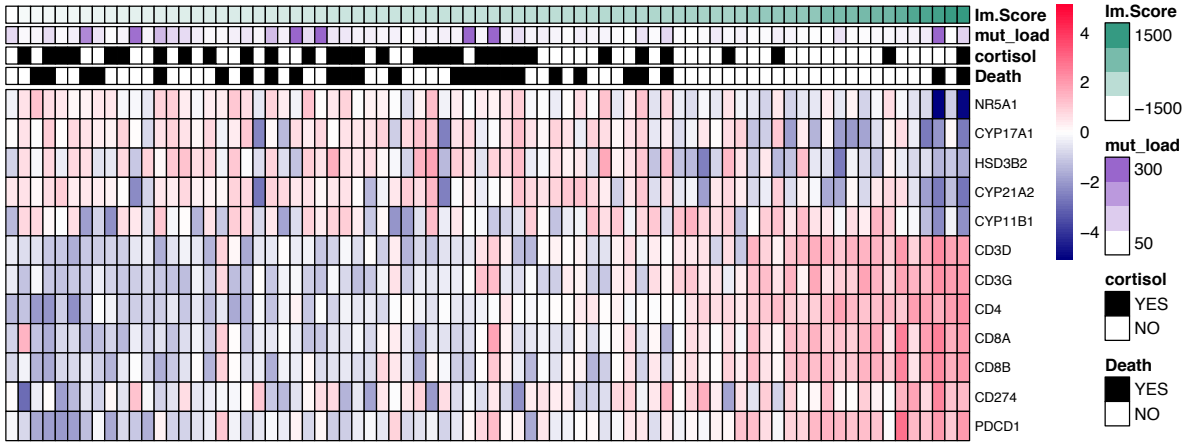

Figure B.1. ACC-TCGA RNA-seq data reveals that immune infiltration and steroid production are inversely associated, and that steroid production and reduced immune infiltration are associated with deadlier disease.
Patient samples are ranked by immune score (Im.Score, ranging from -1500 to 1500, measured as in (Yoshihara et al., 2013)). Higher immune score indicates higher degree of immune infiltration. Mutational load (mut_load) ranges from 50/sample to 300+/sample. Clinical cortisol secretion status and patient live/dead status at the time of ACC-TCGA are indicated accordingly. mRNA expression of genes involved in steroid production (*NR5A1, CYP17A1, HSD3B2, CYP21A2, CYP11B1*), indicative of T cell infiltrate (*CD3D, CD3G, CD4, CD8A, CD8B*), and involved in PD-1/PD-L1 checkpoint (PD-1 encoded by *PDCD1* and PD-L1 encoded by *CD274*) are represented by z-score of log-transformed counts per million according to pink/blue scale right.

Interestingly, immune-poor ACC also exhibits higher mRNA expression of genes involved in steroid production, pathologic cortisol excess (Cushing's syndrome), and dismal clinical outcomes (Zheng et al., 2016) (**Figure B.1, Chapter 3**). Pathologic cortisol secretion is widely recognized as a clinical predictor of poor prognosis for ACC (Else et al., 2014a). However, we were particularly interested in this anti-correlation because glucocorticoids including cortisol are well established potent T cell suppressors (Palacios and Sugawara, 1982). Indeed, recent studies in cancers of the colon and skin have also illuminated a role for abnormal steroidogenesis in cancer, linking intra-tumoral steroid production to T cell exclusion and suppression of T cell function (Cirillo et al., 2017; Sidler et al., 2011). A recent clinical study in patients with non-small cell lung cancer treated with PD-1/PD-L1 inhibition also demonstrated that elevated baseline steroid level is

independently associated with decreased progression-free and overall survival following checkpoint blockade (Arbour et al., 2018). These observations establish a paradigm for clinically meaningful interplay between cancer steroid production and tumor immune biology; however, the therapeutic implications of this relationship remain to be addressed.

The adrenal cortex is a highly steroidogenic tissue, responsible for production of a spectrum of steroid hormones that regulate numerous physiological processes. As ACC are derived from the adrenal cortex, they universally express all cellular machinery required for cortisol and other steroid biosynthesis, though at quantitatively and qualitatively variable levels across the ACC spectrum (**Figure B.1**). Clinically, patients with ACC often present with diverse signs and symptoms of hormone excess including hyperandrogenism, hypercortisolism, and/or hyperaldosteronism, or as hormonally silent. This uncoupling of high steroidogenesis machinery expression with clinical evidence of hormonal secretion suggests that upstream steroid precursors and metabolites may accumulate locally to modulate the ACC microenvironment. Given the strong inverse relationship between immune infiltration and steroidogenesis we observed in ACC-TCGA, ACC therefore represents a unique biological setting to study how subtle shifts in steroid biosynthesis establish a tumor niche hostile to immune cell infiltration.

Taken together, our observations suggest that increased intra-tumoral steroid production in ACC may be a novel mechanism of immune evasion. Characterizing the unknown interface between intra-tumoral steroid production and tumor immunology in ACC has the potential to illuminate novel biology and durable therapeutic strategies

utilizing immunotherapy for patients facing this devastating disease. Ongoing work is focused on the following areas:

Characterization and quantification of ACC intra-tumoral steroidomics and the molecular phenotype of infiltrating immune cells. We will measure tissue concentrations of steroid hormones in frozen ACC samples from the University of Michigan Endocrine Oncology Repository by liquid chromatography-tandem mass spectrometry (LC-MS/MS). We will characterize the spectrum of infiltrating immune cells (including T cells) present in each sample by immunohistochemistry, and evaluate cytokines, immune signatures, and steroidogenic programs differentially expressed across ACC by RNA-seq. Through integrated analyses, we will characterize the immune cell signature associated with a given steroid profile and transcriptional program.

Functional characterization of the impact of ACC-secreted steroids on immune cell function and tumor immune infiltrate. We will characterize secreted steroidomics of ACC-derived cell lines by LC-MS/MS. We will treat CD8+ T cells with conditioned media from ACC-derived cell lines +/- a variety of steroidogenesis inhibitors to evaluate impact of secreted steroids on T cell function *in vitro*. We will test if disrupting steroid receptor signaling using pharmacological antagonists of steroid receptors on T cells reverse these effects, and will extend findings to co-culture experiments with T cells and ACC cell lines. We will treat a steroidogenic, syngeneic xenograft mouse model of metastatic ACC with

PD-1 inhibitors +/- inhibitors of steroid production/action, and measure impact on tumor burden and immune infiltrate.

APPENDIX C. Frequently Used SWI/SNF-Deficient SW13 is not a Model of ACC, but Exhibits Time-Dependent Response to EZH2 Inhibition

C.1. Disclosure of relevant publications

This work has not been published, and is the product of our collaboration with the laboratory of Suely K. N. Marie, MD, PhD, at Faculdade de Medicina da Universidade de Sao Paulo, Sao Paulo, Brazil.

C.2. Brief summary of findings

In this study, we investigated the consequences of EZH2i (GSK126) in a model system that is particularly susceptible to EZH2i secondary to SWI/SNF deficiency (**Table 1.7**), the SW13 cell line. The SW13 cell line comprises two morphologically distinct populations of cells: mesenchymal, SWI/SNF-proficient; and epithelioid, SWI/SNF-deficient ((Yamamichi-Nishina et al., 2003)). This cell line has also been widely misclassified as an ACC cell line because it was developed from a cancer that was residing in the adrenal cortex (Leibovitz et al., 1973). Somatic alterations disrupting SWI/SNF components in ACC are infrequent (Zheng et al., 2016), and SW13 do not express *NR5A1* nor do they possess the capacity for steroidogenesis. We therefore took advantage of our studies in this line to characterize context-specific roles for PRC2. We

compared expression of embryonic PRC2 target genes (BENPORATH_PRC2_TARGETS) between baseline NCI-H295R and SW13, and were intrigued to observe that PRC2 target gene expression was highly variable between the two cell lines (**Figures C.1 – C.2**).

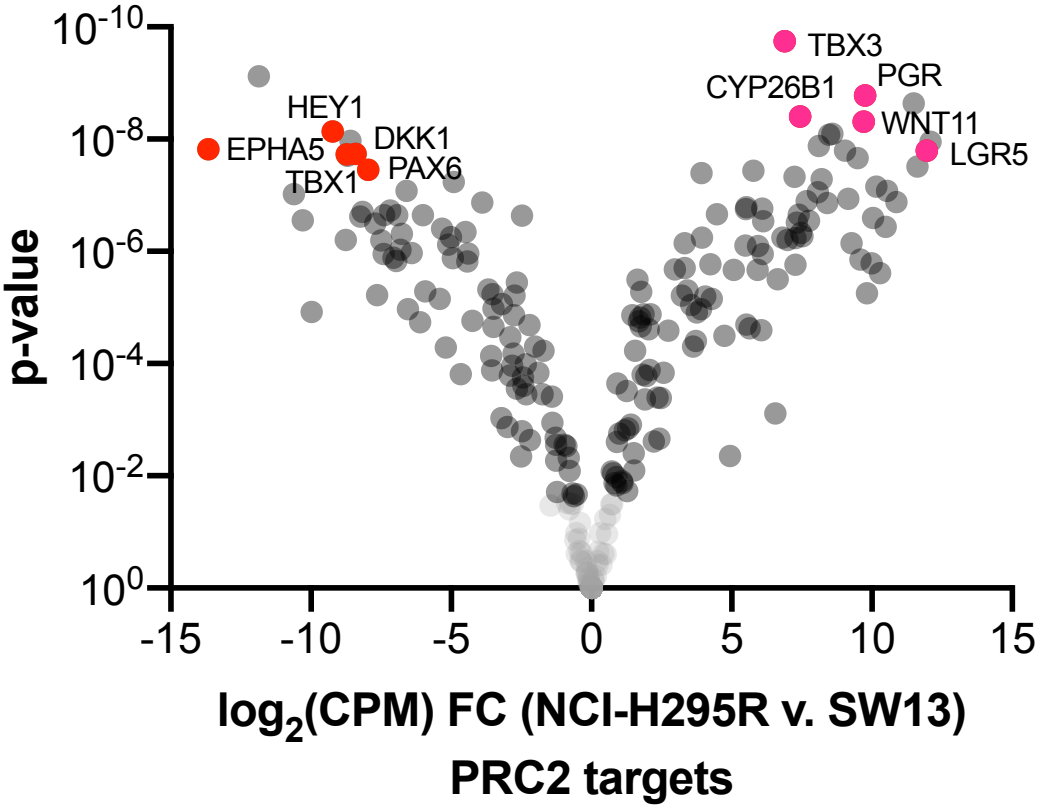

Figure C.1. PRC2 targets are highly differentially expressed between NCI-H295R and SW13. While NCI-H295R express high levels of canonical Wnt/β-catenin targets like *LGR5*, SW13 express high levels of Notch target genes like *HEY1*.

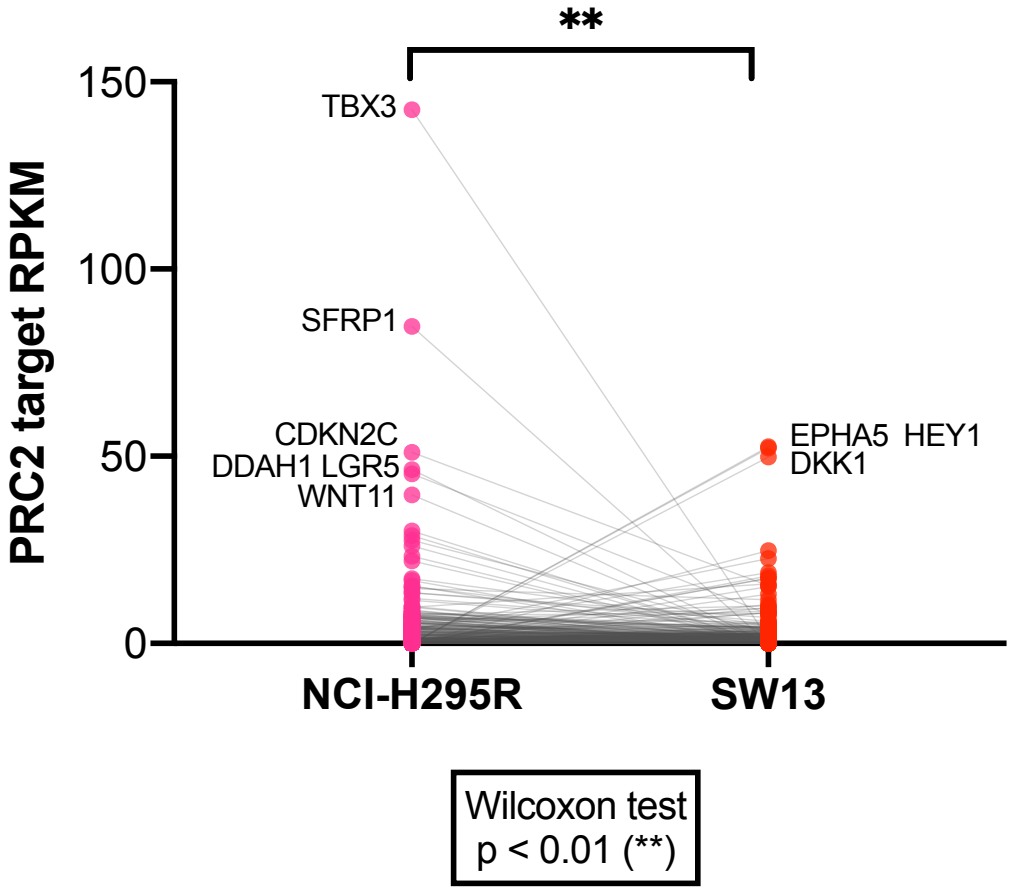

Figure C.2. PRC2 target expression is highly variable between NCI-295R and SW13.

We treated the SW13 cell line with EZH2i GSK126 for 48 or 96 hours, and harvested mRNA for RNA-seq profiling using the Lexogen platform. We observed that SW13 response to GSK126 was time-dependent, and this cell line gradually gained more upregulated than downregulated differentially expressed genes with time (**Figure C.3**).

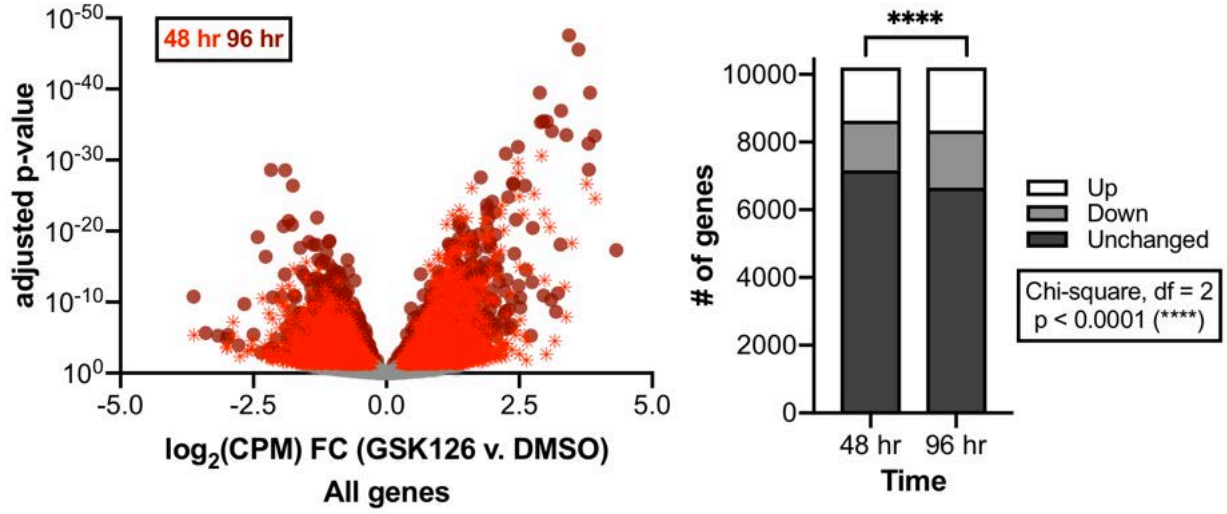

Figure C.3. EZH2i alters the SW13 transcriptome in a time-dependent manner.

This was particularly pronounced at embryonic PRC2 targets (**Figure C.4**).

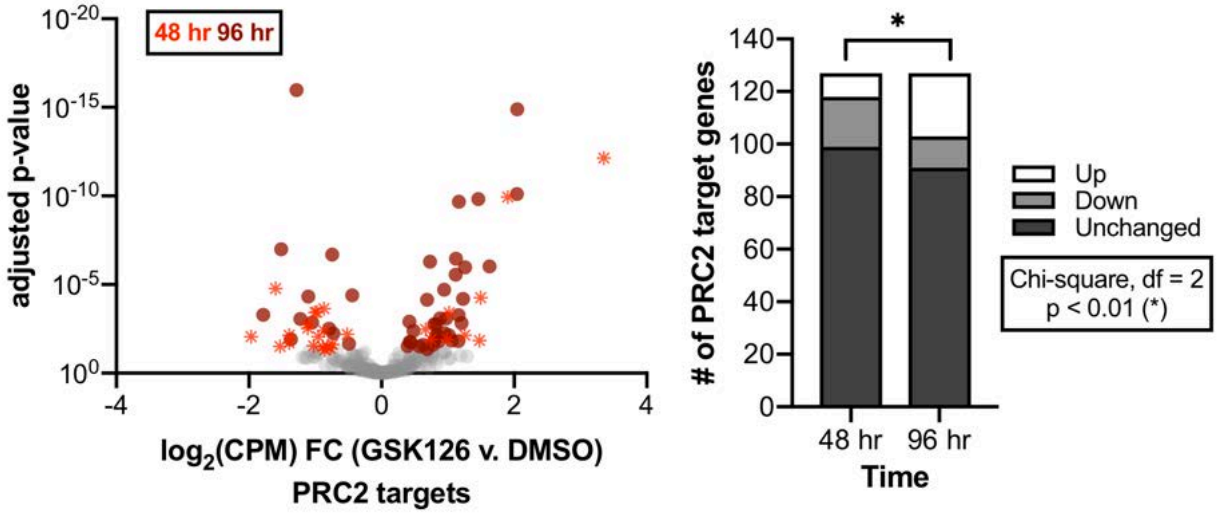

Figure C.4. Embryonic PRC2 target expression in EZH2i-treated SW13 varies with treatment duration.

To try to understand the mechanism for progressive induction of gene expression programs with EZH2i, we analyzed induced genes using a tool that queries publicly

available epigenomics data to infer which transcription factors are driving differential gene expression, BART (Wang et al., 2018). This tool helped us to identify that, initially, EZH2i unmasks lineage-defining programs (in the case of the SW13, we are assuming these programs are Notch-dependent based on **Figure C.1**), and later unmasks core PRC2 programs (**Figure C.5**).

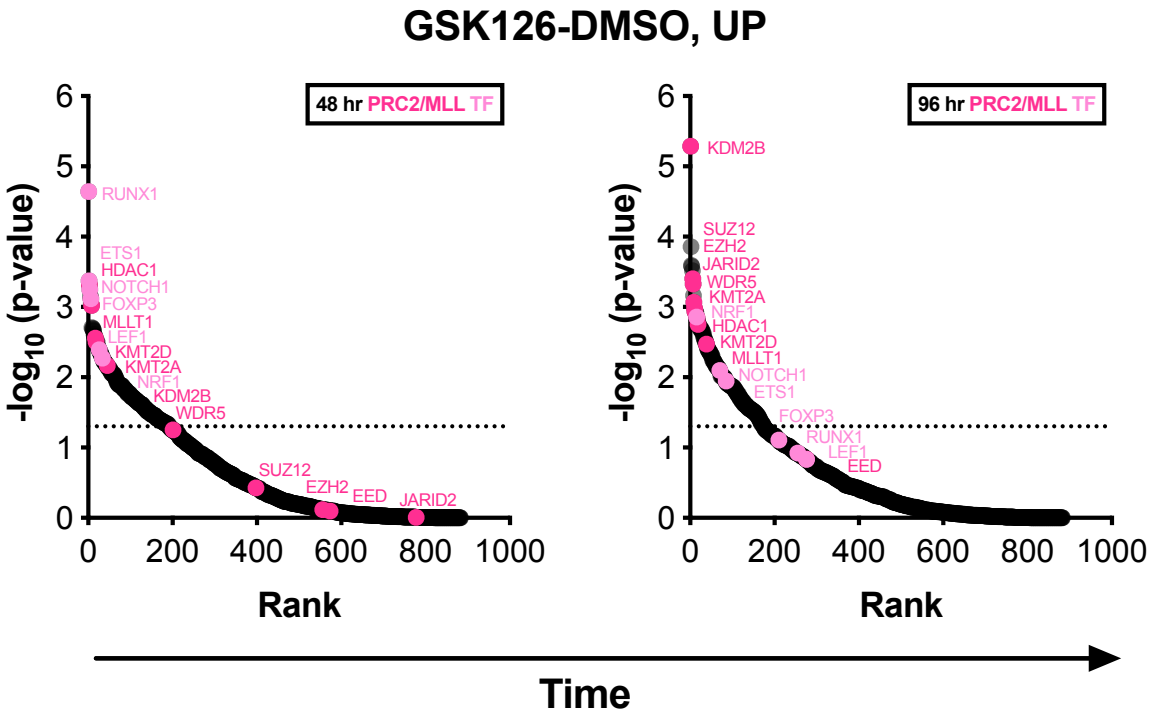

Figure C.5. EZH2i initially unmasks lineage-defining programs which are later displaced by core PRC2 programs.

This preliminary study suggests that ripples in cell identity-defining transcriptional programs may be part of the initial cellular response to EZH2i, which later converges on canonical and perhaps degenerate PRC2 programs.

APPENDIX D. Establishment and Characterization of a Novel Brazilian Population Database, SELAdb

D.1. Disclosure of relevant publications

As part of our group's ongoing collaboration with Faculdade de Medicina da Universidade de Sao Paulo, I had the opportunity to contribute to the analysis and writing of a paper describing a novel Brazilian population database of genetic variability. This work has been published as:

> Lerario AM, **Mohan DR**, Montenegro LR, Funari MFA Nishi MY, Narcizo AM, Benedetti AFF, Oba-Shinjo SM, Vitorino AJ, Santos RASX, Jorge AAL, Onuchic LF, Marie SKNM*, Mendonca BB*. SELAdb: A database of exonic variants in a Brazilian population referred to a quaternary medical center in Sao Paulo. *Clinics (Sao Paulo)*. 2020 Aug 6. 75:e1913. *equal contribution

D.2. Introduction

Advances in high-throughput sequencing technologies in the last decade have enabled systematic genome profiling of thousands of individuals from diverse populations worldwide. Consequently, we now have several publicly available genomic databases that illustrate the profound variability across different ethnic groups, serving as rich resources for investigators seeking to elucidate the molecular basis of human diseases. Indeed, as the cost of next-generation sequencing (NGS) is rapidly declining, NGS-based

approaches including exome sequencing and disease-focused gene panels are quickly becoming the mainstay of molecular diagnostics.

For example, a clinician who has identified a patient with phenotypic features resembling a particular familial syndrome in the absence of family history may elect to perform exome sequencing in genomic DNA from this patient in hopes of identifying a disease-causing genetic variant. However, such an approach routinely results in the identification of thousands of variants. Defining which of these variants is the true disease-causing allele is clinically challenging. An approach that is usually adopted to overcome this obstacle is to filter out common variants in a population. Even this approach, however, has limited utility, as certain populations are underrepresented in many populational databases, and the clinically relevant allele frequencies remain uncharacterized. At Hospital das Clinicas da Faculdade de Medicina da Universidade de Sao Paulo (HCFMUSP), Sao Paulo, Brazil, we adopt NGS-based methods for the diagnosis of putative Mendelian disorders as standard practice. However, the most widely utilized databases (e.g. gnomAD (Lek et al., 2016), 1000 Genomes (Auton et al., 2015)) have poor annotation and underrepresentation of diverse individuals of South American origin (Giolo et al., 2012).

The population of Brazil, in particular, is comprised of many different ethnic groups (Giolo et al., 2012; Kehdy et al., 2015), and provides a unique opportunity to identify novel uncharacterized disease-causing variants unique to this population. Illustrating this point, an unusually high incidence of pediatric adrenocortical tumors in Brazil (nearly twenty times higher than the global incidence) led to the identification of a novel variant in *TP53*

(p.R337H) present in nearly 0.3% of Southeastern Brazil and accounting for 90% of pediatric ACC in this area (Palmero et al., 2008; Pinto et al., 2004; Ribeiro et al., 2001). Subsequent studies demonstrated that the high prevalence of p.R337H in this population can be attributed to founder effect (Pinto et al., 2004), and highlights the critical need of regionally focused studies in population genetics. Recently, investigators at the University of Sao Paulo Institute of Biology developed a database of exomes from 609 elderly individuals, ABraOM, which serves as a powerful resource for clinicians and investigators researching this select group of individuals (Naslavsky et al., 2017). Our goal at HCFMUSP was to take advantage of our expertise as an NGS-based facility with half a decade of experience in using exome sequencing as a diagnostic tool to create a more representative database of our general patient population.

D.3. Materials and methods

Subjects. Our database includes 862 individuals associated with different clinical services (Endocrinology, Neurology, Nephrology, Psychiatric, Gastroenterology, and Rheumatology) at HCFMUSP, comprised of patients with putative Mendelian disorders of uncertain or unknown genetic causes, patients with complex disease traits, patients with sporadic tumors, or unaffected family members. We applied a kinship filter (Team) to remove related individuals to produce a final cohort of 523 unrelated Brazilian individuals (240 males, 283 females).

Sequencing. Exome sequencing was performed using the Illumina HiSeq 2500 platform in Escola Superior de Agricultura “Luiz de Queiroz” (ESALQ - 2013-2014) or Laboratorio de Sequenciamento em Larga Escala da Faculdade de Medicina da Universidade de Sao Paulo (SELA-FMUSP - 2014-2019). Library preparation and exome capture were performed using the Nextera Rapid Capture Enrichment (Illumina, San Diego, CA) or the SureSelect Target Enrichment System All Exon +/- UTRs V4, V5 and V6 (Agilent Technologies, Santa Clara, CA) according to the manufacturer's instructions.

Bioinformatics analysis. After quality-control using *FastQC* (Andrews) and adapter sequencing removal using the *bbduk* tool from *bbmap* (Bushnell, 2014), paired-end reads were aligned to the hg19/GRCh37+decoy version of the human genome (downloaded from ftp://ftp.1000genomes.ebi.ac.uk) using *bwa-mem* (Li, 2013). Aligned reads were then coordinate-sorted, deduplicated, and indexed using *bamsort* and *bammarkduplicate* tools from *biobambam2* (Tischler and Leonard, 2014). Sequencing errors, duplication rates, and coverage metrics were assessed with *qualimap* (Okonechnikov et al., 2016). For variant calling, we used an incremental joint variant calling strategy based on *freebayes* (Garrison and Marth, 2012) as follows: First, we used *freebayes* to perform variant calling on each bam file individually. We filtered out low-coverage and low-quality variants (<10x and QUAL<10, respectively). We performed multiallelic sites decomposition, multiallelic variants decomposition, and left normalization of InDels using *vt decompose*, *vcfallelicprimitives* (from *vcflib*), and *vt normalize* tools (Garrison; Tan et al., 2015). After processing all vcf files in this manner, we created a joint list of variants

using the *vcfoverlay* (Garrison) tool from *vcflib*. We then used this joint list as an input for *freebayes* (using the -@ option) to perform a second round of variant calling. We used the "-l" switch from *freebayes* to restrict calls only to positions of variants reported in the joint list. This final step enables us to report all sites from the joint list, even in samples bearing the reference allele. Sex-specific ploidy was set to regions outside the pseudo-autosomal region of the Y chromosome. We next used *bcftools merge* (Li, 2011) to combine variant information from individual vcf files into a single file containing the sex-corrected allele frequencies for all variants detected in the dataset. We then used *hail* (Team) to remove related individuals from the dataset. Finally, we used *SNPEff* and *SNPSift* (Cingolani et al., 2012a; Cingolani et al., 2012b) to annotate these variants according to genomic loci, functional consequences on protein-coding genes, and dbSNP membership. A summary of the bioinformatics workflow employed to construct SELAdb is depicted in **Figure D.1**. Finally, we used *somalier* (Pedersen et al., 2019) to estimate the ancestry of our population in comparison to the populations included in the 1000 Genomes project, using the individuals in 1000 Genomes as a training set. We represented these ancestry data using principal component analysis (PCA) plots built with *ggplot2* (Wickham, 2016) and used a neural network classifier (Pedersen et al., 2019) to calculate posterior probabilities for the assignment of a sample in our cohort to the populations defined in 1000 Genomes.

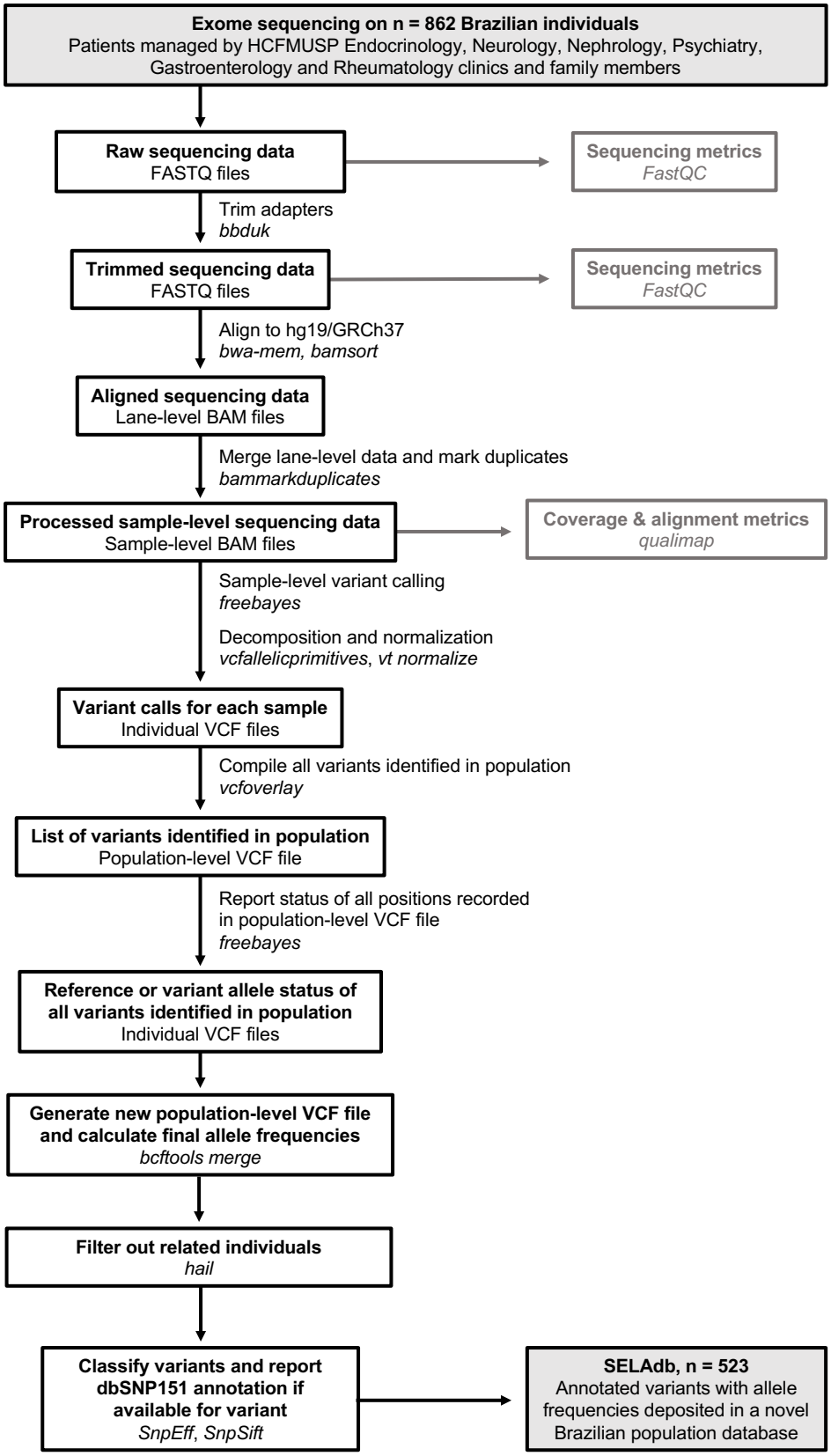

Figure D.1. Flow chart of data processing steps used to generate SELAdb.

Ethics. This study was approved by the Institutional Review Board of HCFMUSP, in accordance with the Helsinki Declaration. Written consent was obtained from all individuals included in SELAdb.

D.4. SELAdb accurately captures the diversity of the southeastern Brazilian population

As detailed in **Figure D.1**, we analyzed exome sequencing data from 862 individuals to generate a final cohort of exomes from 523 unrelated individuals (240 males, 283 females) and a corresponding list of annotated variants with allele frequencies, which we deposited in a novel Brazilian population database, SELAdb. Among 523 individuals, we identified 1,788,789 variants, including 1,615,436 single-nucleotide variants, 47,805 small insertions, 121,255 small deletions, and 4,293 complex substitutions (**Table D.1**).

Table D.1. SELAdb variants classified by type and presence in other databases

Total number of SELAdb variants	1,788,789
Variant type	**Number of variants (% of SELAdb)**
Single nucleotide polymorphism (SNP)	1,615,436 (90.3%)
Insertion	47,805 (2.7%)
Deletion	121,255 (6.8%)
Mixed	4,293 (0.2%)
Database	**Number of variants annotated (% of SELAdb)** **Number of novel variants (% of SELAdb)**
dbSNP151	*Annotated* – 1,286,051 (71.9%) *Novel* – 502,738 (28.1%)
1000 Genomes	*Annotated* – 1,205,879 (67.4%) *Novel* – 582,910 (32.6%)
gnomAD	*Annotated* – 489,563 (27.4%) *Novel* – 1,299,226 (72.6%)
ABraOM	*Annotated* – 915,702 (51.2%) *Novel* – 873,087 (48.8%)

Among these variants, 502,738 (28.1%) are not reported in dbSNP151 and, therefore, may represent novel variants present in the Brazilian population (**Table D.1**). A total of 2,973,280 effects (alterations resulting in potential changes in protein structure, function, and/or expression, such as amino acid changes or abrogation of transcription factor binding sites) could be attributed to these 1,788,789 variants, including 581,757 targeting annotated exons. Included among these are 152,984 synonymous, 207,854 missense, 3,742 stop-gained, 256 stop-lost, 405 start-lost, and 9,653 frameshift variants (**Table D.2**).

Table D.2. Number of effects attributed to variants in SELAdb by region and type

Region	Count	Percent (%)
Downstream	402,130	13.525
Exon	581,757	19.566
Gene	16	0.001
Intergenic	60,291	2.028
Intron	1,091,611	36.714
Motif	8,440	0.284
Splice site acceptor	1,387	0.047
Splice site donor	1,604	0.054
Splice site region	35,011	1.178
Transcript	199,903	6.723
Upstream	374,792	12.605
UTR 3 prime	165,649	5.571
UTR 5 prime	50,689	1.705
Type	**Count**	**Percent (%)**
3’ UTR variant	165,652	5.941
5’ UTR premature start codon gain variant	6,053	0.201
5’ UTR truncation	3	0
5’ UTR variant	44,637	1.48
TFBS ablation	75	0.002
TFBS variant	8,365	0.277
Bidirectional gene fusion	7	0
Conservative inframe DEL	1,150	0.038
Conservative inframe INS	480	0.016
Disruptive inframe DEL	2,133	0.071
Disruptive inframe INS	655	0.022
Downstream gene variant	402,132	13.331
Exon loss variant	3	0
Frameshift variant	9,653	0.32
Gene Fusion	9	0
Initiator codon variant	38	0.001
Intergenic variant	60,291	1.999
Intragenic variant	174,620	5.789
Intron variant	1,123,430	37.241
Missense variant	207,854	6.89
Noncoding transcript exon variant	164,421	5.45
Noncoding transcript variant	90	0.003
Protein-protein contact	476	0.016
Sequence feature	25,193	0.835
Splice acceptor variant	1,414	0.047
Splice donor variant	1,675	0.056
Splice region variant	40,619	1.347
Start lost	405	0.013
Stop gained	3,742	0.124
Stop lost	256	0.008

(Table continued on next page)

Type	Count	Percent (%)
Stop retained variant	123	0.004
Structural interaction variant	43,197	1.432
Synonymous variant	152,984	5.071
Upstream gene variant	374,792	12.424

NOTE. Abbreviations are defined as follows: UTR = “untranslated region,” TFBS = “transcription factor binding site,” DEL = “deletion,” INS = “insertion.”

We next sought to determine the ancestry of the individuals in our cohort using the populations defined by the 1000 Genomes project as a reference. The biplot shown in **Figure D.2** represents the first two principal components that capture most of the variability present in the data. The European (EUR), African (AFR), and East Asian (EAS) populations encompass three well-defined clusters in the extremes of this two-dimensional space, forming vertices of a triangle. The Ad Mixed American population (AMR), as expected, exhibits higher variability, and is dispersed over a larger area of the plot, with limbs extending to the areas delimited by the EUR, AFR, and EAS populations (**Figure D.2**). Similar to previous studies, our results indicate that SELAdb, comprising urban southeastern Brazilian individuals, forms a continuum between EUR and AFR, consistent with a high degree of intermarriage between these two populations in southeastern Brazil (Giolo et al., 2012). Furthermore, we observe here that individuals in SELAdb broadly overlap with a large fraction of the AMR population (**Figure D.2**).

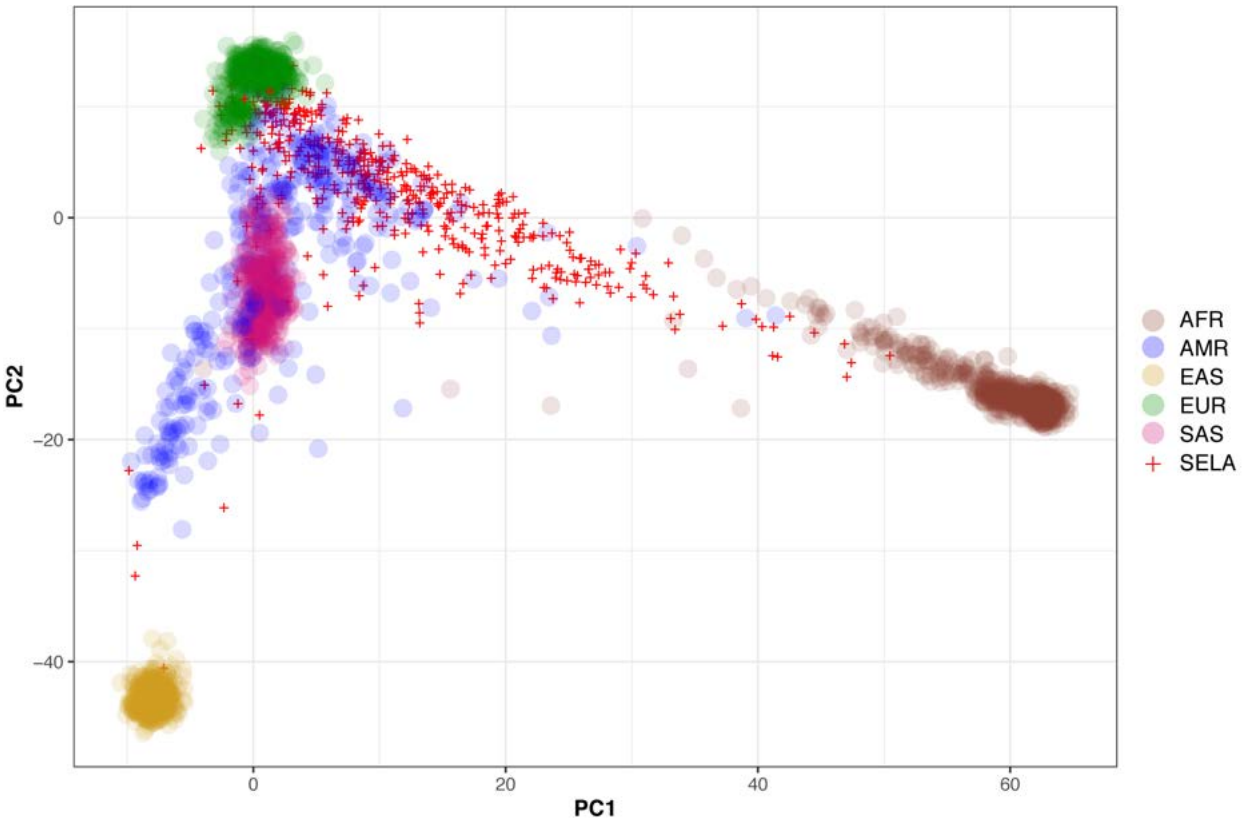

Figure D.2. Biplot depicting genetic variation among different populations in 1000 Genomes and SELAdb.
Biplot depicting the two principal components (x-axis: PC1, y-axis: PC2) capturing the most genetic variation among different populations from 1000 Genomes (colored circles) and SELAdb individuals (red crosses). Each circle or cross represents a single individual. The populations represented by the colored circles are African (AFR), Ad-Mixed American (AMR), East Asian (EAS), European (EUR), and South Asian (SAS).

To better quantify and define the putative ancestry of individuals in SELAdb, we applied a neural network classifier to fit individuals in SELAdb to pre-existing EAS, SAS, EUR, AFR, and AMR categories in 1000 Genomes (**Figure D.3**). This analysis revealed that the majority of individuals in SELAdb indeed classified as AMR (75.5%), followed by EUR (18.0%), AFR (5.2%) and EAS (1.3%) (**Figure D.3B**).

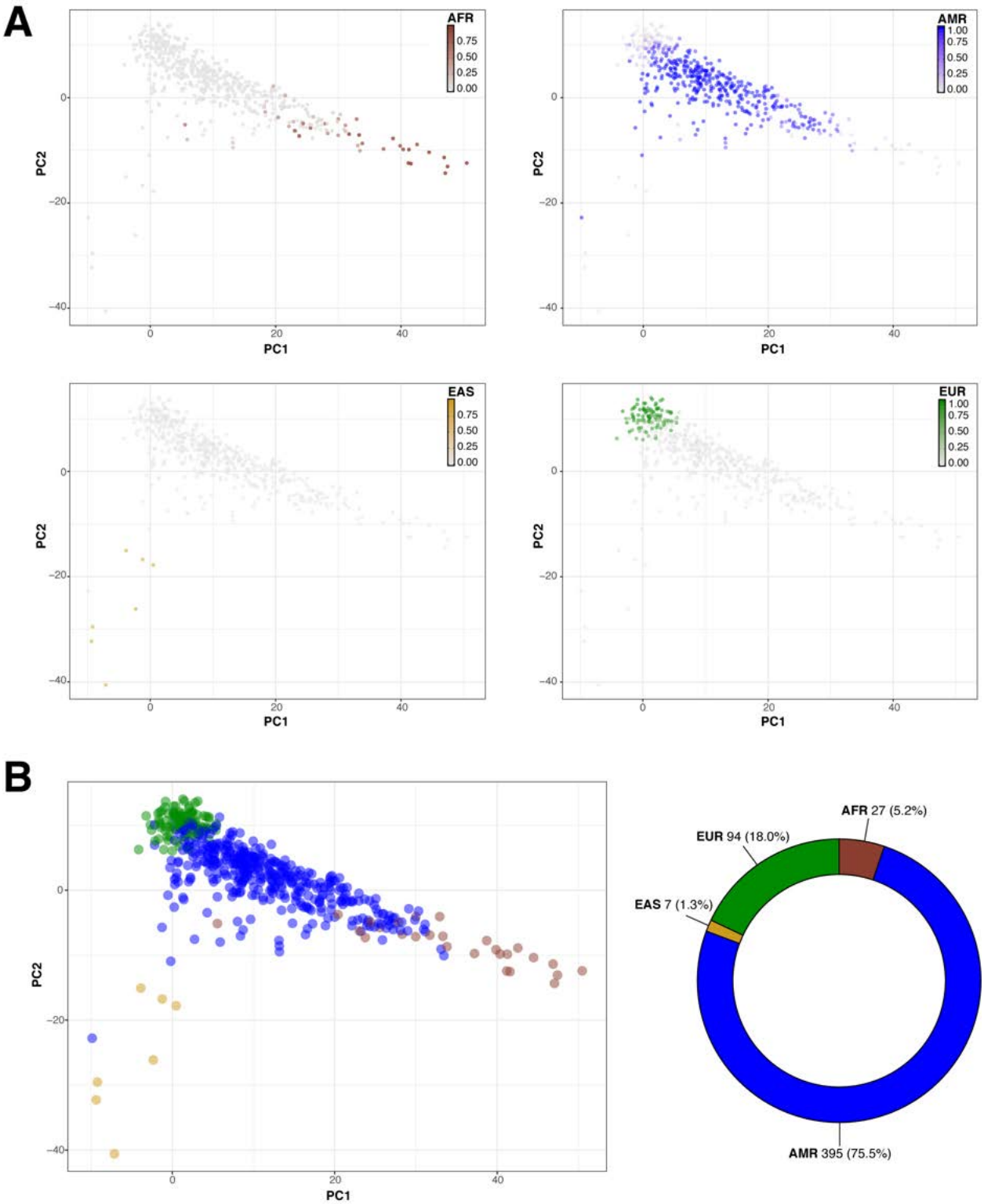

Figure D.3. Classification of SELAdb individuals by a neural network classifier using 1000 Genomes populations as the training set.

Panel A depicts a series of biplots (x-axis: PC1, y-axis: PC2) representing the PCA analysis of SELAdb individuals color-coded according to the posterior probabilities of being classified as a distinct population from 1000 Genomes, including AFR (brown, upper left), AMR (blue, upper right), EAS (yellow, lower left),

and EUR (green, lower right). Panel B depicts a biplot (left; x-axis: PC1, y-axis: PC2) representing each SELAdb individual color-coded according the final classification given by the neural network classifier. The final distribution of individuals in each category are represented in the donut plot (right). Consistent with the distribution of SELAdb individuals in Panel A, most SELAdb individuals classify as AMR.

The AMR population in 1000 Genomes is a heterogeneous group comprised of individuals from different geographic regions of Latin America, but does not include any individuals from Brazil (Auton et al., 2015). Given that the majority of individuals in SELAdb classified as AMR despite the absence of Brazilian individuals in this set, we sought to determine which subgroup of the AMR population in 1000 Genomes is the most similar to individuals from SELAdb. To address this question, we performed a similar PCA analysis but now with the AMR population separated into its constituent subpopulations, including Peruvians of Lima (PEL), Mexicans of Los Angeles (MXL), Colombians (CLM), and Puerto Ricans (PUR) (**Figure D.4A**). From this analysis, we can appreciate that the AMR population is comprised of unique subclusters, in which PEL, MXL, CLM, and PUR populations cluster separately within the region spanned by AMR in **Figure D.2**. This observation suggests that the broad space encompassed by AMR in the biplot may be partially explained by the number of populations of diverse origins defined as AMR, rather than broad heterogeneity dispersed throughout each population. Indeed, **Figure D.4A** illustrates that the MXL and PEL form a distinct cluster that localizes closer to EAS, and farther from EUR and AFR; this observation is consistent with the theory of the Asian origin of native American populations (Reich et al., 2012). In contrast, PUR exhibit a distinct pattern, characterized by a higher influence of both EUR and AFR. Finally, CLM exhibit characteristics of both MXL/PEL and PUR. We observe here that SELAdb largely overlaps with PUR, consistent with the stronger influence of EUR and AFR in the

southeastern Brazilian population (Giolo et al., 2012). Quantifying this overlap further with a neural network classifier using the subdivided AMR groups (**Figure D.4B**), we can observe that a majority of individuals in SELAdb now classify as PUR (60.2%). This observation suggests a similar contribution of European and African ancestries to both PUR and southeastern Brazilian populations, consistent with common historical aspects of colonization of both geographical regions and recent studies defining ancestral contributions to each population (Giolo et al., 2012; Szpiech et al., 2019).

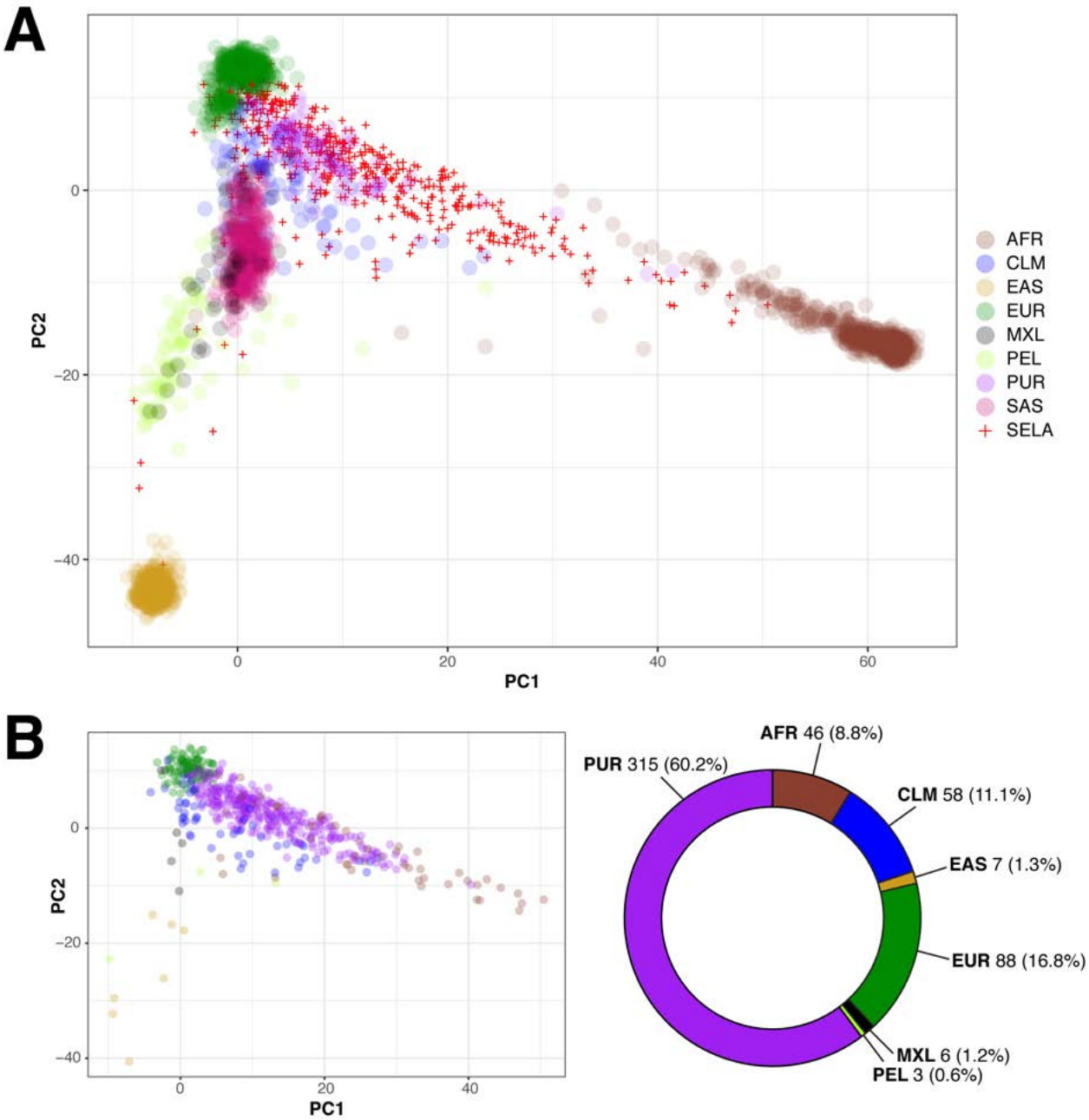

Figure D.4. Biplot depicting overlap between 1000 Genomes with AMR split up reveals SELAdb individuals align with an AMR subpopulation.

Biplot (x-axis: PC1, y-axis: PC2) showing the overlap between 1000 Genomes (colored circles) and SELAdb individuals (red crosses). In this representation, the AMR population is split according to its subpopulations, including Colombians (CLM), Mexicans of Los Angeles (MXL), Peruvians of Lima (PEL), and Puerto Ricans (PUR). Panel B: Neural network classification of SELAdb individuals using the 1000 Genomes as a training set. Consistent with the distribution of SELAdb individuals in Panel A, most SELAdb individuals classify as PUR.

D.5. SELAdb enables identification of novel, potentially disease-causing variants in a Brazilian population

Given the ability of SELAdb to identify novel variants present in the Brazilian population, distinct from other population databases (**Table D.1**), we sought to evaluate its utility in identifying well documented pathogenic variants in a set of 60 genes associated with highly penetrant genetic disorders according to the American College of Medical Genetics and Genomics (ACMG SF v2.0) (Kalia et al., 2017). We were particularly interested in this set of genes, as variants are associated with high risk of diseases associated with early mortality, including cardiovascular disease and familial neoplasia syndromes. We therefore suspected that many of these variants may be unique to the Brazilian population but absent from ABraOM, given the inclusion criteria of the ABraOM databse (Naslavsky et al., 2017).

We identified in SELAdb 24 known pathogenic or likely pathogenic variants according to ClinVar (Landrum et al., 2018) (**Table D.3**). Interestingly, 11 of these variants are exclusive to SELAdb, not reported in gnomAD and ABraOM. 13 variants were also reported in gnomAD and/or ABraOM (7 gnomAD and ABraOM, 6 gnomAD only, 0 ABraOM only). In addition, we identified 7 variants predicted to be pathogenic according to InterVar (Li and Wang, 2017), among which only 4 were present in gnomAD and/or ABraOM (**Table D.4**). These observations highlight the unique contribution of SELAdb in augmenting the spectrum of potential disease-causing variants present in the Brazilian population, and illustrate its clinical and research utility.

Table D.3. SELAdb variants classified as pathogenic/likely pathogenic by ClinVar and recommended to report by ACMG.

Gene	Mutation	dbSNP151	SELAdb allele frequency	Other databases
MUTYH	NM_001128425:p.479_480del	rs587778541	1/1042	gnomAD, ABraOM
MUTYH	NM_001128425:p.Gly396Asp	rs36053993	6/1044	gnomAD, ABraOM
PCSK9	NM_174936:p.Tyr142X	rs67608943	1/1046	gnomAD, ABraOM
LMNA	NM_001282625:p.Cys522X	N/A	1/1044	SELAdb only
TNNT2	NM_001001430:p.Asn271Ile	N/A	1/1046	SELAdb only
PKP2	NM_004572:c.2578-2A>C	N/A	1/1016	SELAdb only
BRCA2	NM_000059:p.Tyr2154fs	rs80359596	1/970	SELAdb only
ATP7B	NM_000053:exon17:c.A3694C: p.T1232P	rs568009639	1/1046	gnomAD, ABraOM
ATP7B	NM_000053:p.Pro1134fs	rs137853281	2/1044	gnomAD, ABraOM
ATP7B	NM_000053:p.His1069Gln	rs76151636	1/1046	gnomAD
ATP7B	NM_000053:p.Pro840Leu	rs768671894	1/1046	SELAdb only
ATP7B	NM_000053:p.Leu708Pro	rs121908000	1/1034	SELAdb only
BRCA1	NM_007294:p.Cys903X	N/A	2/1030	SELAdb only
BRCA1	NM_007294:p.Cys64Arg	rs80357064	1/1004	SELAdb only
LDLR	NM_000527:p.Gly55Gly	rs150644181	1/1046	gnomAD, ABraOM
LDLR	NM_000527:p.Glu418Lys	N/A	1/1038	gnomAD
LDLR	NM_000527:p.Gly592Glu	rs137929307	1/1038	gnomAD
LDLR	NM_000527:p.Arg744X	rs200793488	1/1046	SELAdb only
TNNI3	NM_000363:p.Asp196Asn	rs104894727	1/1042	gnomAD
TNNI3	NM_000363:p.Arg145Gln	rs397516349	1/1026	gnomAD
APOB	NM_000384:p.Ala13fs	N/A	2/1008	SELAdb only
APOB	NM_000384:p.F2181fs	N/A	1/916	gnomAD
PMS2	NM_000535:c.989-2A>G	rs587779347	1/890	SELAdb only
PMS2	NM_000535:p.Met1Val	rs587779333	1/1032	gnomAD, ABraOM

NOTE. Regarding the *BRCA1* mutation NM_007294:p.Cys903X with allele frequency 2/1030: Both alleles are present in the same individual in SELAdb. The phenotype of this individual is described in Freire *et al. Eur. J. Med. Genet.* 2018 (PMID: 29133208).

Table D.4. SELAdb variants classified as pathogenic by InterVar and recommended to report by ACMG

Gene	Mutation	dbSNP151	SELAdb allele frequency	Other databases
PCSK9	NM_174936:p.Gln387X	N/A	1/1020	SELAdb only
CACNA1S	NM_000069:p.Arg1702X	rs550371466	1/1044	gnomAD
RYR2	NM_001035:p.Cys1914X	N/A	1/1030	SELAdb only
SCN5A	NM_198056:p.Glu1053Lys	rs137854617	1/1010	gnomAD, ABraOM
RET	NM_020630:p.Val804Met	rs79658334	1/934	gnomAD, ABraOM
MYBPC3	NM_000256:p.Gly278X	N/A	1/978	SELAdb only
ATP7B	NM_000053:p.Gly170X	N/A	1/1022	gnomAD

D.6. Discussion

The Brazilian population is highly admixed, being comprised of several different ethnic groups, and inadequately represented in publicly available genomic databases (Giolo et al., 2012; Kehdy et al., 2015). Here, we take advantage of our 5-year experience as a large-scale sequencing core facility to build a representative local genomic database for the southeastern Brazilian population, SELAdb. Although many individuals included in SELAdb are patients or family members with rare Mendelian disorders, contributing to the identification of novel disease-causing variants (Chamberlin et al., 2019; Correa et al., 2018; de Bruin et al., 2016; Franca et al., 2017a; Franca et al., 2018; Franca et al., 2017b; França et al., 2018; Freire et al., 2018; Hisado-Oliva et al., 2018; Lessel et al., 2018; Shinjo et al., 2018; Vasques et al., 2017; Veloso et al., 2017), our analyses demonstrate that it adequately represents our local patient population. Through ancestry analysis, we observe that the population captured by SELAdb bears diverse genetic influences characteristic of the admixed southeastern Brazilian population similar to previous reports (Giolo et al., 2012). In this analysis, we also identified a large overlap between SELAdb individuals and the 1000 Genomes AMR population (**Figures D.2 – D.3**), especially with PUR individuals (**Figure D.4**). Taken together, our analyses illustrate the value of regional population databases in better representing individuals of diverse origin.

Our effort adds value to another recently launched genetic database on Brazilian individuals, ABraOM (Naslavsky et al., 2017). However, given the focus of ABraOM on healthy elderly individuals, pathogenic variants that are present in our patient population may be underrepresented. In contrast, our database is focused on a population of patients

or family members with putative genetic diseases, and we identified a spectrum of known and potentially novel pathogenic variants, as illustrated in **Tables D.3 – D.4**. We believe that SELAdb may inform the prevalence of pathogenic variants in the southeastern Brazilian population and facilitate future genetics studies investigating Brazilian individuals.

In conclusion, SELAdb is a publicly available database that is representative of our regional patient population. We believe that, in addition to AbraOM, SELAdb will be a valuable resource for investigators using genomics data from the Brazilian population. SELAdb is rapidly increasing in size; updates and improvements, including more detailed phenotypic annotations associated to specific variants, are expected to be implemented every six months. The data can be freely accessed at http://intranet.fm.usp.br/sela.

APPENDIX E. Author Contributions

I, Dipika R. Mohan, was the sole author and primary contributor to all work detailed in this dissertation, unless stated otherwise. If text was adapted from publications or manuscripts in preparation, this was stated in the first section of each chapter with the list of authors who are contributors to that publication. It is possible that work from this thesis will get incorporated into future manuscripts on which I am a co-author, and it is also possible that the form of publications or manuscripts in preparation change over the course of peer review and manuscript development. Work in this dissertation may have appeared or may appear in part in any of the following research products, with contributing authors credited accordingly:

E.1. Publications

1. Lerario AM, **Mohan DR**, Montenegro LR, Funari MFA Nishi MY, Narcizo AM, Benedetti AFF, Oba-Shinjo SM, Vitorino AJ, Santos RASX, Jorge AAL, Onuchic LF, Marie SKNM*, Mendonca BB*. SELAdb: A database of exonic variants in a Brazilian population referred to a quaternary medical center in Sao Paulo. *Clinics (Sao Paulo)*. 2020 Aug 6. 75:e1913. *equal contribution
2. **Mohan DR**, Lerario AM, Finco I, Hammer GD. New strategies for applying targeted therapies to adrenocortical carcinoma. *Current Opinion in Endocrine and Metabolic Research*. 2019 Oct 1. 8:66-71.
3. Finco I, **Mohan DR**, Hammer GD, Lerario AM. Regulation of stem and progenitor cells in the adrenal cortex. *Current Opinion in Endocrine and Metabolic Research*. 2019 Oct 1. 8:72-79.

4. **Mohan DR***, Lerario AM*, Else T, Mukherjee B, Almeida MQ, Vinco M, Rege J, Mariani BMP, Zerbini MCN, Mendonca BB, Latronico AC, Marie SKN, Rainey WE, Giordano TJ, Fragoso MCBV^, Hammer GD^. Targeted Assessment of *G0S2* Methylation Identifies a Rapidly Recurrent, Routinely Fatal Molecular Subtype of Adrenocortical Carcinoma. *Clinical Cancer Research*. 2019 Jun 1;25(11):3276-3288. *,^ equal contribution
5. Lerario AM, **Mohan DR**, Lirov R, Else T, Hammer GD, 2019, "83. Adrenal Tumors," in DeVita VT, Lawrence TS, Rosenburg SA (Eds.) *DeVita, Hellman, and Rosenberg's Cancer: Principles & Practice of Oncology*. 11th ed. Philadelphia: Wolters Kluwer Health/Lippincott Williams & Wilkins.
6. **Mohan DR**, Lerario AM, Hammer GD. Therapeutic Targets for Adrenocortical Carcinoma in the Genomics Era. *Journal of the Endocrine Society.* 2018 Sep 26;2(11):1259-1274.

E.2. Publications in preparation

Authors list for original manuscripts (with exception of first and senior authors) and article titles may be subject to change.

1. Lerario AM, **Mohan DR**, Giordano TJ, Hammer GD. "10. Genetics of Adrenal Tumors," in New MI, Lekarev O, Parsa A, Yuen TT, O'Malley B, Hammer GD (Eds.) *Genetic Steroid Disorders*. 2nd ed. San Diego: Academic Press. Invited book chapter. Submitted and undergoing editorial review.
2. **Mohan DR**, Borges KS, Finco I, LaPensee CR, Solon A, Rege J, Little III DW, Else T, Almeida MQ, Apfelbaum A, Vinco M, Wakamatsu A, Mariani BMP, Latronico AC, Mendonca BB, Zerbini MCN, Fragoso MCBV, Lawlor ER, Ohi R, Rainey WE, Venneti S, Marie SKN, Giordano TJ, Breault DT, Lerario AM*, Hammer GD*. A differentiation program coordinated by SF1/β-catenin is a targetable epigenetic vulnerability in aggressive adrenocortical carcinoma. In preparation. *co-senior author
3. Lerario AM*, **Mohan DR***, Rege J, Rainey WE, Hammer GD. Meta-analysis of adrenocortical tumors identifies cell of origin programs derailed in tumorigenesis and malignancy. In preparation. *co-first author
4. **Mohan DR,** Lerario AM, Hammer GD. Insights from molecular subtyping in adrenocortical carcinoma. *Endocrinology*. Invited review, in preparation.
5. Lerario AM, **Mohan DR**, Hammer GD. Update on adrenocortical carcinomas: from basic biology to emerging therapies. *Endocrine Reviews*. Invited review, in preparation.

6. Assie G, **Mohan DR**, Lerario AM. “Chapter 96: Adrenal Genomics II: Familial and sporadic neoplasia,” in Hammer GD, *et al.* (Eds.) *DeGroot’s Endocrinology*. 8th ed. Saunders. Invited book chapter, in preparation.

E.3. Patents

1. Patent Pending – U.S. Provisional Patent Application filed Dec 2020 (App. No. 63/123,264) by The Regents of the University of Michigan. “Compositions and Methods for Treating Wnt-Driven Cancer.” Inventors: Lerario AM (34%), **Mohan DR** (34%), Hammer GD (32%)
2. Patent Pending – U.S. Provisional Patent Application filed Jun 2019 (App. No. 62/859,933), and converted to Utility Patent Jun 2020 by The Regents of the University of Michigan. Patent Coop. Treaty App. No. PCT/US2020/0307039. “Compositions and Methods for Treating Cancer.” Inventors: Lerario AM (34%), **Mohan DR** (33%), Hammer GD (33%)
3. Patent Pending – U.S. Provisional Patent Application filed Nov 2017 (App. No. 62/592,009), and converted to Utility Patent Nov 2018 by The Regents of the University of Michigan. Patent Coop. Treaty App. No. PCT/US2018/062709. Nationalized, pending evaluation in the US (Utility App. No. 16/767,886), Australia, China, Europe, Japan. “Compositions and Methods for Characterizing Cancer.” Inventors: Lerario AM (34%), **Mohan DR** (33%), Hammer GD (33%)

E.4. Abstracts & presentations

Presenting author indicated by asterisk (*). **Associated awards/recognition** are indicated after citation.

1. **Mohan DR***, Finco I, LaPensee CR, Rege J, Else T, Almeida MQ, Vinco M, Wakamatsu A, Latronico AC, Mendonca BB, Zerbini MCN, Fragoso MCBV, Rainey WE, Venneti S, Marie SKN, Giordano TJ, Lerario AM, Hammer GD. Repressive epigenetic programs reinforce SF1/β-catenin-dependent differentiation in aggressive adrenocortical carcinoma. Poster. 2020 Virtual University of Michigan Medical Scientist Training Program Retreat on August 28-30, 2020; awarded **Most Aesthetic Poster**.
2. **Mohan DR***, Finco I, LaPensee CR, Rege J, Else T, Almeida MQ, Vinco M, Wakamatsu A, Latronico AC, Mendonca BB, Zerbini MCN, Fragoso MCBV, Rainey WE, Venneti S, Marie SKN, Giordano TJ, Lerario AM, Hammer GD.

Repressive Epigenetic Programs Reinforce Steroidogenic Differentiation and Wnt/β-Catenin Signaling in Aggressive Adrenocortical Carcinoma. Late Breaking Poster. ENDO 2020 (Endocrine Society Annual Meeting), San Francisco, CA, USA, on March 27-31, 2020 – cancelled due to COVID-19; 1 of 5 abstracts selected meeting-wide to compete in **Guided Presidential Poster Competition: Adrenal**. Abstract published in *Journal of the Endocrine Society*. 2020 April-May, Vol. 4 (Supplement_1), SUN-LB34, https://doi.org/10.1210/jendso/bvaa046.2265

3. LaPensee CR*, **Mohan D**, Lerario AM, Hammer GD. ATAC-Seq Reveals Dynamic Changes in Chromatin Accessibility Following PKA Activation in NCI-H295R Adrenocortical Cells. Late Breaking Poster. ENDO 2020 (Endocrine Society Annual Meeting), San Francisco, CA, USA, on March 27-31, 2020 – cancelled due to COVID-19. Abstract published in *Journal of the Endocrine Society*. 2020 April-May, Vol. 4 (Supplement_1), SUN-LB39, https://doi.org/10.1210/jendso/bvaa046.2316
4. **Mohan DR***, Lerario AM, Finco I, Almeida MQ, Fragoso MCBV, Venneti S, Marie SKN, Giordano TJ, Hammer GD. DNA hypermethylation is directed to PRC2 targets and propagated independently of PRC2 in CIMP-high ACC. Oral Presentation. ACC 2019 (Adrenal Cancer Symposium 2019), Clermont-Ferrand, France, on September 27-28, 2019; awarded **Oral Presentation Travel Award (1000 EUR)**.
5. **Mohan DR***, Lerario AM, Finco I, Almeida MQ, Fragoso MCBV, Venneti S, Marie SKN, Giordano TJ, Hammer GD. Unraveling the many layers of oncogenic epigenetic reprogramming in CIMP-high adrenocortical carcinoma. Oral Presentation. 2019 University of Michigan Doctoral Program in Cancer Biology 7th Annual Retreat in Oregon, OH, USA, on September 13-14, 2019; awarded **Best Oral Presentation**.
6. **Mohan DR***, Lerario AM, Finco I, Almeida MQ, Fragoso MCBV, Venneti S, Marie SKN, Giordano TJ, Hammer GD. Unraveling the many layers of oncogenic epigenetic reprogramming in CIMP-high adrenocortical carcinoma. Poster. 2019 University of Michigan Medical Scientist Training Program Retreat in Roscommon, MI, USA, on August 2-4, 2019; awarded **Most Aesthetic Poster**.
7. **Mohan DR***, Lerario AM, Finco I, Almeida MQ, Fragoso MCBV, Venneti S, Marie SKN, Giordano TJ, Hammer GD. Novel tissue-specific roles for Polycomb repressive complex 2 in CIMP-high adrenocortical carcinoma. Poster. 34th Annual National MD/PhD Student Conference in Copper Mountain, CO, USA, on July 12-14, 2019.
8. **Mohan DR***, Lerario AM, Finco I, Almeida MQ, Fragoso MCBV, Venneti S, Marie SKN, Giordano TJ, Hammer GD. Novel tissue-specific roles for PRC2 in CIMP-high adrenocortical carcinoma. Poster. 2019 Gordon Research Conference on Cancer Genetics and Epigenetics – How Alterations in DNA Sequence and Chromatin Modifications Impact Cancer Etiology and Therapy in Lucca, Italy, on April 7-12, 2019; awarded **Rackham International Travel Grant ($1,050 USD)**.

9. **Mohan DR***, Lerario AM, Else T, Almeida MQ, Vinco M, Rege J, Mariani BMP, Zerbini MCN, Mendonca BB, Latronico AC, Marie SKN, Rainey WE, Giordano TJ, Fragoso MCBV, Hammer GD. OR29–3 Targeted Assessment of *G0S2* Methylation Identifies a Rapidly Recurrent, Routinely Fatal Molecular Subtype of Adrenocortical Carcinoma. Oral Presentation. ENDO 2019 (Endocrine Society Annual Meeting), New Orleans, LA, USA, on March 23-26, 2019; awarded **Endocrine Society Outstanding Abstract Award ($500 USD)**. Abstract published in *Journal of the Endocrine Society*. 2019 April-May, Vol. 3 (Supplement_1), OR29–3, https://doi.org/10.1210/js.2019-OR29-3
10. **Mohan DR***, Lerario AM, Else T, Almeida MQ, Vinco M, Rege J, Mariani BMP, Zerbini MCN, Mendonca BB, Latronico AC, Marie SKN, Rainey WE, Giordano TJ, Fragoso MCBV, Hammer GD. *G0S2* hypermethylation identifies a rapidly recurrent, routinely fatal molecular subtype of adrenocortical carcinoma. Poster. 2018 Cancer Biology Training Consortium (CABTRAC), Davenport, IA, USA, on October 28-30, 2018; awarded **Best Predoctoral Poster**.
11. **Mohan DR***, Lerario AM, Almeida MQ, Fragoso MCBV, Venneti S, Marie SKN, Hammer GD. Novel cooperative and tissue-specific roles of EZH2 and DNMT1 in adrenocortical carcinoma. Poster. 2018 University of Michigan Doctoral Program in Cancer Biology 6th Annual Retreat in Ann Arbor, MI, USA, on September 27-28, 2018.
12. **Mohan DR***, Lerario AM, Else T, Almeida MQ, Vinco M, Rege J, Mariani BMP, Zerbini MCN, Mendonca BB, Latronico AC, Marie SKN, Rainey WE, Giordano TJ, Fragoso MCBV, and Hammer GD. *G0S2* hypermethylation predicts rapid recurrence and death in adrenocortical carcinoma. Poster. 2018 University of Michigan Medical Scientist Training Program Retreat in Roscommon, MI, USA, on August 10-12, 2018.
13. **Mohan DR***, Lerario AM, Hammer GD. Chromosomal "noisiness" predicts linsitinib resistance in adrenocortical carcinoma. Poster. The 18th Adrenal Cortex Conference (2018) in Munich, Germany, on June 25-27, 2018; awarded **The 18th Adrenal Cortex Conference Trainee Travel Grant (700 EUR)**.
14. Lerario AM*, **Mohan DR**, Else T, Almeida MQ, Vinco M, Rege J, Mariani BMP, Zerbini MCN, Mendonca BB, Latronico AC, Marie SKN, Rainey WE, Giordano TJ, Fragoso MCBV, Hammer GD. *G0S2* hypermethylation predicts rapid recurrence and death in adrenocortical carcinoma. Poster. The 18th Adrenal Cortex Conference (2018) in Munich, Germany, on June 25-27, 2018
15. **Mohan DR***, Lerario AM, Else T, Almeida MQ, Vinco M, Rege J, Mariani BMP, Zerbini MCN, Mendonca BB, Latronico AC, Marie SKN, Rainey WE, Giordano TJ, Fragoso MCBV, Hammer GD. *G0S2* HYPERMETHYLATION PREDICTS RAPID RECURRENCE AND DEATH IN ADRENOCORTICAL CARCINOMA. Poster. University of Michigan Rogel Cancer Center Spring Research Symposium, Ann Arbor, MI, USA, on June 14, 2018; awarded **3rd Place Best Poster**.

16. **Mohan D***, Lerario A, Fragoso MC, Almeida M, Rainey W, Giordano T, Hammer G. A novel ACC-TCGA-derived molecular assay to stratify adrenocortical carcinoma (ACC) and predict clinical outcomes. Poster. 2017 University of Michigan 16th Annual Pathology Research Symposium in Ann Arbor, MI, on November 10, 2017.
17. **Mohan DR***, Lerario AM, Marie SKN, Hammer GD. Defining the novel roles of dysregulated epigenetic writers in aggressive adrenocortical carcinoma (ACC). Poster. 2017 University of Michigan Doctoral Program in Cancer Biology 5th Annual Retreat in Oregon, OH, USA, on September 29-30, 2017; awarded **1st Place Best Poster.**
18. **Mohan DR***, Lerario AM, Marie SKN, and Hammer GD. Defining the novel roles of dysregulated epigenetic writers in aggressive adrenocortical carcinoma (ACC). Oral Presentation. 2017 University of Michigan Medical Scientist Training Program Retreat in Roscommon, MI, on August 4-6, 2017.

E.5. Grants

1. ***Rackham Graduate Student Research Grant*; Recipient – Mohan: PRC2 in CIMP-high adrenocortical carcinoma. 08/27/20. $3K USD.** *Notice of award received 08/27/20.* We recently demonstrated that CpG island hypermethylation defines a rapidly recurrent, routinely fatal molecular subtype of adrenocortical carcinoma (ACC). Our subsequent studies have identified that this DNA methylation signature may disrupt the actions of other repressive chromatin remodeling complexes, namely the Polycomb repressive complex 2 (PRC2). The goal of this study is to verify that genome-wide DNA methylation is not disrupted by PRC2 inhibition. **Role: Sole grant-writer & sole personnel to be supported by grant.**
2. ***Rogel Cancer Center MD/PhD Student Scholarship;* Recipient – Mohan: PRC2 in CIMP-high adrenocortical carcinoma. 07/01/19-06/31/20. Renewed through 02/2021 (return to medical school). $41.7K USD.** *Notice of award received 06/07/19.* The goal of this study is to elucidate the complex interplay between DNA methylation and PRC2 in wiring the oncogenic, epigenetic landscape that defines CIMP-high ACC. **Role: Sole grant-writer & sole personnel to be supported by grant.**
3. ***Department of Defense (CA180751), FY18 DoD Peer Reviewed Cancer Research Program, Translational Team Science Award;* Initiating PI – Hammer, Partnering PIs – Else, Auchus: Biomarker Development for Diagnosis, Surveillance, and Prognosis for Adrenocortical Carcinoma (ACC). 09/01/19-08/31/23. $1.56M USD.** *Notice of award received 02/25/19.* We and others recently demonstrated that ACC patients exhibit a unique circulating

steroid profile, and that DNA methylation of a single locus (*G0S2*) identifies patients with a rapidly recurrent and routinely fatal ACC. Aim 1: Define serum steroid profiles that distinguish patients with ACC from those with adrenocortical adenomas, and determine if steroids in individual patients with ACC can be used to establish early diagnosis of recurrence and as surrogates for tumor burden. Aim 2: Evaluate the prospective utility of *G0S2* methylation in predicting disease progression and selective response to adjuvant therapy. **Role: 1of 2 lead grant writers, grant assembler, budget coordinator, & research personnel to be supported by grant.**

4. ***Department of Defense (CA180750), FY18 DoD Peer Reviewed Cancer Research Program, Idea Award with Special Focus;* PI – Hammer: Intra-Tumoral Steroid Production as a Mechanism of Immune Evasion in Adrenocortical Carcinoma (ACC). 09/01/19-08/31/21. $617K USD.** *Notice of award received 02/25/19.* The FDA recently accelerated approval of anti-PD-1 therapy for mismatch repair-deficient tumors including ACC. However, recent observations from The Cancer Genome Atlas study on ACC and from leading clinicians in our field suggest that most ACC is immune poor, steroidogenic, and anti-PD-1-resistant. We hypothesize that intra-tumoral steroid production may be a novel mechanism of immune evasion in ACC. Aim 1: Characterize the landscape of steroid precursors and metabolites that accumulate locally in ACC tumors, and measure the associated impact on immune cell infiltration and steroidogenic and immune-related transcriptional programs. Aim 2: Determine if ACC-secreted steroids affect T cell function *in vitro* and *in vivo*, and if this interaction can be targeted therapeutically to restore or increase ACC responsiveness to PD-1/PD-L1 checkpoint inhibition. **Role: 1 of 2 lead grant writers, grant assembler, budget coordinator, & research personnel to be supported by grant.**

5. ***University of Michigan Rogel Cancer Center (U058298), Pilot Project*; PI – Hammer: A novel ACC-TCGA-derived molecular assay to stratify adrenocortical carcinoma (ACC) and predict clinical outcomes. $75K USD**. *Awarded: 09/01/2017 – 08/31/2018; no-cost extension: 09/01/2018 – 08/31/2019.* In The Cancer Genome Atlas (ACC-TCGA), we identified that ACC is comprised of 3 molecular subtypes with distinct clinical prognoses. Here, we propose a novel approach evaluating expression of few key genes and DNA methylation of a single locus to stratify ACC samples according to molecular categories defined by ACC-TCGA. **Role: 1 of 2 lead grant writers, budget coordinator, & research personnel supported by grant.**

BIBLIOGRAPHY

Almeida, M.Q., Soares, I.C., Ribeiro, T.C., Fragoso, M.C., Marins, L.V., Wakamatsu, A., Ressio, R.A., Nishi, M.Y., Jorge, A.A., Lerario, A.M.*, et al.* (2010). Steroidogenic factor 1 overexpression and gene amplification are more frequent in adrenocortical tumors from children than from adults. J Clin Endocrinol Metab *95*, 1458-1462.

Andrews, S. FastQC: A quality control tool for high-throughput sequence data.

Anwar, T., Arellano-Garcia, C., Ropa, J., Chen, Y.C., Kim, H.S., Yoon, E., Grigsby, S., Basrur, V., Nesvizhskii, A.I., Muntean, A.*, et al.* (2018). p38-mediated phosphorylation at T367 induces EZH2 cytoplasmic localization to promote breast cancer metastasis. Nat Commun *9*, 2801.

Arbour, K.C., Mezquita, L., Long, N., Rizvi, H., Auclin, E., Ni, A., Martínez-Bernal, G., Ferrara, R., Lai, W.V., Hendriks, L.E.L.*, et al.* (2018). Impact of Baseline Steroids on Efficacy of Programmed Cell Death-1 and Programmed Death-Ligand 1 Blockade in Patients With Non-Small-Cell Lung Cancer. J Clin Oncol, JCO2018790006.

Aryee, M.J., Jaffe, A.E., Corrada-Bravo, H., Ladd-Acosta, C., Feinberg, A.P., Hansen, K.D., and Irizarry, R.A. (2014). Minfi: a flexible and comprehensive Bioconductor package for the analysis of Infinium DNA methylation microarrays. Bioinformatics *30*, 1363-1369.

Assie, G., Letouze, E., Fassnacht, M., Jouinot, A., Luscap, W., Barreau, O., Omeiri, H., Rodriguez, S., Perlemoine, K., Rene-Corail, F.*, et al.* (2014). Integrated genomic characterization of adrenocortical carcinoma. Nat Genet *46*, 607-612.

Auton, A., Brooks, L.D., Durbin, R.M., Garrison, E.P., Kang, H.M., Korbel, J.O., Marchini, J.L., McCarthy, S., McVean, G.A., Abecasis, G.R.*, et al.* (2015). A global reference for human genetic variation. Nature *526*, 68-74.

Azad, N., Zahnow, C.A., Rudin, C.M., and Baylin, S.B. (2013). The future of epigenetic therapy in solid tumours--lessons from the past. Nat Rev Clin Oncol *10*, 256-266.

Azizan, E.A., Poulsen, H., Tuluc, P., Zhou, J., Clausen, M.V., Lieb, A., Maniero, C., Garg, S., Bochukova, E.G., Zhao, W.*, et al.* (2013). Somatic mutations in ATP1A1 and CACNA1D underlie a common subtype of adrenal hypertension. Nat Genet *45*, 1055-1060.

Azuma, T., Yao, S., Zhu, G., Flies, A.S., Flies, S.J., and Chen, L. (2008). B7-H1 is a ubiquitous antiapoptotic receptor on cancer cells. Blood *111*, 3635-3643.

Baba, T., Otake, H., Sato, T., Miyabayashi, K., Shishido, Y., Wang, C.Y., Shima, Y., Kimura, H., Yagi, M., Ishihara, Y.*, et al.* (2014). Glycolytic genes are targets of the nuclear receptor Ad4BP/SF-1. Nat Commun *5*, 3634.

Ballaré, C., Lange, M., Lapinaite, A., Martin, G.M., Morey, L., Pascual, G., Liefke, R., Simon, B., Shi, Y., Gozani, O.*, et al.* (2012). Phf19 links methylated Lys36 of histone H3 to regulation of Polycomb activity. Nat Struct Mol Biol *19*, 1257-1265.

Bandiera, R., Vidal, V.P., Motamedi, F.J., Clarkson, M., Sahut-Barnola, I., von Gise, A., Pu, W.T., Hohenstein, P., Martinez, A., and Schedl, A. (2013). WT1 maintains adrenal-gonadal primordium identity and marks a population of AGP-like progenitors within the adrenal gland. Dev Cell *27*, 5-18.

Banito, A., Li, X., Laporte, A.N., Roe, J.S., Sanchez-Vega, F., Huang, C.H., Dancsok, A.R., Hatzi, K., Chen, C.C., Tschaharganeh, D.F.*, et al.* (2018). The SS18-SSX Oncoprotein Hijacks KDM2B-PRC1.1 to Drive Synovial Sarcoma. Cancer Cell *33*, 527-541.e528.

Barker, N., Ridgway, R.A., van Es, J.H., van de Wetering, M., Begthel, H., van den Born, M., Danenberg, E., Clarke, A.R., Sansom, O.J., and Clevers, H. (2009). Crypt stem cells as the cells-of-origin of intestinal cancer. Nature *457*, 608-611.

Barlaskar, F.M., Spalding, A.C., Heaton, J.H., Kuick, R., Kim, A.C., Thomas, D.G., Giordano, T.J., Ben-Josef, E., and Hammer, G.D. (2009). Preclinical targeting of the type I insulin-like growth factor receptor in adrenocortical carcinoma. J Clin Endocrinol Metab *94*, 204-212.

Barreau, O., Assie, G., Wilmot-Roussel, H., Ragazzon, B., Baudry, C., Perlemoine, K., Rene-Corail, F., Bertagna, X., Dousset, B., Hamzaoui, N.*, et al.* (2013). Identification of a CpG island methylator phenotype in adrenocortical carcinomas. J Clin Endocrinol Metab *98*, E174-184.

Bartke, T., Vermeulen, M., Xhemalce, B., Robson, S.C., Mann, M., and Kouzarides, T. (2010). Nucleosome-interacting proteins regulated by DNA and histone methylation. Cell *143*, 470-484.

Basham, K.J., Rodriguez, S., Turcu, A.F., Lerario, A.M., Logan, C.Y., Rysztak, M.R., Gomez-Sanchez, C.E., Breault, D.T., Koo, B.K., Clevers, H.*, et al.* (2019). A ZNRF3-dependent Wnt/β-catenin signaling gradient is required for adrenal homeostasis. Genes Dev *33*, 209-220.

Bassett, M.H., White, P.C., and Rainey, W.E. (2004). A role for the NGFI-B family in adrenal zonation and adrenocortical disease. Endocr Res *30*, 567-574.

Batisse-Lignier, M., Sahut-Barnola, I., Tissier, F., Dumontet, T., Mathieu, M., Drelon, C., Pointud, J.C., Damon-Soubeyrand, C., Marceau, G., Kemeny, J.L.*, et al.* (2017). P53/Rb inhibition induces metastatic adrenocortical carcinomas in a preclinical transgenic model. Oncogene *36*, 4445-4456.

Bayliss, J., Mukherjee, P., Lu, C., Jain, S.U., Chung, C., Martinez, D., Sabari, B., Margol, A.S., Panwalkar, P., Parolia, A.*, et al.* (2016). Lowered H3K27me3 and DNA hypomethylation define poorly prognostic pediatric posterior fossa ependymomas. Sci Transl Med *8*, 366ra161.

Ben-Porath, I., Thomson, M.W., Carey, V.J., Ge, R., Bell, G.W., Regev, A., and Weinberg, R.A. (2008). An embryonic stem cell-like gene expression signature in poorly differentiated aggressive human tumors. Nat Genet *40*, 499-507.

Berest, I., Arnold, C., Reyes-Palomares, A., Palla, G., Rasmussen, K.D., Giles, H., Bruch, P.M., Huber, W., Dietrich, S., Helin, K.*, et al.* (2019). Quantification of Differential Transcription Factor Activity and Multiomics-Based Classification into Activators and Repressors: diffTF. Cell Rep *29*, 3147-3159.e3112.

Beringer, M., Pisano, P., Di Carlo, V., Blanco, E., Chammas, P., Vizán, P., Gutiérrez, A., Aranda, S., Payer, B., Wierer, M.*, et al.* (2016). EPOP Functionally Links Elongin and Polycomb in Pluripotent Stem Cells. Mol Cell *64*, 645-658.

Bernstein, B.E., Mikkelsen, T.S., Xie, X., Kamal, M., Huebert, D.J., Cuff, J., Fry, B., Meissner, A., Wernig, M., Plath, K.*, et al.* (2006). A bivalent chromatin structure marks key developmental genes in embryonic stem cells. Cell *125*, 315-326.

Berruti, A., Grisanti, S., Pulzer, A., Claps, M., Daffara, F., Loli, P., Mannelli, M., Boscaro, M., Arvat, E., Tiberio, G.*, et al.* (2017). Long-Term Outcomes of Adjuvant Mitotane Therapy in Patients With Radically Resected Adrenocortical Carcinoma. J Clin Endocrinol Metab *102*, 1358-1365.

Bertherat, J., Groussin, L., Sandrini, F., Matyakhina, L., Bei, T., Stergiopoulos, S., Papageorgiou, T., Bourdeau, I., Kirschner, L.S., Vincent-Dejean, C.*, et al.* (2003). Molecular and functional analysis of PRKAR1A and its locus (17q22-24) in sporadic adrenocortical tumors: 17q losses, somatic mutations, and protein kinase A expression and activity. Cancer Res *63*, 5308-5319.

Berthon, A., Sahut-Barnola, I., Lambert-Langlais, S., de Joussineau, C., Damon-Soubeyrand, C., Louiset, E., Taketo, M.M., Tissier, F., Bertherat, J., Lefrançois-Martinez, A.M.*, et al.* (2010). Constitutive beta-catenin activation induces adrenal hyperplasia and promotes adrenal cancer development. Hum Mol Genet *19*, 1561-1576.

Beuschlein, F., Boulkroun, S., Osswald, A., Wieland, T., Nielsen, H.N., Lichtenauer, U.D., Penton, D., Schack, V.R., Amar, L., Fischer, E.*, et al.* (2013). Somatic mutations in ATP1A1 and ATP2B3 lead to aldosterone-producing adenomas and secondary hypertension. Nat Genet *45*, 440-444, 444e441-442.

Beuschlein, F., Fassnacht, M., Assié, G., Calebiro, D., Stratakis, C.A., Osswald, A., Ronchi, C.L., Wieland, T., Sbiera, S., Faucz, F.R.*, et al.* (2014). Constitutive activation of PKA catalytic subunit in adrenal Cushing's syndrome. The New England journal of medicine *370*, 1019-1028.

Beuschlein, F., Jakoby, J., Mentz, S., Zambetti, G., Jung, S., Reincke, M., Süss, R., and Hantel, C. (2016). IGF1-R inhibition and liposomal doxorubicin: Progress in preclinical evaluation for the treatment of adrenocortical carcinoma. Mol Cell Endocrinol *428*, 82-88.

Beuschlein, F., Weigel, J., Saeger, W., Kroiss, M., Wild, V., Daffara, F., Libe, R., Ardito, A., Al Ghuzlan, A., Quinkler, M.*, et al.* (2015). Major prognostic role of Ki67 in localized adrenocortical carcinoma after complete resection. J Clin Endocrinol Metab *100*, 841-849.

Bhattacharyya, M., De, S., and Chakrabarti, S. (2020). Origin and Evolution of DNA methyltransferases (DNMT) along the tree of life: A multi-genome survey. bioRxiv.

Bingham, N.C., Verma-Kurvari, S., Parada, L.F., and Parker, K.L. (2006). Development of a steroidogenic factor 1/Cre transgenic mouse line. Genesis *44*, 419-424.

Bird, A.P. (1980). DNA methylation and the frequency of CpG in animal DNA. Nucleic Acids Res *8*, 1499-1504.

Biton, A., Bernard-Pierrot, I., Lou, Y., Krucker, C., Chapeaublanc, E., Rubio-Pérez, C., López-Bigas, N., Kamoun, A., Neuzillet, Y., Gestraud, P.*, et al.* (2014). Independent component analysis uncovers the landscape of the bladder tumor transcriptome and reveals insights into luminal and basal subtypes. Cell Rep *9*, 1235-1245.

Blank, C., Brown, I., Peterson, A.C., Spiotto, M., Iwai, Y., Honjo, T., and Gajewski, T.F. (2004). PD-L1/B7H-1 inhibits the effector phase of tumor rejection by T cell receptor (TCR) transgenic CD8+ T cells. Cancer Res *64*, 1140-1145.

Bonneville, R., Krook, M.A., Kautto, E.A., Miya, J., Wing, M.R., Chen, H.Z., Reeser, J.W., Yu, L., and Roychowdhury, S. (2017). Landscape of Microsatellite Instability Across 39 Cancer Types. JCO Precis Oncol *2017*.

Borges, K.S., Andrade, A.F., Silveira, V.S., Marco Antonio, D.S., Vasconcelos, E.J.R., Antonini, S.R.R., Tone, L.G., and Scrideli, C.A. (2017). The aurora kinase inhibitor AMG 900 increases apoptosis and induces chemosensitivity to anticancer drugs in the NCI-H295 adrenocortical carcinoma cell line. Anticancer Drugs *28*, 634-644.

Borges, K.S., Pignatti, E., Leng, S., Kariyawasam, D., Ruiz-Babot, G., Ramalho, F.S., Taketo, M.M., Carlone, D.L., and Breault, D.T. (2020). Wnt/β-catenin activation cooperates with loss of p53 to cause adrenocortical carcinoma in mice. Oncogene *39*, 5282-5291.

Bracken, A.P., Pasini, D., Capra, M., Prosperini, E., Colli, E., and Helin, K. (2003). EZH2 is downstream of the pRB-E2F pathway, essential for proliferation and amplified in cancer. EMBO J *22*, 5323-5335.

Brahmer, J.R., Tykodi, S.S., Chow, L.Q., Hwu, W.J., Topalian, S.L., Hwu, P., Drake, C.G., Camacho, L.H., Kauh, J., Odunsi, K.*, et al.* (2012). Safety and activity of anti-PD-L1 antibody in patients with advanced cancer. N Engl J Med *366*, 2455-2465.

Bushnell, B. (2014). BBMap: A fast, accurate, Splice-Aware Aligner. Paper presented at: 9th Annual Genomics of Energy & Environment Meeting, March 17-20, 2014 (Walnut Creek, CA).

Bussey, K.J., Bapat, A., Linnehan, C., Wandoloski, M., Dastrup, E., Rogers, E., Gonzales, P., and Demeure, M.J. (2016). Targeting polo-like kinase 1, a regulator of p53, in the treatment of adrenocortical carcinoma. Clin Transl Med *5*, 1.

Béguelin, W., Popovic, R., Teater, M., Jiang, Y., Bunting, K.L., Rosen, M., Shen, H., Yang, S.N., Wang, L., Ezponda, T.*, et al.* (2013). EZH2 is required for germinal center formation and somatic EZH2 mutations promote lymphoid transformation. Cancer Cell *23*, 677-692.

Béguelin, W., Teater, M., Gearhart, M.D., Calvo Fernández, M.T., Goldstein, R.L., Cárdenas, M.G., Hatzi, K., Rosen, M., Shen, H., Corcoran, C.M.*, et al.* (2016). EZH2 and BCL6 Cooperate to Assemble CBX8-BCOR Complex to Repress Bivalent Promoters, Mediate Germinal Center Formation and Lymphomagenesis. Cancer Cell *30*, 197-213.

Béguelin, W., Teater, M., Meydan, C., Hoehn, K.B., Phillip, J.M., Soshnev, A.A., Venturutti, L., Rivas, M.A., Calvo-Fernández, M.T., Gutierrez, J.*, et al.* (2020). Mutant EZH2 Induces a Pre-malignant Lymphoma Niche by Reprogramming the Immune Response. Cancer Cell *37*, 655-673.e611.

Cao, J., O'Day, D.R., Pliner, H.A., Kingsley, P.D., Deng, M., Daza, R.M., Zager, M.A., Aldinger, K.A., Blecher-Gonen, R., Zhang, F.*, et al.* (2020). A human cell atlas of fetal gene expression. Science *370*.

Cao, J., Spielmann, M., Qiu, X., Huang, X., Ibrahim, D.M., Hill, A.J., Zhang, F., Mundlos, S., Christiansen, L., Steemers, F.J.*, et al.* (2019). The single-cell transcriptional landscape of mammalian organogenesis. Nature *566*, 496-502.

Cao, R., and Zhang, Y. (2004). SUZ12 is required for both the histone methyltransferase activity and the silencing function of the EED-EZH2 complex. Mol Cell *15*, 57-67.

Cao, Y., He, M., Gao, Z., Peng, Y., Li, Y., Li, L., Zhou, W., Li, X., Zhong, X., Lei, Y.*, et al.* (2014). Activating hotspot L205R mutation in PRKACA and adrenal Cushing's syndrome. Science (New York, NY) *344*, 913-917.

Carithers, L.J., Ardlie, K., Barcus, M., Branton, P.A., Britton, A., Buia, S.A., Compton, C.C., DeLuca, D.S., Peter-Demchok, J., Gelfand, E.T.*, et al.* (2015). A Novel Approach to High-Quality Postmortem Tissue Procurement: The GTEx Project. Biopreserv Biobank *13*, 311-319.

Caron, K.M., Soo, S.C., Wetsel, W.C., Stocco, D.M., Clark, B.J., and Parker, K.L. (1997). Targeted disruption of the mouse gene encoding steroidogenic acute regulatory protein provides insights into congenital lipoid adrenal hyperplasia. Proc Natl Acad Sci U S A *94*, 11540-11545.

Catania, S., Dumesic, P.A., Pimentel, H., Nasif, A., Stoddard, C.I., Burke, J.E., Diedrich, J.K., Cook, S., Shea, T., Geinger, E.*, et al.* (2020). Evolutionary Persistence of DNA Methylation for Millions of Years after Ancient Loss of a De Novo Methyltransferase. Cell *180*, 263-277.e220.

Cerquetti, L., Bucci, B., Marchese, R., Misiti, S., De Paula, U., Miceli, R., Muleti, A., Amendola, D., Piergrossi, P., Brunetti, E.*, et al.* (2008). Mitotane increases the radiotherapy inhibitory effect and induces G2-arrest in combined treatment on both H295R and SW13 adrenocortical cell lines. Endocr Relat Cancer *15*, 623-634.

Chamberlin, A., Huether, R., Machado, A.Z., Groden, M., Liu, H.M., Upadhyay, K., O, V., Gomes, N.L., Lerario, A.M., Nishi, M.Y.*, et al.* (2019). Mutations in MAP3K1 that cause 46,XY disorders of sex development disrupt distinct structural domains in the protein. Hum Mol Genet.

Chang, H.H., Hemberg, M., Barahona, M., Ingber, D.E., and Huang, S. (2008). Transcriptome-wide noise controls lineage choice in mammalian progenitor cells. Nature *453*, 544-547.

Chang, X., Monitto, C.L., Demokan, S., Kim, M.S., Chang, S.S., Zhong, X., Califano, J.A., and Sidransky, D. (2010). Identification of hypermethylated genes associated with cisplatin resistance in human cancers. Cancer Res *70*, 2870-2879.

Chen, S., Jiao, L., Liu, X., and Yang, X. (2020). A Dimeric Structural Scaffold for PRC2-PCL Targeting to CpG Island Chromatin. Mol Cell *77*, 1265-1278.e1267.

Chen, S., Jiao, L., Shubbar, M., Yang, X., and Liu, X. (2018). Unique Structural Platforms of Suz12 Dictate Distinct Classes of PRC2 for Chromatin Binding. Mol Cell *69*, 840-852.e845.

Chen, T., Hevi, S., Gay, F., Tsujimoto, N., He, T., Zhang, B., Ueda, Y., and Li, E. (2007). Complete inactivation of DNMT1 leads to mitotic catastrophe in human cancer cells. Nat Genet *39*, 391-396.

Ching, S., and Vilain, E. (2009). Targeted disruption of Sonic Hedgehog in the mouse adrenal leads to adrenocortical hypoplasia. Genesis *47*, 628-637.

Choi, J., Bachmann, A.L., Tauscher, K., Benda, C., Fierz, B., and Müller, J. (2017). DNA binding by PHF1 prolongs PRC2 residence time on chromatin and thereby promotes H3K27 methylation. Nat Struct Mol Biol *24*, 1039-1047.

Choi, M., Scholl, U.I., Yue, P., Bjorklund, P., Zhao, B., Nelson-Williams, C., Ji, W., Cho, Y., Patel, A., Men, C.J.*, et al.* (2011). K+ channel mutations in adrenal aldosterone-producing adenomas and hereditary hypertension. Science *331*, 768-772.

Choufani, S., Gibson, W.T., Turinsky, A.L., Chung, B.H.Y., Wang, T., Garg, K., Vitriolo, A., Cohen, A.S.A., Cyrus, S., Goodman, S.*, et al.* (2020). DNA Methylation Signature for EZH2 Functionally Classifies Sequence Variants in Three PRC2 Complex Genes. Am J Hum Genet *106*, 596-610.

Chung, C., Sweha, S.R., Pratt, D., Tamrazi, B., Panwalkar, P., Banda, A., Bayliss, J., Hawes, D., Yang, F., Lee, H.J.*, et al.* (2020). Integrated Metabolic and Epigenomic Reprograming by H3K27M Mutations in Diffuse Intrinsic Pontine Gliomas. Cancer Cell *38*, 334-349.e339.

Cingolani, P., Patel, V.M., Coon, M., Nguyen, T., Land, S.J., Ruden, D.M., and Lu, X. (2012a). Using Drosophila melanogaster as a Model for Genotoxic Chemical Mutational Studies with a New Program, SnpSift. Front Genet *3*, 35.

Cingolani, P., Platts, A., Wang, l.L., Coon, M., Nguyen, T., Wang, L., Land, S.J., Lu, X., and Ruden, D.M. (2012b). A program for annotating and predicting the effects of single nucleotide polymorphisms, SnpEff: SNPs in the genome of Drosophila melanogaster strain w1118; iso-2; iso-3. Fly (Austin) *6*, 80-92.

Cirillo, N., Morgan, D.J., Pedicillo, M.C., Celentano, A., Lo Muzio, L., McCullough, M.J., and Prime, S.S. (2017). Characterisation of the cancer-associated glucocorticoid system: key role of 11β-hydroxysteroid dehydrogenase type 2. Br J Cancer *117*, 984-993.

Clarke, M.F., and Fuller, M. (2006). Stem cells and cancer: two faces of eve. Cell *124*, 1111-1115.

Consortium, A.P.G. (2017). AACR Project GENIE: Powering Precision Medicine through an International Consortium. Cancer Discov *7*, 818-831.

Conway, E., Jerman, E., Healy, E., Ito, S., Holoch, D., Oliviero, G., Deevy, O., Glancy, E., Fitzpatrick, D.J., Mucha, M.*, et al.* (2018). A Family of Vertebrate-Specific Polycombs Encoded by the LCOR/LCORL Genes Balance PRC2 Subtype Activities. Mol Cell *70*, 408-421.e408.

Cooper, D.N., Taggart, M.H., and Bird, A.P. (1983). Unmethylated domains in vertebrate DNA. Nucleic Acids Res *11*, 647-658.

Corces, M.R., Granja, J.M., Shams, S., Louie, B.H., Seoane, J.A., Zhou, W., Silva, T.C., Groeneveld, C., Wong, C.K., Cho, S.W.*, et al.* (2018). The chromatin accessibility landscape of primary human cancers. Science *362*.

Corces, M.R., Trevino, A.E., Hamilton, E.G., Greenside, P.G., Sinnott-Armstrong, N.A., Vesuna, S., Satpathy, A.T., Rubin, A.J., Montine, K.S., Wu, B.*, et al.* (2017). An improved ATAC-seq protocol reduces background and enables interrogation of frozen tissues. Nature Methods *14*, 959-962.

Correa, F.A., Jorge, A.A., Nakaguma, M., Canton, A.P., Costa, S.S., Funari, M.F., Lerario, A.M., Franca, M.M., Carvalho, L.R., Krepischi, A.C.*, et al.* (2018). Pathogenic copy number variants in patients with congenital hypopituitarism associated with complex phenotypes. Clin Endocrinol (Oxf) *88*, 425-431.

Coulter, C.L., and Jaffe, R.B. (1998). Functional maturation of the primate fetal adrenal in vivo: 3. Specific zonal localization and developmental regulation of CYP21A2 (P450c21) and CYP11B1/CYP11B2 (P450c11/aldosterone synthase) lead to integrated concept of zonal and temporal steroid biosynthesis. Endocrinology *139*, 5144-5150.

Dabe, E.C., Sanford, R.S., Kohn, A.B., Bobkova, Y., and Moroz, L.L. (2015). DNA Methylation in Basal Metazoans: Insights from Ctenophores. Integr Comp Biol *55*, 1096-1110.

de Bruin, C., Finlayson, C., Funari, M.F., Vasques, G.A., Lucheze Freire, B., Lerario, A.M., Andrew, M., Hwa, V., Dauber, A., and Jorge, A.A. (2016). Two Patients with Severe Short Stature due to a FBN1 Mutation (p.Ala1728Val) with a Mild Form of Acromicric Dysplasia. Horm Res Paediatr *86*, 342-348.

de Reynies, A., Assie, G., Rickman, D.S., Tissier, F., Groussin, L., Rene-Corail, F., Dousset, B., Bertagna, X., Clauser, E., and Bertherat, J. (2009). Gene expression profiling reveals a new classification of adrenocortical tumors and identifies molecular predictors of malignancy and survival. J Clin Oncol *27*, 1108-1115.

Decmann, A., Bancos, I., Khanna, A., Thomas, M.A., Turai, P., Perge, P., Pintér, J.Z., Tóth, M., Patócs, A., and Igaz, P. (2019). Comparison of plasma and urinary microRNA-483-5p for the diagnosis of adrenocortical malignancy. J Biotechnol *297*, 49-53.

Deevy, O., and Bracken, A.P. (2019). PRC2 functions in development and congenital disorders. Development *146*.

DeLuca, D.S., Levin, J.Z., Sivachenko, A., Fennell, T., Nazaire, M.D., Williams, C., Reich, M., Winckler, W., and Getz, G. (2012). RNA-SeQC: RNA-seq metrics for quality control and process optimization. Bioinformatics *28*, 1530-1532.

Dixon, J.R., Selvaraj, S., Yue, F., Kim, A., Li, Y., Shen, Y., Hu, M., Liu, J.S., and Ren, B. (2012). Topological domains in mammalian genomes identified by analysis of chromatin interactions. Nature *485*, 376-380.

Dobin, A., Davis, C.A., Schlesinger, F., Drenkow, J., Zaleski, C., Jha, S., Batut, P., Chaisson, M., and Gingeras, T.R. (2013). STAR: ultrafast universal RNA-seq aligner. Bioinformatics *29*, 15-21.

Doghman, M., Karpova, T., Rodrigues, G.A., Arhatte, M., De Moura, J., Cavalli, L.R., Virolle, V., Barbry, P., Zambetti, G.P., Figueiredo, B.C.*, et al.* (2007). Increased steroidogenic factor-1 dosage triggers adrenocortical cell proliferation and cancer. Mol Endocrinol *21*, 2968-2987.

Domcke, S., Hill, A.J., Daza, R.M., Cao, J., O'Day, D.R., Pliner, H.A., Aldinger, K.A., Pokholok, D., Zhang, F., Milbank, J.H.*, et al.* (2020). A human cell atlas of fetal chromatin accessibility. Science *370*.

Douillet, D., Sze, C.C., Ryan, C., Piunti, A., Shah, A.P., Ugarenko, M., Marshall, S.A., Rendleman, E.J., Zha, D., Helmin, K.A.*, et al.* (2020). Uncoupling histone H3K4 trimethylation from developmental gene expression via an equilibrium of COMPASS, Polycomb and DNA methylation. Nat Genet *52*, 615-625.

Drelon, C., Berthon, A., Mathieu, M., Ragazzon, B., Kuick, R., Tabbal, H., Septier, A., Rodriguez, S., Batisse-Lignier, M., Sahut-Barnola, I.*, et al.* (2016a). EZH2 is overexpressed in adrenocortical carcinoma and is associated with disease progression. Hum Mol Genet *25*, 2789-2800.

Drelon, C., Berthon, A., Sahut-Barnola, I., Mathieu, M., Dumontet, T., Rodriguez, S., Batisse-Lignier, M., Tabbal, H., Tauveron, I., Lefrancois-Martinez, A.M.*, et al.* (2016b). PKA inhibits WNT signalling in adrenal cortex zonation and prevents malignant tumour development. Nat Commun *7*, 12751.

Dutta, R.K., Arnesen, T., Heie, A., Walz, M., Alesina, P., Soderkvist, P., and Gimm, O. (2019). A somatic mutation in CLCN2 identified in a sporadic aldosterone-producing adenoma. Eur J Endocrinol *181*, K37-k41.

Ellis, S.J., Gomez, N.C., Levorse, J., Mertz, A.F., Ge, Y., and Fuchs, E. (2019). Distinct modes of cell competition shape mammalian tissue morphogenesis. Nature *569*, 497-502.

Else, T., Kim, A.C., Sabolch, A., Raymond, V.M., Kandathil, A., Caoili, E.M., Jolly, S., Miller, B.S., Giordano, T.J., and Hammer, G.D. (2014a). Adrenocortical carcinoma. Endocr Rev *35*, 282-326.

Else, T., Williams, A.R., Sabolch, A., Jolly, S., Miller, B.S., and Hammer, G.D. (2014b). Adjuvant therapies and patient and tumor characteristics associated with survival of adult patients with adrenocortical carcinoma. J Clin Endocrinol Metab *99*, 455-461.

Erhardt, S., Su, I.H., Schneider, R., Barton, S., Bannister, A.J., Perez-Burgos, L., Jenuwein, T., Kouzarides, T., Tarakhovsky, A., and Surani, M.A. (2003). Consequences of the depletion of zygotic and embryonic enhancer of zeste 2 during preimplantation mouse development. Development *130*, 4235-4248.

Espiard, S., Knape, M.J., Bathon, K., Assié, G., Rizk-Rabin, M., Faillot, S., Luscap-Rondof, W., Abid, D., Guignat, L., Calebiro, D.*, et al.* (2018). Activating PRKACB somatic mutation in cortisol-producing adenomas. JCI Insight *3*.

Ezhkova, E., Lien, W.H., Stokes, N., Pasolli, H.A., Silva, J.M., and Fuchs, E. (2011). EZH1 and EZH2 cogovern histone H3K27 trimethylation and are essential for hair follicle homeostasis and wound repair. Genes Dev *25*, 485-498.

Farin, H.F., Jordens, I., Mosa, M.H., Basak, O., Korving, J., Tauriello, D.V., de Punder, K., Angers, S., Peters, P.J., Maurice, M.M.*, et al.* (2016). Visualization of a short-range Wnt gradient in the intestinal stem-cell niche. Nature *530*, 340-343.

Fassnacht, M., Berruti, A., Baudin, E., Demeure, M.J., Gilbert, J., Haak, H., Kroiss, M., Quinn, D.I., Hesseltine, E., Ronchi, C.L.*, et al.* (2015). Linsitinib (OSI-906) versus placebo for patients with locally advanced or metastatic adrenocortical carcinoma: a double-blind, randomised, phase 3 study. Lancet Oncol *16*, 426-435.

Fassnacht, M., Dekkers, O.M., Else, T., Baudin, E., Berruti, A., de Krijger, R., Haak, H.R., Mihai, R., Assie, G., and Terzolo, M. (2018). European Society of Endocrinology Clinical Practice Guidelines on the management of adrenocortical carcinoma in adults, in collaboration with the European Network for the Study of Adrenal Tumors. Eur J Endocrinol *179*, G1-G46.

Fassnacht, M., Kroiss, M., and Allolio, B. (2013). Update in adrenocortical carcinoma. J Clin Endocrinol Metab *98*, 4551-4564.

Fassnacht, M., Terzolo, M., Allolio, B., Baudin, E., Haak, H., Berruti, A., Welin, S., Schade-Brittinger, C., Lacroix, A., Jarzab, B.*, et al.* (2012). Combination chemotherapy in advanced adrenocortical carcinoma. N Engl J Med *366*, 2189-2197.

Faust, C., Lawson, K.A., Schork, N.J., Thiel, B., and Magnuson, T. (1998). The Polycomb-group gene eed is required for normal morphogenetic movements during gastrulation in the mouse embryo. Development *125*, 4495-4506.

Faust, C., Schumacher, A., Holdener, B., and Magnuson, T. (1995). The eed mutation disrupts anterior mesoderm production in mice. Development *121*, 273-285.

Figueroa, M.E., Abdel-Wahab, O., Lu, C., Ward, P.S., Patel, J., Shih, A., Li, Y., Bhagwat, N., Vasanthakumar, A., Fernandez, H.F.*, et al.* (2010). Leukemic IDH1 and IDH2 mutations result in a hypermethylation phenotype, disrupt TET2 function, and impair hematopoietic differentiation. Cancer Cell *18*, 553-567.

Finco, I., and Hammer, G.D. (2018). Isolation, Fixation, and Immunofluorescence Imaging of Mouse Adrenal Glands. J Vis Exp.

Finco, I., Lerario, A.M., and Hammer, G.D. (2018). Sonic Hedgehog and WNT Signaling Promote Adrenal Gland Regeneration in Male Mice. Endocrinology *159*, 579-596.

Fiorentini, C., Fragni, M., Tiberio, G.A.M., Galli, D., Roca, E., Salvi, V., Bosisio, D., Missale, C., Terzolo, M., Memo, M.*, et al.* (2018). Palbociclib inhibits proliferation of human adrenocortical tumor cells. Endocrine *59*, 213-217.

Fiorentini, C., Grisanti, S., Cosentini, D., Abate, A., Rossini, E., Berruti, A., and Sigala, S. (2019). Molecular Drivers of Potential Immunotherapy Failure in Adrenocortical Carcinoma. J Oncol *2019*, 6072863.

Flavahan, W.A., Drier, Y., Johnstone, S.E., Hemming, M.L., Tarjan, D.R., Hegazi, E., Shareef, S.J., Javed, N.M., Raut, C.P., Eschle, B.K.*, et al.* (2019). Altered chromosomal topology drives oncogenic programs in SDH-deficient GISTs. Nature *575*, 229-233.

Fragoso, M.C., Almeida, M.Q., Mazzuco, T.L., Mariani, B.M., Brito, L.P., Goncalves, T.C., Alencar, G.A., Lima Lde, O., Faria, A.M., Bourdeau, I.*, et al.* (2012). Combined expression of BUB1B, DLGAP5, and PINK1 as predictors of poor outcome in adrenocortical tumors: validation in a Brazilian cohort of adult and pediatric patients. Eur J Endocrinol *166*, 61-67.

Franca, M.M., Funari, M.F.A., Lerario, A.M., Nishi, M.Y., Pita, C.C., Fontenele, E.G.P., and Mendonca, B.B. (2017a). A novel homozygous 1-bp deletion in the NOBOX gene in two Brazilian sisters with primary ovarian failure. Endocrine *58*, 442-447.

Franca, M.M., Funari, M.F.A., Nishi, M.Y., Narcizo, A.M., Domenice, S., Costa, E.M.F., Lerario, A.M., and Mendonca, B.B. (2018). Identification of the first homozygous 1-bp deletion in GDF9 gene leading to primary ovarian insufficiency by using targeted massively parallel sequencing. Clin Genet *93*, 408-411.

Franca, M.M., Lerario, A.M., Funari, M.F.A., Nishi, M.Y., Narcizo, A.M., de Mello, M.P., Guerra-Junior, G., Maciel-Guerra, A.T., and Mendonca, B.B. (2017b). A Novel Homozygous Missense FSHR Variant Associated with Hypergonadotropic Hypogonadism in Two Siblings from a Brazilian Family. Sex Dev *11*, 137-142.

Franken, N.A., Rodermond, H.M., Stap, J., Haveman, J., and van Bree, C. (2006). Clonogenic assay of cells in vitro. Nat Protoc *1*, 2315-2319.

França, M.M., Nishi, M.Y., Funari, M.F.A., Lerario, A.M., Baracat, E.C., Hayashida, S.A.Y., Maciel, G.A.R., Jorge, A.A.L., and Mendonca, B.B. (2018). Two rare loss-of-function variants in the STAG3 gene leading to primary ovarian insufficiency. Eur J Med Genet.

Freedman, B.D., Kempna, P.B., Carlone, D.L., Shah, M., Guagliardo, N.A., Barrett, P.Q., Gomez-Sanchez, C.E., Majzoub, J.A., and Breault, D.T. (2013). Adrenocortical zonation results from lineage conversion of differentiated zona glomerulosa cells. Dev Cell *26*, 666-673.

Freeman, G.J., Long, A.J., Iwai, Y., Bourque, K., Chernova, T., Nishimura, H., Fitz, L.J., Malenkovich, N., Okazaki, T., Byrne, M.C.*, et al.* (2000). Engagement of the PD-1 immunoinhibitory receptor by a novel B7 family member leads to negative regulation of lymphocyte activation. J Exp Med *192*, 1027-1034.

Freire, B.L., Homma, T.K., Funari, M.F.A., Lerario, A.M., Leal, A.M., Velloso, E., Malaquias, A.C., and Jorge, A.A.L. (2018). Homozygous loss of function BRCA1 variant causing a Fanconi-anemia-like phenotype, a clinical report and review of previous patients. Eur J Med Genet *61*, 130-133.

Gal-Yam, E.N., Egger, G., Iniguez, L., Holster, H., Einarsson, S., Zhang, X., Lin, J.C., Liang, G., Jones, P.A., and Tanay, A. (2008). Frequent switching of Polycomb repressive marks and DNA hypermethylation in the PC3 prostate cancer cell line. Proc Natl Acad Sci U S A *105*, 12979-12984.

Gara, S.K., Lack, J., Zhang, L., Harris, E., Cam, M., and Kebebew, E. (2018). Metastatic adrenocortical carcinoma displays higher mutation rate and tumor heterogeneity than primary tumors. Nat Commun *9*, 4172.

Gardiner-Garden, M., and Frommer, M. (1987). CpG islands in vertebrate genomes. J Mol Biol *196*, 261-282.

Garinet, S., Nectoux, J., Neou, M., Pasmant, E., Jouinot, A., Sibony, M., Orhant, L., Pipoli da Fonseca, J., Perlemoine, K., Bricaire, L.*, et al.* (2018). Detection and monitoring of circulating tumor DNA in adrenocortical carcinoma. Endocr Relat Cancer *25*, L13-L17.

Garrison, E. A C++ library for parsing and manipulation VCF files.

Garrison, E., and Marth, G. (2012). Haplotype-based variant detection from short-read sequencing. arXivorg *arXiv:1207.3907v2[q-bio.GN]*.

Gaspar, J.M. (2018). Genrich: detecting sites of genomic enrichment.

Gerlinger, M., Rowan, A.J., Horswell, S., Math, M., Larkin, J., Endesfelder, D., Gronroos, E., Martinez, P., Matthews, N., Stewart, A.*, et al.* (2012). Intratumor heterogeneity and branched evolution revealed by multiregion sequencing. N Engl J Med *366*, 883-892.

Gicquel, C., Raffin-Sanson, M.L., Gaston, V., Bertagna, X., Plouin, P.F., Schlumberger, M., Louvel, A., Luton, J.P., and Le Bouc, Y. (1997). Structural and functional abnormalities at 11p15 are associated with the malignant phenotype in sporadic adrenocortical tumors: study on a series of 82 tumors. J Clin Endocrinol Metab *82*, 2559-2565.

Giolo, S.R., Soler, J.M., Greenway, S.C., Almeida, M.A., de Andrade, M., Seidman, J.G., Seidman, C.E., Krieger, J.E., and Pereira, A.C. (2012). Brazilian urban population genetic structure reveals a high degree of admixture. Eur J Hum Genet *20*, 111-116.

Giordano, T.J. (2011). The argument for mitotic rate-based grading for the prognostication of adrenocortical carcinoma. Am J Surg Pathol *35*, 471-473.

Giordano, T.J., Kuick, R., Else, T., Gauger, P.G., Vinco, M., Bauersfeld, J., Sanders, D., Thomas, D.G., Doherty, G., and Hammer, G. (2009). Molecular classification and prognostication of adrenocortical tumors by transcriptome profiling. Clin Cancer Res *15*, 668-676.

Giordano, T.J., Thomas, D.G., Kuick, R., Lizyness, M., Misek, D.E., Smith, A.L., Sanders, D., Aljundi, R.T., Gauger, P.G., Thompson, N.W.*, et al.* (2003). Distinct transcriptional profiles of adrenocortical tumors uncovered by DNA microarray analysis. Am J Pathol *162*, 521-531.

Glenn, J.A., Else, T., Hughes, D.T., Cohen, M.S., Jolly, S., Giordano, T.J., Worden, F.P., Gauger, P.G., Hammer, G.D., and Miller, B.S. (2018). Longitudinal patterns of recurrence in patients with adrenocortical carcinoma. Surgery.

Glenn, J.A., Else, T., Hughes, D.T., Cohen, M.S., Jolly, S., Giordano, T.J., Worden, F.P., Gauger, P.G., Hammer, G.D., and Miller, B.S. (2019). Longitudinal patterns of recurrence in patients with adrenocortical carcinoma. Surgery *165*, 186-195.

Goh, G., Scholl, U.I., Healy, J.M., Choi, M., Prasad, M.L., Nelson-Williams, C., Kunstman, J.W., Korah, R., Suttorp, A.-C., Dietrich, D.*, et al.* (2014). Recurrent activating mutation in PRKACA in cortisol-producing adrenal tumors. Nature genetics *46*, 613-617.

Gould, A.P., Lai, R.Y., Green, M.J., and White, R.A. (1990). Blocking cell division does not remove the requirement for Polycomb function in Drosophila embryogenesis. Development *110*, 1319-1325.

Greenberg, M.V., Glaser, J., Borsos, M., Marjou, F.E., Walter, M., Teissandier, A., and Bourc'his, D. (2017). Transient transcription in the early embryo sets an epigenetic state that programs postnatal growth. Nat Genet *49*, 110-118.

Greenberg, M.V.C., and Bourc'his, D. (2019). The diverse roles of DNA methylation in mammalian development and disease. Nat Rev Mol Cell Biol *20*, 590-607.

Gregorieff, A., Liu, Y., Inanlou, M.R., Khomchuk, Y., and Wrana, J.L. (2015). Yap-dependent reprogramming of Lgr5(+) stem cells drives intestinal regeneration and cancer. Nature *526*, 715-718.

Grijzenhout, A., Godwin, J., Koseki, H., Gdula, M.R., Szumska, D., McGouran, J.F., Bhattacharya, S., Kessler, B.M., Brockdorff, N., and Cooper, S. (2016). Functional analysis of AEBP2, a PRC2 Polycomb protein, reveals a Trithorax phenotype in embryonic development and in ESCs. Development *143*, 2716-2723.

Gummow, B.M., Winnay, J.N., and Hammer, G.D. (2003). Convergence of Wnt signaling and steroidogenic factor-1 (SF-1) on transcription of the rat inhibin alpha gene. J Biol Chem *278*, 26572-26579.

Göllner, S., Oellerich, T., Agrawal-Singh, S., Schenk, T., Klein, H.U., Rohde, C., Pabst, C., Sauer, T., Lerdrup, M., Tavor, S.*, et al.* (2017). Loss of the histone methyltransferase EZH2 induces resistance to multiple drugs in acute myeloid leukemia. Nat Med *23*, 69-78.

Habra, M.A. (2017). 6th International Adrenal Cancer Symposium. Paper presented at: 6th International Adrenal Cancer Symposium (Sao Paulo, SP, Brazil).

Hadjadj, D., Kim, S.J., Denecker, T., Ben Driss, L., Cadoret, J.C., Maric, C., Baldacci, G., and Fauchereau, F. (2017). A hypothesis-driven approach identifies CDK4 and CDK6 inhibitors as candidate drugs for treatments of adrenocortical carcinomas. Aging (Albany NY) *9*, 2695-2716.

Haluska, P., Worden, F., Olmos, D., Yin, D., Schteingart, D., Batzel, G.N., Paccagnella, M.L., de Bono, J.S., Gualberto, A., and Hammer, G.D. (2010). Safety, tolerability, and pharmacokinetics of the anti-IGF-1R monoclonal antibody figitumumab in patients with refractory adrenocortical carcinoma. Cancer Chemother Pharmacol *65*, 765-773.

Hamanishi, J., Mandai, M., Iwasaki, M., Okazaki, T., Tanaka, Y., Yamaguchi, K., Higuchi, T., Yagi, H., Takakura, K., Minato, N.*, et al.* (2007). Programmed cell death 1 ligand 1 and tumor-infiltrating CD8+ T lymphocytes are prognostic factors of human ovarian cancer. Proc Natl Acad Sci U S A *104*, 3360-3365.

Hamid, O., Robert, C., Daud, A., Hodi, F.S., Hwu, W.J., Kefford, R., Wolchok, J.D., Hersey, P., Joseph, R.W., Weber, J.S.*, et al.* (2013). Safety and tumor responses with lambrolizumab (anti-PD-1) in melanoma. N Engl J Med *369*, 134-144.

Hammer, G.D., Krylova, I., Zhang, Y., Darimont, B.D., Simpson, K., Weigel, N.L., and Ingraham, H.A. (1999). Phosphorylation of the nuclear receptor SF-1 modulates cofactor recruitment: integration of hormone signaling in reproduction and stress. Mol Cell *3*, 521-526.

Han, X., Zhou, Z., Fei, L., Sun, H., Wang, R., Chen, Y., Chen, H., Wang, J., Tang, H., Ge, W.*, et al.* (2020). Construction of a human cell landscape at single-cell level. Nature *581*, 303-309.

Hanahan, D., and Weinberg, R.A. (2000). The hallmarks of cancer. Cell *100*, 57-70.

Hanahan, D., and Weinberg, R.A. (2011). Hallmarks of cancer: the next generation. Cell *144*, 646-674.

Hansen, K.H., Bracken, A.P., Pasini, D., Dietrich, N., Gehani, S.S., Monrad, A., Rappsilber, J., Lerdrup, M., and Helin, K. (2008). A model for transmission of the H3K27me3 epigenetic mark. Nat Cell Biol *10*, 1291-1300.

Hantel, C., and Beuschlein, F. (2016). Xenograft models for adrenocortical carcinoma. Mol Cell Endocrinol *421*, 28-33.

Hantel, C., Shapiro, I., Poli, G., Chiapponi, C., Bidlingmaier, M., Reincke, M., Luconi, M., Jung, S., and Beuschlein, F. (2016). Targeting heterogeneity of adrenocortical carcinoma: Evaluation and extension of preclinical tumor models to improve clinical translation. Oncotarget *7*, 79292-79304.

Hawkins, R.D., Hon, G.C., Lee, L.K., Ngo, Q., Lister, R., Pelizzola, M., Edsall, L.E., Kuan, S., Luu, Y., Klugman, S.*, et al.* (2010). Distinct epigenomic landscapes of pluripotent and lineage-committed human cells. Cell Stem Cell *6*, 479-491.

Healy, E., Mucha, M., Glancy, E., Fitzpatrick, D.J., Conway, E., Neikes, H.K., Monger, C., Van Mierlo, G., Baltissen, M.P., Koseki, Y.*, et al.* (2019). PRC2.1 and PRC2.2 Synergize to Coordinate H3K27 Trimethylation. Mol Cell *76*, 437-452.e436.

Heaton, J.H., Wood, M.A., Kim, A.C., Lima, L.O., Barlaskar, F.M., Almeida, M.Q., Fragoso, M.C., Kuick, R., Lerario, A.M., Simon, D.P.*, et al.* (2012). Progression to adrenocortical tumorigenesis in mice and humans through insulin-like growth factor 2 and β-catenin. Am J Pathol *181*, 1017-1033.

Heikkila, M., Peltoketo, H., Leppaluoto, J., Ilves, M., Vuolteenaho, O., and Vainio, S. (2002). Wnt-4 deficiency alters mouse adrenal cortex function, reducing aldosterone production. Endocrinology *143*, 4358-4365.

Heinz, S., Benner, C., Spann, N., Bertolino, E., Lin, Y.C., Laslo, P., Cheng, J.X., Murre, C., Singh, H., and Glass, C.K. (2010). Simple combinations of lineage-determining transcription factors prime cis-regulatory elements required for macrophage and B cell identities. Mol Cell *38*, 576-589.

Heyn, P., Logan, C.V., Fluteau, A., Challis, R.C., Auchynnikava, T., Martin, C.A., Marsh, J.A., Taglini, F., Kilanowski, F., Parry, D.A.*, et al.* (2019). Gain-of-function DNMT3A mutations cause microcephalic dwarfism and hypermethylation of Polycomb-regulated regions. Nat Genet *51*, 96-105.

Hisado-Oliva, A., Ruzafa-Martin, A., Sentchordi, L., Funari, M.F.A., Bezanilla-López, C., Alonso-Bernáldez, M., Barraza-García, J., Rodriguez-Zabala, M., Lerario, A.M., Benito-Sanz, S.*, et al.* (2018). Mutations in C-natriuretic peptide (NPPC): a novel cause of autosomal dominant short stature. Genet Med *20*, 91-97.

Hnisz, D., Abraham, B.J., Lee, T.I., Lau, A., Saint-André, V., Sigova, A.A., Hoke, H.A., and Young, R.A. (2013). Super-enhancers in the control of cell identity and disease. Cell *155*, 934-947.

Hnisz, D., Schuijers, J., Lin, C.Y., Weintraub, A.S., Abraham, B.J., Lee, T.I., Bradner, J.E., and Young, R.A. (2015). Convergence of developmental and oncogenic signaling pathways at transcriptional super-enhancers. Mol Cell *58*, 362-370.

Hoadley, K.A., Yau, C., Hinoue, T., Wolf, D.M., Lazar, A.J., Drill, E., Shen, R., Taylor, A.M., Cherniack, A.D., Thorsson, V.*, et al.* (2018). Cell-of-Origin Patterns Dominate the Molecular Classification of 10,000 Tumors from 33 Types of Cancer. Cell *173*, 291-304.e296.

Hoffmeyer, K., Junghans, D., Kanzler, B., and Kemler, R. (2017). Trimethylation and Acetylation of β-Catenin at Lysine 49 Represent Key Elements in ESC Pluripotency. Cell Rep *18*, 2815-2824.

Holliday, R., and Grigg, G.W. (1993). DNA methylation and mutation. Mutat Res *285*, 61-67.

Holm, T.M., Jackson-Grusby, L., Brambrink, T., Yamada, Y., Rideout, W.M., and Jaenisch, R. (2005). Global loss of imprinting leads to widespread tumorigenesis in adult mice. Cancer Cell *8*, 275-285.

Horvath, S. (2013). DNA methylation age of human tissues and cell types. Genome Biol *14*, R115.

Hovestadt, V., and Zapatka, M. (2020). conumee: Enhanced copy-number variation analysis using Illumina DNA methylation arrays (R package version 1.9.0).

Hsu, Y.C., Li, L., and Fuchs, E. (2014). Transit-amplifying cells orchestrate stem cell activity and tissue regeneration. Cell *157*, 935-949.

Huang, C.C., Liu, C., and Yao, H.H. (2012). Investigating the role of adrenal cortex in organization and differentiation of the adrenal medulla in mice. Mol Cell Endocrinol *361*, 165-171.

Huang, C.C., Miyagawa, S., Matsumaru, D., Parker, K.L., and Yao, H.H. (2010). Progenitor cell expansion and organ size of mouse adrenal is regulated by sonic hedgehog. Endocrinology *151*, 1119-1128.

Hänzelmann, S., Castelo, R., and Guinney, J. (2013). GSVA: gene set variation analysis for microarray and RNA-seq data. BMC Bioinformatics *14*, 7.

Højfeldt, J.W., Laugesen, A., Willumsen, B.M., Damhofer, H., Hedehus, L., Tvardovskiy, A., Mohammad, F., Jensen, O.N., and Helin, K. (2018). Accurate H3K27 methylation can be established de novo by SUZ12-directed PRC2. Nat Struct Mol Biol *25*, 225-232.

Ikeuchi, M., Iwase, A., Rymen, B., Harashima, H., Shibata, M., Ohnuma, M., Breuer, C., Morao, A.K., de Lucas, M., De Veylder, L.*, et al.* (2015). PRC2 represses dedifferentiation of mature somatic cells in Arabidopsis. Nat Plants *1*, 15089.

Ingraham, H.A., Lala, D.S., Ikeda, Y., Luo, X., Shen, W.H., Nachtigal, M.W., Abbud, R., Nilson, J.H., and Parker, K.L. (1994). The nuclear receptor steroidogenic factor 1 acts at multiple levels of the reproductive axis. Genes Dev *8*, 2302-2312.

Irizarry, R.A., Hobbs, B., Collin, F., Beazer-Barclay, Y.D., Antonellis, K.J., Scherf, U., and Speed, T.P. (2003). Exploration, normalization, and summaries of high density oligonucleotide array probe level data. Biostatistics *4*, 249-264.

Iwafuchi-Doi, M., and Zaret, K.S. (2014). Pioneer transcription factors in cell reprogramming. Genes Dev *28*, 2679-2692.

Iwai, Y., Ishida, M., Tanaka, Y., Okazaki, T., Honjo, T., and Minato, N. (2002). Involvement of PD-L1 on tumor cells in the escape from host immune system and tumor immunotherapy by PD-L1 blockade. Proc Natl Acad Sci U S A *99*, 12293-12297.

Jadhav, U., Manieri, E., Nalapareddy, K., Madha, S., Chakrabarti, S., Wucherpfennig, K., Barefoot, M., and Shivdasani, R.A. (2020). Replicational Dilution of H3K27me3 in Mammalian Cells and the Role of Poised Promoters. Mol Cell *78*, 141-151.e145.

Jain, S.U., Do, T.J., Lund, P.J., Rashoff, A.Q., Diehl, K.L., Cieslik, M., Bajic, A., Juretic, N., Deshmukh, S., Venneti, S.*, et al.* (2019). PFA ependymoma-associated protein EZHIP inhibits PRC2 activity through a H3 K27M-like mechanism. Nat Commun *10*, 2146.

Jiang, D., and Berger, F. (2017). DNA replication-coupled histone modification maintains Polycomb gene silencing in plants. Science *357*, 1146-1149.

Jouinot, A., Assie, G., Libe, R., Fassnacht, M., Papathomas, T., Barreau, O., de la Villeon, B., Faillot, S., Hamzaoui, N., Neou, M.*, et al.* (2017). DNA Methylation Is an Independent Prognostic Marker of Survival in Adrenocortical Cancer. J Clin Endocrinol Metab *102*, 923-932.

Jung, I., Schmitt, A., Diao, Y., Lee, A.J., Liu, T., Yang, D., Tan, C., Eom, J., Chan, M., Chee, S.*, et al.* (2019). A compendium of promoter-centered long-range chromatin interactions in the human genome. Nat Genet *51*, 1442-1449.

Kadoch, C., and Crabtree, G.R. (2013). Reversible disruption of mSWI/SNF (BAF) complexes by the SS18-SSX oncogenic fusion in synovial sarcoma. Cell *153*, 71-85.

Kadoch, C., Hargreaves, D.C., Hodges, C., Elias, L., Ho, L., Ranish, J., and Crabtree, G.R. (2013). Proteomic and bioinformatic analysis of mammalian SWI/SNF complexes identifies extensive roles in human malignancy. Nat Genet *45*, 592-601.

Kadoch, C., Williams, R.T., Calarco, J.P., Miller, E.L., Weber, C.M., Braun, S.M., Pulice, J.L., Chory, E.J., and Crabtree, G.R. (2017). Dynamics of BAF-Polycomb complex opposition on heterochromatin in normal and oncogenic states. Nat Genet *49*, 213-222.

Kagey, M.H., Newman, J.J., Bilodeau, S., Zhan, Y., Orlando, D.A., van Berkum, N.L., Ebmeier, C.C., Goossens, J., Rahl, P.B., Levine, S.S.*, et al.* (2010). Mediator and cohesin connect gene expression and chromatin architecture. Nature *467*, 430-435.

Kahn, M. (2014). Can we safely target the WNT pathway? Nat Rev Drug Discov *13*, 513-532.

Kalia, S.S., Adelman, K., Bale, S.J., Chung, W.K., Eng, C., Evans, J.P., Herman, G.E., Hufnagel, S.B., Klein, T.E., Korf, B.R.*, et al.* (2017). Recommendations for reporting of secondary findings in clinical exome and genome sequencing, 2016 update (ACMG SF

v2.0): a policy statement of the American College of Medical Genetics and Genomics. Genet Med *19*, 249-255.

Kartheuser, A., Walon, C., West, S., Breukel, C., Detry, R., Gribomont, A.C., Hamzehloei, T., Hoang, P., Maiter, D., Pringot, J.*, et al.* (1999). Familial adenomatous polyposis associated with multiple adrenal adenomas in a patient with a rare 3' APC mutation. J Med Genet *36*, 65-67.

Kasinath, V., Faini, M., Poepsel, S., Reif, D., Feng, X.A., Stjepanovic, G., Aebersold, R., and Nogales, E. (2018). Structures of human PRC2 with its cofactors AEBP2 and JARID2. Science *359*, 940-944.

Kehdy, F.S., Gouveia, M.H., Machado, M., Magalhaes, W.C., Horimoto, A.R., Horta, B.L., Moreira, R.G., Leal, T.P., Scliar, M.O., Soares-Souza, G.B.*, et al.* (2015). Origin and dynamics of admixture in Brazilians and its effect on the pattern of deleterious mutations. Proc Natl Acad Sci U S A *112*, 8696-8701.

Kerkhofs, T.M., Verhoeven, R.H., Van der Zwan, J.M., Dieleman, J., Kerstens, M.N., Links, T.P., Van de Poll-Franse, L.V., and Haak, H.R. (2013). Adrenocortical carcinoma: a population-based study on incidence and survival in the Netherlands since 1993. Eur J Cancer *49*, 2579-2586.

Killick, R.K., and Eckley, I.A. (2014). changepoint: An R Package for Changepoint Analysis. Journal of Statistical Software *58*, 1-19.

Kim, A.C., Reuter, A.L., Zubair, M., Else, T., Serecky, K., Bingham, N.C., Lavery, G.G., Parker, K.L., and Hammer, G.D. (2008). Targeted disruption of beta-catenin in Sf1-expressing cells impairs development and maintenance of the adrenal cortex. Development *135*, 2593-2602.

Kim, J., Woo, A.J., Chu, J., Snow, J.W., Fujiwara, Y., Kim, C.G., Cantor, A.B., and Orkin, S.H. (2010). A Myc network accounts for similarities between embryonic stem and cancer cell transcription programs. Cell *143*, 313-324.

Kim, K., Jang, I., Kim, M., Choi, J., Kim, M.S., Lee, B., and Jung, I. (2020). 3DIV update for 2021: a comprehensive resource of 3D genome and 3D cancer genome. Nucleic Acids Res.

Kim, Y., Margonis, G.A., Prescott, J.D., Tran, T.B., Postlewait, L.M., Maithel, S.K., Wang, T.S., Evans, D.B., Hatzaras, I., Shenoy, R.*, et al.* (2016). Nomograms to Predict Recurrence-Free and Overall Survival After Curative Resection of Adrenocortical Carcinoma. JAMA Surg *151*, 365-373.

King, P., Paul, A., and Laufer, E. (2009). Shh signaling regulates adrenocortical development and identifies progenitors of steroidogenic lineages. Proc Natl Acad Sci U S A *106*, 21185-21190.

Kiseljak-Vassiliades, K., Zhang, Y., Bagby, S.M., Kar, A., Pozdeyev, N., Xu, M., Gowan, K., Sharma, V., Raeburn, C.D., Albuja-Cruz, M.*, et al.* (2018a). Development of new preclinical models to advance adrenocortical carcinoma research. Endocr Relat Cancer *25*, 437-451.

Kiseljak-Vassiliades, K., Zhang, Y., Kar, A., Razzaghi, R., Xu, M., Gowan, K., Raeburn, C.D., Albuja-Cruz, M., Jones, K.L., Somerset, H.*, et al.* (2018b). Elucidating the Role of the Maternal Embryonic Leucine Zipper Kinase in Adrenocortical Carcinoma. Endocrinology *159*, 2532-2544.

Kloet, S.L., Makowski, M.M., Baymaz, H.I., van Voorthuijsen, L., Karemaker, I.D., Santanach, A., Jansen, P.W.T.C., Di Croce, L., and Vermeulen, M. (2016). The dynamic interactome and genomic targets of Polycomb complexes during stem-cell differentiation. Nat Struct Mol Biol *23*, 682-690.

Knijnenburg, T.A., Wang, L., Zimmermann, M.T., Chambwe, N., Gao, G.F., Cherniack, A.D., Fan, H., Shen, H., Way, G.P., Greene, C.S.*, et al.* (2018). Genomic and Molecular Landscape of DNA Damage Repair Deficiency across The Cancer Genome Atlas. Cell Rep *23*, 239-254.e236.

Kolde, R. (2018). pheatmap: Pretty Heatmaps.

Krivtsov, A.V., Evans, K., Gadrey, J.Y., Eschle, B.K., Hatton, C., Uckelmann, H.J., Ross, K.N., Perner, F., Olsen, S.N., Pritchard, T.*, et al.* (2019). A Menin-MLL Inhibitor Induces Specific Chromatin Changes and Eradicates Disease in Models of MLL-Rearranged Leukemia. Cancer Cell *36*, 660-673.e611.

Kuhn, M., Wing, J., Weston, S., Williams, A., Keefer, C., Engelhardt, A., Cooper, T., Mayer, Z., Kenkel, B., Team, t.R.C.*, et al.* (2018). caret: Classification and Regression Training. R.

Kuzmichev, A., Nishioka, K., Erdjument-Bromage, H., Tempst, P., and Reinberg, D. (2002). Histone methyltransferase activity associated with a human multiprotein complex containing the Enhancer of Zeste protein. Genes Dev *16*, 2893-2905.

LaFave, L.M., Béguelin, W., Koche, R., Teater, M., Spitzer, B., Chramiec, A., Papalexi, E., Keller, M.D., Hricik, T., Konstantinoff, K.*, et al.* (2015). Loss of BAP1 function leads to EZH2-dependent transformation. Nat Med *21*, 1344-1349.

Laible, G., Wolf, A., Dorn, R., Reuter, G., Nislow, C., Lebersorger, A., Popkin, D., Pillus, L., and Jenuwein, T. (1997). Mammalian homologues of the Polycomb-group gene Enhancer of zeste mediate gene silencing in Drosophila heterochromatin and at S. cerevisiae telomeres. EMBO J *16*, 3219-3232.

Lala, D.S., Rice, D.A., and Parker, K.L. (1992). Steroidogenic factor I, a key regulator of steroidogenic enzyme expression, is the mouse homolog of fushi tarazu-factor I. Mol Endocrinol *6*, 1249-1258.

Landeira, D., and Fisher, A.G. (2011). Inactive yet indispensable: the tale of Jarid2. Trends Cell Biol *21*, 74-80.

Landrum, M.J., Lee, J.M., Benson, M., Brown, G.R., Chao, C., Chitipiralla, S., Gu, B., Hart, J., Hoffman, D., Jang, W.*, et al.* (2018). ClinVar: improving access to variant interpretations and supporting evidence. Nucleic Acids Res *46*, D1062-D1067.

Langlois, D.K., Fritz, M.C., Schall, W.D., Bari Olivier, N., Smedley, R.C., Pearson, P.G., Bailie, M.B., and Hunt, S.W. (2018). ATR-101, a selective ACAT1 inhibitor, decreases ACTH-stimulated cortisol concentrations in dogs with naturally occurring Cushing's syndrome. BMC Endocr Disord *18*, 24.

Langmead, B., and Salzberg, S.L. (2012). Fast gapped-read alignment with Bowtie 2. Nat Methods *9*, 357-359.

LaPensee, C.R., Mann, J.E., Rainey, W.E., Crudo, V., Hunt, S.W., and Hammer, G.D. (2016). ATR-101, a Selective and Potent Inhibitor of Acyl-CoA Acyltransferase 1, Induces Apoptosis in H295R Adrenocortical Cells and in the Adrenal Cortex of Dogs. Endocrinology *157*, 1775-1788.

Larsen, F., Gundersen, G., Lopez, R., and Prydz, H. (1992). CpG islands as gene markers in the human genome. Genomics *13*, 1095-1107.

Lavarone, E., Barbieri, C.M., and Pasini, D. (2019). Dissecting the role of H3K27 acetylation and methylation in PRC2 mediated control of cellular identity. Nat Commun *10*, 1679.

Le, D.T., Durham, J.N., Smith, K.N., Wang, H., Bartlett, B.R., Aulakh, L.K., Lu, S., Kemberling, H., Wilt, C., Luber, B.S.*, et al.* (2017). Mismatch repair deficiency predicts response of solid tumors to PD-1 blockade. Science *357*, 409-413.

Le, D.T., Uram, J.N., Wang, H., Bartlett, B.R., Kemberling, H., Eyring, A.D., Skora, A.D., Luber, B.S., Azad, N.S., Laheru, D.*, et al.* (2015). PD-1 Blockade in Tumors with Mismatch-Repair Deficiency. N Engl J Med *372*, 2509-2520.

Le Tourneau, C., Hoimes, C., Zarwan, C., Wong, D.J., Bauer, S., Claus, R., Wermke, M., Hariharan, S., von Heydebreck, A., Kasturi, V.*, et al.* (2018). Avelumab in patients with previously treated metastatic adrenocortical carcinoma: phase 1b results from the JAVELIN solid tumor trial. J Immunother Cancer *6*, 111.

Leach, D.R., Krummel, M.F., and Allison, J.P. (1996). Enhancement of antitumor immunity by CTLA-4 blockade. Science *271*, 1734-1736.

Lee, C.H., Holder, M., Grau, D., Saldaña-Meyer, R., Yu, J.R., Ganai, R.A., Zhang, J., Wang, M., LeRoy, G., Dobenecker, M.W.*, et al.* (2018). Distinct Stimulatory Mechanisms Regulate the Catalytic Activity of Polycomb Repressive Complex 2. Mol Cell *70*, 435-448.e435.

Lee, W., Teckie, S., Wiesner, T., Ran, L., Prieto Granada, C.N., Lin, M., Zhu, S., Cao, Z., Liang, Y., Sboner, A.*, et al.* (2014). PRC2 is recurrently inactivated through EED or SUZ12 loss in malignant peripheral nerve sheath tumors. Nat Genet *46*, 1227-1232.

Lee, Y., Song, A.J., Baker, R., Micales, B., Conway, S.J., and Lyons, G.E. (2000). Jumonji, a nuclear protein that is necessary for normal heart development. Circ Res *86*, 932-938.

Leibovitz, A., McCombs, W.M., Johnston, D., McCoy, C.E., and Stinson, J.C. (1973). New human cancer cell culture lines. I. SW-13, small-cell carcinoma of the adrenal cortex. J Natl Cancer Inst *51*, 691-697.

Lek, M., Karczewski, K.J., Minikel, E.V., Samocha, K.E., Banks, E., Fennell, T., O'Donnell-Luria, A.H., Ware, J.S., Hill, A.J., Cummings, B.B.*, et al.* (2016). Analysis of protein-coding genetic variation in 60,706 humans. Nature *536*, 285-291.

Lerario, A.M. (2014). 16. Cortex da Adrenal, 2 edn (Sao Paulo, SP, Brazil: AC FARMACEUTICA LTDA.).

Lerario, A.M., Mohan, D.R., Lirov, R., Else, T., and Hammer, G.D. (2019). 83. Adrenal Tumors. In DeVita, Hellman, and Rosenberg's Cancer: Principles & Practice of Oncology, V.T. DeVita, T.S. Lawrence, and S.A. Rosenburg, eds. (Philadelphia: Wolters Kluwer Health/Lippincott Williams & Wilkins).

Lerario, A.M., Worden, F.P., Ramm, C.A., Hesseltine, E.A., Hasseltine, E.A., Stadler, W.M., Else, T., Shah, M.H., Agamah, E., Rao, K.*, et al.* (2014). The combination of insulin-like growth factor receptor 1 (IGF1R) antibody cixutumumab and mitotane as a first-line therapy for patients with recurrent/metastatic adrenocortical carcinoma: a multi-institutional NCI-sponsored trial. Horm Cancer *5*, 232-239.

Lessel, D., Gehbauer, C., Bramswig, N.C., Schluth-Bolard, C., Venkataramanappa, S., van Gassen, K.L.I., Hempel, M., Haack, T.B., Baresic, A., Genetti, C.A.*, et al.* (2018). BCL11B mutations in patients affected by a neurodevelopmental disorder with reduced type 2 innate lymphoid cells. Brain.

Lewis, E.B. (1978). A gene complex controlling segmentation in Drosophila. Nature *276*, 565-570.

Li, E., and Zhang, Y. (2014). DNA methylation in mammals. Cold Spring Harb Perspect Biol *6*, a019133.

Li, G., Margueron, R., Ku, M., Chambon, P., Bernstein, B.E., and Reinberg, D. (2010). Jarid2 and PRC2, partners in regulating gene expression. Genes Dev *24*, 368-380.

Li, H. (2011). A statistical framework for SNP calling, mutation discovery, association mapping and population genetical parameter estimation from sequencing data. Bioinformatics *27*, 2987-2993.

Li, H. (2013). Aligning sequence reads, clone sequences and assembly contigs with BWA-MEM. arXiv.

Li, H., Handsaker, B., Wysoker, A., Fennell, T., Ruan, J., Homer, N., Marth, G., Abecasis, G., Durbin, R., and Subgroup, G.P.D.P. (2009). The Sequence Alignment/Map format and SAMtools. Bioinformatics *25*, 2078-2079.

Li, H., Liefke, R., Jiang, J., Kurland, J.V., Tian, W., Deng, P., Zhang, W., He, Q., Patel, D.J., Bulyk, M.L.*, et al.* (2017). Polycomb-like proteins link the PRC2 complex to CpG islands. Nature *549*, 287-291.

Li, Q., and Wang, K. (2017). InterVar: Clinical Interpretation of Genetic Variants by the 2015 ACMG-AMP Guidelines. Am J Hum Genet *100*, 267-280.

Li, Y., Zhang, Z., Chen, J., Liu, W., Lai, W., Liu, B., Li, X., Liu, L., Xu, S., Dong, Q.*, et al.* (2018). Stella safeguards the oocyte methylome by preventing de novo methylation mediated by DNMT1. Nature *564*, 136-140.

Liao, Y., Smyth, G.K., and Shi, W. (2014). featureCounts: an efficient general purpose program for assigning sequence reads to genomic features. Bioinformatics *30*, 923-930.

Liberzon, A., Subramanian, A., Pinchback, R., Thorvaldsdóttir, H., Tamayo, P., and Mesirov, J.P. (2011). Molecular signatures database (MSigDB) 3.0. Bioinformatics *27*, 1739-1740.

Lieberman-Aiden, E., van Berkum, N.L., Williams, L., Imakaev, M., Ragoczy, T., Telling, A., Amit, I., Lajoie, B.R., Sabo, P.J., Dorschner, M.O.*, et al.* (2009). Comprehensive mapping of long-range interactions reveals folding principles of the human genome. Science *326*, 289-293.

Liefke, R., Karwacki-Neisius, V., and Shi, Y. (2016). EPOP Interacts with Elongin BC and USP7 to Modulate the Chromatin Landscape. Mol Cell *64*, 659-672.

Liefke, R., and Shi, Y. (2015). The PRC2-associated factor C17orf96 is a novel CpG island regulator in mouse ES cells. Cell Discov *1*, 15008.

Lippert, J., Appenzeller, S., Liang, R., Sbiera, S., Kircher, S., Altieri, B., Nanda, I., Weigand, I., Gehrig, A., Steinhauer, S.*, et al.* (2018). Targeted Molecular Analysis in Adrenocortical Carcinomas: A Strategy Toward Improved Personalized Prognostication. J Clin Endocrinol Metab *103*, 4511-4523.

Lister, R., Pelizzola, M., Dowen, R.H., Hawkins, R.D., Hon, G., Tonti-Filippini, J., Nery, J.R., Lee, L., Ye, Z., Ngo, Q.M.*, et al.* (2009). Human DNA methylomes at base resolution show widespread epigenomic differences. Nature *462*, 315-322.

Liu, J., Li, X.D., Vaheri, A., and Voutilainen, R. (2004). DNA methylation affects cell proliferation, cortisol secretion and steroidogenic gene expression in human adrenocortical NCI-H295R cells. J Mol Endocrinol *33*, 651-662.

Long, H.K., King, H.W., Patient, R.K., Odom, D.T., and Klose, R.J. (2016). Protection of CpG islands from DNA methylation is DNA-encoded and evolutionarily conserved. Nucleic Acids Res *44*, 6693-6706.

Lovén, J., Hoke, H.A., Lin, C.Y., Lau, A., Orlando, D.A., Vakoc, C.R., Bradner, J.E., Lee, T.I., and Young, R.A. (2013). Selective inhibition of tumor oncogenes by disruption of super-enhancers. Cell *153*, 320-334.

Lu, C., Ward, P.S., Kapoor, G.S., Rohle, D., Turcan, S., Abdel-Wahab, O., Edwards, C.R., Khanin, R., Figueroa, M.E., Melnick, A.*, et al.* (2012). IDH mutation impairs histone demethylation and results in a block to cell differentiation. Nature *483*, 474-478.

Luo, X., Ikeda, Y., and Parker, K.L. (1994). A cell-specific nuclear receptor is essential for adrenal and gonadal development and sexual differentiation. Cell *77*, 481-490.

Mack, S.C., Witt, H., Piro, R.M., Gu, L., Zuyderduyn, S., Stütz, A.M., Wang, X., Gallo, M., Garzia, L., Zayne, K.*, et al.* (2014). Epigenomic alterations define lethal CIMP-positive ependymomas of infancy. Nature *506*, 445-450.

Maegawa, S., Hinkal, G., Kim, H.S., Shen, L., Zhang, L., Zhang, J., Zhang, N., Liang, S., Donehower, L.A., and Issa, J.P. (2010). Widespread and tissue specific age-related DNA methylation changes in mice. Genome Res *20*, 332-340.

Majdic, G., Young, M., Gomez-Sanchez, E., Anderson, P., Szczepaniak, L.S., Dobbins, R.L., McGarry, J.D., and Parker, K.L. (2002). Knockout mice lacking steroidogenic factor 1 are a novel genetic model of hypothalamic obesity. Endocrinology *143*, 607-614.

Margueron, R., Justin, N., Ohno, K., Sharpe, M.L., Son, J., Drury, W.J., Voigt, P., Martin, S.R., Taylor, W.R., De Marco, V.*, et al.* (2009). Role of the polycomb protein EED in the propagation of repressive histone marks. Nature *461*, 762-767.

Margueron, R., Li, G., Sarma, K., Blais, A., Zavadil, J., Woodcock, C.L., Dynlacht, B.D., and Reinberg, D. (2008). Ezh1 and Ezh2 maintain repressive chromatin through different mechanisms. Mol Cell *32*, 503-518.

Marshall, W.H., Martin, F.I., and Mackay, I.R. (1967). Gardner's syndrome with adrenal carcinoma. Australasian annals of medicine *16*, 242-244.

Matei, D., Fang, F., Shen, C., Schilder, J., Arnold, A., Zeng, Y., Berry, W.A., Huang, T., and Nephew, K.P. (2012). Epigenetic resensitization to platinum in ovarian cancer. Cancer Res *72*, 2197-2205.

Matei, D., Ghamande, S., Roman, L., Alvarez Secord, A., Nemunaitis, J., Markham, M.J., Nephew, K.P., Jueliger, S., Oganesian, A., Naim, S.*, et al.* (2018). A Phase I Clinical Trial of Guadecitabine and Carboplatin in Platinum-Resistant, Recurrent Ovarian Cancer: Clinical, Pharmacokinetic, and Pharmacodynamic Analyses. Clin Cancer Res *24*, 2285-2293.

Mathieu, M., Drelon, C., Rodriguez, S., Tabbal, H., Septier, A., Damon-Soubeyrand, C., Dumontet, T., Berthon, A., Sahut-Barnola, I., Djari, C.*, et al.* (2018). Steroidogenic differentiation and PKA signaling are programmed by histone methyltransferase EZH2 in the adrenal cortex. Proc Natl Acad Sci U S A *115*, E12265-E12274.

McBride, M.J., Mashtalir, N., Winter, E.B., Dao, H.T., Filipovski, M., D'Avino, A.R., Seo, H.S., Umbreit, N.T., St Pierre, R., Valencia, A.M.*, et al.* (2020). The nucleosome acidic patch and H2A ubiquitination underlie mSWI/SNF recruitment in synovial sarcoma. Nat Struct Mol Biol *27*, 836-845.

McBride, M.J., Pulice, J.L., Beird, H.C., Ingram, D.R., D'Avino, A.R., Shern, J.F., Charville, G.W., Hornick, J.L., Nakayama, R.T., Garcia-Rivera, E.M.*, et al.* (2018). The SS18-SSX Fusion Oncoprotein Hijacks BAF Complex Targeting and Function to Drive Synovial Sarcoma. Cancer Cell *33*, 1128-1141.e1127.

McCabe, M.J., Pinese, M., Chan, C.L., Sheriff, N., Thompson, T.J., Grady, J., Wong, M., Gauthier, M.A., Puttick, C., Gayevskiy, V.*, et al.* (2019). Genomic stratification and liquid biopsy in a rare adrenocortical carcinoma (ACC) case, with dual lung metastases. Cold Spring Harb Mol Case Stud *5*.

McCabe, M.T., Ott, H.M., Ganji, G., Korenchuk, S., Thompson, C., Van Aller, G.S., Liu, Y., Graves, A.P., Della Pietra, A., Diaz, E.*, et al.* (2012). EZH2 inhibition as a therapeutic strategy for lymphoma with EZH2-activating mutations. Nature *492*, 108-112.

McCarthy, D.J., Chen, Y., and Smyth, G.K. (2012). Differential expression analysis of multifactor RNA-Seq experiments with respect to biological variation. Nucleic Acids Res *40*, 4288-4297.

McGrath, J., and Solter, D. (1984). Completion of mouse embryogenesis requires both the maternal and paternal genomes. Cell *37*, 179-183.

Merika, M., Williams, A.J., Chen, G., Collins, T., and Thanos, D. (1998). Recruitment of CBP/p300 by the IFN beta enhanceosome is required for synergistic activation of transcription. Mol Cell *1*, 277-287.

Mesiano, S., and Jaffe, R.B. (1997). Developmental and functional biology of the primate fetal adrenal cortex. Endocr Rev *18*, 378-403.

Miller, B.F., Sánchez-Vega, F., and Elnitski, L. (2016). The Emergence of Pan-Cancer CIMP and Its Elusive Interpretation. Biomolecules *6*.

Miller, B.S., Gauger, P.G., Hammer, G.D., Giordano, T.J., and Doherty, G.M. (2010). Proposal for modification of the ENSAT staging system for adrenocortical carcinoma using tumor grade. Langenbecks Arch Surg *395*, 955-961.

Miller, O.J., Schnedl, W., Allen, J., and Erlanger, B.F. (1974). 5-Methylcytosine localised in mammalian constitutive heterochromatin. Nature *251*, 636-637.

Milne, T.A., Briggs, S.D., Brock, H.W., Martin, M.E., Gibbs, D., Allis, C.D., and Hess, J.L. (2002). MLL targets SET domain methyltransferase activity to Hox gene promoters. Mol Cell *10*, 1107-1117.

Mizusaki, H., Kawabe, K., Mukai, T., Ariyoshi, E., Kasahara, M., Yoshioka, H., Swain, A., and Morohashi, K. (2003). Dax-1 (dosage-sensitive sex reversal-adrenal hypoplasia congenita critical region on the X chromosome, gene 1) gene transcription is regulated by wnt4 in the female developing gonad. Mol Endocrinol *17*, 507-519.

Mohammad, F., Weissmann, S., Leblanc, B., Pandey, D.P., Højfeldt, J.W., Comet, I., Zheng, C., Johansen, J.V., Rapin, N., Porse, B.T.*, et al.* (2017). EZH2 is a potential therapeutic target for H3K27M-mutant pediatric gliomas. Nat Med *23*, 483-492.

Mohan, D.R., Lerario, A.M., Else, T., Mukherjee, B., Almeida, M.Q., Vinco, M., Rege, J., Mariani, B.M.P., Zerbini, M.C.N., Mendonca, B.B.*, et al.* (2019). Targeted Assessment of *G0S2* Methylation Identifies a Rapidly Recurrent, Routinely Fatal Molecular Subtype of Adrenocortical Carcinoma. Clin Cancer Res *25*, 3276-3288.

Mohandas, T., Sparkes, R.S., and Shapiro, L.J. (1981). Reactivation of an inactive human X chromosome: evidence for X inactivation by DNA methylation. Science *211*, 393-396.

Monnier, P., Martinet, C., Pontis, J., Stancheva, I., Ait-Si-Ali, S., and Dandolo, L. (2013). H19 lncRNA controls gene expression of the Imprinted Gene Network by recruiting MBD1. Proc Natl Acad Sci U S A *110*, 20693-20698.

Montgomery, N.D., Yee, D., Chen, A., Kalantry, S., Chamberlain, S.J., Otte, A.P., and Magnuson, T. (2005). The murine polycomb group protein Eed is required for global histone H3 lysine-27 methylation. Curr Biol *15*, 942-947.

Mootha, V.K., Lindgren, C.M., Eriksson, K.F., Subramanian, A., Sihag, S., Lehar, J., Puigserver, P., Carlsson, E., Ridderstråle, M., Laurila, E.*, et al.* (2003). PGC-1alpha-responsive genes involved in oxidative phosphorylation are coordinately downregulated in human diabetes. Nat Genet *34*, 267-273.

Morin, R.D., Johnson, N.A., Severson, T.M., Mungall, A.J., An, J., Goya, R., Paul, J.E., Boyle, M., Woolcock, B.W., Kuchenbauer, F.*, et al.* (2010). Somatic mutations altering EZH2 (Tyr641) in follicular and diffuse large B-cell lymphomas of germinal-center origin. Nat Genet *42*, 181-185.

Morohashi, K., Honda, S., Inomata, Y., Handa, H., and Omura, T. (1992). A common trans-acting factor, Ad4-binding protein, to the promoters of steroidogenic P-450s. J Biol Chem *267*, 17913-17919.

Mota, J.M., Sousa, L.G., Braghiroli, M.I., Siqueira, L.T., Neto, J.E.B., Chapchap, P., Hoff, A.A.O., and Hoff, P.M. (2018). Pembrolizumab for metastatic adrenocortical carcinoma with high mutational burden: Two case reports. Medicine (Baltimore) *97*, e13517.

Motoyama, J., Kitajima, K., Kojima, M., Kondo, S., and Takeuchi, T. (1997). Organogenesis of the liver, thymus and spleen is affected in jumonji mutant mice. Mech Dev *66*, 27-37.

Muntean, A.G., Tan, J., Sitwala, K., Huang, Y., Bronstein, J., Connelly, J.A., Basrur, V., Elenitoba-Johnson, K.S., and Hess, J.L. (2010). The PAF complex synergizes with MLL fusion proteins at HOX loci to promote leukemogenesis. Cancer Cell *17*, 609-621.

Nachtigal, M.W., Hirokawa, Y., Enyeart-VanHouten, D.L., Flanagan, J.N., Hammer, G.D., and Ingraham, H.A. (1998). Wilms' tumor 1 and Dax-1 modulate the orphan nuclear receptor SF-1 in sex-specific gene expression. Cell *93*, 445-454.

Nakayama, R.T., Pulice, J.L., Valencia, A.M., McBride, M.J., McKenzie, Z.M., Gillespie, M.A., Ku, W.L., Teng, M., Cui, K., Williams, R.T.*, et al.* (2017). SMARCB1 is required for widespread BAF complex-mediated activation of enhancers and bivalent promoters. Nat Genet *49*, 1613-1623.

Nanba, K., Blinder, A.R., Rege, J., Hattangady, N.G., Else, T., Liu, C.J., Tomlins, S.A., Vats, P., Kumar-Sinha, C., Giordano, T.J.*, et al.* (2020). Somatic CACNA1H Mutation As a Cause of Aldosterone-Producing Adenoma. Hypertension *75*, 645-649.

Naslavsky, M.S., Yamamoto, G.L., de Almeida, T.F., Ezquina, S.A.M., Sunaga, D.Y., Pho, N., Bozoklian, D., Sandberg, T.O.M., Brito, L.A., Lazar, M.*, et al.* (2017). Exomic variants of an elderly cohort of Brazilians in the ABraOM database. Hum Mutat *38*, 751-763.

NCI (2005-2018). The Cancer Genome Atlas (National Cancer Institute).

Neff, T., Sinha, A.U., Kluk, M.J., Zhu, N., Khattab, M.H., Stein, L., Xie, H., Orkin, S.H., and Armstrong, S.A. (2012). Polycomb repressive complex 2 is required for MLL-AF9 leukemia. Proc Natl Acad Sci U S A *109*, 5028-5033.

Neri, F., Krepelova, A., Incarnato, D., Maldotti, M., Parlato, C., Galvagni, F., Matarese, F., Stunnenberg, H.G., and Oliviero, S. (2013). Dnmt3L antagonizes DNA methylation at

bivalent promoters and favors DNA methylation at gene bodies in ESCs. Cell *155*, 121-134.

Nishimoto, K., Tomlins, S.A., Kuick, R., Cani, A.K., Giordano, T.J., Hovelson, D.H., Liu, C.J., Sanjanwala, A.R., Edwards, M.A., Gomez-Sanchez, C.E.*, et al.* (2015). Aldosterone-stimulating somatic gene mutations are common in normal adrenal glands. Proc Natl Acad Sci U S A *112*, E4591-4599.

Nishisho, I., Nakamura, Y., Miyoshi, Y., Miki, Y., Ando, H., Horii, A., Koyama, K., Utsunomiya, J., Baba, S., and Hedge, P. (1991). Mutations of chromosome 5q21 genes in FAP and colorectal cancer patients. Science *253*, 665-669.

Nomi, T., Sho, M., Akahori, T., Hamada, K., Kubo, A., Kanehiro, H., Nakamura, S., Enomoto, K., Yagita, H., Azuma, M.*, et al.* (2007). Clinical significance and therapeutic potential of the programmed death-1 ligand/programmed death-1 pathway in human pancreatic cancer. Clin Cancer Res *13*, 2151-2157.

Novoselova, T.V., Hussain, M., King, P.J., Guasti, L., Metherell, L.A., Charalambous, M., Clark, A.J.L., and Chan, L.F. (2018). MRAP deficiency impairs adrenal progenitor cell differentiation and gland zonation. FASEB J, fj201701274RR.

Ntziachristos, P., Tsirigos, A., Van Vlierberghe, P., Nedjic, J., Trimarchi, T., Flaherty, M.S., Ferres-Marco, D., da Ros, V., Tang, Z., Siegle, J.*, et al.* (2012). Genetic inactivation of the polycomb repressive complex 2 in T cell acute lymphoblastic leukemia. Nat Med *18*, 298-301.

Nusse, R., and Clevers, H. (2017). Wnt/β-Catenin Signaling, Disease, and Emerging Therapeutic Modalities. Cell *169*, 985-999.

O'Carroll, D., Erhardt, S., Pagani, M., Barton, S.C., Surani, M.A., and Jenuwein, T. (2001). The polycomb-group gene Ezh2 is required for early mouse development. Mol Cell Biol *21*, 4330-4336.

Ohm, J.E., McGarvey, K.M., Yu, X., Cheng, L., Schuebel, K.E., Cope, L., Mohammad, H.P., Chen, W., Daniel, V.C., Yu, W.*, et al.* (2007). A stem cell-like chromatin pattern may predispose tumor suppressor genes to DNA hypermethylation and heritable silencing. Nat Genet *39*, 237-242.

Okano, M., Bell, D.W., Haber, D.A., and Li, E. (1999). DNA methyltransferases Dnmt3a and Dnmt3b are essential for de novo methylation and mammalian development. Cell *99*, 247-257.

Okonechnikov, K., Conesa, A., and Garcia-Alcalde, F. (2016). Qualimap 2: advanced multi-sample quality control for high-throughput sequencing data. Bioinformatics *32*, 292-294.

Oliviero, G., Brien, G.L., Waston, A., Streubel, G., Jerman, E., Andrews, D., Doyle, B., Munawar, N., Wynne, K., Crean, J.*, et al.* (2016). Dynamic Protein Interactions of the Polycomb Repressive Complex 2 during Differentiation of Pluripotent Cells. Mol Cell Proteomics *15*, 3450-3460.

Pajtler, K.W., Wen, J., Sill, M., Lin, T., Orisme, W., Tang, B., Hübner, J.M., Ramaswamy, V., Jia, S., Dalton, J.D.*, et al.* (2018). Molecular heterogeneity and CXorf67 alterations in posterior fossa group A (PFA) ependymomas. Acta Neuropathol *136*, 211-226.

Palacios, R., and Sugawara, I. (1982). Hydrocortisone abrogates proliferation of T cells in autologous mixed lymphocyte reaction by rendering the interleukin-2 Producer T cells unresponsive to interleukin-1 and unable to synthesize the T-cell growth factor. Scand J Immunol *15*, 25-31.

Palmero, E.I., Schuler-Faccini, L., Caleffi, M., Achatz, M.I., Olivier, M., Martel-Planche, G., Marcel, V., Aguiar, E., Giacomazzi, J., Ewald, I.P.*, et al.* (2008). Detection of R337H, a germline TP53 mutation predisposing to multiple cancers, in asymptomatic women participating in a breast cancer screening program in Southern Brazil. Cancer Lett *261*, 21-25.

Papathomas, T.G., Pucci, E., Giordano, T.J., Lu, H., Duregon, E., Volante, M., Papotti, M., Lloyd, R.V., Tischler, A.S., van Nederveen, F.H.*, et al.* (2016). An International Ki67 Reproducibility Study in Adrenal Cortical Carcinoma. Am J Surg Pathol *40*, 569-576.

Pasini, D., Bracken, A.P., Jensen, M.R., Lazzerini Denchi, E., and Helin, K. (2004). Suz12 is essential for mouse development and for EZH2 histone methyltransferase activity. EMBO J *23*, 4061-4071.

Pasini, D., Cloos, P.A., Walfridsson, J., Olsson, L., Bukowski, J.P., Johansen, J.V., Bak, M., Tommerup, N., Rappsilber, J., and Helin, K. (2010). JARID2 regulates binding of the Polycomb repressive complex 2 to target genes in ES cells. Nature *464*, 306-310.

Paz-Ares, L., Luft, A., Vicente, D., Tafreshi, A., Gümüş, M., Mazières, J., Hermes, B., Çay Şenler, F., Csőszi, T., Fülöp, A.*, et al.* (2018). Pembrolizumab plus Chemotherapy for Squamous Non-Small-Cell Lung Cancer. N Engl J Med *379*, 2040-2051.

Pedersen, B., Bhetariya, P., Brown, J., Marth, G., Jensen, R., Bronner, M., Underhill, H., and Quinlan, A. (2019). Somalier: rapid relatedness estimation for cancer and germline studies using efficient genome sketches (bioRXiv).

Peng, J.C., Valouev, A., Swigut, T., Zhang, J., Zhao, Y., Sidow, A., and Wysocka, J. (2009). Jarid2/Jumonji coordinates control of PRC2 enzymatic activity and target gene occupancy in pluripotent cells. Cell *139*, 1290-1302.

Pereira, F.A., Qiu, Y., Tsai, M.J., and Tsai, S.Y. (1995). Chicken ovalbumin upstream promoter transcription factor (COUP-TF): expression during mouse embryogenesis. J Steroid Biochem Mol Biol *53*, 503-508.

Perino, M., van Mierlo, G., Karemaker, I.D., van Genesen, S., Vermeulen, M., Marks, H., van Heeringen, S.J., and Veenstra, G.J.C. (2018). MTF2 recruits Polycomb Repressive Complex 2 by helical-shape-selective DNA binding. Nat Genet *50*, 1002-1010.

Peters, T.J., Buckley, M.J., Statham, A.L., Pidsley, R., Samaras, K., V Lord, R., Clark, S.J., and Molloy, P.L. (2015). De novo identification of differentially methylated regions in the human genome. Epigenetics Chromatin *8*, 6.

Pham, T.N.D., Kumar, K., DeCant, B.T., Shang, M., Munshi, S.Z., Matsangou, M., Ebine, K., and Munshi, H.G. (2019). Induction of MNK Kinase-dependent eIF4E Phosphorylation by Inhibitors Targeting BET Proteins Limits Efficacy of BET Inhibitors. Mol Cancer Ther *18*, 235-244.

Pignatti, E., Leng, S., Yuchi, Y., Borges, K.S., Guagliardo, N.A., Shah, M.S., Ruiz-Babot, G., Kariyawasam, D., Taketo, M.M., Miao, J.*, et al.* (2020). Beta-Catenin Causes Adrenal Hyperplasia by Blocking Zonal Transdifferentiation. Cell Rep *31*, 107524.

Pinto, E.M., Billerbeck, A.E., Villares, M.C., Domenice, S., Mendonca, B.B., and Latronico, A.C. (2004). Founder effect for the highly prevalent R337H mutation of tumor suppressor p53 in Brazilian patients with adrenocortical tumors. Arq Bras Endocrinol Metabol *48*, 647-650.

Pinto, E.M., Morton, C., Rodriguez-Galindo, C., McGregor, L., Davidoff, A.M., Mercer, K., Debelenko, L.V., Billups, C., Ribeiro, R.C., and Zambetti, G.P. (2013). Establishment and characterization of the first pediatric adrenocortical carcinoma xenograft model identifies topotecan as a potential chemotherapeutic agent. Clin Cancer Res *19*, 1740-1747.

Piunti, A., Hashizume, R., Morgan, M.A., Bartom, E.T., Horbinski, C.M., Marshall, S.A., Rendleman, E.J., Ma, Q., Takahashi, Y.H., Woodfin, A.R.*, et al.* (2017). Therapeutic targeting of polycomb and BET bromodomain proteins in diffuse intrinsic pontine gliomas. Nat Med *23*, 493-500.

Piunti, A., Smith, E.R., Morgan, M.A.J., Ugarenko, M., Khaltyan, N., Helmin, K.A., Ryan, C.A., Murray, D.C., Rickels, R.A., Yilmaz, B.D.*, et al.* (2019). CATACOMB: An endogenous inducible gene that antagonizes H3K27 methylation activity of Polycomb repressive complex 2 via an H3K27M-like mechanism. Sci Adv *5*, eaax2887.

Pott, S., and Lieb, J.D. (2015). What are super-enhancers? Nat Genet *47*, 8-12.

Pradhan, S., Bacolla, A., Wells, R.D., and Roberts, R.J. (1999). Recombinant human DNA (cytosine-5) methyltransferase. I. Expression, purification, and comparison of de novo and maintenance methylation. J Biol Chem *274*, 33002-33010.

Pulliam, N., Fang, F., Ozes, A.R., Tang, J., Adewuyi, A., Keer, H., Lyons, J., Baylin, S.B., Matei, D., Nakshatri, H.*, et al.* (2018). An Effective Epigenetic-PARP Inhibitor Combination Therapy for Breast and Ovarian Cancers Independent of BRCA Mutations. Clin Cancer Res *24*, 3163-3175.

Qiu, X., Hill, A., Packer, J., Lin, D., Ma, Y.A., and Trapnell, C. (2017a). Single-cell mRNA quantification and differential analysis with Census. Nat Methods *14*, 309-315.

Qiu, X., Mao, Q., Tang, Y., Wang, L., Chawla, R., Pliner, H.A., and Trapnell, C. (2017b). Reversed graph embedding resolves complex single-cell trajectories. Nat Methods *14*, 979-982.

Quinlan, A.R., and Hall, I.M. (2010). BEDTools: a flexible suite of utilities for comparing genomic features. Bioinformatics *26*, 841-842.

Ragazzini, R., Pérez-Palacios, R., Baymaz, I.H., Diop, S., Ancelin, K., Zielinski, D., Michaud, A., Givelet, M., Borsos, M., Aflaki, S.*, et al.* (2019). EZHIP constrains Polycomb Repressive Complex 2 activity in germ cells. Nat Commun *10*, 3858.

Ragazzon, B., Lefrançois-Martinez, A.M., Val, P., Sahut-Barnola, I., Tournaire, C., Chambon, C., Gachancard-Bouya, J.L., Begue, R.J., Veyssière, G., and Martinez, A. (2006). Adrenocorticotropin-dependent changes in SF-1/DAX-1 ratio influence steroidogenic genes expression in a novel model of glucocorticoid-producing adrenocortical cell lines derived from targeted tumorigenesis. Endocrinology *147*, 1805-1818.

Ragazzon, B., Libé, R., Assié, G., Tissier, F., Barreau, O., Houdayer, C., Perlemoine, K., Audebourg, A., Clauser, E., René-Corail, F.*, et al.* (2014). Mass-array screening of frequent mutations in cancers reveals RB1 alterations in aggressive adrenocortical carcinomas. Eur J Endocrinol *170*, 385-391.

Raisner, R., Kharbanda, S., Jin, L., Jeng, E., Chan, E., Merchant, M., Haverty, P.M., Bainer, R., Cheung, T., Arnott, D.*, et al.* (2018). Enhancer Activity Requires CBP/P300 Bromodomain-Dependent Histone H3K27 Acetylation. Cell Rep *24*, 1722-1729.

Raj, N., Zheng, Y., Kelly, V., Katz, S.S., Chou, J., Do, R.K.G., Capanu, M., Zamarin, D., Saltz, L.B., Ariyan, C.E.*, et al.* (2020). PD-1 Blockade in Advanced Adrenocortical Carcinoma. J Clin Oncol *38*, 71-80.

Ramírez, F., Ryan, D.P., Grüning, B., Bhardwaj, V., Kilpert, F., Richter, A.S., Heyne, S., Dündar, F., and Manke, T. (2016). deepTools2: a next generation web server for deep-sequencing data analysis. Nucleic Acids Res *44*, W160-165.

Raymond, V.M., Everett, J.N., Furtado, L.V., Gustafson, S.L., Jungbluth, C.R., Gruber, S.B., Hammer, G.D., Stoffel, E.M., Greenson, J.K., Giordano, T.J.*, et al.* (2013). Adrenocortical carcinoma is a lynch syndrome-associated cancer. J Clin Oncol *31*, 3012-3018.

Rege, J., Turcu, A.F., Else, T., Auchus, R.J., and Rainey, W.E. (2019). Steroid biomarkers in human adrenal disease. J Steroid Biochem Mol Biol *190*, 273-280.

Reich, D., Patterson, N., Campbell, D., Tandon, A., Mazieres, S., Ray, N., Parra, M.V., Rojas, W., Duque, C., Mesa, N.*, et al.* (2012). Reconstructing Native American population history. Nature *488*, 370-374.

Rhodes, D.R., Kalyana-Sundaram, S., Mahavisno, V., Barrette, T.R., Ghosh, D., and Chinnaiyan, A.M. (2005). Mining for regulatory programs in the cancer transcriptome. Nat Genet *37*, 579-583.

Ribeiro, R.C., Sandrini, F., Figueiredo, B., Zambetti, G.P., Michalkiewicz, E., Lafferty, A.R., DeLacerda, L., Rabin, M., Cadwell, C., Sampaio, G.*, et al.* (2001). An inherited p53 mutation that contributes in a tissue-specific manner to pediatric adrenal cortical carcinoma. Proc Natl Acad Sci U S A *98*, 9330-9335.

Ritchie, M.E., Phipson, B., Wu, D., Hu, Y., Law, C.W., Shi, W., and Smyth, G.K. (2015). limma powers differential expression analyses for RNA-sequencing and microarray studies. Nucleic Acids Res *43*, e47.

Rizvi, N.A., Hellmann, M.D., Snyder, A., Kvistborg, P., Makarov, V., Havel, J.J., Lee, W., Yuan, J., Wong, P., Ho, T.S.*, et al.* (2015). Cancer immunology. Mutational landscape determines sensitivity to PD-1 blockade in non-small cell lung cancer. Science *348*, 124-128.

Robinson, M.D., McCarthy, D.J., and Smyth, G.K. (2010). edgeR: a Bioconductor package for differential expression analysis of digital gene expression data. Bioinformatics *26*, 139-140.

Roca, E., Berruti, A., Sbiera, S., Rapa, I., Oneda, E., Sperone, P., Ronchi, C.L., Ferrari, L., Grisanti, S., Germano, A.*, et al.* (2017). Topoisomerase 2α and thymidylate synthase expression in adrenocortical cancer. Endocr Relat Cancer *24*, 319-327.

Ronchi, C.L., Di Dalmazi, G., Faillot, S., Sbiera, S., Assié, G., Weigand, I., Calebiro, D., Schwarzmayr, T., Appenzeller, S., Rubin, B.*, et al.* (2016). Genetic Landscape of Sporadic Unilateral Adrenocortical Adenomas Without PRKACA p.Leu206Arg Mutation. The Journal of clinical endocrinology and metabolism *101*, 3526-3538.

Ross-Innes, C.S., Stark, R., Teschendorff, A.E., Holmes, K.A., Ali, H.R., Dunning, M.J., Brown, G.D., Gojis, O., Ellis, I.O., Green, A.R.*, et al.* (2012). Differential oestrogen receptor binding is associated with clinical outcome in breast cancer. Nature *481*, 389-393.

Rothberg, J.L.M., Maganti, H.B., Jrade, H., Porter, C.J., Palidwor, G.A., Cafariello, C., Battaion, H.L., Khan, S.T., Perkins, T.J., Paulson, R.F.*, et al.* (2018). Mtf2-PRC2 control of canonical Wnt signaling is required for definitive erythropoiesis. Cell Discov *4*, 21.

Rošić, S., Amouroux, R., Requena, C.E., Gomes, A., Emperle, M., Beltran, T., Rane, J.K., Linnett, S., Selkirk, M.E., Schiffer, P.H.*, et al.* (2018). Evolutionary analysis indicates that DNA alkylation damage is a byproduct of cytosine DNA methyltransferase activity. Nat Genet *50*, 452-459.

Ruggiero, C., Doghman-Bouguerra, M., Ronco, C., Benhida, R., Rocchi, S., and Lalli, E. (2018). The GRP78/BiP inhibitor HA15 synergizes with mitotane action against adrenocortical carcinoma cells through convergent activation of ER stress pathways. Mol Cell Endocrinol *474*, 57-64.

Ruggiero, C., Doghman-Bouguerra, M., Sbiera, S., Sbiera, I., Parsons, M., Ragazzon, B., Morin, A., Robidel, E., Favier, J., Bertherat, J.*, et al.* (2017). Dosage-dependent regulation of *VAV2* expression by steroidogenic factor-1 drives adrenocortical carcinoma cell invasion. Sci Signal *10*.

Russo, D., Arturi, F., Schlumberger, M., Caillou, B., Monier, R., Filetti, S., and Suárez, H.G. (1995). Activating mutations of the TSH receptor in differentiated thyroid carcinomas. Oncogene *11*, 1907-1911.

Sabari, B.R., Dall'Agnese, A., Boija, A., Klein, I.A., Coffey, E.L., Shrinivas, K., Abraham, B.J., Hannett, N.M., Zamudio, A.V., Manteiga, J.C.*, et al.* (2018). Coactivator condensation at super-enhancers links phase separation and gene control. Science *361*.

Sanyal, A., Lajoie, B.R., Jain, G., and Dekker, J. (2012). The long-range interaction landscape of gene promoters. Nature *489*, 109-113.

Sarma, K., Margueron, R., Ivanov, A., Pirrotta, V., and Reinberg, D. (2008). Ezh2 requires PHF1 to efficiently catalyze H3 lysine 27 trimethylation in vivo. Mol Cell Biol *28*, 2718-2731.

Sato, Y., Maekawa, S., Ishii, R., Sanada, M., Morikawa, T., Shiraishi, Y., Yoshida, K., Nagata, Y., Sato-Otsubo, A., Yoshizato, T.*, et al.* (2014). Recurrent somatic mutations underlie corticotropin-independent Cushing's syndrome. Science (New York, NY) *344*, 917-920.

Sbiera, S., Leich, E., Liebisch, G., Sbiera, I., Schirbel, A., Wiemer, L., Matysik, S., Eckhardt, C., Gardill, F., Gehl, A.*, et al.* (2015). Mitotane Inhibits Sterol-O-Acyl Transferase 1 Triggering Lipid-Mediated Endoplasmic Reticulum Stress and Apoptosis in Adrenocortical Carcinoma Cells. Endocrinology *156*, 3895-3908.

Sbiera, S., Sbiera, I., Ruggiero, C., Doghman-Bouguerra, M., Korpershoek, E., de Krijger, R.R., Ettaieb, H., Haak, H., Volante, M., Papotti, M.*, et al.* (2017). Assessment of VAV2 Expression Refines Prognostic Prediction in Adrenocortical Carcinoma. J Clin Endocrinol Metab *102*, 3491-3498.

Schimmer, B.P., and White, P.C. (2010). Minireview: steroidogenic factor 1: its roles in differentiation, development, and disease. Mol Endocrinol *24*, 1322-1337.

Schindelin, J., Arganda-Carreras, I., Frise, E., Kaynig, V., Longair, M., Pietzsch, T., Preibisch, S., Rueden, C., Saalfeld, S., Schmid, B.*, et al.* (2012). Fiji: an open-source platform for biological-image analysis. Nat Methods *9*, 676-682.

Schoeftner, S., Sengupta, A.K., Kubicek, S., Mechtler, K., Spahn, L., Koseki, H., Jenuwein, T., and Wutz, A. (2006). Recruitment of PRC1 function at the initiation of X inactivation independent of PRC2 and silencing. EMBO J *25*, 3110-3122.

Schoffski, P., Agulnik, M., Stacchiotti, S., Davis, L.E., Villalobos, V.M., Italiano, A., George, S., Cote, G.M., Blakemore, S., Clawson, A.*, et al.* (2017). Phase 2 multicenter study of the EZH2 inhibitor tazemetostat in adults with synovial sarcoma (NCT02601950). Journal of Clinical Oncology *35*, 11057-11057.

Scholl, U.I., Goh, G., Stolting, G., de Oliveira, R.C., Choi, M., Overton, J.D., Fonseca, A.L., Korah, R., Starker, L.F., Kunstman, J.W.*, et al.* (2013). Somatic and germline CACNA1D calcium channel mutations in aldosterone-producing adenomas and primary aldosteronism. Nat Genet *45*, 1050-1054.

Schreiber, A.R., Kar, A., Goodspeed, A.E., Pozdeyev, N., Somerset, H., Raeburn, C.D., Tan, A.C., Leong, S., Wierman, M.E., and Kiseljak-Vassiliades, K. (2020). Leptomeningeal Metastasis from Adrenocortical Carcinoma: A Case Report. J Endocr Soc *4*, bvaa017.

Schuettengruber, B., Bourbon, H.M., Di Croce, L., and Cavalli, G. (2017). Genome Regulation by Polycomb and Trithorax: 70 Years and Counting. Cell *171*, 34-57.

Schwartzentruber, J., Korshunov, A., Liu, X.Y., Jones, D.T., Pfaff, E., Jacob, K., Sturm, D., Fontebasso, A.M., Quang, D.A., Tönjes, M.*, et al.* (2012). Driver mutations in histone H3.3 and chromatin remodelling genes in paediatric glioblastoma. Nature *482*, 226-231.

Schweitzer, S., Kunz, M., Kurlbaum, M., Vey, J., Kendl, S., Deutschbein, T., Hahner, S., Fassnacht, M., Dandekar, T., and Kroiss, M. (2019). Plasma steroid metabolome profiling for the diagnosis of adrenocortical carcinoma. Eur J Endocrinol *180*, 117-125.

Scollo, C., Russo, M., Trovato, M.A., Sambataro, D., Giuffrida, D., Manusia, M., Sapuppo, G., Malandrino, P., Vigneri, R., and Pellegriti, G. (2016). Prognostic Factors for Adrenocortical Carcinoma Outcomes. Front Endocrinol (Lausanne) *7*, 99.

Seamon, K.B., Padgett, W., and Daly, J.W. (1981). Forskolin: unique diterpene activator of adenylate cyclase in membranes and in intact cells. Proc Natl Acad Sci U S A *78*, 3363-3367.

Segal, N.H., Parsons, D.W., Peggs, K.S., Velculescu, V., Kinzler, K.W., Vogelstein, B., and Allison, J.P. (2008). Epitope landscape in breast and colorectal cancer. Cancer Res *68*, 889-892.

Seidel, E., Walenda, G., Messerschmidt, C., Obermayer, B., Peitzsch, M., Wallace, P., Bahethi, R., Yoo, T., Choi, M., Schrade, P.*, et al.* (2020). Generation and characterization of a mitotane-resistant adrenocortical cell line. Endocr Connect *9*, 122-134.

Shao, Z., Zhang, Y., Yuan, G.C., Orkin, S.H., and Waxman, D.J. (2012). MAnorm: a robust model for quantitative comparison of ChIP-Seq data sets. Genome Biol *13*, R16.

Sharifi, N., Gulley, J.L., and Dahut, W.L. (2005). Androgen deprivation therapy for prostate cancer. JAMA *294*, 238-244.

Shen, X., Kim, W., Fujiwara, Y., Simon, M.D., Liu, Y., Mysliwiec, M.R., Yuan, G.C., Lee, Y., and Orkin, S.H. (2009). Jumonji modulates polycomb activity and self-renewal versus differentiation of stem cells. Cell *139*, 1303-1314.

Shen, X., Liu, Y., Hsu, Y.J., Fujiwara, Y., Kim, J., Mao, X., Yuan, G.C., and Orkin, S.H. (2008). EZH1 mediates methylation on histone H3 lysine 27 and complements EZH2 in maintaining stem cell identity and executing pluripotency. Mol Cell *32*, 491-502.

Shibamoto, S., Higano, K., Takada, R., Ito, F., Takeichi, M., and Takada, S. (1998). Cytoskeletal reorganization by soluble Wnt-3a protein signalling. Genes Cells *3*, 659-670.

Shinjo, S.K., Oba-Shinjo, S.M., Lerario, A.M., and Marie, S.K.N. (2018). A Brazilian family with inclusion body myopathy associated with Paget's disease of bone and frontotemporal dementia linked to the VCP pGly97Glu mutation. Clin Rheumatol *37*, 1129-1136.

Shumacher, A., Faust, C., and Magnuson, T. (1996). Positional cloning of a global regulator of anterior-posterior patterning in mice. Nature *383*, 250-253.

Sidler, D., Renzulli, P., Schnoz, C., Berger, B., Schneider-Jakob, S., Flück, C., Inderbitzin, D., Corazza, N., Candinas, D., and Brunner, T. (2011). Colon cancer cells produce immunoregulatory glucocorticoids. Oncogene *30*, 2411-2419.

Simard, J., Ricketts, M.L., Gingras, S., Soucy, P., Feltus, F.A., and Melner, M.H. (2005). Molecular biology of the 3beta-hydroxysteroid dehydrogenase/delta5-delta4 isomerase gene family. Endocr Rev *26*, 525-582.

Sneeringer, C.J., Scott, M.P., Kuntz, K.W., Knutson, S.K., Pollock, R.M., Richon, V.M., and Copeland, R.A. (2010). Coordinated activities of wild-type plus mutant EZH2 drive tumor-associated hypertrimethylation of lysine 27 on histone H3 (H3K27) in human B-cell lymphomas. Proc Natl Acad Sci U S A *107*, 20980-20985.

Squazzo, S.L., O'Geen, H., Komashko, V.M., Krig, S.R., Jin, V.X., Jang, S.W., Margueron, R., Reinberg, D., Green, R., and Farnham, P.J. (2006). Suz12 binds to silenced regions of the genome in a cell-type-specific manner. Genome Res *16*, 890-900.

Stambolic, V., Ruel, L., and Woodgett, J.R. (1996). Lithium inhibits glycogen synthase kinase-3 activity and mimics wingless signalling in intact cells. Curr Biol *6*, 1664-1668.

Stark, R., and Brown, G. (2011). DiffBind: differential binding analysis of ChIP-Seq peak data.

Steward, F.C.a.M.M.O.a.M.K. (1958). GROWTH AND ORGANIZED DEVELOPMENT OF CULTURED CELLS. II. Organization in Cultures Grown from Freely Suspended Cell. American Journal of Botany *45*, 705-708.

Struhl, G. (1981). A gene product required for correct initiation of segmental determination in Drosophila. Nature *293*, 36-41.

Stuart, T., Butler, A., Hoffman, P., Hafemeister, C., Papalexi, E., Mauck, W.M., Hao, Y., Stoeckius, M., Smibert, P., and Satija, R. (2019). Comprehensive Integration of Single-Cell Data. Cell *177*, 1888-1902.e1821.

Su, I.H., Basavaraj, A., Krutchinsky, A.N., Hobert, O., Ullrich, A., Chait, B.T., and Tarakhovsky, A. (2003). Ezh2 controls B cell development through histone H3 methylation and Igh rearrangement. Nat Immunol *4*, 124-131.

Subramanian, A., Tamayo, P., Mootha, V.K., Mukherjee, S., Ebert, B.L., Gillette, M.A., Paulovich, A., Pomeroy, S.L., Golub, T.R., Lander, E.S.*, et al.* (2005). Gene set enrichment analysis: a knowledge-based approach for interpreting genome-wide expression profiles. Proc Natl Acad Sci U S A *102*, 15545-15550.

Suh, I., Weng, J., Fernandez-Ranvier, G., Shen, W.T., Duh, Q.Y., Clark, O.H., and Kebebew, E. (2010). Antineoplastic effects of decitabine, an inhibitor of DNA promoter methylation, in adrenocortical carcinoma cells. Arch Surg *145*, 226-232.

Sun, R., Limkin, E.J., Vakalopoulou, M., Dercle, L., Champiat, S., Han, S.R., Verlingue, L., Brandao, D., Lancia, A., Ammari, S.*, et al.* (2018). A radiomics approach to assess tumour-infiltrating CD8 cells and response to anti-PD-1 or anti-PD-L1 immunotherapy: an imaging biomarker, retrospective multicohort study. Lancet Oncol *19*, 1180-1191.

Sun, Z., Wu, Y., Ordog, T., Baheti, S., Nie, J., Duan, X., Hojo, K., Kocher, J.P., Dyck, P.J., and Klein, C.J. (2014). Aberrant signature methylome by DNMT1 hot spot mutation in hereditary sensory and autonomic neuropathy 1E. Epigenetics *9*, 1184-1193.

Supek, F., Bošnjak, M., Škunca, N., and Šmuc, T. (2011). REVIGO summarizes and visualizes long lists of gene ontology terms. PLoS One *6*, e21800.

Surani, M.A., Barton, S.C., and Norris, M.L. (1984). Development of reconstituted mouse eggs suggests imprinting of the genome during gametogenesis. Nature *308*, 548-550.

Suzuki, T., Takahashi, K., Darnel, A.D., MoriyaT, Murakami, O., Narasaka, T., Takeyama, J., and Sasano, H. (2000). Chicken ovalbumin upstream promoter transcription factor II in the human adrenal cortex and its disorders. J Clin Endocrinol Metab *85*, 2752-2757.

Szpiech, Z.A., Mak, A.C.Y., White, M.J., Hu, D., Eng, C., Burchard, E.G., and Hernandez, R.D. (2019). Ancestry-Dependent Enrichment of Deleterious Homozygotes in Runs of Homozygosity. Am J Hum Genet *105*, 747-762.

Tabbal, H., Septier, A., Mathieu, M., Drelon, C., Rodriguez, S., Djari, C., Batisse-Lignier, M., Tauveron, I., Pointud, J.C., Sahut-Barnola, I.*, et al.* (2019). EZH2 cooperates with E2F1 to stimulate expression of genes involved in adrenocortical carcinoma aggressiveness. British Journal of Cancer *121*, 384-394.

Takeuchi, T., Kojima, M., Nakajima, K., and Kondo, S. (1999). jumonji gene is essential for the neurulation and cardiac development of mouse embryos with a C3H/He background. Mech Dev *86*, 29-38.

Takeuchi, T., Yamazaki, Y., Katoh-Fukui, Y., Tsuchiya, R., Kondo, S., Motoyama, J., and Higashinakagawa, T. (1995). Gene trap capture of a novel mouse gene, jumonji, required for neural tube formation. Genes Dev *9*, 1211-1222.

Tan, A., Abecasis, G.R., and Kang, H.M. (2015). Unified representation of genetic variants. Bioinformatics *31*, 2202-2204.

Tanay, A., O'Donnell, A.H., Damelin, M., and Bestor, T.H. (2007). Hyperconserved CpG domains underlie Polycomb-binding sites. Proc Natl Acad Sci U S A *104*, 5521-5526.

Tang, Z., Li, C., Kang, B., Gao, G., and Zhang, Z. (2017). GEPIA: a web server for cancer and normal gene expression profiling and interactive analyses. Nucleic Acids Res *45*, W98-W102.

Tao, Y., Kang, B., Petkovich, D.A., Bhandari, Y.R., In, J., Stein-O'Brien, G., Kong, X., Xie, W., Zachos, N., Maegawa, S.*, et al.* (2019). Aging-like Spontaneous Epigenetic Silencing Facilitates Wnt Activation, Stemness, and Braf. Cancer Cell *35*, 315-328.e316.

Taube, J.M., Klein, A., Brahmer, J.R., Xu, H., Pan, X., Kim, J.H., Chen, L., Pardoll, D.M., Topalian, S.L., and Anders, R.A. (2014). Association of PD-1, PD-1 ligands, and other features of the tumor immune microenvironment with response to anti-PD-1 therapy. Clin Cancer Res *20*, 5064-5074.

Team, H. Hail 0.2.13-81ab564db2b4.

Team, R.C. (2016). R: A language and environment for statistical computing (Vienna, Austria: R Foundation for Statistical Computing).

Terzolo, M., Angeli, A., Fassnacht, M., Daffara, F., Tauchmanova, L., Conton, P.A., Rossetto, R., Buci, L., Sperone, P., Grossrubatscher, E.*, et al.* (2007). Adjuvant mitotane treatment for adrenocortical carcinoma. N Engl J Med *356*, 2372-2380.

Terzolo, M., Baudin, A.E., Ardito, A., Kroiss, M., Leboulleux, S., Daffara, F., Perotti, P., Feelders, R.A., deVries, J.H., Zaggia, B.*, et al.* (2013). Mitotane levels predict the outcome of patients with adrenocortical carcinoma treated adjuvantly following radical resection. Eur J Endocrinol *169*, 263-270.

Thompson, R.H., Dong, H., Lohse, C.M., Leibovich, B.C., Blute, M.L., Cheville, J.C., and Kwon, E.D. (2007). PD-1 is expressed by tumor-infiltrating immune cells and is associated with poor outcome for patients with renal cell carcinoma. Clin Cancer Res *13*, 1757-1761.

Thorsson, V., Gibbs, D.L., Brown, S.D., Wolf, D., Bortone, D.S., Ou Yang, T.H., Porta-Pardo, E., Gao, G.F., Plaisier, C.L., Eddy, J.A.*, et al.* (2018). The Immune Landscape of Cancer. Immunity *48*, 812-830.e814.

Tischler, G., and Leonard, S. (2014). biobambam: tools for read pair collation based algorithms on BAM files. Source Code Biol Med *9*, 1-18.

Tissier, F., Cavard, C., Groussin, L., Perlemoine, K., Fumey, G., Hagneré, A.M., René-Corail, F., Jullian, E., Gicquel, C., Bertagna, X.*, et al.* (2005). Mutations of beta-catenin in adrenocortical tumors: activation of the Wnt signaling pathway is a frequent event in both benign and malignant adrenocortical tumors. Cancer Res *65*, 7622-7627.

Tokumaru, Y., Yamashita, K., Osada, M., Nomoto, S., Sun, D.I., Xiao, Y., Hoque, M.O., Westra, W.H., Califano, J.A., and Sidransky, D. (2004). Inverse correlation between cyclin A1 hypermethylation and p53 mutation in head and neck cancer identified by reversal of epigenetic silencing. Cancer Res *64*, 5982-5987.

Topalian, S.L., Hodi, F.S., Brahmer, J.R., Gettinger, S.N., Smith, D.C., McDermott, D.F., Powderly, J.D., Carvajal, R.D., Sosman, J.A., Atkins, M.B.*, et al.* (2012). Safety, activity, and immune correlates of anti-PD-1 antibody in cancer. N Engl J Med *366*, 2443-2454.

Topalian, S.L., Taube, J.M., Anders, R.A., and Pardoll, D.M. (2016). Mechanism-driven biomarkers to guide immune checkpoint blockade in cancer therapy. Nat Rev Cancer *16*, 275-287.

Topper, M.J., Vaz, M., Marrone, K.A., Brahmer, J.R., and Baylin, S.B. (2020). The emerging role of epigenetic therapeutics in immuno-oncology. Nat Rev Clin Oncol *17*, 75-90.

Tran, E., Robbins, P.F., Lu, Y.C., Prickett, T.D., Gartner, J.J., Jia, L., Pasetto, A., Zheng, Z., Ray, S., Groh, E.M.*, et al.* (2016). T-Cell Transfer Therapy Targeting Mutant KRAS in Cancer. N Engl J Med *375*, 2255-2262.

Trapnell, C., Cacchiarelli, D., Grimsby, J., Pokharel, P., Li, S., Morse, M., Lennon, N.J., Livak, K.J., Mikkelsen, T.S., and Rinn, J.L. (2014). The dynamics and regulators of cell fate decisions are revealed by pseudotemporal ordering of single cells. Nat Biotechnol *32*, 381-386.

Trejter, M., Hochol, A., Tyczewska, M., Ziolkowska, A., Jopek, K., Szyszka, M., Malendowicz, L.K., and Rucinski, M. (2015). Visinin-like peptide 1 in adrenal gland of the rat. Gene expression and its hormonal control. Peptides *63*, 22-29.

Tumeh, P.C., Harview, C.L., Yearley, J.H., Shintaku, I.P., Taylor, E.J., Robert, L., Chmielowski, B., Spasic, M., Henry, G., Ciobanu, V.*, et al.* (2014). PD-1 blockade induces responses by inhibiting adaptive immune resistance. Nature *515*, 568-571.

Turcan, S., Rohle, D., Goenka, A., Walsh, L.A., Fang, F., Yilmaz, E., Campos, C., Fabius, A.W., Lu, C., Ward, P.S.*, et al.* (2012). IDH1 mutation is sufficient to establish the glioma hypermethylator phenotype. Nature *483*, 479-483.

Val, P., Martinez-Barbera, J.P., and Swain, A. (2007). Adrenal development is initiated by Cited2 and Wt1 through modulation of Sf-1 dosage. Development *134*, 2349-2358.

Valencia, A.M., Collings, C.K., Dao, H.T., St Pierre, R., Cheng, Y.C., Huang, J., Sun, Z.Y., Seo, H.S., Mashtalir, N., Comstock, D.E.*, et al.* (2019). Recurrent SMARCB1 Mutations Reveal a Nucleosome Acidic Patch Interaction Site That Potentiates mSWI/SNF Complex Chromatin Remodeling. Cell *179*, 1342-1356.e1323.

van Iterson, M., Tobi, E.W., Slieker, R.C., den Hollander, W., Luijk, R., Slagboom, P.E., and Heijmans, B.T. (2014). MethylAid: visual and interactive quality control of large Illumina 450k datasets. Bioinformatics *30*, 3435-3437.

van Weerden, W.M., Bierings, H.G., van Steenbrugge, G.J., de Jong, F.H., and Schröder, F.H. (1992). Adrenal glands of mouse and rat do not synthesize androgens. Life Sci *50*, 857-861.

Varghese, J., and Habra, M.A. (2017). Update on adrenocortical carcinoma management and future directions. Curr Opin Endocrinol Diabetes Obes *24*, 208-214.

Vasques, G.A., Hisado-Oliva, A., Funari, M.F., Lerario, A.M., Quedas, E.P., Solberg, P., Heath, K.E., and Jorge, A.A. (2017). Long-term response to growth hormone therapy in a patient with short stature caused by a novel heterozygous mutation in NPR2. J Pediatr Endocrinol Metab *30*, 111-116.

Vaz, M., Hwang, S.Y., Kagiampakis, I., Phallen, J., Patil, A., O'Hagan, H.M., Murphy, L., Zahnow, C.A., Gabrielson, E., Velculescu, V.E.*, et al.* (2017). Chronic Cigarette Smoke-Induced Epigenomic Changes Precede Sensitization of Bronchial Epithelial Cells to Single-Step Transformation by KRAS Mutations. Cancer Cell *32*, 360-376.e366.

Veloso, M.P., Neves, P.D.M.M., Jorge, L.B., Dias, C.B., Yu, L., Pinheiro, R.B.B., Testagrossa, L.A., Malheiros, D.M., Balbo, B.E.P., Lerário, A.M.*, et al.* (2017). Female Patient with Alport Syndrome and Concomitant Membranous Nephropathy: Susceptibility or Association of Two Diseases? Nephron *136*, 158-162.

Vidal, V., Sacco, S., Rocha, A.S., da Silva, F., Panzolini, C., Dumontet, T., Doan, T.M., Shan, J., Rak-Raszewska, A., Bird, T.*, et al.* (2016). The adrenal capsule is a signaling center controlling cell renewal and zonation through Rspo3. Genes Dev *30*, 1389-1394.

Vilain, R.E., Menzies, A.M., Wilmott, J.S., Kakavand, H., Madore, J., Guminski, A., Liniker, E., Kong, B.Y., Cooper, A.J., Howle, J.R.*, et al.* (2017). Dynamic Changes in PD-L1 Expression and Immune Infiltrates Early During Treatment Predict Response to PD-1 Blockade in Melanoma. Clin Cancer Res *23*, 5024-5033.

Vinson, G.P. (2016). Functional Zonation of the Adult Mammalian Adrenal Cortex. Front Neurosci *10*, 238.

Viré, E., Brenner, C., Deplus, R., Blanchon, L., Fraga, M., Didelot, C., Morey, L., Van Eynde, A., Bernard, D., Vanderwinden, J.M., *et al.* (2006). The Polycomb group protein EZH2 directly controls DNA methylation. Nature *439*, 871-874.

Visakorpi, T., Hyytinen, E., Koivisto, P., Tanner, M., Keinänen, R., Palmberg, C., Palotie, A., Tammela, T., Isola, J., and Kallioniemi, O.P. (1995). In vivo amplification of the androgen receptor gene and progression of human prostate cancer. Nat Genet *9*, 401-406.

Visvader, J.E. (2011). Cells of origin in cancer. Nature *469*, 314-322.

Wajchenberg, B.L., Albergaria Pereira, M.A., Medonca, B.B., Latronico, A.C., Campos Carneiro, P., Alves, V.A., Zerbini, M.C., Liberman, B., Carlos Gomes, G., and Kirschner, M.A. (2000). Adrenocortical carcinoma: clinical and laboratory observations. Cancer *88*, 711-736.

Walczak, E.M., Kuick, R., Finco, I., Bohin, N., Hrycaj, S.M., Wellik, D.M., and Hammer, G.D. (2014). Wnt signaling inhibits adrenal steroidogenesis by cell-autonomous and non-cell-autonomous mechanisms. Mol Endocrinol *28*, 1471-1486.

Walter, M.J., Shen, D., Ding, L., Shao, J., Koboldt, D.C., Chen, K., Larson, D.E., McLellan, M.D., Dooling, D., Abbott, R., *et al.* (2012). Clonal architecture of secondary acute myeloid leukemia. N Engl J Med *366*, 1090-1098.

Wang, H., Maurano, M.T., Qu, H., Varley, K.E., Gertz, J., Pauli, F., Lee, K., Canfield, T., Weaver, M., Sandstrom, R., *et al.* (2012). Widespread plasticity in CTCF occupancy linked to DNA methylation. Genome Res *22*, 1680-1688.

Wang, L., Zhang, J., Duan, J., Gao, X., Zhu, W., Lu, X., Yang, L., Li, G., Ci, W., Li, W., *et al.* (2014). Programming and inheritance of parental DNA methylomes in mammals. Cell *157*, 979-991.

Wang, T., and Rainey, W.E. (2012). Human adrenocortical carcinoma cell lines. Mol Cell Endocrinol *351*, 58-65.

Wang, X., Paucek, R.D., Gooding, A.R., Brown, Z.Z., Ge, E.J., Muir, T.W., and Cech, T.R. (2017). Molecular analysis of PRC2 recruitment to DNA in chromatin and its inhibition by RNA. Nat Struct Mol Biol *24*, 1028-1038.

Wang, Y., Yang, J., Zheng, H., Tomasek, G.J., Zhang, P., McKeever, P.E., Lee, E.Y., and Zhu, Y. (2009). Expression of mutant p53 proteins implicates a lineage relationship between neural stem cells and malignant astrocytic glioma in a murine model. Cancer Cell *15*, 514-526.

Wang, Z., Civelek, M., Miller, C.L., Sheffield, N.C., Guertin, M.J., and Zang, C. (2018). BART: a transcription factor prediction tool with query gene sets or epigenomic profiles. Bioinformatics *34*, 2867-2869.

Ward, P.S., Patel, J., Wise, D.R., Abdel-Wahab, O., Bennett, B.D., Coller, H.A., Cross, J.R., Fantin, V.R., Hedvat, C.V., Perl, A.E.*, et al.* (2010). The common feature of leukemia-associated IDH1 and IDH2 mutations is a neomorphic enzyme activity converting alpha-ketoglutarate to 2-hydroxyglutarate. Cancer Cell *17*, 225-234.

Wassef, M., Luscan, A., Aflaki, S., Zielinski, D., Jansen, P.W.T.C., Baymaz, H.I., Battistella, A., Kersouani, C., Servant, N., Wallace, M.R.*, et al.* (2019). EZH1/2 function mostly within canonical PRC2 and exhibit proliferation-dependent redundancy that shapes mutational signatures in cancer. Proc Natl Acad Sci U S A *116*, 6075-6080.

Weinberg, D.N., Papillon-Cavanagh, S., Chen, H., Yue, Y., Chen, X., Rajagopalan, K.N., Horth, C., McGuire, J.T., Xu, X., Nikbakht, H.*, et al.* (2019). The histone mark H3K36me2 recruits DNMT3A and shapes the intergenic DNA methylation landscape. Nature *573*, 281-286.

Weiss, L.M., Medeiros, L.J., and Vickery, A.L., Jr. (1989). Pathologic features of prognostic significance in adrenocortical carcinoma. Am J Surg Pathol *13*, 202-206.

Whyte, W.A., Orlando, D.A., Hnisz, D., Abraham, B.J., Lin, C.Y., Kagey, M.H., Rahl, P.B., Lee, T.I., and Young, R.A. (2013). Master transcription factors and mediator establish super-enhancers at key cell identity genes. Cell *153*, 307-319.

Wickham, H. (2016). ggplot2: Elegant Graphics for Data Analysis (Springer-Verlag New York).

Wiese, K.E., Nusse, R., and van Amerongen, R. (2018). Wnt signalling: conquering complexity. Development *145*.

Wilhelm, D., and Englert, C. (2002). The Wilms tumor suppressor WT1 regulates early gonad development by activation of Sf1. Genes Dev *16*, 1839-1851.

Williams, T.A., Monticone, S., Crudo, V., Warth, R., Veglio, F., and Mulatero, P. (2012). Visinin-like 1 is upregulated in aldosterone-producing adenomas with KCNJ5 mutations and protects from calcium-induced apoptosis. Hypertension *59*, 833-839.

Wilson, B.G., Wang, X., Shen, X., McKenna, E.S., Lemieux, M.E., Cho, Y.J., Koellhoffer, E.C., Pomeroy, S.L., Orkin, S.H., and Roberts, C.W. (2010). Epigenetic antagonism between polycomb and SWI/SNF complexes during oncogenic transformation. Cancer Cell *18*, 316-328.

Wilson, T.E., Mouw, A.R., Weaver, C.A., Milbrandt, J., and Parker, K.L. (1993). The orphan nuclear receptor NGFI-B regulates expression of the gene encoding steroid 21-hydroxylase. Mol Cell Biol *13*, 861-868.

Wong, T.N., Ramsingh, G., Young, A.L., Miller, C.A., Touma, W., Welch, J.S., Lamprecht, T.L., Shen, D., Hundal, J., Fulton, R.S.*, et al.* (2015). Role of TP53 mutations in the origin and evolution of therapy-related acute myeloid leukaemia. Nature *518*, 552-555.

Wood, M.A., Acharya, A., Finco, I., Swonger, J.M., Elston, M.J., Tallquist, M.D., and Hammer, G.D. (2013). Fetal adrenal capsular cells serve as progenitor cells for steroidogenic and stromal adrenocortical cell lineages in M. musculus. Development *140*, 4522-4532.

Wortzel, R.D., Philipps, C., and Schreiber, H. (1983). Multiple tumour-specific antigens expressed on a single tumour cell. Nature *304*, 165-167.

Wu, G., Broniscer, A., McEachron, T.A., Lu, C., Paugh, B.S., Becksfort, J., Qu, C., Ding, L., Huether, R., Parker, M.*, et al.* (2012). Somatic histone H3 alterations in pediatric diffuse intrinsic pontine gliomas and non-brainstem glioblastomas. Nat Genet *44*, 251-253.

Xiang, Y., Tanaka, Y., Patterson, B., Hwang, S.M., Hysolli, E., Cakir, B., Kim, K.Y., Wang, W., Kang, Y.J., Clement, E.M.*, et al.* (2020). Dysregulation of BRD4 Function Underlies the Functional Abnormalities of MeCP2 Mutant Neurons. Mol Cell *79*, 84-98.e89.

Xie, H., Xu, J., Hsu, J.H., Nguyen, M., Fujiwara, Y., Peng, C., and Orkin, S.H. (2014). Polycomb repressive complex 2 regulates normal hematopoietic stem cell function in a developmental-stage-specific manner. Cell Stem Cell *14*, 68-80.

Xie, W., Kagiampakis, I., Pan, L., Zhang, Y.W., Murphy, L., Tao, Y., Kong, X., Kang, B., Xia, L., Carvalho, F.L.F.*, et al.* (2018). DNA Methylation Patterns Separate Senescence from Transformation Potential and Indicate Cancer Risk. Cancer Cell *33*, 309-321.e305.

Xing, Y., Edwards, M.A., Ahlem, C., Kennedy, M., Cohen, A., Gomez-Sanchez, C.E., and Rainey, W.E. (2011). The effects of ACTH on steroid metabolomic profiles in human adrenal cells. J Endocrinol *209*, 327-335.

Xu, J., Shao, Z., Li, D., Xie, H., Kim, W., Huang, J., Taylor, J.E., Pinello, L., Glass, K., Jaffe, J.D.*, et al.* (2015). Developmental control of polycomb subunit composition by GATA factors mediates a switch to non-canonical functions. Mol Cell *57*, 304-316.

Xu, K., Wu, Z.J., Groner, A.C., He, H.H., Cai, C., Lis, R.T., Wu, X., Stack, E.C., Loda, M., Liu, T.*, et al.* (2012). EZH2 oncogenic activity in castration-resistant prostate cancer cells is Polycomb-independent. Science *338*, 1465-1469.

Yagi, M., Kabata, M., Tanaka, A., Ukai, T., Ohta, S., Nakabayashi, K., Shimizu, M., Hata, K., Meissner, A., Yamamoto, T.*, et al.* (2020). Identification of distinct loci for de novo DNA methylation by DNMT3A and DNMT3B during mammalian development. Nat Commun *11*, 3199.

Yakulov, T., Raggioli, A., Franz, H., and Kemler, R. (2013). Wnt3a-dependent and -independent protein interaction networks of chromatin-bound β-catenin in mouse embryonic stem cells. Mol Cell Proteomics *12*, 1980-1994.

Yamamichi-Nishina, M., Ito, T., Mizutani, T., Yamamichi, N., Watanabe, H., and Iba, H. (2003). SW13 cells can transition between two distinct subtypes by switching expression of BRG1 and Brm genes at the post-transcriptional level. J Biol Chem *278*, 7422-7430.

Yang, D., Jang, I., Choi, J., Kim, M.S., Lee, A.J., Kim, H., Eom, J., Kim, D., Jung, I., and Lee, B. (2018). 3DIV: A 3D-genome Interaction Viewer and database. Nucleic Acids Res *46*, D52-D57.

Yang, H., Berry, S., Olsson, T.S.G., Hartley, M., Howard, M., and Dean, C. (2017). Distinct phases of Polycomb silencing to hold epigenetic memory of cold in. Science *357*, 1142-1145.

Yang, X., Lu, X., Lombès, M., Rha, G.B., Chi, Y.I., Guerin, T.M., Smart, E.J., and Liu, J. (2010). The G(0)/G(1) switch gene 2 regulates adipose lipolysis through association with adipose triglyceride lipase. Cell Metab *11*, 194-205.

Yasumura, Y., Buonassisi, V., and Sato, G. (1966). Clonal analysis of differentiated function in animal cell cultures. I. Possible correlated maintenance of differentiated function and the diploid karyotype. Cancer Res *26*, 529-535.

Yim, C.Y., Bikorimana, E., Khan, E., Warzecha, J.M., Shin, L., Rodriguez, J., Dmitrovsky, E., Freemantle, S.J., and Spinella, M.J. (2017). G0S2 represses PI3K/mTOR signaling and increases sensitivity to PI3K/mTOR pathway inhibitors in breast cancer. Cell Cycle *16*, 2146-2155.

Yim, C.Y., Sekula, D.J., Hever-Jardine, M.P., Liu, X., Warzecha, J.M., Tam, J., Freemantle, S.J., Dmitrovsky, E., and Spinella, M.J. (2016). G0S2 Suppresses Oncogenic Transformation by Repressing a MYC-Regulated Transcriptional Program. Cancer Res *76*, 1204-1213.

Yin, J., Leavenworth, J.W., Li, Y., Luo, Q., Xie, H., Liu, X., Huang, S., Yan, H., Fu, Z., Zhang, L.Y.*, et al.* (2015). Ezh2 regulates differentiation and function of natural killer cells through histone methyltransferase activity. Proc Natl Acad Sci U S A *112*, 15988-15993.

Yoshihara, K., Shahmoradgoli, M., Martínez, E., Vegesna, R., Kim, H., Torres-Garcia, W., Treviño, V., Shen, H., Laird, P.W., Levine, D.A.*, et al.* (2013). Inferring tumour purity and stromal and immune cell admixture from expression data. Nat Commun *4*, 2612.

Young, M.D., Wakefield, M.J., Smyth, G.K., and Oshlack, A. (2010). Gene ontology analysis for RNA-seq: accounting for selection bias. Genome Biol *11*, R14.

Yu, G., Wang, L.G., and He, Q.Y. (2015). ChIPseeker: an R/Bioconductor package for ChIP peak annotation, comparison and visualization. Bioinformatics *31*, 2382-2383.

Zamudio, A.V., Dall'Agnese, A., Henninger, J.E., Manteiga, J.C., Afeyan, L.K., Hannett, N.M., Coffey, E.L., Li, C.H., Oksuz, O., Sabari, B.R.*, et al.* (2019). Mediator Condensates Localize Signaling Factors to Key Cell Identity Genes. Mol Cell *76*, 753-766.e756.

Zemach, A., McDaniel, I.E., Silva, P., and Zilberman, D. (2010). Genome-wide evolutionary analysis of eukaryotic DNA methylation. Science *328*, 916-919.

Zemach, A., and Zilberman, D. (2010). Evolution of eukaryotic DNA methylation and the pursuit of safer sex. Curr Biol *20*, R780-785.

Zern, N.K., Eaton, K.D., and Roth, M.Y. (2019). Aldosterone-Secreting Adrenocortical Carcinoma Presenting With Cardiac Arrest. J Endocr Soc *3*, 1678-1681.

Zheng, S., Cherniack, A.D., Dewal, N., Moffitt, R.A., Danilova, L., Murray, B.A., Lerario, A.M., Else, T., Knijnenburg, T.A., Ciriello, G.*, et al.* (2016). Comprehensive Pan-Genomic Characterization of Adrenocortical Carcinoma. Cancer Cell *29*, 723-736.

Zhu, P., Wang, Y., Huang, G., Ye, B., Liu, B., Wu, J., Du, Y., He, L., and Fan, Z. (2016). lnc-β-Catm elicits EZH2-dependent β-catenin stabilization and sustains liver CSC self-renewal. Nat Struct Mol Biol *23*, 631-639.

Zubair, M., Parker, K.L., and Morohashi, K. (2008). Developmental links between the fetal and adult zones of the adrenal cortex revealed by lineage tracing. Mol Cell Biol *28*, 7030-7040.

Åkerström, T., Maharjan, R., Sven Willenberg, H., Cupisti, K., Ip, J., Moser, A., Stålberg, P., Robinson, B., Alexander Iwen, K., Dralle, H.*, et al.* (2016). Activating mutations in CTNNB1 in aldosterone producing adenomas. Sci Rep *6*, 19546.